



JAEA-Review
2008-045

JAEA-Review

Review of JT-60U Experimental Results in 2005 and 2006

The JT-60 Team

Fusion Research and Development Directorate

October 2008

Japan Atomic Energy Agency

日本原子力研究開発機構

本レポートは独立行政法人日本原子力研究開発機構が不定期に発行する成果報告書です。
本レポートの入手並びに著作権利用に関するお問い合わせは、下記あてにお問い合わせ下さい。
なお、本レポートの全文は日本原子力研究開発機構ホームページ (<http://www.jaea.go.jp>)
より発信されています。

独立行政法人日本原子力研究開発機構 研究技術情報部 研究技術情報課
〒319-1195 茨城県那珂郡東海村白方白根 2 番地 4
電話 029-282-6387, Fax 029-282-5920, E-mail:ird-support@jaea.go.jp

This report is issued irregularly by Japan Atomic Energy Agency
Inquiries about availability and/or copyright of this report should be addressed to
Intellectual Resources Section, Intellectual Resources Department,
Japan Atomic Energy Agency
2-4 Shirakata Shirane, Tokai-mura, Naka-gun, Ibaraki-ken 319-1195 Japan
Tel +81-29-282-6387, Fax +81-29-282-5920, E-mail:ird-support@jaea.go.jp

© Japan Atomic Energy Agency, 2008

Review of JT-60U Experimental Results in 2005 and 2006

The JT-60 Team

Division of Advanced Plasma Research and Division of Tokamak System Technology
Fusion Research and Development Directorate, Japan Atomic Energy Agency
Naka-shi, Ibaraki-ken

(Received July 24,2008)

The results from the JT-60U experiments in 2005 and 2006 are reviewed. In this experimental campaign, significant progress has been made in development of steady-state advanced tokamak scenarios leading to realization of attractive fusion reactors and establishment of the physics basis for ITER. Ferritic steel tiles have been installed to reduce the toroidal field ripple and reduce fast ion losses. Thus increase of the net NB heating power and enhancement of controllability of the toroidal plasma rotation by reduction of the counter plasma rotation drive has enabled to expand the high-performance operation limits. High normalized beta ($\beta_N \sim 4.2$) exceeding the no-wall ideal limit has been achieved in high β_p ELMy H-mode plasmas with a large volume configuration, in which the wall stabilization and the heating power increase by the reduction of the ripple losses is effective. Moreover, the experimental result has shown that the critical plasma rotation velocity for stabilization of the resistive wall mode is $\sim 0.3\%$ of the Alfvén velocity, which is much smaller compared with the previous prediction. High normalized beta ($\beta_N \sim 2.3$) together with high confinement ($HH_{98(y,2)} \sim 1$) has been sustained for 23.1 s, which is significantly longer than the current diffusion time ($\sim 12 \tau_R$), in high β_p ELMy H-mode plasmas. The experimental result has revealed that the duration of the confinement improvement is limited by recycling enhancement and density increase owing to decrease in the wall-pumping rate. On the other hand, in high-density ELMy H-mode discharges, the density control for ~ 30 s without the wall pumping has been successfully demonstrated by the divertor pumping. Controllability of reversed shear plasmas with high bootstrap current fraction has been also investigated to establish efficient control of the self-regulating plasmas in fusion reactors. Furthermore, physics oriented research have been performed in various aspects. Extension of the injection pulse length of the ECRF and N-NB heating to 21 s and development of new diagnostic systems with high-temporal high-spatial resolution contributed the successful experiments.

Keywords:

Fusion Reactor, Tokamak, JT-60U, Advanced Tokamak, Steady-State Operation, Ripple Loss, Ferritic Steel Tile, Plasma Rotation, Normalized Beta, Bootstrap Current, Divertor

Editors: Hirotaka KUBO, Yutaka KAMADA, Nobuyuki ASAKURA, Shunsuke IDE,
Kei MASAKI, Naoyuki OYAMA, Manabu TAKECHI, Hidenobu TAKENAGA

The JT-60 Team

N.Aiba¹⁾, H.Akasaka, N.Akino, T.Ando²⁾, K.Anno, T.Arai, N.Asakura, N.Ashikawa³⁾, H.Azechi⁴⁾, M.Azumi, L.Bruskin⁵⁾, S.Chiba, T.Cho⁶⁾, B. J.Ding⁷⁾, N.Ebisawa, T.Fujii, K.Fujimoto¹⁾, T.Fujita, T.Fukuda⁴⁾, M.Fukumoto⁴⁾, A.Fukuyama⁸⁾, H.Funaba³⁾, M.Furukawa⁹⁾, H.Furukawa¹⁰⁾, P.Gohil¹¹⁾, Y.Gotoh¹⁰⁾, L.Grisham¹²⁾, S.Haga¹⁰⁾, K.Hamamatsu, T.Hamano¹⁰⁾, K.Hanada¹³⁾, K.Hasegawa, H.Hashizume¹⁴⁾, T.Hatae, A.Hatayama¹⁵⁾, T.Hayashi¹⁰⁾, N.Hayashi, T.Hayashi, H.Higaki⁶⁾, S.Higashijima, U.Higashizono⁶⁾, T.Hino¹⁶⁾, T.Hiraishi¹⁷⁾, S.Hiranai, Y.Hirano¹⁸⁾, H.Hiratsuka, Y.Hirohata¹⁶⁾, J.Hobirk¹⁹⁾, M.Honda⁸⁾, A.Honda, M.Honda, H.Horiike⁴⁾, K.Hoshino, N.Hosogane, H.Hosoyama¹⁰⁾, H.Ichige, M.Ichimura⁶⁾, K.Ida³⁾, S.Ide, T.Idehara²⁰⁾, H.Idei¹³⁾, Y.Idomura, K.Igarashi¹⁰⁾, S.Iio²¹⁾, Y.Ikeda, T.Imai⁶⁾, S.Inagaki³⁾, D.Inoue⁶⁾, A.Inoue¹⁰⁾, M.Isaka, A.Isayama, S.Ishida, K.Ishii¹⁰⁾, Y.Ishii, M.Ishikawa¹⁴⁾, Y.Ishimoto¹⁾, K.Itami, T.Itoga¹⁴⁾, Sanae Itoh¹³⁾, Satoshi Itoh¹³⁾, K.Iwasaki¹⁰⁾, Y.Kagei¹⁾, S.Kajiyama²²⁾, S.Kakinoto⁶⁾, M.Kamada¹⁾, Y.Kamada, A.Kaminaga, K.Kamiya, S.Kasai, K.Kashiwa, K.Katayama¹³⁾, T.Kato³⁾, M.Kawai, Y.Kawamata, Y.Kawano, T.Kawasaki¹³⁾, H.Kawashima, M.Kazawa, K.Kikuchi¹⁰⁾, H.Kikuchi¹⁰⁾, M.Kikuchi, A.Kimura⁸⁾, H.Kimura²³⁾, H.Kimura, Y.Kishimoto⁸⁾, S.Kitamura, K.Kiyono, K.Kizu, N.Kobatake²²⁾, S.Kobayashi⁸⁾, Y.Kobayashi⁸⁾, M.Kobayashi¹⁰⁾, T.Kobuchi³⁾, K.Kodama, Y.Kogil³⁾, Y.Koide, A.Kojima¹⁾, S.Kokubo¹⁷⁾, S.Kokusen¹⁰⁾, M.Komata, A.Komori³⁾, T.Kondoh, S.Konishi⁸⁾, S.Konoshima, S.Konovaliv²⁴⁾, A.Koyama⁸⁾, M.Koyanagitsu²³⁾, T.Kubo⁴⁾, H.Kubo, Y.Kudoh, R.Kurihara, K.Kurihara, G.Kurita, M.Kuriyama, Y.Kusama, N.Kusanagi¹⁰⁾, J.Li²⁴⁾, J.Lönnroth²⁵⁾, T.Luce¹¹⁾, T.Maekawa⁸⁾, K.Masaki, A.Mase¹³⁾, M.Matsukawa, T.Matsumoto, M.Matsuoka²⁶⁾, Y.Matsuzawa¹⁰⁾, H.Matsumura¹⁰⁾, G.Matsunaga¹⁾, K.Meguro¹⁰⁾, K.Mima⁴⁾, O.Mitarai²⁷⁾, Y.Y.Miura⁴⁾, Y.Miura, N.Miya, S.Miyamoto⁴⁾, A.Miyamoto¹⁰⁾, N.Miyato, H.Miyauchi²³⁾, Y.Miyo, R.Mizuuchi⁸⁾, K.Mogaki, Y.Morimoto²³⁾, S.Moriyama, M.Nagami, Y.Nagasaka²²⁾, K.Nagasaki⁸⁾, Y.Nagase¹³⁾, S.Nagaya, Y.Nagayama³⁾, H.Naito²⁸⁾, O.Naito, T.Nakahata²³⁾, N.Nakajima³⁾, Y.Nakamura³⁾, K.Nakamura¹³⁾, T.Nakano, Y.Nakashima⁶⁾, M.Nakatsuka⁴⁾, M.Nakazato¹⁰⁾, Y.Narushima³⁾, R.Nazikian¹²⁾, H.Ninomiya, M.Nishikawa¹³⁾, K.Nishimura³⁾, N.Nishino²⁹⁾, T.Nishitani, T.Nishiyama, Y.Nobuta¹⁾, N.Noda³⁾, K.Noto¹⁰⁾, H.Nuga⁹⁾, K.Oasa, T.Obuchi³⁾, Y.Ogawa⁹⁾, I.Ogawa²⁰⁾, H.Ogawa, T.Ohga²⁾, N.Ohno¹⁷⁾, K.Ohshima¹⁰⁾, K.Ohya³⁰⁾, T.Oikawa, A.Oikawa, M.Okabayashi¹²⁾, N.Okamoto¹⁷⁾, K.Okano³¹⁾, F.Okano, J.Okano, K.Okuno²³⁾, Y.Omori, A.Onoshi²³⁾, Y.Ono⁹⁾, H.Oohara, T.Oshima, Y.Oya⁹⁾, N.Oyama, T.Ozeki, V.Parail²⁵⁾, H.Parchamy³⁾, B.J.Peterson³⁾, G. D.Porter³²⁾, Y.Sadamoto³³⁾, A.Sagara³⁾, G.Saibene³⁴⁾, T.Saito⁶⁾, M.Sakamoto¹³⁾, Y.Sakamoto, A.Sakasai, S.Sakata, T.Sakuma¹⁰⁾, S.Sakurai, T.Sasajima, M.Sasao¹⁴⁾, F.Sato¹⁰⁾, M.Sato, K.Sawada³⁵⁾, M.Sawahata, M.Seimiya, M.Seki, J. P.Sharpe³⁶⁾, T.Shibahara¹⁷⁾, K.Shibata¹⁰⁾, T.Shibata, T.Shiina, R.Shimada²¹⁾, K.Shimada, A.Shimizu¹³⁾, K.Shimizu, M.Shimizu, K.Shimomura²¹⁾, M.Shimono, K.Shinohara, S.Shinozaki, S.Shiraiwa⁹⁾, M.Shitomi, S.Sudo³⁾, M.Sueoka, A.Sugawara¹⁰⁾, T.Sugie,

K.Sugiyama¹⁷⁾, A.M.Sukegawa, H.Sunaoshi, Masaei Suzuki¹⁰⁾, Mitsuhiro Suzuki¹⁰⁾, Yutaka Suzuki¹⁰⁾, S.Suzuki, Yoshio Suzuki, T.Suzuki, M.Takahashi¹⁰⁾, R.Takahashi¹⁰⁾, K.Takahashi¹⁰⁾, S.Takamura¹⁷⁾, S.Takano¹⁰⁾, Y.Takase⁹⁾, M.Takechi, N.Takei, T.Takeishi¹³⁾, H.Takenaga, T.Takenouchi¹⁰⁾, T.Takizuka, H.Tamai, N.Tamura³⁾, T.Tanabe¹³⁾, Y.Tanai¹⁰⁾, S.Tanaka⁸⁾, J.Tanaka⁸⁾, S.Tanaka⁹⁾, T.Tani, K.Tani, H.Terakado¹⁰⁾, M.Terakado, T.Terakado, K.Toi³⁾, S.Tokuda, T.Totsuka, Y.Toudo³⁾, N.Tsubota¹⁰⁾, K.Tsuchiya, Y.Tsukahara, K.Tsutsumi¹⁰⁾, K.Tsuzuki, T.Tuda, T.Uda³⁾, Y.Ueda⁴⁾, T.Uehara¹⁰⁾, K.Uehara, Y.Ueno⁸⁾, Y.Uesugi³⁷⁾, N.Umeda, H.Urano, K.Urata¹⁰⁾, M.Ushigome⁹⁾, K.Usui, K.Wada¹⁰⁾, M.Wade¹¹⁾, K.Watanabe³⁾, T.Watari³⁾, M.Yagi¹³⁾, Y.Yagi¹⁸⁾, H.Yagisawa¹⁰⁾, J.Yagyu, H.Yamada³⁾, Y.Yamamoto⁸⁾, T.Yamamoto, Y.Yamashita¹⁰⁾, K.Yamazaki³⁾, H.Yamazaki¹⁰⁾, K.Yatsu⁶⁾, K.Yokokura, I.Yonekawa²⁾, M.Yoshida¹⁾, H.Yoshida⁴⁾, N.Yoshida¹³⁾, M.Yoshida¹³⁾, H.Yoshida¹⁶⁾, H.Yoshida, A.Yoshikawa²³⁾, M.Yoshinuma³⁾, H.Zushi¹³⁾

1) Post-Doctoral Fellow, 2) Nippon Advanced Technology Co.Ltd., Japan, 3) National Institute for Fusion Science, Japan, 4) Osaka University, Japan, 5) Japan Society of the Promotion of Science Invitation Fellowship, 6) University of Tsukuba, Japan, 7) Southwestern Institute of Physics, China, 8) Kyoto University, Japan, 9) The University of Tokyo, Japan, 10) Staff on loan, 11) General Atomics, USA, 12) Princeton Plasma Physics Laboratory, USA, 13) Kyushu University, Japan, 14) Tohoku University, Japan, 15) Keio University, Japan, 16) Hokkaido University, Japan, 17) Nagoya University, Japan, 18) National Institute of Advanced Industrial Science and Technology, Japan, 19) Max-Planck-Institut fur Plasmaphysik, Germany, 20) Fukui University, Japan, 21) Tokyo Institute of Technology, Japan, 22) Hiroshima Institute of Technology, Japan, 23) Shizuoka University, Japan, 24) JAERI Fellow, 25) Euratom/UKAEA Association, UK, 26) Mie University, Japan, 27) Kyushu Tokai University, Japan, 28) Yamaguchi University, Japan, 29) Hiroshima University, Japan, 30) Tokushima University, 31) Central Research Institute of Electric Power Industry, Japan, 32) Lawrence Livermore National Laboratory, USA, 33) Joetsu University of Education, 34) EFDA Closed Support Unit, Germany, 35) Shinshu University, Japan, 36) Idaho National Engineering and Environmental Laboratory, USA, 37) Kanazawa University, Japan

JT-60U 実験結果のレビュー (2005 年～2006 年)

日本原子力研究開発機構核融合研究開発部門
先進プラズマ研究開発ユニット・トカマクシステム技術開発ユニット
JT-60 チーム

(2008 年 7 月 24 日 受理)

2005年及び2006年のJT-60Uの実験結果をレビューする。本実験期間では、魅力ある核融合炉の実現とITERの物理基盤の確立に向けて、先進定常トカマクシナリオの開発において大きな進展を得た。トロイダル磁場リップルを低減して高速イオン損失を低減するために、フェライト鋼板を設置した。この結果、中性粒子ビーム加熱の加熱パワーが実効的に増加し、またプラズマ電流と反対方向のプラズマ回転駆動の減少によってトロイダルプラズマ回転の制御性が增大することによって、高性能運転の領域拡大が可能になった。自由境界理想MHD限界を超える高規格化ベータ値($\beta_N \sim 4.2$)を、壁安定化とリップル損失低減による加熱パワーの増大が有効な大体積配位の高 β_p ELMy Hモードプラズマにおいて達成した。更に、抵抗性壁モードの安定化に必要なプラズマ回転速度が従来の予想より非常に小さい（アルベン速度の約0.3%）ことを発見した。また、高 β_p ELMy Hモードプラズマにおいて、高規格化ベータ値($\beta_N \sim 2.3$)と高閉じ込め改善度($HH_{98(y,2)} \sim 1$)を、電流拡散時間より十分に長い時間（23.1秒間、電流拡散時間の約12倍）同時に維持することに成功した。ここでは、壁排気速度の減少によるリサイクリングの増大と密度の上昇によって閉じ込め改善の時間が制限されることがわかった。一方で、高密度のELMy Hモード放電では、壁排気がない状態でダイバータ排気を用いて約30秒間の密度制御を実証した。核融合炉の自律性の高いプラズマの効率的な制御を確立するために、ブートストラップ電流割合の高い負磁気シアプラズマの制御性に関する研究も進めた。更に、種々の観点において物理的研究を進めた。上記の実験成果を達成するうえにおいて、電子サイクロトロン加熱および負イオン源中性粒子ビーム加熱の入射時間の伸長（21秒間）、及び高時間・高空間分解能を有する新しい計測装置の開発が寄与した。

那珂核融合研究所（駐在）：〒311-0193 茨城県那珂市向山 801-1

編集者：久保 博孝、鎌田 裕、朝倉 伸幸、井手 俊介、正木 圭、大山 直幸、
武智 学、竹永 秀信

JT-60 チーム

相羽 信行¹⁾, 赤坂 博美, 秋野 昇, 安藤 俊就²⁾, 安納 勝人, 新井 貴, 朝倉 伸幸, 芦川 直子³⁾, 畦地 宏⁴⁾, 安積 正史, L.Bruskin⁵⁾, 千葉 真一, 長 照二⁶⁾, Ding, B. J.⁷⁾, 海老沢 昇, 藤井 常幸, 藤本 加代子¹⁾, 藤田 隆明, 福田 武司⁴⁾, 福本 正勝⁴⁾, 福山 淳⁸⁾, 舟場 久芳³⁾, 古川 勝⁹⁾, 古川 弘¹⁰⁾, P.Gohil¹¹⁾, 後藤 純孝¹⁰⁾, L.Grisham¹²⁾, 芳賀 三郎¹⁰⁾, 濱松 清隆, 濱野 隆¹⁰⁾, 花田 和明¹³⁾, 長谷川 浩一, 橋爪 秀利¹⁴⁾, 波多江 仰紀, 畑山 明聖¹⁵⁾, 林 利光¹⁰⁾, 林 伸彦, 林 孝夫, 檜垣 浩之⁶⁾, 東島 智, 東園 雄大⁶⁾, 日野 友明¹⁶⁾, 平石 剛大¹⁷⁾, 平内 慎一, 平野 洋一¹⁸⁾, 平塚 一, 廣畑 優子¹⁶⁾, Hobirk, J.¹⁹⁾, 本多 充⁸⁾, 本田 敦, 本田 正男, 堀池 寛⁴⁾, 星野 克道, 細金 延幸, 細山 博己¹⁰⁾, 市毛 尚志, 市村 真⁶⁾, 居田 克巳³⁾, 井手 俊介, 出原 敏孝²⁰⁾, 出射 浩¹³⁾, 井戸村 泰宏, 五十嵐 浩一¹⁰⁾, 飯尾 俊二²¹⁾, 池田 佳隆, 今井 剛⁶⁾, 稲垣 滋³⁾, 井上 大輔⁶⁾, 井上 昭¹⁰⁾, 井坂 正義, 諫山 明彦, 石田 真一, 石井 和宏¹⁰⁾, 石井 康友, 石川 正男¹⁴⁾, 石本 祐樹¹⁾, 伊丹 潔, 糸賀 俊朗¹⁴⁾, 伊藤 早苗¹³⁾, 伊藤 智之¹³⁾, 岩崎 慶太¹⁰⁾, 影井 康弘¹⁾, 梶山 真治²²⁾, 柿本 真吾⁶⁾, 鎌田 正輝¹⁾, 鎌田 裕, 神永 敦嗣, 神谷 健作, 河西 敏, 柏 好敏, 片山 一成¹³⁾, 加藤 隆子³⁾, 河合 視己人, 川俣 陽一, 河野 康則, 川崎 貴史¹³⁾, 川島 寿人, 梶澤 稔, 菊池 勝美¹⁰⁾, 菊池 弘¹⁰⁾, 菊池 満, 木村 晃彦⁸⁾, 木村 宏美²³⁾, 木村 晴行, 岸本 泰明⁸⁾, 北村 繁, 清野 公広, 木津 要, 小畑 敬義²²⁾, 小林 進二⁸⁾, 小林 靖典⁸⁾, 小林 昌幸¹⁰⁾, 小淵 隆³⁾, 児玉 幸三, 近木 祐一郎¹³⁾, 小出 芳彦, 小島 有志¹⁾, 小久保 慎平¹⁷⁾, 石仙 茂晴¹⁰⁾, 小又 将夫, 小森 彰夫³⁾, 近藤 貴, 小西 哲之⁸⁾, 木島 滋, S.Konvalov²⁴⁾, 香山 晃⁸⁾, 小柳津 誠²³⁾, 久保 亨⁴⁾, 久保 博孝, 工藤 祐介, 栗原 良一, 栗原 研一, 栗田 源一, 栗山 正明, 草間 義紀, 草薨 直人¹⁰⁾, Jiqan Li²⁴⁾, J.Lönnroth²⁵⁾, T.C.Luce¹¹⁾, 前川 孝⁸⁾, 正木 圭, 間瀬 淳¹³⁾, 松川 誠, 松本 太郎, 松岡 守²⁶⁾, 松沢 行洋¹⁰⁾, 松村 宏¹⁰⁾, 松永 剛¹⁾, 目黒 和美¹⁰⁾, 三間 圀興⁴⁾, 御手洗 修²⁷⁾, 三浦 友史⁴⁾, 三浦 幸俊, 宮 直之, 宮本 斉児⁴⁾, 宮本 篤¹⁰⁾, 宮戸 直亮, 宮内 英夫²³⁾, 三代 康彦, 水内 亨⁸⁾, 藻垣 和彦, 森本 泰臣²³⁾, 森山 伸一, 永見 正幸, 長坂 康史²²⁾, 長崎 百伸⁸⁾, 永瀬 裕康¹³⁾, 永谷 進, 長山 好夫³⁾, 内藤 裕志²⁸⁾, 内藤 磨, 中畑 俊彦²³⁾, 中島 徳嘉³⁾, 中村 幸男³⁾, 中村 一男¹³⁾, 仲野 友英, 中島 洋輔⁶⁾, 中塚 正大⁴⁾, 中里 命¹⁰⁾, 成嶋 吉朗³⁾, R.Nazikian¹²⁾, 二宮 博正, 西川 正史¹³⁾, 西村 清彦³⁾, 西野 信博²⁹⁾, 西谷 健夫, 西山 友和, 信太 祐二¹⁾, 野田 信明³⁾, 能登 勝也¹⁰⁾, 奴賀 秀男⁹⁾, 大麻 和美, 小淵 隆³⁾, 小川 雄一⁹⁾, 小川 勇²⁰⁾, 小川 宏明, 大賀 徳道²⁾, 大野 哲靖¹⁷⁾, 大島 克己¹⁰⁾, 大宅 薫³⁰⁾, 及川 聡洋, 及川 晃, M.Okabayashi¹²⁾, 岡本 征晃¹⁷⁾, 岡野 邦彦³¹⁾, 岡野 文則, 岡野 潤, 奥野 健二²³⁾, 大森 栄和, 大西 祥広²³⁾, 小野 靖⁹⁾, 大原 比呂志, 大島 貴幸, 大矢 恭久⁹⁾, 大山 直幸, 小関 隆久, V.Parail²⁵⁾, H. Parchamy³⁾, B.J.Peterson³⁾, Porter, G. D.³²⁾, 定本 嘉郎³³⁾, 相良 明男³⁾,

G.Saibene³⁴⁾, 齊藤 輝雄⁶⁾, 坂本 瑞樹¹³⁾, 坂本 宜照, 逆井 章, 坂田 信也, 佐久間 猛¹⁰⁾, 櫻井 真治, 笹島 唯之, 笹尾 真実子¹⁴⁾, 佐藤 文明¹⁰⁾, 佐藤 稔, 澤田 圭司³⁵⁾, 沢島 正之, 清宮 宗孝, 関 正美, Sharpe, J. P.³⁶⁾, 柴原 孝宏¹⁷⁾, 柴田 一之¹⁰⁾, 柴田 孝俊, 椎名 富雄, 嶋田 隆一²¹⁾, 島田 勝弘, 清水 昭比古¹³⁾, 清水 勝宏, 清水 正亜, 下村 浩司²¹⁾, 下野 貢, 篠原 孝司, 篠崎 信一, 白岩 俊一⁹⁾, 薮 守正, 須藤 滋³⁾, 末岡 通治, 菅原 章博¹⁰⁾, 杉江 達夫, 杉山 一慶¹⁷⁾, 助川 篤彦, 砂押 秀則, 鈴木 昌栄¹⁰⁾, 鈴木 光博¹⁰⁾, 鈴木 優¹⁰⁾, 鈴木 貞明, 鈴木 善雄, 鈴木 隆博, 高橋 正己¹⁰⁾, 高橋 龍吉¹⁰⁾, 高橋 弘行¹⁰⁾, 高村 秀一¹⁷⁾, 高野 正二¹⁰⁾, 高瀬 雄一⁹⁾, 武智 学, 武井 奈帆子, 竹石 敏治¹³⁾, 竹永 秀信, 竹ノ内 忠¹⁰⁾, 滝塚 知典, 玉井 広史, 田村 直樹³⁾, 田辺 哲朗¹³⁾, 棚井 豊¹⁰⁾, 田中 茂利⁸⁾, 田中 仁⁸⁾, 田中 知⁹⁾, 谷 孝志, 谷 啓二, 寺門 祐之¹⁰⁾, 寺門 正之, 寺門 恒久, 東井 和夫³⁾, 徳田 伸二, 戸塚 俊之, 藤堂 泰³⁾, 坪田 直明¹⁰⁾, 土屋 勝彦, 塚原 美光, 堤 和昌¹⁰⁾, 都筑 和泰, 津田 孝, 宇田 達彦³⁾, 上田 良夫⁴⁾, 上原 聡明¹⁰⁾, 上原 和也, 上野 幸久⁸⁾, 上杉 喜彦³⁷⁾, 梅田 尚孝, 浦野 創, 浦田 一宏¹⁰⁾, 牛込 雅裕⁹⁾, 薄井 勝富, 和田 健次¹⁰⁾, M.Wade¹¹⁾, 渡邊 清政³⁾, 渡利 徹夫³⁾, 矢木 雅敏¹³⁾, 八木 康之¹⁸⁾, 八木 澤博¹⁰⁾, 柳生 純一, 山田 弘司³⁾, 山本 靖⁸⁾, 山本 巧, 山下 睦樹¹⁰⁾, 山崎 耕造³⁾, 山崎 晴幸¹⁰⁾, 谷津 潔⁶⁾, 横倉 賢治, 米川 出²⁾, 吉田 麻衣子¹⁾, 吉田 英次⁴⁾, 吉田 直亮¹³⁾, 吉田 雅史¹³⁾, 吉田 肇¹⁶⁾, 吉田 英俊, 吉河 朗²³⁾, 吉沼 幹朗³⁾, 凶子 秀樹¹³⁾

1) 博士研究員, 2) 日本アドバンステクノロジー (株), 3) 核融合科学研究所, 4) 大阪大学, 5) 日本学術振興会招聘フェロー, 6) 筑波大学, 7) 西南物理研究院, 中国, 8) 京都大学, 9) 東京大学, 10) 業務協力員, 11) ジェネラルアトムクス社, 米国, 12) プリンストンプラズマ物理研究所, 米国, 13) 九州大学, 14) 東北大学, 15) 慶応大学, 16) 北海道大学, 17) 名古屋大学, 18) 産業技術総合研究所, 19) マックスプランクプラズマ物理研究所, 独国, 20) 福井大学, 21) 東京工業大学, 22) 広島工業大学, 23) 静岡大学, 24) 原研リサーチフェロー, 25) イギリス原子力公社/欧州原子力共同体, 英国, 26) 三重大学, 27) 九州東海大学, 28) 山口大学, 29) 広島大学, 30) 徳島大学, 31) 電力中央研究所, 32) ローレンスリバモア国立研究所, 米国, 33) 上越教育大学, 34) 欧州核融合開発協定サポートユニット, 独国, 35) 信州大学, 36) アイダホ国立工学環境研究所, 米国, 37) 金沢大学

Contents

1. Introduction	
H. Kubo and Y. Kamada	1
2. Overview of Experimental Results	
2.1 Extension of Operation Regimes	
S. Ide	3
2.2 Transport in Core Plasmas	
H. Takenaga	3
2.3 H-mode Confinement and Pedestal	
N. Oyama	4
2.4 MHD Instability and High-energy Ions	
M. Takechi	5
2.5 Plasma Control and Operation	
H. Takenaga	6
2.6 Divertor and SOL Plasmas	
N. Asakura	7
2.7 Plasma Facing Materials	
K. Masaki	8
2.8 Diagnostics	
H. Kubo	8
2.9 Heating Systems	
S. Ide	9
3. Extension of Operation Regimes	
3.1 Improved Performance in Long-Pulse ELMy H-mode Plasmas with Internal Transport Barrier	
N. Oyama <i>et al.</i>	10
3.2 Achievement of the High Beta Plasma by Stabilization of Resistive Wall Mode	
M. Takechi <i>et al.</i>	11
3.3 Long Sustainment of Large Bootstrap Current Fraction Plasmas by Introducing New Real Time Control Logic	
Y. Sakamoto <i>et al.</i>	12
3.4 Evolution of Bootstrap-Sustained Discharge	
Y. Takase <i>et al.</i>	13
4. Transport in Core Plasmas	
4.1 Response of Large Bootstrap Current Plasma	
Y. Sakamoto <i>et al.</i>	14

4.2	Temporal Variation of Density Fluctuation and Transport in Reversed Shear Plasmas	
	H. Takenaga <i>et al.</i>	15
4.3	Observation on Decoupling of Electron Heat Transport and Long-spatial-scale Density Fluctuations in a Reversed Shear Plasma	
	H. Takenaga <i>et al.</i>	16
4.4	Dynamic Transport Study of the Plasmas with Transport Improvement in LHD and JT-60U	
	K. Ida <i>et al.</i>	17
4.5	Studies on Impact of Electron Cyclotron Wave Injection on the Internal Transport Barriers	
	S. Ide <i>et al.</i>	18
4.6	Physics of Strong Internal Transport Barriers in Reversed Shear Plasmas	
	N. Hayashi <i>et al.</i>	19
4.7	Effects of Low Central Fuelling on Density and Ion Temperature Profiles in Reversed Shear Plasmas	
	H. Takenaga <i>et al.</i>	20
4.8	Comparisons of Density Profiles in JT-60U Tokamak and LHD Helical Plasmas with Low Collisionality	
	H. Takenaga <i>et al.</i>	21
4.9	Study of Highly Ionized Xe Spectra in Reversed Shear Plasmas	
	H. Kubo <i>et al.</i>	22
4.10	Study of Impurity Injection Scenario in Burning Plasmas	
	H. Takenaga <i>et al.</i>	23
4.11	Effects of Ripple Loss of Fast Ions on Toroidal Rotation	
	M. Yoshida <i>et al.</i>	24
4.12	Momentum Transport and Toroidal Rotation Profile in L-mode plasmas	
	M. Yoshida <i>et al.</i>	25
4.13	Observation of Spontaneous Toroidal Rotation with Large Pressure Gradient	
	M. Yoshida <i>et al.</i>	26
4.14	Response of Toroidal Rotation Velocity to Electron Cyclotron Wave and Lower Hybrid Wave Injection	
	Y. Sakamoto <i>et al.</i>	27
5.	H-mode Confinement and Pedestal	
5.1	H-mode Pedestal Structure in the Variation of Toroidal Rotation and Toroidal Field Ripple	
	H. Urano <i>et al.</i>	28
5.2	Roles of Edge Toroidal Rotation, Toroidal Field Ripple and Configuration on ELM Characteristics	
	K. Kamiya <i>et al.</i>	29

5.3	Effect of Toroidal Field Ripple in JET/JT-60U Similarity Experiments N. Oyama <i>et al.</i>	33
5.4	ELM Frequency Dependence on Toroidal Rotation in the Grassy ELM Regime N. Oyama <i>et al.</i>	37
6.	MHD Instability and High-Energy Ions	
6.1	Control of Growth of Neoclassical Tearing Mode by Central Co-ECCD A. Isayama <i>et al.</i>	38
6.2	Stabilization of an $m/n=2/1$ Neoclassical Tearing Mode by Electron Cyclotron Current Drive A. Isayama <i>et al.</i>	39
6.3	Effect of Plasma-Wall Separation on the Stability of Resistive Wall Modes G. Matsunaga <i>et al.</i>	40
6.4	Identification of a Low Plasma-Rotation Threshold for Stabilization of the Resistive-Wall Mode M. Takechi <i>et al.</i>	41
6.5	Confinement Degradation and Transport of Energetic Ions due to RSAEs and TAEs in Weak Shear Plasmas M. Ishikawa <i>et al.</i>	42
6.6	Orbit Following Calculation of Energetic Ions in the Design of Ferritic Insertion K. Shinohara <i>et al.</i>	43
6.7	Observation of Spontaneously Excited Waves in the Ion Cyclotron Frequency Range M. Ichimura <i>et al.</i>	44
7.	Plasma Control and Operational Limit	
7.1	Plasma Shape Calculation in a Magnetic Environment with Ferritic Steel Tiles K. Shinohara <i>et al.</i>	45
7.2	Real-time Control of Current Profile in High-beta Plasmas T. Suzuki <i>et al.</i>	46
7.3	Off-axis NBCD Profile Measurement T. Suzuki <i>et al.</i>	47
7.4	Real-time Measurement and Feedback Control of Ion Temperature using Filter CXRS and RTP Systems M. Yoshida <i>et al.</i>	48
7.5	Real-time Control of Ion Temperature Gradient S. Kobayashi <i>et al.</i>	49
7.6	Burn Control Simulation Experiments K. Shimomura <i>et al.</i>	50

7.7	Response of Fusion Gain to Density in Burning Plasma Simulation	
	H. Takenaga <i>et al.</i>	51
7.8	Magnetic Flux Constant Control	
	H. Takenaga <i>et al.</i>	52
7.9	Plasma Current Start-up Experiment by ECH	
	T. Maekawa <i>et al.</i>	55
7.10	Interlock of Neutral Beam Injection for Small Dome-separatrix Gap	
	H. Takenaga <i>et al.</i>	59
7.11	Gas Fuelling from High-field-side in ELMy H-mode Plasmas	
	H. Takenaga <i>et al.</i>	62
7.12	Density Limit in Discharges with High Internal Inductance	
	H. Yamada <i>et al.</i>	66
8. Divertor and SOL Plasmas		
8.1	Particle Control in Long-pulse High-density H-mode Plasmas	
	T. Nakano <i>et al.</i>	67
8.2	Ar Injection under Wall Saturated Condition	
	N. Asakura <i>et al.</i>	69
8.3	Metal Impurity from the Ferritic Steel Tiles	
	T. Nakano <i>et al.</i>	71
8.4	Understanding the SOL Flow in L-mode Plasma on Divertor Tokamaks, and Its Influence on the Plasma Transport	
	N. Asakura <i>et al.</i>	74
8.5	ELM Propagation Characteristics in Scrape-Off Layer	
	N. Asakura <i>et al.</i>	75
8.6	ELM Propagation at High-Field-Side SOL and Divertor	
	N. Asakura <i>et al.</i>	76
8.7	Transient Response of Divertor Plasma during Transition to ELM Free H-Mode Phase	
	H. Takenaga <i>et al.</i>	80
8.8	Fluctuation Characteristics of the L-mode SOL Plasmas	
	N. Ohno <i>et al.</i>	81
8.9	Temporal Evolutions of Electron Temperature and Density with ELM in the Divertor Plasma	
	T. Nakano <i>et al.</i>	85
8.10	Revisited : Measurement of Chemical Sputtering Yields	
	T. Nakano <i>et al.</i>	90
8.11	Volume Recombination of C ⁴⁺ in Detached Divertor Plasmas	
	T. Nakano <i>et al.</i>	94
8.12	Ionizing and Recombining Components of Deuterium Emission in Detached Divertor Plasmas	
	K. Fujimoto <i>et al.</i>	96

8.13	Evaluation of the Electron Distribution Function for Detached Plasma Y. Sadamoto <i>et al.</i>	100
8.14	Modeling of Divertor Pumping Using SOLDOR/ NEUT2D Code H. Kawashima <i>et al.</i>	104
8.15	A New Fast Velocity-Diffusion Modelling for Impurity Transport in Integrated Edge Plasma Simulation K. Shimizu <i>et al.</i>	105
9. Plasma Facing Materials		
9.1	Hydrogen Retention and Carbon Deposition in Plasma Facing Wall and Shadowed Area K. Masaki <i>et al.</i>	106
9.2	Long-Term Erosion and Re-Deposition of Carbon in the Divertor Region Y. Gotoh <i>et al.</i>	107
9.3	Modeling of Asymmetric Redeposition Distribution between Inner and Outer Regions of W-Shaped Divertor K. Ohya <i>et al.</i>	108
9.4	Transport of Carbon Impurity using $^{13}\text{CH}_4$ Gas Puffing Y. Nobuta <i>et al.</i>	109
9.5	Distribution of Hydrogen Isotopes Retained in the Divertor Tiles Y. Hirohata <i>et al.</i>	113
9.6	Hydrogen Isotope Behavior in the First Wall after DD Discharge Y. Oya <i>et al.</i>	114
9.7	Deuterium Depth Profiling in JT-60U Tiles Using the $\text{D}(\text{}^3\text{He}, \text{p})\text{}^4\text{He}$ Resonant Nuclear Reaction T. Hayashi <i>et al.</i>	115
9.8	Ion Beam Analysis of H and D Retention in the Near Surface Layers of Plasma Facing Wall Tiles K. Sugiyama <i>et al.</i>	116
9.9	Surface Studies of Tungsten Erosion and Deposition Y. Ueda <i>et al.</i>	117
9.10	Light Elements Behavior in Fusion Devices Studies with JT-60 and Oxygen Discharge S. Konishi <i>et al.</i>	118
10. Diagnostics		
10.1	Modulation CXRS K. Ida <i>et al.</i>	119
10.2	Application of Phase Conjugate Mirror to Thomson Scattering Diagnostics T. Hatae <i>et al.</i>	120

10.3	Development of Polarization Interferometer Based on Fourier Transform Spectroscopy for Thomson Scattering Diagnostics T. Hatae <i>et al.</i>	121
10.4	Development of Fast Measurement System of Neutron Emission Profile Using a Digital Signal Processing Technique M. Ishikawa <i>et al.</i>	122
10.5	Density Fluctuation Measurement Using Motional Stark Effect Optics T. Suzuki <i>et al.</i>	123
10.6	Improvement of Tomography Technique for Two-Dimensional Visible Spectroscopic System of Divertor Plasmas K. Fujimoto <i>et al.</i>	124
10.7	Measurements of Dust Movement in Main Chamber and Divertor N. Asakura <i>et al.</i>	126
10.8	CO ₂ Laser for Collective Thomson Scattering Diagnostic of α -particles in Burning Plasmas T. Kondoh <i>et al.</i>	130
10.9	High-Brightness and Low-Divergence Ion Gun for Lithium Beam Zeeman Polarimetry A. Kojima <i>et al.</i>	132
10.10	Fast Data Acquisition System Based on Digital Oscilloscopes for Fluctuation Measurements in a Long-Pulse Plasma G. Matsunaga <i>et al.</i>	137
11.	Heating Systems	
11.1	A 21 s, 3.2 MW D ⁰ Beam Injection from Negative-Ion-Based NBI M. Hanada <i>et al.</i>	138
11.2	Oscillation Control on the ECRF System and Performance of the LHRF Launcher S. Moriyama <i>et al.</i>	139
	Acknowledgments	142

目次

1. 緒言		
久保、鎌田	1
2. 実験結果概要		
2.1 運転領域拡大		
井手	3
2.2 コアプラズマ輸送		
竹永	3
2.3 Hモード閉じ込め及びペデスタル特性		
大山	4
2.4 MHD不安定性及び高エネルギーイオン		
武智	5
2.5 プラズマ制御と運転限界		
竹永	6
2.6 ダイバータ及びSOLプラズマ		
朝倉	7
2.7 プラズマ対向壁材		
正木	8
2.8 計測装置		
久保	8
2.9 加熱装置		
井手	9
3. 運転領域拡大		
3.1 内部輸送障壁を持つ長時間ELMy Hモード放電の性能改善		
大山 他	10
3.2 抵抗性壁モードの抑制による高ベータプラズマの達成		
武智 他	11
3.3 新実時間制御による高自発電流割合プラズマの長時間維持		
坂本 他	12
3.4 ブートストラップ電流により維持された放電の時間発展		
高瀬 他	13
4. コアプラズマ輸送		
4.1 高自発電流割合プラズマの応答		
坂本 他	14
4.2 負磁気シアプラズマでの密度揺動と輸送の時間変化		
竹永 他	15
4.3 負磁気シアプラズマでの電子系熱輸送と長波長密度揺動との無相関性の観測		
竹永 他	16

4.4	LHD と JT-60U における輸送改善を伴うプラズマでの動的輸送研究 居田 他	17
4.5	電子サイクロトロン波入射の内部輸送障壁への影響に関する研究 井手 他	18
4.6	負磁気シアプラズマでの強い内部輸送障壁の物理 林 他	19
4.7	負磁気シアプラズマでの低中心粒子供給の密度およびイオン温度分布への影響 竹永 他	20
4.8	JT-60U トカマクと LHD ヘリカルプラズマにおける低衝突周波数領域での密度分布の比較 竹永 他	21
4.9	負磁気シアプラズマにおける高電離 Xe スペクトルの研究 久保 他	22
4.10	燃焼プラズマでの不純物入射シナリオの研究 竹永 他	23
4.11	高速イオンのリップル損失がトロイダル回転へ与える影響 吉田 他	24
4.12	L モードプラズマにおける運動量輸送とトロイダル回転分布 吉田 他	25
4.13	高圧力勾配領域での自発トロイダル回転の観測 吉田 他	26
4.14	電子サイクロトロン波と低域混成波入射に対するトロイダル回転速度の応答 坂本 他	27
5.	Hモード閉じ込め及びペデスタル特性	
5.1	トロイダル回転及びトロイダル磁場リップルによる H モードペデスタル構造特性 浦野 他	28
5.2	周辺部局在化モードにおけるトロイダル回転、トロイダルリップルおよび配位の役割 神谷 他	29
5.3	JET/JT-60U 相似実験におけるトロイダル磁場リップルの影響 大山 他	33
5.4	Grassy ELM 領域における ELM 周波数のトロイダル回転依存性 大山 他	37
6.	MHD 不安定性及び高エネルギーイオン	
6.1	中心 Co-ECCD による新古典テアリングモードの成長の制御 諫山 他	38

6.2	電子サイクロトロン電流駆動による $m/n=2/1$ 新古典テアリングモードの安定化	
	諫山 他	39
6.3	抵抗性壁モードの安定性に対するプラズマ-壁距離の効果	
	松永 他	40
6.4	抵抗性壁モードの安定化に対する低いプラズマ回転閾値の同定	
	武智 他	41
6.5	弱磁気シアプラズマにおける負磁気シアアルヴェン固有モードおよびトロイダルアルヴェン固有モードによる高エネルギーイオンの閉じ込め劣化及び輸送	
	石川 他	42
6.6	フェライト鋼挿入における高エネルギーイオンの軌道追跡計算	
	篠原 他	43
6.7	中性粒子ビーム入射時に自然に励起されるイオンサイクロトロン周波数帯の波動の観測	
	市村 他	44
7. プラズマ制御と運転限界		
7.1	フェライト鋼タイトルの磁場環境下におけるプラズマ形状計算	
	篠原 他	45
7.2	高ベータプラズマにおける電流分布の実時間制御	
	鈴木 他	46
7.3	周辺部 NBCD 分布計測	
	鈴木 他	47
7.4	フィルターCXRS と RTP システムを用いたイオン温度の実時間計測と制御	
	吉田 他	48
7.5	イオン温度勾配の実時間制御	
	小林 他	49
7.6	燃焼模擬実験	
	下村 他	50
7.7	燃焼模擬プラズマにおける核融合増倍率の密度変化に対する応答	
	竹永 他	51
7.8	磁気束一定制御	
	竹永 他	52
7.9	ECH によるプラズマ電流立ち上げ実験	
	前川 他	55
7.10	ドーム・セパトトリックス間距離による NB 加熱インターロック	
	竹永 他	59
7.11	ELMy H モードプラズマへの高磁場側からのガス供給	
	竹永 他	62
7.12	高内部インダクタンス放電での密度限界	
	山田 他	66

8.	ダイバータ及び SOL プラズマ	
8.1	長パルス高密度 H モードプラズマにおける粒子制御 仲野 他	67
8.2	壁飽和状態でのアルゴン入射実験 朝倉 他	69
8.3	フェライト鋼タイルからの金属不純物 仲野 他	71
8.4	トカマクにおける SOL プラズマ流の理解とプラズマ輸送への影響 朝倉 他	74
8.5	スクレイプオフ層における ELM プラズマ輸送特性 朝倉 他	75
8.6	高磁場側スクレイプオフ層およびダイバータにおける ELM 伝搬 朝倉 他	76
8.7	ELM フリー H モード状態への遷移時におけるダイバータプラズマの過渡応答 竹永 他	80
8.8	L モード SOL プラズマの揺動特性 大野 他	81
8.9	ダイバータプラズマにおける ELM に伴う電子温度と密度の時間変化 仲野 他	85
8.10	化学スパッタリング率の再評価 仲野 他	90
8.11	非接触ダイバータプラズマにおける C^{+} の体積再結合 仲野 他	94
8.12	非接触ダイバータプラズマにおける重水素原子発光の電離および再結合成分 藤本 他	96
8.13	デタッチプラズマにおける電子分布関数の評価 定本 他	100
8.14	SOLDOR/NEUT2D コードによるダイバータ排気のシミュレーション 川島 他	104
8.15	統合周辺プラズマの不純物輸送における高速な速度空間拡散モデリング 清水 他	105
9.	プラズマ対向壁材	
9.1	プラズマ対向機器及び影部における水素蓄積と炭素堆積 正木 他	106
9.2	ダイバータ部における炭素タイル表面の損耗・再堆積分布の長期的評価 後藤 他	107
9.3	W 型ダイバータにおける再堆積分布の内外非対称性のモデリング 大宅 他	108
9.4	$^{13}CH_4$ ガスパフを用いた炭素不純物輸送 信太 他	109

9.5	ダイバータタイル中の水素同位体分布 広畑 他	113
9.6	重水素放電後の第一壁中水素同位体挙動 大矢 他	114
9.7	D(³ He, p) ⁴ He 核反応分析法を用いたタイル中重水素深さ分析 林 他	115
9.8	プラズマ対向壁における H/D 蓄積のイオンビーム分析 杉山 他	116
9.9	タングステンの損耗と再堆積 上田 他	117
9.10	JT-60 放電と酸素放電による核融合装置中軽元素挙動 小西 他	118
10. 計測装置		
10.1	モジュレーション荷電交換分光 居田 他	119
10.2	位相共役鏡のトムソン散乱計測への応用 波多江 他	120
10.3	トムソン散乱計測のためのフーリエ変換分光に基づく偏向干渉計の開発 波多江 他	121
10.4	スチルベンシンチレータとフラッシュ ADC を用いた高速中性子束計測 石川 他	122
10.5	モーショナルシュタルク効果光学系を用いた密度揺動計測 鈴木 他	123
10.6	ダイバータプラズマの二次元可視分光測定に向けたトモグラフィー手法の改良 藤本 他	124
10.7	主容器及びダイバータにおけるダスト運動測定 朝倉 他	126
10.8	燃焼プラズマの α 粒子計測のための炭酸ガスレーザー協同トムソン散乱計測 近藤 他	130
10.9	周辺電流分布計測用高輝度低発散リチウムビームイオン銃の開発 小島 他	132
10.10	長時間放電に向けた揺動計測のためのデジタルオシロスコープを用いた高速データ収集系 松永 他	137
11. 加熱装置		
11.1	負イオン NBI 装置による 3.2 MW, 21 秒入射 花田 他	138

11.2 ECRF システムにおける発振制御と LHRF ランチャーの運転実績	
森山 他	139
謝辞	142

1. Introduction

The JT-60U project has been addressing development of steady-state advanced tokamak scenarios leading to realization of attractive fusion reactors and establishment of the physics basis for ITER. In the experimental campaign in 2005 and 2006, significant progress has been made in development of steady-state high- β operation towards JT-60SA and DEMO [1]. Ferritic steel tiles have been installed to reduce the toroidal field ripple and reduce fast ion losses. Thus increase of the net neutral beam (NB) heating power and enhancement of controllability of the toroidal plasma rotation by reduction of the counter plasma rotation drive has enabled to expand the high-performance operation limits, highlighted by achievement of a high normalized beta (β_N) exceeding the no-wall ideal limit and long sustainment of a high- β_N together with high confinement. An integrated research project focusing on the plasma rotation covering transport, stability, pedestal, and steady-state operation has been promoted by taking advantage of the various neutral beam injection (NBI), such as perpendicular and co- and counter-tangential injection. Controllability of advanced tokamak plasmas with high bootstrap current fraction has been also investigated to establish efficient control of the self-regulating plasmas in fusion reactors. Another key issue for the steady-state operation in future devices is particle control under wall saturation. The recycling and density control under wall saturation has been successfully demonstrated by the divertor pumping in long-pulse high-density ELMy H-mode discharges. Furthermore, physics oriented research that would lead to better predictive capability and optimization of plasma performance in future, have been performed in various aspects.

It should be stressed that the substantial achievement owes much to significant progress in performance of the heating devices, such as extension of the heating duration of negative-ion-based (NBI) and electron cyclotron range of frequency (ECRF). New diagnostic systems have also provided reliable data with high-temporal and high-spatial resolution. In addition, newly developed techniques of advanced plasma control have been successfully utilized.

For development of the physics basis for the burning plasmas in ITER, contribution to International Tokamak Physics Activity (ITPA) is also an important aspect of the JT-60U research. Most of research items in this experimental campaign have contributed to the ITPA topics, such as the transport physics, confinement database and modeling, edge pedestal physics, scrape-off-layer and divertor physics, magneto hydrodynamic (MHD), steady state operation, and diagnostics. Domestic collaboration with universities and National Institute for Fusion Science (NIFS) has been promoted, since the JT-60U tokamak was assigned as a core national device for fusion research by the Nuclear Fusion Working Group of the Special Committee on Basic Issues of the Subdivision on Science in the Science Council in January,

2003. The experiment was successfully planned by the theme leaders and the co-leaders for the sub-themes including professionals of universities and NIFS*.

Reference

[1] Takenaga, H. and the JT-60 Team, Nucl. Fusion **47**, S563 (2007).

* Theme Leaders:

Y. Kamada, H. Kubo, and Y. Miura¹⁾.

1) until March, 2006.

Co-Leaders for Sub-Themes:

S. Ide and Y. Takase¹⁾ for Extension of Operation Regime and Improvement of Performance,

H. Takenaga and K. Ida²⁾ for Transport,

N. Oyama and T. Mizuuchi³⁾ for Pedestal,

M. Takechi and K. Toi²⁾ for MHD and Energetic Particle,

N. Asakura and N. Ohno⁴⁾ for Divertor and SOL,

K. Masaki and T. Tanabe⁵⁾ for Plasma Material Interaction.

1) The University of Tokyo, 2) National Institute for Fusion Science,

3) Kyoto University, 4) Nagoya University, 5) Kyushu University.

2. Overview of Experimental Results

2.1 Extension of Operation Regimes

Owing to the installation of ferritic steel tiles (FSTs), which cover ~10% of the vacuum vessel surface, net heating power increased. This increased flexibility in heating and input torque controls. As the result, sustained duration of $\beta_N=2.3$ has been extended to 28.6s by eliminating the neoclassical tearing modes (NTMs). In this plasma, a peaked pressure profile without NTMs and detectable sawteeth was kept throughout the discharge. The improved core confinement provided high $\beta_N H_H > 2.2$ with a bootstrap current fraction of $\geq 40\%$ sustained for 23.1s ($\sim 12 \beta_R$) at $q_{95} \sim 3.3$, which gives a high G-factor (larger than 0.2). These long-pulse plasmas are possible candidates for the ITER hybrid operation scenario. The increase in the net heating power allowed us to explore higher β_N regime. Towards the high β_N regime, the resistive wall mode (RWM) is limiting the access. It was found that RWM can be suppressed by rotating a plasma in toroidal direction. By increased NB deposition power, suppressing RWM and raising ideal wall limit by controlling plasma profile, we successfully achieved high $\beta_N \sim 4.2$ exceeding ideal limit at $l_i < 1.2$ and $V_p > 70 \text{m}^3$ ($\beta_N \sim 3.4$ w/o FST). A large bootstrap current fraction ($f_{BS} \sim 75\%$) is required for the concept of steady-state fusion tokamak reactor. By utilizing the real time control logic, a large $f_{BS} \sim 70\%$ was sustained for ~ 8 s and a high confinement enhancement factor over the H-mode scaling $HH_{98y2} \sim 1.8$ was obtained. In the later 3 s of this plasma, the q profile becomes flat in the core region due to the penetration of the inductive current with keeping the good ITB. The profile of the internal loop voltage evaluated from the equilibrium reconstruction using MSE measurement is flattened in time, indicating the plasma approached the stationary condition. Further large $f_{BS} \sim 100\%$ or even higher has also been achieved. A loop voltage profile of nearly zero or slightly negative across the cross section was maintained for 0.2 s in a discharge with constant OH primary current. In this discharge, of the total I_p of 543 kA, the calculated beam driven current was ~ 35 kA and the inductive current was ~ 5 kA. In the newly implemented constant plasma surface flux feedback mode, which ensures no net flux input to the plasma, a steady I_p ramp up at a rate of 10 kA/s was achieved for 0.5 s. These results provide evidence of bootstrap overdrive.

2.2 Transport in Core Plasmas

A dynamic change in the current profile (q_{\min} value and its location) was induced by a change in the pressure profile in the RS plasmas with the high bootstrap current fraction of 70%. The ITB radius moved in the wake of the q_{\min} location. These observations indicated a strong linkage between the pressure and current profiles. Further reduction of the transport was induced by the external perturbations such as a pellet or electron cyclotron (EC) wave injection after the strong ITB formation in the RS plasmas. After the pellet injection, the O-mode reflectometer signal was drastically reduced, indicating reduction of the density fluctuations with a wave number of the order of 1 cm^{-1} . The ion thermal diffusivity and the effective particle diffusivity decreased by one order of magnitude. However, the electron thermal diffusivity remained constant. The transient electron heat transport analysis also

indicated decoupling of the electron heat transport and the measured density fluctuations. After the EC wave injection, when no reduction of the O-mode reflectometer signal was observed, the electron thermal diffusivity decreased by a factor of $\sim 2-3$, while decreases in the ion thermal diffusivity and the effective particle diffusivity were small. In the weak shear plasmas, the EC wave injection entailed a degradation of the T_i -ITB. This degradation became smaller for a higher plasma current and was less sensitive to the EC deposition (on- or off-axis). The scaling for the energy confinement inside the ITB in RS plasmas was studied through the modeling on the 1.5D transport simulation. It was found that the scaling is equivalent to a saturation value of the core poloidal beta due to the MHD equilibrium. Effects of low central fuelling on the n_e and T_i -ITBs were investigated in RS plasmas. Similar n_e and T_i -ITBs were observed with both low and high central fuelling rate. The density profile was also less sensitive to the particle source distribution in the ELMy H-mode plasmas. On the other hand, the density peaking factor increased with decreasing the collisionality. High Z impurity transport was also investigated in RS plasmas. Several lines for Xe XLI and XLII were newly identified. Soft X-ray emission profiles indicated that the accumulation of the Xe ions is larger than that of C, Ne and Ar ions. The less ctr-rotation with perp-NBs was observed in the large volume configuration by installing the FSTs as a consequence of the reduction in the ripple losses in the peripheral region. The method of the transient momentum transport analysis was developed for the estimation of the toroidal momentum transport coefficients, where perturbation of the ctr-rotation was introduced by the modulated perp-NB injection through the ripple losses. The toroidal momentum diffusivity χ_ϕ was estimated to be 2-25 m²/s at $r/a \sim 0.6$ in the L-mode plasmas, which was comparable to the ion thermal diffusivity. The convection velocity V_{conv} was in the range from 0 to -12 m/s at $r/a \sim 0.6$. The toroidal rotation profile in the core region was almost reproduced by using the evaluated χ_ϕ and V_{conv} in the case with a small pressure gradient. In the case with a large pressure gradient, the measured toroidal rotation profile was shifted toward ctr-direction from the reproduced one, which could be explained by the effect of the spontaneous rotation.

2.3 H-mode Confinement and Pedestal

Since the performance of ELMy H-mode plasmas can be determined by the performance of pedestal, it is important to understand what physics determines the pedestal performance for the better prediction of pedestal plasmas in ITER. In addition to this, mitigation of instantaneous ELM heat load should be established to achieve required lifetime of divertor target plates in ITER. To address these issues, various experiments have been performed. Effects of toroidal field ripple on the pedestal performance and ELM characteristics were investigated by comparing with and without ferritic steel tiles (FSTs) using various plasma configurations including JET/JT-60U similarity configuration. As a co-toroidal rotation increased, the pedestal pressure tends to increase except for JET/JT-60U similarity configuration. Especially in large plasma configuration where toroidal field ripple without FSTs was large ($\sim 2\%$), improvement of the pedestal pressure was observed even at fixed toroidal rotation indicating distinct effect of toroidal field ripple. As for the size of type I ELMs, on the other hand, normalized ELM size to the pedestal stored energy ($\Delta W_{\text{ELM}}/W_{\text{ped}}$)

decreased with increasing counter rotation in all configurations. The fact that there was a systematic difference in the variation of $\Delta W_{\text{ELM}}/W_{\text{ped}}$ as a function of toroidal rotation indicated that the plasma configuration itself, such as the plasma shape, aspect ratio and other hidden parameters, is one of the important parameters to determine the ELM characteristics rather than the toroidal field ripple. ELM frequency dependence in grassy ELM regime ($\delta > 0.5$ and $q_{95} > 6$) was investigated in terms of the toroidal rotation at the pedestal and total poloidal beta (β_p). As the counter rotation increased, the ELM frequency clearly increased up to ~ 1400 Hz independent of β_p from 0.84 to 1.88. Even in the no-rotating plasma with balanced-NBIs similar to ITER condition, higher ELM frequency of ~ 400 Hz has been observed without large energy loss (less than 1% of pedestal stored energy). QH-mode experiment as an inter-machine experiment with DIII-D was performed to understand the mechanism of QH mode transition with co-NBIs. The new CXRS system revealed that similar depth of E_r well of ~ 40 kV/m was observed both in ELM phase (just before an ELM) and QH phase in JT-60U in contrast to DIII-D, where deeper E_r well of ~ 100 kV/m has been observed. By making use of recent improvement of edge diagnostics with fast time resolution, studies of ELM dynamics have been progressed. Just after a current ramp up, a higher pedestal pressure could be achieved together with larger type I ELMs, which may relate to the improvement of edge stability.

2.4 MHD Instability and High-energy Ions

Growth of an NTM with poloidal mode number $m = 3$ and toroidal mode number $n = 2$ has been suppressed by ECCD inside the sawtooth inversion radius in the co-direction. Stabilization of an $m/n = 2/1$ NTM by ECCD at the mode rational surface has been demonstrated with a small ratio of the current density driven by the electron cyclotron wave to the local bootstrap current density (~ 0.5). An $m/n = 2/1$ NTM can be completely stabilized with the misalignment of the ECCD location less than about half of the full island width, and that the $m/n = 2/1$ NTM is destabilized with the misalignment comparable to the full island width.

To clarify the effect of the plasma-wall separation on the stability of the resistive wall modes (RWM), current-driven RWM experiments in the ohmic plasmas have been performed. The plasma-wall separation was systematically changed, and it is found that the growth rates became smaller with decreasing the plasma-wall separation. Additionally, the observed growth rates have been compared with the AEOLUS-FT code. The dependence of the observed growth rate on the wall position is in qualitative agreement with these numerical results. The plasma rotation necessary for stabilization of RWMs is investigated by controlling the toroidal plasma rotation with external momentum input by injection of tangential neutral beams. The observed threshold is 0.3% of the Alfvén velocity and much smaller than the previous experimental results obtained with magnetic braking. This low critical rotation has a very weak β dependence as the ideal wall limit is approached.

In order to investigate radial transport of energetic ions due to TAE and RSAE modes, line-integrated neutron emission profile, changes in energy distribution and flux of the charge exchange (CX) neutral particle are measured and compared with the calculated value by a

classical theory using a transport code TOPICS. The results indicate that radial transport of energetic ions is induced by the resonance interaction between energetic ions and AEs.

The design work of ferritic insertion was carried out aiming at effective, machine-safe, and short-term installation. In the design work, the enhanced confinement of energetic ions and absence of the large heat flux on the first wall has been assessed for the NB ions using the fully three dimensional magnetic field orbit-following Monte-Carlo code. The loss power ratio to the injected NB power is reduced by larger than 10 % in a large volume plasma.

Spontaneously excited waves in the ion cyclotron range of frequency (ICRF) are experimentally observed. The fluctuations in ICRF are driven by the presence of non-thermal ion distribution in magnetically confined plasmas. Two types of magnetic fluctuations are detected: one is due to high-energy D ions from neutral beam (NB) injections and the other is due to fusion products (Fops) of 3 He and T ions. The spatial structures of the excited modes in the poloidal and toroidal directions have been firstly measured.

2.5 Plasma Control and Operation

Real-time control of plasma shape and position was successfully demonstrated with the ferritic steel tiles (FSTs) using the CCS code newly developed with consideration of the magnetic field produced by the FSTs. The effect of the magnetic field by the FSTs was very small, less than 0.5% of the field without the FSTs, in a plasma region. On the other hand, the effect on some magnetic sensors was large, about 10%, and should be taken into account for the precise shape and position control. The real-time current profile control system was modified to control the minimum value of the safety factor (q_{\min}) using the LH power. The real-time q_{\min} control was successfully demonstrated in self-regulated plasmas, where the pressure and current profiles are linked through the bootstrap current and the transport properties. The change in the total current profile induced by the off-axis NBCD was spatially localized at about $r/a = 0.65-0.8$, which was outward shifted from the calculation by $\sim 0.2a$. Real-time feedback control of T_i profile was also developed with a filter charge exchange recombination spectroscopy system. The central T_i was controlled to the reference using the NB power within a difference of ~ 0.5 keV. The value of ∇T_i was also controlled by changing the combination of the core and edge NB heating power. In the $\nabla T_i^{\text{reference}}$ ramp-down phase from -6.9 to -2.8 keV/m ($\rho=0.26-0.65$), ∇T_i was almost controlled to the reference. In the $\nabla T_i^{\text{reference}}$ re-ramp up phase, however, ∇T_i did not recover up to the reference due to the occurrence of the MHD instabilities. The burning plasma simulation scheme was developed using two NB groups, where one simulates α -particle heating and the other simulates external heating. The NB power for the simulation of α -particle heating (P^α) was controlled proportionally to the measured DD neutron yield rate. On the other hand, the NB power for the simulation of external heating (P^{ex}) was determined with a feedback control system against the stored energy. Oscillation of P^{ex} was larger in the RS plasmas than that in the ELMy H-mode plasmas to control the stored energy constant. Numerical analysis using the TOPICS code indicated that the linkage between the thermal diffusivity and the heating power triggers the larger oscillation. For the improvement of the burning plasma simulation scheme, P^α was calculated with consideration of temperature dependence of DT

fusion reaction rate using real-time measurements of line averaged electron density and ion temperature. When temperature dependence of the fusion reaction rate was assumed to be proportional to T_i^2 as in the range of $T_i = 10\text{-}25$ keV, density dependence of the simulated fusion gain stronger than square of density was observed due to change in a confinement improvement factor and/or a pressure profile. The plasma current of 17 kA was obtained in the ECH start-up experiment with the vertical field from outboard VT coil and VR coil. Although there was no clear closed flux surface, the current position was significantly apart from the outboard wall. Plasma images suggested that while the discharge took place at the ECR layer, the plasma expanded quickly toward the lower field side and at the same time an initial current appeared. The current locations were always far from the ECR layer. High densities exceeding the Greenwald limit by a factor of 1.7 was obtained with high internal inductances of ℓ_i as high as 2.8. In addition to the extension of the operational regime limited by disruptions, confinement performance remains as good as an H_{89PL} factor of 1.5 even above the Greenwald limit.

2.6 Divertor and SOL Plasmas

Wall saturation and fuel retention has been investigated in 30s long pulse ELMy H-mode discharges under the high (300°C) and medium (150°C) baking temperatures. Wall saturation (outgassing) was observed after a few discharges, and the outgas rate was correlated with an increase in the tile surface temperature near the outer strike point. Prompt response of the outgas flux was also observed when the divertor-pumping flux was increased by opening the shutter of the divertor cryopumps. On the other hand, in high density discharges, wall-pumping was observed over the long pulse. Sustainment of the high density ELMy H-mode plasma with large radiation loss, using argon gas seeding, was tried under the wall saturated condition.

Studies of ELM plasma propagation both at high-field-side (HFS) and low-field-side (LFS) SOLs have been progressed by three Mach probe measurements. ELM propagation to the LFS first wall was faster than the parallel convection time to the outer divertor, suggesting part of ELM plasma loading to the first wall. Deposition image of ELM filaments to outer baffle was measured with new fast TV camera. In the HFS SOL, large plasma flux was transported only in narrow region near separatrix. Reversal of the parallel plasma flow was widely observed at HFS after the ELM deposition. Fast measurements of low ionization spectral lines such as three He I as well as D_α at the LFS divertor showed that dynamic in T_e , n_e , and recycled neutrals. Statistical analysis was applied to L- and H-mode SOL plasma fluctuations.

Measurement of the absolute intensities of C IV lines emitted from radiation peak at the X-point MARFE, using 2-dimensional spectrometer system, could determine the population density ratio of the C^{3+} excited levels. Line-radiation power from the C^{3+} ionizing corresponded to large (60%) compared to that of the volume recombination, while the recombination of C^{4+} is a main process to produce C^{3+} . Two-dimensional structure of the volume recombination of deuterium, i.e. D^+ and e^- , was also investigated in the detached divertor. Two-dimensionally distributions of the deuterium Balmer-series line emissivities

were reconstructed with a tomography technique. Emissivity ratio of Balmer-series lines determined the volume recombination as well as ionization process in the inner and outer divertors. By the local gas puffing, CH₄, CD₄, C₂H₄ and C₂H₆ loss events per CH, CD and C₂ photon were measured carefully to determine the chemical sputtering yield.

The integration code “SONIC” has been developed and examined to simulate the SOL and divertor plasmas. SOLDOR and NEUT2D codes have been applied to analysis of L-mode plasma with the X-point MARFE. Transport of carbon ions generated at the private dome is enhanced in the private plasma, causing the large radiation peaking near the X-point. The pumping capability was also evaluated through the simulation.

2.7 Plasma Facing Materials

Poloidal profiles of erosion/deposition in the divertor region were quite non-uniform with heavy deposition in the inner divertor and the outer dome wing, while the outer divertor and the inner dome wing were erosion dominant regions. The asymmetry of the erosion/deposition was simulated using EDDY code. Long-term net deposition of carbon in the divertor region is 0.55 kg. About 60 % of the net deposition originated from the erosion in the divertor area, while remaining 40% should be attributed to the erosion at the first wall (main chamber).

The (H+D)/C ratios of the plasma facing wall tiles were not very much high: it was ~ 0.07 at a maximum in the divertor samples except for the deposition on the dome outer wing tile, which was ~ 0.13. Redeposited layers of ~2μm thick were found at the plasma-shadowed area underneath the dome with low vessel temperature of ~420 K. The hydrogen retention in the layers was ~0.8 in (H+D)/C.

The carbon transport generated on the outer divertor region has been investigated using the ¹³CH₄ gas puffing in JT-60. On the surface of the inner and outer dome tiles, the ¹³C areal density rapidly decreased towards the dome-top. This result indicates the ¹³C flux to the dome-wing tiles surface decreases toward the dome top and/or the ¹³C deposited near the dome top is re-eroded. The poloidal distribution of the ¹³C areal density on the inner divertor tiles had a peak at a little outboard side of the inner strike point. It might be caused by a transport through the private flux region. In the outer divertor region, ¹³C was deposited only in the down-stream direction indicating ¹³C ion particles were transported to down-stream by a plasma flow.

Erosion/deposition of the tungsten tiles and its migration was studied. On the inner divertor tile, tungsten was mainly deposited around the inner strike position. This suggests that tungsten transport from the outer divertor to inner divertor is common phenomenon for divertor tokamaks. By comparing deposition profiles of tungsten with ¹³C, puffed as ¹³CH₄ from the outer divertor position, deposition profiles showed that the ratio of tungsten deposition to ¹³C deposition was higher on the outer wing tile than the inner divertor tile by about an order of magnitude at the same toroidal section.

2.8 Diagnostics

New diagnostic systems, such as modulation charge exchange recombination

spectroscopy (Modulation CXRS), beam emission spectroscopy (BES), two-dimensional visible spectroscopic measurement system for divertor plasmas, and fast visible TV camera, have provided reliable data with high-temporal and high-spatial resolution. In addition, substantial development of components for advanced diagnostic systems in future, such as Thomson scattering diagnostics using Fourier transform spectroscopy, collective Thomson scattering diagnostics, and Zeeman polarimetry, has been made.

A new technique using the charge exchange spectroscopy system with space modulation optics has successfully obtained the first and second derivative of ion temperature profile. By setting the frame rate of the CCD detector at 200 Hz and the modulation frequency at 10 Hz, the radial profile of the ion temperature with 310 points is obtained every 50 ms. For the Thomson scattering diagnostics, a high performance phase conjugate mirror based on stimulated Brillouin scattering has been applied to improve the performance and a prototype high-throughput polarization interferometer has been developed to demonstrate the utility of Fourier transform spectroscopy. Flash analog-to-digital converters have been applied to the stilbene neutron detectors, and improvement in the neutron count rate up to $\sim 10^6$ counts/s has been demonstrated. The motional Stark effect diagnostic system has been modified to measure density fluctuation profile, together with the pitch angle of the magnetic field, as a BES diagnostics by fast sampling (0.5-1 MHz) of the photo-multiplier signals. For divertor study, a wide-spectral-band spectrometer with 92 view channels (vertically 60 channels, horizontally 32 channels) with a spatial resolution of ~ 1 cm has provided two-dimensional distribution of deuterium and carbon emission with an improved tomography technique. A fast visible TV camera has been installed to observe trajectories and velocities of dusts in the main chamber and divertor. For collective Thomson scattering diagnostics to observe confined α -particles in future burning plasmas, a transversely excited atmospheric (TEA) CO₂ laser has been developed and a high pulse energy of 17 J with a high repetition rate of 15 Hz has been achieved in a single-mode operation. For measurement of the edge current profile, a Zeeman polarimetry using a lithium beam has been under development. The prototype lithium ion gun has demonstrated a large current extraction over 10 mA. A new ion gun has been designed to improve the beam divergence and transport. For study of fast frequency MHD events in long pulse discharges, a new data acquisition system with a fast sampling rate has been successfully employed for measurements of various fluctuations obtained through magnetic probes, BES and so on.

2.9 Heating Systems

Extension of injection pulse length has been one of most important issues for both ECRF and N-NB heating and current drive systems. In this campaign, large efforts have been done to extend the injection pulse length in each systems. As the result, injection of 21 s is achieved in both systems. In the ECRF development, controls of the anode voltage and the heater succeeded to avoid decrease of the beam current which led to termination of oscillation, then to achieve 21 s injection. In the N-NB development, clarifying operational ranges for a stable voltage holding capability and an allowable grid power loading brought the success of 21 s injection.

3. Extension of Operation Regimes

3.1 Improved Performance in Long-Pulse ELMy H-mode Plasmas with Internal Transport Barrier [1]

N. Oyama, A. Isayama, T. Suzuki, Y. Koide, H. Takenaga, S. Ide, T. Nakano, N. Asakura, H. Kubo, M. Takechi, Y. Sakamoto, Y. Kamada, H. Urano, M. Yoshida, K. Tsuzuki, G. Matsunaga, C. Gormezano and the JT-60 Team

In JT-60U, the advanced tokamak (AT) plasma regime for the realization of a steady-state tokamak fusion reactor has been investigated. Further pursuit of long sustainment of high performance plasmas has been limited by the loss of fast ions due to the toroidal field ripple from the viewpoint of the available net heating power and controllability of the toroidal rotation profile due to the formation of an inward electric field. In order to reduce the toroidal field ripple, ferritic steel tiles (FSTs), which cover $\sim 10\%$ of the vacuum vessel surface, have been installed inside the JT-60U vacuum vessel on the low field side.

After the installation of FSTs, fast ion losses have been reduced by $1/2\sim 1/3$ at 1.6T. The increase in the absorbed power at the same injection power can reduce the required number of NB units to sustain a given β_N . The slower increment of the divertor temperature due to the lower heating power could keep the lower recycling level and edge density longer than in the previous long-pulse experiments. As the edge temperature decreased by increasing the edge density due to higher recycling, core T_i including inside ITB region degraded. Therefore, a higher edge temperature is essential in keeping the peaked pressure/temperature profile and the long-sustainment of a lower recycling with FSTs contributes to the improvement of thermal plasma confinement. In addition to this, lower fast ion losses reduced the effective torque for ctr-rotation and increase the flexibility of torque input by increasing the available combination of tangential NB units. The fact that co-rotation provides better quality of T_e -ITB also contributes to the improvement of thermal plasma confinement. In these long-pulse plasmas, these two mechanisms related to the reduction of fast ion losses are equally important for the improved performance.

Making use of these advantages to sustain good ITBs, sustained duration of $\beta_N=2.3$ has been extended to 28.6s. In this plasma, a peaked pressure profile without NTMs and detectable sawteeth was kept throughout the discharge. The improved core confinement provided high $\beta_N H_{95} > 2.2$ with bootstrap current fraction of $\geq 40\%$ sustained for 23.1s ($\sim 12 \tau_R$) at $q_{95} \sim 3.3$, which gives high G-factor (larger than 0.2). Therefore, these long-pulse plasmas are possible candidates for the ITER hybrid operation scenario.

Reference

- [1] Oyama, N., *et al.*, in Fusion Energy 2006 (Proc. 21st Int. Conf. Chengdu, 2006) IAEA-CN-149/EX/1-3, submitted to Nuclear Fusion.

3.2 Achievement of the High Beta Plasma by Stabilization of Resistive Wall Mode [1]

M. Takechi, G. Matsunaga, T. Ozeki, N. Aiba, G. Kurita, A. Isayama, Y. Koide, Y. Sakamoto, T. Fujita Y. Kamada and the JT-60 team

To realize the economical fusion reactor the achievement of high beta plasmas is important because the fusion output power is proportion to square of the normalized beta β_N . However the resistive wall mode (RWM), which has the slow growth time equivalent to the time constant of the wall, restrict the achievable beta. The RWM can be suppressed by the plasma rotation and the active magnetic feedback control.

Ferritic steel tiles (FSTs) are installed inside the JT-60U vacuum vessel to reduce the toroidal field ripple. Monte-Carlo simulations considering fully 3-D magnetic field structure using the F3D OFMC code indicate that total absorbed power increases by $\sim 30\%$ at $B_T = 2$ T for the large volume configuration close to the wall. By increased NB deposition power, suppressing RWM and raising ideal wall limit by controlling plasma profile, we successfully achieved high $\beta_N \sim 4.2$ exceeding ideal limit at $l_i < 1.2$ and $V_p > 70\text{m}^3$ ($\beta_N \sim 3.4$ w/o FST).

The experiment for high β_N has been mainly performed on the plasma with the clearance between plasma surface and first wall at low field mid-plane of 20 cm, which is equivalent to the ratio of diameter of first wall to that of plasma of 1.2. The PNB of 20 MW and the NNB of 3MW were injected simultaneously into the plasma of $I_p=0.9\text{MA}$ and $B_t=1.58\text{T}$. The shear of q was weak and $q_{\min} \sim 1.1$ and $q_{95} \sim 3.5$. Achieved beta is restricted by the $n=1$ MHD instability. The main poloidal mode number of the $n=1$ mode was $m=3$ and has a ballooning structure. The mode amplitude increases with growth time of $1/\gamma \sim 1$ ms. Frequency of the mode of $f \sim 5$ kHz is corresponding to the rotation of 100 km/s at plasma inner region. The MHD stability has been calculated by MARG2D code for the plasma with $\beta_N \sim 3.8$ because we measured T_i , T_e , n_e and q profile of this plasma. Calculated no-wall beta limit is $\beta_N \sim 3.1$ and ideal wall limit is $\beta_N \sim 3.9$ for the plasma with wall at $d/a=1.2$. Therefore the beta of the plasma has seemed to reach to ideal wall limit. The dominate poloidal component was $m=1$ due to low $q_{\min} \sim 1.1$ and large pressure gradient of internal transport barrier. The observed growth time of the $n=1$ mode $1/\gamma \sim 1$ ms is much faster than the skin time of the first wall of 10 ms. This also indicates that the plasma reaches to the ideal wall limit. The achievable beta limited by MHD instability decrease as confinement decrease. Calculated critical beta decreases in the region $q_{\min} < 1.1$ and dominant fourier component of the mode is $m=1$. The bootstrap current fraction of these plasmas was 0.5 and bootstrap current was large at inner region of $r/a = \sim 0.2-0.5$ and peripheral region due to ITB and ETB. It is seemed that better confinement raises the ideal wall limit by increasing q_{\min} because the large inner bootstrap current raises the q_{\min} . The experimental minimum q for high beta case was $q_{\min} \sim 1.08$. The critical beta is also affected by the peripheral plasma current. Therefore, we have performed the small current rump down before NB injection to scrape the peripheral current. By this procedure, we achieved highest beta $\beta_N \sim 4.2$.

Reference

[1] Takechi, M., *et al.*, to be submitted to NF.

3.3 Long Sustainment of Large Bootstrap Current Fraction Plasmas by Introducing New Real Time Control Logic [1]

Y. Sakamoto, H. Takenaga, T. Suzuki, S. Ide, T. Fujita, M. Takechi, N. Oyama

Large bootstrap current fraction ($f_{BS} \sim 75\%$) is required for the concept of steady-state fusion tokamak reactor. In previous experiments in JT-60U, the long sustainment of the reversed magnetic shear plasma with large $f_{BS} \sim 75\%$ for 7.4s was demonstrated under nearly full non-inductive current drive condition by the control of the pressure gradient at the ITB through the control of the toroidal rotation profile to avoid disruption at $q_{min} \sim 4$ [2], where the injection timing of the tangential neutral beam (tang-NB) was controlled by pre-program setting. Since the timing of q_{min} being integer depends on the time evolution of the plasma current profile, it is difficult to adjust the timing of the rotation control as the pre-programmed setting with good reproducibility.

One of the subjects for avoidance of the collapse and the disruption with good reproducibility is how to set up the timing to apply the toroidal rotation control at q_{min} being integer. Recently the real time control system of q profile had been developed in JT-60U. This system calculates q profile in real time including the value of q_{min} and the location of q_{min} ($\rho_{q_{min}}$) using the motional Stark effect (MSE) diagnostic. The real time control logic for the avoidance of collapses at q_{min} being integer by the control of the toroidal rotation has newly been installed in JT-60U. In the new real time control logic, the injection timing of the tang-NB can be controlled based on the real time detection of q_{min} using MSE diagnostic. The range of q_{min} and the control period are used to determine the injection timing of co-NBs or ctr-NBs as the setting parameter. For example, ctr-NB is turned off for 0.5 s when the value of the real time detected q_{min} is in the range of 3.8 to 4.2.

By utilizing the above real time control logic, large $f_{BS} \sim 70\%$ was sustained for ~ 8 s and high confinement enhancement factor over the H-mode scaling $HH_{98y2} \sim 1.8$ was obtained. In the later 3 s of this plasma, q profile becomes flat in the core region due to the penetration of the inductive current with keeping the good ITB. The profile of the internal loop voltage evaluated from the equilibrium reconstruction using MSE measurement is flattened in time, indicating the plasma approached the stationary condition. The large f_{BS} phase is terminated by the major collapse even at the value of q_{min} being not integer. MHD analysis using MARG2D code indicates that the collapse is attributed to ideal beta limit. Pressure profile control is required even after the current profile approaches the stationary condition to demonstrate the longer sustainment of large f_{BS} plasmas.

References

- [1] Y. Sakamoto et al., Nucl. Fusion 47 (2007) 1506.
- [2] Y. Sakamoto et al., Nucl. Fusion 45 (2005) 574.

3.4 Evolution of Bootstrap-Sustained Discharge

Y. Takase¹⁾, H. Nuga¹⁾, S. Ide, JT-60 Team

1) The University of Tokyo

A large improvement in the cost of electricity of a fusion power plant can be achieved by increasing the fraction of self-generated plasma current (*i.e.*, bootstrap current fraction, $f_{BS} = I_{BS}/I_p$). Furthermore, if it were possible to achieve $f_{BS} > 1$ (*i.e.*, bootstrap overdrive), this can be used for I_p ramp-up. In this case the requirement for external current drive (CD) can be reduced substantially, and elimination of the CD system may even be possible eventually.

A self-sustained state driven by I_{BS} was achieved in JT-60U. A loop voltage profile of nearly zero or slightly negative across the cross section was maintained for 0.2 s in a discharge with constant OH primary current. In this discharge, of the total I_p of 543 kA, the calculated beam driven current was -35 kA and the inductive current was -5 kA. In the newly implemented constant plasma surface flux feedback mode, which ensures no net flux input to the plasma, a steady I_p rampup at a rate of 10 kA/s was achieved for 0.5 s. These results provide evidence of bootstrap overdrive. Repetitive cycles of β collapse and self-recovery were often observed in such a self-driven plasma. In discharges without β collapses, the duration of self-driven state was limited by a slow degradation of ITB. A more sophisticated control of the pressure profile and/or current profile would be necessary to maintain the self-sustained state in steady state. Extension of these results to higher I_p (lower q), and a more complete characterization of the controllability of such plasmas, including approach to a steady state, remain topics of further research. Since ST reactors can operate at high q of around 10, bootstrap-dominated operation assisted by a small amount of external current drive may be utilized by developing appropriate control methods.

[1] Y. Takase, et al., 21st IAEA Fusion Energy Conf. (Chengdu, China, 16-21 October 2006) IAEA-CN-149/EX/1-4.

4. Transport in Core Plasmas

4.1 Response of Large Bootstrap Current Plasma [1]

Y. Sakamoto, H. Takenaga, T. Suzuki, S. Ide, T. Fujita

A large bootstrap current fraction (f_{BS}) plasma can be characterized as a self-regulating system because the pressure, current and rotation profiles are linked each other as follows: The pressure profile affects the current profile through the self-generated bootstrap current, where the total current profile is almost determined by the pressure profile with the increase in the bootstrap current fraction. And also, the current profile determines the magnetic shear profile, which affects strength of ITB. Furthermore, the pressure profile affects the rotation profile through the self-generated spontaneous rotation and the rotation profile affects the pressure profile through transport in the ITB region.

The dynamic change in the current profile, especially q_{min} , was observed in the series of large f_{BS} experiments, where the degradation of ITB was observed by the ctr-NB turning on while the recovery of ITB by the ctr-NB turning off. The increase in q_{min} was quickly observed just after the recovery of the ITB, while the decrease just after the degradation of the ITB. Since the increase in the ion temperature gradient at the ITB that locates around q_{min} generates the bootstrap current locally, q profile near q_{min} is flattened and q_{min} increases. The response of q_{min} to the change in the ion temperature gradient at the ITB is investigated in the plasmas with $f_{BS} \sim 70\%$ and $\sim 50\%$. The data for $f_{BS} \sim 70\%$ come from the discharge with $I_p \sim 0.8\text{MA}$, while those for $f_{BS} \sim 50\%$ come from the other reversed magnetic shear discharge with $I_p \sim 1\text{MA}$. In both cases, the values of q_{min} are ~ 4 . The strong response is found in the large $f_{BS} \sim 70\%$ plasmas compared with that in the $f_{BS} \sim 50\%$ plasmas. The reason for the difference of the response of the q_{min} to the change in the ion temperature gradient is considered as follows. In the case of $f_{BS} \sim 70\%$, q profile is almost determined by the bootstrap current profile. Therefore the change in the bootstrap current modifies q profile directly. In the case of $f_{BS} \sim 50\%$, on the other hand, the inductive current also contributes to the off-axis current for the formation of the reversed magnetic shear configuration transiently. Therefore the change in q profile with $f_{BS} \sim 50\%$ is smaller than that with $f_{BS} \sim 70\%$.

Since the disruption is frequently occurred at q_{min} being integer, it is necessary to maintain q_{min} in the self-regulating system by the external current drive for the compensation for the change in the bootstrap current.

Reference

[1] Y. Sakamoto *et al.*, Nucl. Fusion **47** (2007) 1506.

4.2 Temporal Variation of Density Fluctuation and Transport in Reversed Shear Plasmas [1]

H. Takenaga, N. Oyama, L. G. Bruskin¹⁾, A. Mase¹⁾, T. Takizuka, T. Fujita

1) Art, Science and Technology Center for Cooperative Research, Kyushu University,

Many types of fluctuation with various spatial scales exist in plasmas and enhance the transport from the neoclassical level. The anomalous turbulent heat transport for ion and electron channels and also the anomalous turbulent particle transport could be dominated by different types of fluctuation with different spatial scale such as ion temperature gradient (ITG) mode, trapped electron mode (TEM) and electron temperature gradient (ETG) mode. Investigation of the relation between the fluctuation and the electron and ion heat transport and the particle transport in the region of internal transport barrier (ITB) is important for understanding dominant fluctuation for each transport element. This paper focuses on the relationship between the fluctuation and the transport when further reduction of the transport was induced by the external perturbations such as a pellet or electron cyclotron (EC) wave injection after the strong ITB formation in the reversed shear plasmas.

After the pellet injection ($I_p=2.2$ MA, $B_T=4.3$ T and $q_{95}=3.8$), the O-mode reflectometer signal drastically decreased in the frequency ranges of $|f| > 200$ kHz and 50 kHz $> |f| > 20$ kHz, indicating reduction of the electron density fluctuation level. The density fluctuation level was estimated to be 1-2% before and 0.4-0.5% after the pellet injection, respectively, using the O-mode reflectometer signal and simulation results based on the analytical solution of time-dependent 2D full-wave equation. The ion thermal diffusivity decreased by one order of magnitude and reached the neoclassical level. The effective particle diffusivity also decreased by one order of magnitude, but the electron thermal diffusivity remained constant. After EC wave injection ($I_p=1.3$ MA, $B_T=3.7$ T and $q_{95}=4.9$), when no reduction of the O-mode reflectometer signal was observed, the electron thermal diffusivity decreased by a factor of $\sim 2-3$, while decreases in the ion thermal diffusivity and the effective particle diffusivity are small. These results indicated that the ion heat transport and the particle transport were coupled with the measured density fluctuation, but the electron heat transport was decoupled. The wave number of the measured density fluctuation was estimated to be order of 1 cm⁻¹ in the pellet case, which is consistent with the spatial scale of ITG and/or TEM. The electron heat transport in the strong ITB region seems to be insensitive to such fluctuation modes and to be dominated by other fluctuation mode with a smaller spatial scale such as ETG.

Reference

[1] H. Takenaga *et al.*, Plasma Phys. Control. Fusion **48** (2006) A401.

4.3 Observation on Decoupling of Electron Heat Transport and Long-spatial-scale Density Fluctuations in a Reversed Shear Plasma [1]

H. Takenaga, N. Oyama, A. Isayama, T. Takizuka, T. Fujita

In the reversed shear plasma, suppression of long-spatial-scale density fluctuations with a wave number of the order of 1 cm^{-1} was observed in the ITB region, after a cold pulse was induced by the shallow pellet injection at the plasma edge. As discussed in the previous section, the particle and power balance analysis with fully recovered temperature profiles after the cold pulse propagation indicated that the particle and ion heat transport is coupled with the long-spatial-scale density fluctuations, while the electron heat transport is not coupled with them. In this section, transient response of the electron heat transport during the cold pulse propagation is investigated for better understanding of relation between the electron heat transport and the long-spatial-scale density fluctuations.

The edge electron temperature (T_e) at $r/a \sim 0.85$ was sharply dropped by the ablation of pellet cloud at $t = 6.32$ s. The cold pulse induced by the pellet ablation propagated into the ITB region. When the cold pulse propagated to the position of $r/a = 0.54$ in the ITB region at $t = 6.325$ s, integrated power of high frequency component ($|f| > 200$ kHz) of the O-mode reflectometer signal was drastically reduced with a fast time scale (< 5 ms), indicating reduction of the density fluctuation. At this timing, T_e outside the ITB ($r/a = 0.64-0.85$) was decreased by the cold pulse propagation, while T_e in the inner ITB portion ($r/a < 0.54$) was not changed due to slower propagation speed of the cold pulse in the ITB region. Thus, T_e gradient became large in the outer ITB portion ($r/a = 0.54-0.64$). The value of T_e at $r/a = 0.54$ largely decreased after the density fluctuation reduction, and the ITB structure seems to be destroyed in the outer ITB portion at $t = 6.35$ s.

In order to reproduce the time evolution of T_e by the 1-D transient transport calculation, T_e and ∇T_e dependence of electron thermal diffusivity (χ_e) was introduced as follows,

$$\chi_e(r, \Delta t) = \chi_e(r, \Delta t = 0 \text{ms}) \left(\frac{T_e(r, \Delta t)}{T_e(r, \Delta t = 0 \text{ms})} \right)^\alpha \left(\frac{\nabla T_e(r, \Delta t)}{\nabla T_e(r, \Delta t = 0 \text{ms})} \right)^\beta$$

The values of α and β are summarized in Table 1. Strong and weak negative T_e dependence was assumed in the outer ITB portion ($r/a = 0.54-0.62$) and outside the ITB ($r/a > 0.63$), respectively. Furthermore, in the inner ITB portion ($r/a = 0.3-0.5$), it was assumed that χ_e is inversely proportional to ∇T_e . In this case, the value of χ_e decreased in the inner ITB portion around the layer for the density fluctuation measurement during the cold pulse propagation. However, it was slower (~ 15 ms) than the reduction of the density fluctuation level (< 5 ms). In the outer ITB portion, χ_e transiently increased. These results indicated decoupling of the electron heat transport and the long-spatial-scale density fluctuations as well as the results of the power balance analysis.

r/a	0.00-0.29	0.30-0.50	0.51-0.53	0.54-0.62	0.63-1.0
α	0	0	0	-2.3	-0.5
β	0	-1	0	0	0

Table 1 α and β used in the 1-D transient transport calculation.

Reference

[1] H. Takenaga *et al.*, Plasma Phys. Control. Fusion **49** (2007) 525.

4.4 Dynamic Transport Study of the Plasmas with Transport Improvement in LHD and JT-60U [1]

K. Ida¹⁾, Y. Sakamoto, S. Inagaki²⁾, H. Takenaga, A. Isayama, R. Sakamoto¹⁾, K. Tanaka¹⁾, S. Ide, T. Fujita, H. Funaba¹⁾, S. Kubo¹⁾, M. Yoshinuma¹⁾, T. Shimosuma¹⁾, Y. Takeiri¹⁾, K. Ikeda¹⁾, C. Michael¹⁾, T. Tokuzawa¹⁾, LHD experimental group and the JT-60 Team

1) National Institute for Fusion Science

2) Research Institute for Applied Mechanics, Kyushu University

The concept of a profile transition has been employed in order to understand the formation and dynamics of a self-sustained radial profile in inhomogeneous plasmas. The transitions in the profiles in H-mode plasmas are caused by the S-curve property (cusp-type catastrophe) in the gradient-flux relation, showing a feature analogous to the first-order phase transition. The slow transition to the improved transport mode [2], which is often observed in other types of improved modes or internal transport barrier (ITB) plasmas, is categorized as a type of second-order transition in contrast to a first-order transition such as the L/H transition. Transport analysis during the transient phase of heating (a dynamic transport study) is applied to plasmas with internal transport barriers (ITBs) in the Large Helical Device (LHD) heliotron and in the JT-60U tokamak. In the dynamic transport study 1) a slow transition between two transport branches is observed, 2) the time of the transition from the L-mode plasma to the ITB plasma is clearly determined by the onset of flattening of the temperature profile in the core region and 3) a spontaneous phase transition from a weak, wide ITB to a strong, narrow ITB and back-transition are observed both in LHD and JT-60U [1].

The time scale of the slow transition between two transport branches is on the order of the energy confinement time. The time scale of the transition from the L-mode plasma to the ITB mode plasma is also on the order of the energy confinement time, which make it difficult to specify the starting time of the TB formation. In a strong ITB, the flattening of the temperature in the core region is often observed. This flattening starts in the early phase of the ITB formation not in the later time of the ITB when the electron temperature becomes high. Therefore the flattening is considered to be due to the localization of improved transport during the formation of the ITB. The flattening of the core region of the ITB transition and the back-transition between a wide ITB and a narrow ITB suggest the strong interaction of turbulent transport in space, where turbulence suppression at certain locations in the plasma causes the enhancement of turbulence and thermal diffusivity nearby. Because of this mechanism, the ITB is naturally localized in space and the location and width of the ITB can change by itself without a significant change in the magnetic structure. This behaviour also indicates that there are multi meta-stable states in the transport and the spontaneous transition between these meta-stable states occurs on a transport time scale.

References

- [1] K. Ida *et al.*, submitted to Phys. Rev. Lett.
 [2] K. Ida *et al.*, Phys. Rev. Lett. **96** (2006) 125006.

4.5 Studies on Impact of Electron Cyclotron Wave Injection on the Internal Transport Barriers [1, 2]

S. Ide, H. Takenaga, A. Isayama, Y. Sakamoto, M. Yoshida and C. Gormezano

It has been observed that injection of the electron cyclotron range of frequency (ECRF) entails a degradation of the ion temperature internal transport barrier (T_i ITB). Since electron heating will be dominant in a fusion plasma, similar phenomenon could occur. In order to clarify the effect of ECRF injection on the T_i ITB in a weak shear plasma, systematic studies have been carried out in JT-60U.

It is shown that the effect increases as the injected EC power (P_{EC}) increases. It is also shown that the effect becomes smaller for a higher plasma current (I_p). However, it is found that the safety factor and the magnetic shear profiles are not different very much in the ITB region. On the other hand, it is also shown that the EC current drive is not responsible for this phenomenon. These results suggest that the poloidal magnetic field and/or the magnetic shear in the ITB region are not the keys for this effect. It seems that EC injection affects the toroidal rotation (V_t) and presumably the radial electric field (E_r) profiles. With ECRF injection, the V_t profile is flattened no matter the direction the target V_t profile peaks. This indicates that EC injection influences the background structure, the E_r profile or the ITB structure, directly. Moreover, it is shown that the effect on the T_i ITB is less sensitive to the EC deposition. Degradation of the T_i ITB occurs for both on- or off-axis deposition. Within the time resolution of 5 ms, no clear delay was observed in both T_i and V_t signal in the ITB region. This indicates that ECRF is acting on a certain background structure which has a semi-global nature. This work would contribute to identify the operational region where the T_i ITB degradation can be avoided when ECRF is utilized neo-classical tearing mode (NTM) suppression. However on the other hand, this effect can be utilized for ITB control. Smooth and continuous dependence without hysteresis on P_{EC} is preferable for control and insensitivity to deposition do not require the precision linked to spatial control. ECRF can be a more realistic tool than others such as the V_t profile control in a burning plasma. A fundamental physics mechanism which plays the main role in this phenomenon is not clear yet. It is not clear even if this is intrinsic to ECRF or not. Detailed comparison with other electron heating schemes, such as negative ion source NB injection or lower hybrid wave heating, would be necessary in future work.

References

- [1] S. Ide *et al.*, Fusion Energy 2006 (Proc. of 21st Int. Conf. Chengdu, 2006),
IAEA-CN-149/EX/P1-5 and http://www-naweb.iaea.org/naweb/physics/fec/fec2006/papers/ex_p1-5.pdf.
[2] S. Ide *et al.*, Nucl. Fusion **47** (2007) 1499.

4.6 Physics of Strong Internal Transport Barriers in Reversed Shear Plasmas [1]

N. Hayashi, T. Takizuka, Y. Sakamoto, T. Fujita, Y. Kamada, S. Ide and Y. Koide

Improved confinement with the formation of internal transport barriers (ITBs) is beneficial for the steady-state operation of ITER and advanced tokamak reactors. The ITB formation has been observed in many tokamaks with the reversed-shear (RS) configuration. The RS plasma is one of the attractive candidates for the advanced tokamak reactor because of its compatibility with the large bootstrap current produced by the ITB. The physical mechanism of the ITB structure in the RS plasma has not fully been understood yet. The improved performance with the ITB was surveyed in multi-machine comparisons. In JT-60U, there are typically two kinds of ITB profiles: box type and parabolic type. On the basis of JT-60U experimental database of the box-type ITB, two scalings for the narrow ITB width and the stored energy inside the ITB, W_{core} , have been developed. The former scaling shows that the ITB width is proportional to the ion poloidal gyroradius at the ITB center. The latter scaling is equivalent to a condition for the core poloidal beta, $\beta_{\text{p,core}} = 4\mu_0 W_{\text{core}} / (3V_{\text{core}} B_{\text{p,f}}^2)$, i.e., $\varepsilon_f \beta_{\text{p,core}} \approx 0.25$ where V_{core} is the volume inside the ITB, $B_{\text{p,f}}$ is the poloidal magnetic field at the outer midplane ITB foot and ε_f is the inverse aspect ratio at the ITB foot. The scalings were reproduced by the 1.5 dimensional (1.5D) transport simulation with a transport model where the anomalous transport is sharply reduced below the neoclassical-level in the RS region.

In this paper, the physics of strong ITBs in JT-60U RS plasmas has been studied through the modeling on the 1.5D transport simulation. We modify artificially physical models in the 1.5D transport code and compare simulation results with experimental ones. Key physics to produce the above scalings are identified. As for the scaling for the narrow ITB width proportional to the ion poloidal gyroradius, the following three physics are important: (1) the sharp reduction of the anomalous transport below the neoclassical level in the RS region, (2) the autonomous formation of pressure and current profiles through the neoclassical transport and the bootstrap current, and (3) the large difference between the neoclassical transport and the anomalous transport in the normal-shear region. As for the scaling for the stored energy inside the ITB, the value of 0.25 is found to be a saturation value due to the MHD equilibrium. The value of $\varepsilon_f \beta_{\text{p,core}}$ reaches the saturation value, when the box-type ITB is formed in the strong RS plasma with the large asymmetry of the poloidal magnetic field, regardless of details of the transport and the non-inductively driven current. In other words, as the asymmetry of the poloidal magnetic field increases, both $B_{\text{p,f}}$ and W_{core} increases so that $\varepsilon_f \beta_{\text{p,core}} = 0.25$.

Reference

[1] N. Hayashi *et al.*, Plasma Phys. Control. Fusion **48** (2006) A55.

4.7 Effects of Low Central Fuelling on Density and Ion Temperature Profiles in Reversed Shear Plasmas [1]

H. Takenaga, S. Ide, Y. Sakamoto, T. Fujita and the JT-60 Team

It is crucial issue for prediction of fusion performance in an advanced steady state tokamak reactor whether a density internal transport barrier (n_e -ITB) can be formed with low central fuelling or not. In ELMy H-mode plasmas, tokamak experiments have shown that a density peaking factor increases with decreasing effective collisionality due to anomalous inward pinch driven by drift wave instabilities such as ITG/TEM [2]. On the other hand, in advanced scenarios such as reversed shear (RS) plasmas, mechanisms for determining the density profile are not understood well. It is expected that the anomalous inward pinch can play less important role in the ITB region, where anomalous transport is reduced by suppressing instabilities. Also, investigation of correlation between n_e -ITB and an ion temperature ITB (T_i -ITB) is important, because the large density gradient can assist formation of T_i -ITB through suppression of ITG.

Effects of low central fuelling on n_e - and T_i -ITBs have been investigated using negative ion based neutral beam injection (N-NBI) and electron cyclotron heating (ECH) in RS plasmas. Strong n_e - and T_i -ITBs were maintained, when central fuelling was decreased by switching positive ion based neutral beam injection (P-NBI) to ECH after the strong ITB formation. The effective electron diffusivity defined by considering only diffusion term was smaller in the low central fuelling case than that in the high central fuelling case at the same range of the ion thermal diffusivity. The outward diffusive flux could be almost balanced with the inward convective flux and small unbalance between these two fluxes corresponds to the flux produced by the central fuelling. Therefore, the central fuelling might have only small effects on the density profile. Similar n_e - and T_i -ITBs were formed for the low and high central fuelling cases during the plasma current ramp-up phase. In the low central fuelling case, N-NBI and ECH were used in addition to small heating power from P-NBI for diagnostics. In the high central fuelling case, P-NBI was only used. An anomalous inward pinch could be still important with suppressed instabilities in these discharges, because n_e - and T_i -ITBs were not so strong. Possibility for the formation of the strong n_e - and T_i -ITBs with ion thermal transport reduced to the neoclassical level and role of anomalous inward pinch in such strong ITB region are future issues. Strong correlation between the density gradient and the ion temperature gradient was observed, when the density gradient in the ITB region was increased by stopping gas-puffing and decreased by L-H transition. However, their causality was not well understood yet. These results support that the n_e - and T_i -ITBs can be formed under reactor relevant conditions.

References

- [1] H. Takenaga *et al.*, J. Phys.: Conf. Ser. at press.
- [2] C. Angioni *et al.*, Phys. Rev. Lett. **90** (2003) 205003.

4.8 Comparisons of Density Profiles in JT-60U Tokamak and LHD Helical Plasmas with Low Collisionality [1]

H. Takenaga, K. Tanaka¹⁾, K. Muraoka²⁾, H. Urano, N. Oyama, Y. Kamada, M. Yokoyama¹⁾,
H. Yamada¹⁾, T. Tokuzawa¹⁾ and I. Yamada¹⁾

1) National Institute for Fusion Science 2) Chubu University

In order to understand particle transport systematically in toroidal plasmas, electron density profiles were compared in JT-60U tokamak and LHD helical plasmas with low collisionality. Comparative studies between tokamak and helical plasmas may help expand the understanding of both common physics in toroidal systems and unique physics depending on each magnetic configuration. The neoclassical particle transport in a low collisionality regime is significantly different for tokamak and helical plasmas. In non-axisymmetric helical plasmas, the $1/\nu$ regime exists, where neoclassical transport is enhanced as being proportional to $1/\nu$ (ν is collisionality) from the level of axisymmetric tokamak plasmas due to the presence of helical ripples [2]. On the other hand, anomalous transport in both plasmas seems to be related to common physics. Gyrokinetic analyses showed that the quasilinear particle flux driven by drift wave instabilities, such as ion temperature gradient mode and trapped electron mode, exhibits weak dependence on the magnetic configuration [3]. Note that scaling studies indicated that these plasmas have the same weak gyro-Bohm like global energy confinement feature.

In the ELMy H-mode plasmas on JT-60U, the density peaking factor increased with decreasing collisionality. Dependence of the density peaking factor on the effective collisionality, which provides an estimate of the growth rate of drift wave instabilities, was consistent with the interpretation that anomalous inward pinch driven by turbulent transport significantly affects the density peaking. The density peaking factor correlated with the ion temperature peaking factor rather than with the electron temperature peaking factor in the case of ion dominant heating. In addition, the toroidal momentum input (or toroidal rotation velocity) affected the density peaking factor, while the particle source distribution was less sensitive on determination of the density peaking factor. In LHD plasmas, the density peaking factor decreased with decreasing electron-ion collision frequencies normalized by the collisionality for an upper boundary of the $1/\nu$ region, ν_{*h}^* , for the magnetic axes of 3.6, 3.75 and 3.9 m. This result indicated that neoclassical transport enhanced by helical ripples largely affects the density profile in LHD plasmas, while this collisionality dependence was less pronounced for the LHD plasmas having small effective helical ripples at the magnetic axis of 3.5 m ($\nu_{*h}^* \geq 1$). For the LHD data analyzed here, neoclassical transport is smaller for more inwardly shifted magnetic configuration [2]. Thus, density profiles in LHD plasmas tended to approach those in JT-60U as the contribution of neoclassical transport is reduced, namely by moving the magnetic axis more inward.

References

- [1] H. Takenaga *et al.*, Nucl. Fusion **48** (2008) 075004.
- [2] S. Murakami *et al.*, Nucl. Fusion **42** (2002) L19.
- [3] O. Yamagishi *et al.*, Phys. Plasmas **14** (2007) 012505.

4.9 Study of Highly Ionized Xe Spectra in Reversed Shear Plasmas [1]

H. Kubo, A. Sasaki, K. Moribayashi, S. Higashijima, H. Takenaga,
K. Shimizu, T. Nakano, A. Whiteford¹⁾, T. Sugie

1) Univ. of Strathclyde

In next-step fusion reactors such as ITER, tungsten is a candidate material for the plasma facing components. However, high-Z elements such as tungsten radiate more efficiently than low-Z elements and their accumulation is a concern for improved confinement plasmas. On the other hand, radiation loss power enhancement is useful for mitigating the severe problem of concentrated power loading of the divertor plates, and controlled impurity gas injection is an effective technique for the radiation loss power enhancement. In some tokamaks, Xe has been injected to study high-Z impurity behavior or to enhance radiation loss power. For such studies, analysis of vacuum ultra-violet spectra from highly ionized Xe atoms is essential. However, little investigation has been performed on these spectra.

In JT-60U, Xe has been injected into reversed shear plasmas with internal transport barriers (ITB) to study high-Z impurity transport. Spectra of highly ionized Xe atoms with 3s-3p and 3p-3d transitions were observed in a wavelength range of 4 - 16 nm and analyzed using relativistic atomic structure codes, a collisional radiative model, and an impurity transport code. The observed spectra were compared with spectra calculated for Xe XXXVII-XLV 3s-3p and 3p-3d transitions. Several lines for Xe XLI and XLII have been newly identified. However, the calculation could not explain some strong line emission. The Xe XLII $3s^2 3p^2 P_{3/2} - 3s^2 3d^2 D_{5/2}$ line was strong comparably to the $3s^2 3p^2 P_{1/2} - 3s^2 3d^2 D_{3/2}$ line, although the calculation showed that the former should be much weaker than the latter for heavy species such as Xe.

Soft X-ray emission profiles have also been analyzed to investigate the Xe ions accumulated inside the ITB. The analysis indicated that the Xe ions accumulated inside the ITB. Considering previous investigation on C, Ne and Ar ion transport, this result showed that accumulation was large for high-Z impurities. Control of high-Z impurity behavior in improved confinement plasmas with ITBs is an important issue.

Reference

[1] H. Kubo *et al.*, J. Nucl. Mater. **363-365** (2007) 1441.

4.10 Study of Impurity Injection Scenario in Burning Plasmas [1]

H. Takenaga, H. Kubo, Y. Kamada, Y. Miura, Y. Kishimoto, T. Ozeki

In a fusion reactor, reduction of heat load localized to the divertor plates is essential for a steady-state operation. Impurity injection is considered for dispersing the localized heat load to wide area by radiation losses from the injected seed impurities. In order to significantly disperse the heat load to the wide area, enhancement of the radiation loss power is necessary not only in the divertor plasma but also in the main and SOL plasmas. In the A-SSTR2 design, the radiation loss power is set to be 400 MW (about 45% of the heating power) in the main and SOL plasmas. On the other hand, it is necessary to suppress enhancement of the radiation loss power in the core plasma caused by strong accumulation of the injected seed impurity. The enhancement of the radiation loss power in the core plasma reduces the effective heating power, which requires higher confinement to sustain a burning condition. The peaked density profile raises the concern of impurity accumulation, although it has an advantage for higher fusion output even with the low edge density.

Required confinement and edge density for satisfying the fusion output of 4 GW and the radiation loss power of 400 MW in the main and SOL plasmas were estimated using the A-SSTR2 design parameters for various impurity accumulation levels and density profiles. The analysis using the 1-D transport code TOPICS/IMPACT indicated that the argon density profile twice as peaked as the electron density profile can yield acceptable radiation profile even with a peaked density profile. The required effective confinement improvement factor over the IPB98(y,2) scaling (HH_{y2}^{eff}) slightly increased from 1.4 with the flat density profile to 1.5 with the peaked electron density profile at $n_e(r/a=0)/n_e(r/a=0.7) \sim 3$. Here, an effective heating power calculated by subtracting the radiation loss power inside the position of $r/a = 0.9$ from the total heating power was used for the estimation of HH_{y2}^{eff} . At the same time, required edge density can be reduced below the Greenwald density. This result suggested advantage of the peaked density profile in a burning plasma. When the argon density profile was determined by neoclassical transport, the radiation loss in the core plasma intensively increased with the peaked density profile, which requires higher HH_{y2}^{eff} of 1.9 at $n_e(r/a=0)/n_e(r/a=0.7) \sim 3$. In the JT-60U ITB plasmas with a weak magnetic shear, Ar density profile is more peaked by a factor of 2 than the electron density profile. In JT-60U reversed shear plasmas, impurity accumulation is larger than that in the weak shear plasmas, but is smaller than the neoclassical prediction. These analyses indicated that the impurity injection scenario could be applicable to a burning plasma with the density peaking.

Reference

[1] H. Takenaga *et al.*, Fusion Sci. Tech. **50** (2006) 503.

4.11 Effects of Ripple Loss of Fast Ions on Toroidal Rotation [1]

M. Yoshida, Y. Koide, H. Takenaga, H. Urano, N. Oyama, K. Kamiya,
Y. Sakamoto, Y. Kamada and the JT-60 Team

It is now widely recognized that the plasma rotation profile plays the critical roles in determining transport and MHD stability in tokamak plasmas. In particular in operating the self-regulating systems, such as burning high beta plasmas, we need integrated plasma control schemes including rotation profile from the edge pedestal to the core plasma regimes. Towards this goal, we have to construct the physics basis on driving mechanism of plasma rotation and on momentum transport. In JT-60U, near-perpendicular neutral beam (PERP-NB) heated plasmas exhibit a CTR rotation in the toroidal [2]. An inward electric field induced by a ripple loss of fast ions was considered as a candidate for the CTR rotation in the peripheral region. In order to reduce the toroidal field ripple, ferritic steel tiles (FSTs) have been installed inside the JT-60U vacuum vessel on the low field side.

In this report, effects of the ripple loss of fast ions on the toroidal rotation velocity (V_t) are investigated by using data with and without FSTs. The reduction in CTR rotation with PERP-NB injection has been obtained by inserting FSTs. The ratio of ripple loss power to the input power on this discharge ($I_p=1.23$ MA, $B_T=2.6$ T, $q_{95}=4.1$, $Vol.=77$ m³) reduces by installing FSTs from ~4% to ~1% for CO-NBs and from ~30% to ~10% for PERP-NBs, respectively. The magnitude of CTR rotation increases with increasing the ripple loss power in the peripheral region. The CTR rotation with PERP-NBs reduces by installing FSTs as a consequence of the reduction in the ripple losses. The driving mechanism of CTR rotation and the location of the driving source with PERP-NBI are investigated using OFMC code and a beam perturbation experiment ($I_p=0.87$ MA, $B_T=3.8$ T, $q_{95}=8.2$, $Vol.=72$ m³). Location of the driving source of CTR rotation is recognized in the peripheral region ($0.7 < r/a < 0.9$) and agrees with the region where fast ion losses mainly take place. The toroidal rotation profile in the core region is also discussed from the viewpoint of a moment transport by means of data from the beam perturbation experiment. The toroidal momentum diffusivity χ_ϕ and the convection velocity V_{conv} in the core region ($0.2 < r/a < 0.65$) are evaluated from the transient momentum transport analysis using the radial profiles of the amplitude of the modulated part of V_t (V_{t0}) and of the phase delay of V_{t0} . The toroidal momentum diffusivity χ_ϕ is comparable to the ion thermal diffusivity, and V_{conv} is about -5 m/s (inward) at $r/a \sim 0.5$ in this plasma. In addition, V_t profile in the core region can be almost reproduced by χ_ϕ and V_{conv} .

References

- [1] M. Yoshida *et al.*, Plasma Phys. Control. Fusion **48** (2006) 1673.
- [2] Y. Koide *et al.*, Plasma Phys. Control. Nucl. Fusion Research **1** (1992) 777.

4.12 Momentum Transport and Toroidal Rotation Profile in L-mode plasmas [1]

M. Yoshida, Y. Koide, H. Takenaga, H. Urano, N. Oyama, K. Kamiya,
Y. Sakamoto, G. Matsunaga, Y. Kamada and the JT-60 Team

Burning plasmas in ITER and fusion reactors are highly self-regulating governed by strong linkages among pressure, current and rotation profiles. In addition, recent tokamak studies have been emphasizing that the plasma rotation profile plays essential roles in determining confinement and stability. In order to understand and control the plasma rotation profile, the construction of physics based momentum transport and those effects on rotation profiles are required. Concerning toroidal momentum transport, most of the previous works evaluated the diffusive term utilizing the steady state momentum balance equation. However, it is recognized that the measured toroidal rotation velocity (V_t) profiles cannot be explained by the momentum transport coefficient evaluated by the steady state equation.

In this paper, parameter dependence of the toroidal momentum diffusivity (χ_ϕ) and the convection velocity (V_{conv}), and the relation between χ_ϕ and heat diffusivity (χ_i) are systematically investigated in typical JT-60 L-mode plasmas using the transient analysis by using the momentum source modulation [2]. Even in the L-mode regime, these plasmas stay in a low collisionality and small Lamore radius regime with $\rho_{pol}^* \sim 0.03-0.06$ and $\nu^* \sim 0.07-0.26$. Experiments have been carried out to investigate the momentum transport as the absorbed power is varied from 2.4 to 10.7 MW under otherwise similar conditions ($I_p=1.5$ MA, $B_T=3.8$ T, $q_{95}=4.2$, $\delta=0.3$, $Vol.=74$ m³). The momentum diffusivity increases with increasing the heating power, and the shape of χ_ϕ is nearly identical. The inward V_{conv} exists and has maximum value at $r/a \sim 0.6$. The momentum diffusivity at $r/a=0.6$ roughly scaled linearly with heating power in this data set. The momentum diffusivity increases with increasing χ_i , and a dependence of χ_ϕ/χ_i on β_N is observed. We also investigate I_p dependence on χ_ϕ and V_{conv} . During this I_p scan ($I_p=0.87, 1.5, 1.77$ MA), one CO tangential NB and one PERP-NB are injected with a similar absorbed power $P_{ABS}=3.3-4$ MW and other plasma parameters were $B_T=3.8-4.1$ T, $\delta=0.3$ and $\bar{n}_e=1.3-1.9 \times 10^{19}$ m⁻³. The inverse χ_ϕ at $r/a=0.6$ increases linearly with I_p . Such improvement of the momentum confinement is identified by steady toroidal momentum profiles. It is also found that toroidal rotation velocity profiles in the case with and without external torque input can be almost reproduced by χ_ϕ and V_{conv} estimated from the transient momentum transport analysis at low β ($\beta_N < 0.4$).

References

- [1] M. Yoshida *et al.*, Nucl. Fusion **47** (2007) 856.
[2] M. Yoshida *et al.*, Plasma Phys. Control. Fusion **48** (2006) 1673.

4.13 Observation of Spontaneous Toroidal Rotation with Large Pressure Gradient [1]

M. Yoshida, Y. Kamada, H. Takenaga, Y. Sakamoto, H. Urano,
N. Oyama, G. Matsunaga, and the JT-60 Team

The toroidal rotation velocity (V_t) profile is determined by momentum transport, the external momentum source and the spontaneously induced plasma rotation. It is important to separately evaluate contributions of the spontaneous rotation and the external induced rotation, and to understand the mechanism responsible for the generation of spontaneous rotation. Although the worldwide progress in understanding the physics of momentum transport and rotation has been made experimentally and theoretically, the characteristics of the rotation profile including the spontaneous term is not yet sufficiently understood. This is due mainly to an experimental difficulty in separating the non-diffusive term and the spontaneous term.

In this paper, we have identified the spontaneous rotation, which is not determined by the momentum transport coefficients and the external momentum input. The momentum transport coefficients can be obtained separately as the toroidal momentum diffusivity (χ_ϕ) and the convection velocity (V_{conv}) from the transient momentum transport analysis and the V_t profile is calculated using these coefficients, the external torque and the boundary condition of V_t . From this approach, we have identified roles of external induced rotation and the spontaneous rotation on the measured V_t profiles. The heating power scan is performed both in L-mode ($I_p=1.5$ MA, $B_T=3.8$ T, $q_{95}=4.2$, $\delta\sim 0.3$, $\kappa\sim 1.3-1.4$) and in H-mode plasmas ($I_p=1.2$ MA, $B_T=2.8$ T, $\delta\sim 0.33$, $\kappa\sim 1.4$) in order to investigate the effect of plasma pressure on the spontaneous rotation. The absorbed power (P_{ABS}) is varied over the range $2.4 \text{ MW} < P_{ABS} < 11 \text{ MW}$ for the L-mode plasma discharges, and $4.8 \text{ MW} < P_{ABS} < 10 \text{ MW}$ for the H-mode discharges. Although the measured V_t agrees with the calculation in the region $0.45 < r/a < 0.65$, the measured V_t deviates from the calculated one in the CTR-direction in the core region $0.2 < r/a < 0.45$. The difference in V_t is observed in the region where such large pressure gradients are measured. A good correlation between the difference in V_t (i.e. $V_t(\text{calculation}) - V_t(\text{measurement})$) and the pressure gradient is found during the heating power scan: ΔV_t increases with increasing pressure gradient in all cases including L-mode, H-mode, CO-, and CTR-rotating plasmas. These results indicate that the local pressure gradient plays the role of the local value of spontaneous rotation velocity.

References

- [1] M. Yoshida *et al.*, Phys. Rev. Lett. **100** (2008) 105002.
- [2] M. Yoshida *et al.*, Plasma Phys. Control. Fusion **48** (2006) 1673.

4.14 Response of Toroidal Rotation Velocity to Electron Cyclotron Wave and Lower Hybrid Wave Injection [1]

Y. Sakamoto, S. Ide, M. Yoshida, Y. Koide, T. Fujita, H. Takenaga

In tokamak plasmas, toroidal rotation velocity and its shear (or radial electric field (E_r) shear) play an important role for stability and transport. In present tokamak devices, the toroidal rotation velocity profile can be easily controlled by toroidal momentum input from neutral beams (NBs). In contrast, the control of toroidal rotation velocity profile by NBs will be difficult in a burning plasma. Therefore the development of other actuators to control toroidal rotation velocity profile is important for the control of a burning plasma. The study of spontaneous toroidal rotation velocity under the no/low direct toroidal momentum input is one of the issues towards a fusion reactor.

Toroidal rotation profile under the pure electron heating such as the combined heating of EC and LH was investigated in JT-60U reversed magnetic shear plasmas. In order to evaluate the toroidal rotation profile in pure electron heating phase, the first CXRS spectrum after 16.7 ms from the start of perp-NB injection is analyzed. In the experiments, I_p , B_T and q_{95} are 1.2 MA, 3.6T and 6.2 for the fundamental EC central injection, and the line averaged electron density is $\sim 0.4 \times 10^{19} \text{ m}^{-3}$, and the working gas is hydrogen. In the case of EC injection only, where EC power of 1.5MW, the peaked electron temperature profile with 12 keV at the centre and the flat toroidal rotation profile in the co-direction were observed. In the case of the combined heating of LH and EC where the injected powers of LH and EC are $\sim 2\text{MW}$ and 1.5MW respectively, on the other hand, the higher electron temperature of 17 keV with box-type strong ITB with higher co-rotation was observed. In these plasmas, positive E_r profiles are formed, which may cause the toroidal rotation velocity in the co-direction, and the E_r in the combined heating case is significantly larger than that in the EC injection case.

The strong correlation between the toroidal rotation velocity near the centre and the stored energy of the plasma was obtained, which is similar to that obtained in other devices with ICRF heated plasmas. Furthermore the strong correlation is found in the relation between the toroidal rotation velocity and the soft X-ray signal from the divertor plate that is sensitive to photons in the energy range of 2-14 keV. These results suggested that the observed spontaneous toroidal rotation velocity in the co-direction is caused by the formation of positive E_r due to the direct loss of energetic electrons produced by EC and LH injection.

Furthermore the short pulse off-axis EC injection experiment shows that the perturbation of toroidal rotation velocity towards co-direction (or reduced counter-rotation) propagates to the centre with increasing its amplitude, suggesting inward pinch in momentum transport.

Reference

[1] Y. Sakamoto *et al.*, Plasma Phys. Control. Fusion **48** (2006) A63.

5. H-mode Confinement and Pedestal

5.1 H-mode Pedestal Structure in the Variation of Toroidal Rotation and Toroidal Field Ripple [1]

H. Urano, N. Oyama, K. Kamiya, Y. Koide, H. Takenaga, T. Takizuka, M. Yoshida, Y. Kamada and the JT-60 Team

The edge pedestal structure characterized by the formation of the H-mode edge transport barrier (ETB) is known to determine the boundary condition of the heat/particle transport in the plasma core as well as the characteristics of ELMs. In the current ITER design, the toroidal field (TF) ripple δ_r is estimated as $\sim 1\%$ without ferritic steel tiles (FSTs). It is presumed that in the peripheral region an inward electric field is produced by the losses of fast ions due to TF ripple, which drive toroidal rotation V_T in the ctr-direction.

In this study, comparing between the plasmas before and after the installation of FSTs, the effects of the TF ripple on the edge pedestal properties were examined in JT-60U. In addition, conducting the power scans for a variation of the toroidal momentum sources, the characteristics of the H-mode pedestal structure depending on toroidal rotation were also investigated.

By the reduction of toroidal field (TF) ripple with FSTs, the spatial profile of V_T became less counter particularly in case where co-NBI was used in the large volume configuration with a large TF ripple of $\sim 2\%$. In this case, the plasma pressure was raised in whole plasma. At the plasma edge, higher pedestal temperature was obtained with the growth of pedestal width. However, the effect of FSTs became less significant in the small volume configuration with a small TF ripple of $\sim 0.4\%$ where the pedestal pressure and the energy confinement were not clearly improved.

As the V_T became less counter at the pedestal, ELM frequency f_{ELM} was reduced and ELM energy loss ΔW_{ELM} was increased. In the case of V_T in relatively co-direction, ELM affected area of the electron temperature profiles extends radially more inward than those for the case of V_T in ctr-direction. In addition, the inter-ELM transport loss is reduced and the pedestal pressure p^{ped} is weakly raised. The effect of FSTs appeared clearly in the large volume configuration where p^{ped} is raised even at a given V_T at the pedestal while p^{ped} is not changed by FSTs in the small volume configuration, suggesting that the reduction of TF ripple, the magnitude of which can affect the V_T profile, plays a role in increasing of p^{ped} . For increased p^{ped} due to the edge toroidal rotation in co-direction and the reduction of TF ripple, the spatial width of H-mode pedestal became wider.

References

- [1] Urano H et al., Nucl. Fusion **47** (2007) 706

5.2 Roles of Edge Toroidal Rotation, Toroidal Field Ripple and Configuration on ELM Characteristics [1-4]

K. Kamiya, H. Urano, N. Oyama, and Y. Kamada

1. Introduction

High confinement mode (H-mode) operation having an Edge Localized Mode (ELM) is considered as the reference inductive operational scenario for ITER (e.g., a ratio of the fusion power to the additional heating power, $Q_{DT}=10$). One of the most remarkable phenomena in the H-mode plasmas having Type-I ELMs (so-called, “Type-I” ELMy H-mode) is the large and periodic power and particles directed toward the divertor and/or the first-wall, which is normally observed for the best performing H-mode in many tokamaks. For the ITER reference inductive scenario in ELMy H-mode operation, periodic ELM crash and recovery have a potential for controlling plasma density and impurity (He ash and light/heavy metals) accumulation in the plasma core, which is essential for a steady state operation, though ELMs induced energy and particle losses can potentially limit the divertor’s lifetime (e.g., an acceptable divertor lifetime could be realized only by an upper limit of ELM energy loss normalized by pedestal stored energy, $\Delta W_{ELM}/W_{ped}\sim 5\text{-}6\%$). The goal of this research area is to understand the roles of the toroidal rotation at the plasma edge, toroidal field ripple (TF-ripple), and configuration in ELM energy loss. The physics which determines the edge processes, such as ELM characteristics, may offer a key to develop an operational scenario in future devices. This paper presents a systematic study of the Type-I ELM characteristics in tangential co-, balanced-, and counter-NBI plus perpendicular NBI-heated plasmas with various configurations. In this study, the ELM characteristics are related to the change in the toroidal rotation at the plasma edge, TF-ripple, and plasma configuration.

2. Effects of toroidal field ripple on ELMs

It is well known that a significant $V_{T,ped}$ in the direction counter to the plasma current has been observed as an offset toroidal rotation in the peripheral region even in the co-NBI (+ perp.) heated discharge at a given heating power crossing the separatrix, P_{SEP} ($=P_{ABS}-P_{RAD}-dW/dt$; here, P_{ABS} is the absorbed power, P_{RAD} radiation loss power, and dW/dt the increasing rate of the total stored energy in the plasma.), which is related to the losses of fast ions due to perpendicular NBI and the formation of negative E_r . From the results described above, it is suggested that the effect of the resultant toroidal rotation at the plasma edge caused by the losses of the fast ions due to the TF-ripple on ELMs is also an interesting edge phenomenon, which may also provide a controllable parameter for ELM mitigation.

TF-ripple scan experiments were performed on configurations having TF-ripples at the plasma edge, δ_{ripple} , of $\sim 0.4\%$ (small $V_P\sim 50\text{ m}^3$), $\sim 1.0\%$ (middle $V_P\sim 65\text{ m}^3$), and $\sim 2\%$ (large $V_P\sim 75\text{ m}^3$) under the condition of the $I_p=1.0\text{ MA}$ (small), 1.1 MA (middle), and 1.2 MA (large) at a fixed $B_T=2.6$ at a $n_e/n_{GW}\sim 0.4\text{-}0.5$, scanning combinations of tangential NBI and heating power of perpendicular NBI. The magnetic equilibrium with $\delta/\kappa\sim 0.24/1.59$, $\sim 0.35/1.45$ and $\sim 0.33/1.40$ for the discharges of the small, middle, and large V_P configurations, respectively, are shown in Fig.1 (Left). It is noted that the q_{95} at each configuration is almost the same value of ~ 4 due to an increased I_p in the case of a larger plasma volume (or surface area).

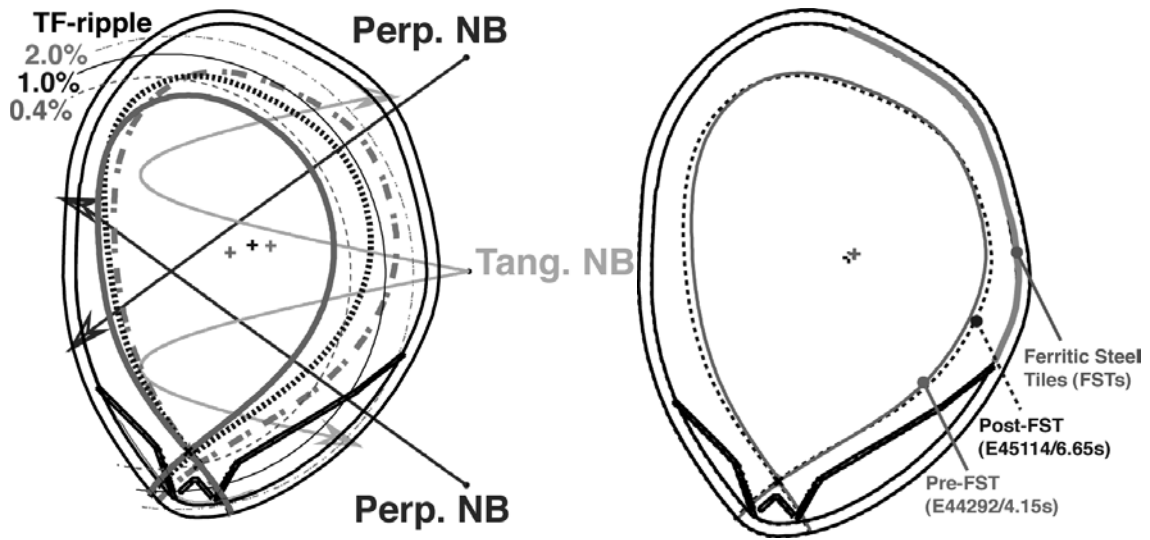


Fig. 1 (Left) The magnetic equilibrium with $\delta/\kappa \sim 0.24/1.59$, $\sim 0.35/1.45$, and $\sim 0.33/1.40$ for discharges of small $V_P \sim 50 \text{ m}^3$ (solid line), middle $V_P \sim 65 \text{ m}^3$ (dotted line), and large $V_P \sim 75 \text{ m}^3$ (chained line) configurations, respectively. The contours of toroidal field ripples δ_{ripple} of 0.4% (small $V_P \sim 50 \text{ m}^3$), 1.0% (middle $V_P \sim 65 \text{ m}^3$), and 2% (large $V_P \sim 75 \text{ m}^3$) are also shown. (Right) Poloidal cross-sectional view of JT-60U, comparing pre- (solid line) and post-FSTs (dotted line) campaigns for “large” volume plasmas ($V_P \sim 75 \text{ m}^3$). The locations of the FSTs are also shown.

Figure 2 (a) shows a dependence of the $\Delta W_{\text{ELM}}/W_{\text{ped}}$ on the $V_{\text{T,ped}}$ under a $P_{\text{SEP}} \sim 5\text{-}6$ MW at each configuration. A reason for the narrower dynamic range toward the co-direction in the $V_{\text{T,ped}}$ for the larger volume configuration is due to an offset toroidal rotation towards the counter-direction at the edge plasma region due to larger losses of fast ions from perpendicular NBI. As shown in Fig.2 (b), the power fraction lost by fast ions is less than 15% in the configuration having small plasma volume, while it is more than 30% in the configuration having a large plasma volume. Also, the power fraction lost by fast ions in the configuration having a middle plasma volume is intermediate between them. Here, the power fraction lost by fast ions is defined as $(P_{\text{orbit}} + P_{\text{ripple}} + P_{\text{CX}})/(P_{\text{NBI}} - P_{\text{ST}})$, which is the sum of the powers of the orbit loss, P_{orbit} , ripple loss, P_{ripple} , and charge exchange loss, P_{CX} , normalized by the NBI power, P_{NBI} , from which shine-through power, P_{ST} , is subtracted.

The most important point in Fig.2 (a) is a systematic difference in the $\Delta W_{\text{ELM}}/W_{\text{ped}}$ (in other words, offset $\Delta W_{\text{ELM}}/W_{\text{ped}}$) varying from $\sim 9\%$ (small-volume), $\sim 6\%$ (middle-volume), and $\sim 4\%$ (large-volume) at a given $V_{\text{T,ped}} \sim 50 \text{ km/s}$, suggesting important roles of other parameters in determining the edge stability, such as TF-ripple (or losses of fast ions) and plasma configuration. It should be noted that the pedestal pressure and/or poloidal beta tends to decrease when plasma volume increases. However, the decrease in ΔW_{ELM} is larger than that seen in W_{ped} , and hence $\Delta W_{\text{ELM}}/W_{\text{ped}}$ decreases when plasma volume or δ_{ripple} increases.

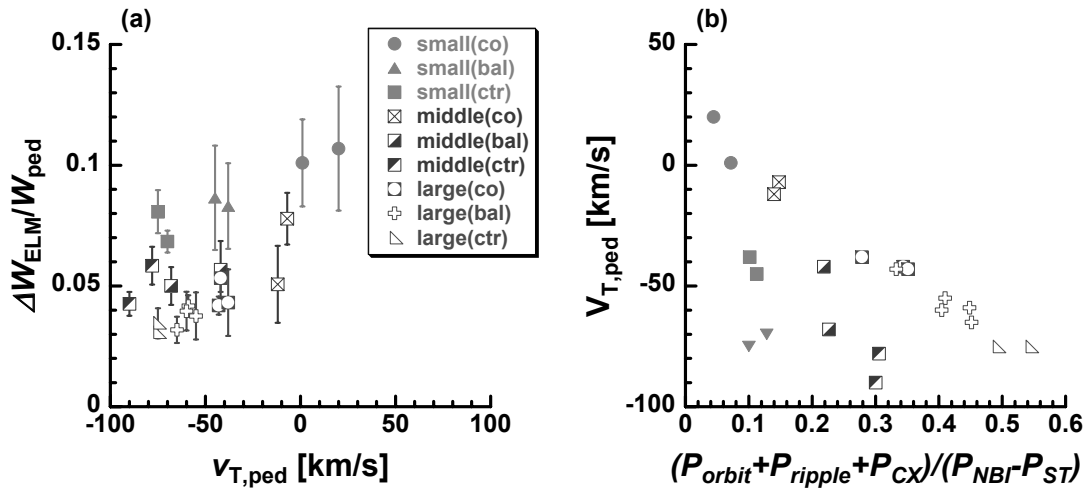


Fig. 2. (a) ELM energy loss normalized by the pedestal stored energy, $\Delta W_{ELM}/W_{ped}$, plotted against toroidal rotation at the top of the pedestal, $v_{T,ped}$, and (b) the $v_{T,ped}$ plotted against the power fraction lost by fast ions in the tangential co- (full circles), balanced- (full triangles), and counter- (full squares) plus perpendicular-NBI heated plasmas at a $P_{SEP} \sim 5-6$ MW for the configurations having toroidal field ripples of $\delta_{ripple} \sim 0.4\%$ (red; small $V_P \sim 50$ m³), 1.0% (blue; middle $V_P \sim 65$ m³), and 2% (green; large $V_P \sim 75$ m³), respectively. The power fraction lost by fast ions are defined as $(P_{orbit} + P_{ripple} + P_{CX}) / (P_{NBI} - P_{ST})$, which is the sum of the powers of the orbit loss, P_{orbit} , ripple loss, P_{ripple} , and charge exchange loss, P_{CX} , normalized by the NBI power, P_{NBI} , from which shine-through power, P_{ST} , is subtracted.

3. Effects of reduced TF-ripple on ELMs

Recent experiments run on JT-60U have successfully demonstrated a reduction of the toroidal field ripple after the installation of Ferritic Steel Tiles (FSTs) inside the vacuum vessel. One of the advantages of H-mode studies on JT-60U is that a comparison between the pre- and the post-FSTs campaigns makes it possible to clarify the effects of reduced TF-ripple on ELMs and the pedestal under the matched plasma configurations as shown in Fig.1 (Right), eliminating uncertainties in the shaping effect.

An enhanced $v_{T,ped}$ into the co-direction due to reduced losses of fast ions from perp.-NBI is clearly observed after the installation of FSTs only at the large V_P configurations (~ 75 m³) shown in Fig.1 (Right), and the p_{ped} tends to increase with $v_{T,ped}$. The result from the calculation using the Fully Three-Dimensional magnetic field Orbit-Following Monte-Carlo (F3D OFMC) code shows that the power fraction lost by fast ions is reduced from 30-40% in the pre-FSTs campaign to 15-20% in the post-FSTs campaign in the configuration having large plasma volume with co-tangential plus perpendicular-NBI discharges. Furthermore, compared to the pre- and the post-FSTs campaigns, a higher p_{ped} is obtained in the case with FSTs even at a given $v_{T,ped}$, again. The extended width of the H-mode pedestal with enhanced $v_{T,ped}$ into the co-direction and a reduced TF ripple are also demonstrated after installation of FSTs only at the large V_P configurations so far. These experimental results are obtained by a systematic comparison between the pre- and the post-FSTs campaigns at a matched plasma shape with almost the same wall conditions, eliminating uncertainties regarding both the shaping effect and neutral recycling. So far, no significant enhanced pedestal performances, such as higher pedestal height and/or wider pedestal width, have been achieved in other configurations (e.g., small and middle volume cases).

A comparison of the pre- and post-FSTs campaigns shows that they share a similarity regarding the dependence of $\Delta W_{\text{ELM}}/W_{\text{ped}}$ on $V_{\text{T,ped}}$ as shown in Fig.3. This is because both ELM energy loss ΔW_{ELM} and pedestal stored energy W_{ped} increase according to the enhanced $V_{\text{T,ped}}$ toward the co-direction, and hence, dependences of the normalized ELM energy loss $\Delta W_{\text{ELM}}/W_{\text{ped}}$ on $V_{\text{T,ped}}$ remain unchanged even after FSTs installation. So, it is suggested that the role of “configuration” is more important than δ_{ripple} in the appearance of small Type-I ELM in large volume plasma, and the TF-ripple itself and/or losses of fast ions may not be directly related to the normalized ELM energy loss, $\Delta W_{\text{ELM}}/W_{\text{ped}}$.

4. Summary

Recent experimental studies are presented regarding ELMy H-mode plasma having Type-I ELMs in the JT-60U. No remarkable effect of reduced toroidal field ripple due to the installation of Ferritic Steel Tile (FSTs) inside the vacuum vessel on the JT-60U on ELMs for large volume plasma is seen in the ELM energy loss normalized by the pedestal stored energy, $\Delta W_{\text{ELM}}/W_{\text{ped}}$. In a comparison of the pre- and the post-FSTs campaigns, the similar dependences of the $\Delta W_{\text{ELM}}/W_{\text{ped}}$ on the $V_{\text{T,ped}}$ was seen. It is due to the increase in both ΔW_{ELM} and W_{ped} according to the enhanced $V_{\text{T,ped}}$ in the co-direction, suggest that plasma configuration plays a more important role than δ_{ripple} in the appearance of small Type-I ELM in large volume plasma. The TF-ripple itself and/or losses of fast ions may not directly affect the normalized ELM energy loss, $\Delta W_{\text{ELM}}/W_{\text{ped}}$.

Reference

- [1] H. Urano et al., *Plasma Phys. Control. Fusion* **48**, A193 (2006).
- [2] H. Urano et al., Proc. 21st IAEA Fusion Energy Conf., Chengdu (China), 2006, appear in CD-ROM paper IAEA-CN-149/EX/5-1 (*Nucl. Fusion* **47**, 706 (2007)).
- [3] Kamiya K., et al., *Plasma Phys. Control. Fusion* **48**, A131 (2006).
- [4] Kamiya K., et al., *Plasma and Fusion Research* **2**, 005 (2007).

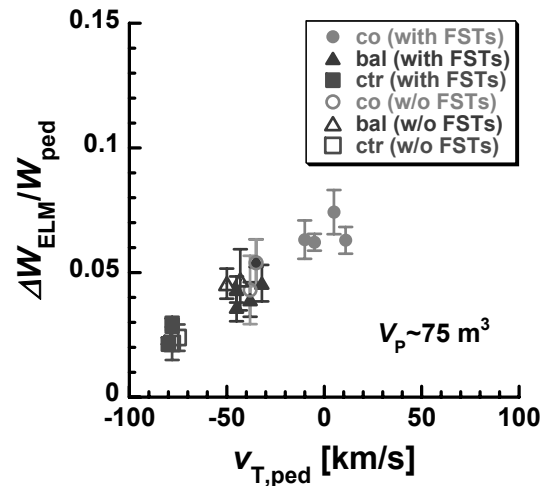


Fig. 3 A comparison of pre- and post-FSTs campaigns in terms of ELM energy loss normalized by the stored energy in the pedestal region, $\Delta W_{\text{ELM}}/W_{\text{ped}}$, plotted against the toroidal rotation at the top of the pedestal, $V_{\text{T,ped}}$, in the tangential co- (circles), balanced- (triangles), and counter- (squares) plus perpendicular-NBI heated plasmas at $P_{\text{SEP}} \sim 5$ MW for the configuration having large plasma volume ($V_p \sim 75$ m³).

5.3 Effect of Toroidal Field Ripple in JET/JT-60U Similarity Experiments

N. Oyama, G. Saibene¹⁾, V. Parail²⁾, H. Urano, J. Lönnroth³⁾, Y. Kamada

1) EFDA Close Support Unit – Garching

2) Euratom/UKAEA Fusion Association

3) Association Euratom-Tekes, Helsinki University of Technology, Finland.

1. Introduction

Inter-machine comparison is a very powerful tool to identify the physics mechanism determining the plasma behavior, as well as a way to validate the physics assumptions at the basis of physics based scalings used for the prediction of the plasma parameters of ITER. In 2003-2004 experimental campaign, successful identity experiments were performed in both devices aimed at the comparison of the plasma pedestal characteristics and ELM behavior in the two devices. The experimental results indicated that the observed differences between JET and JT-60U H-mode pedestal in matched shape plasmas may be due to toroidal field ripple (see Fig. 1) and/or resultant differences in toroidal rotation [1], because the analysis shows that MHD stability of both tokamaks is similar and probably cannot explain the observed difference in ELMy H-mode performance [2]. In this experimental campaign, therefore, the pedestal performance and ELM characteristics with reduced ripple using Ferritic Steel Tiles (FSTs) are compared with previous experiments without FSTs.

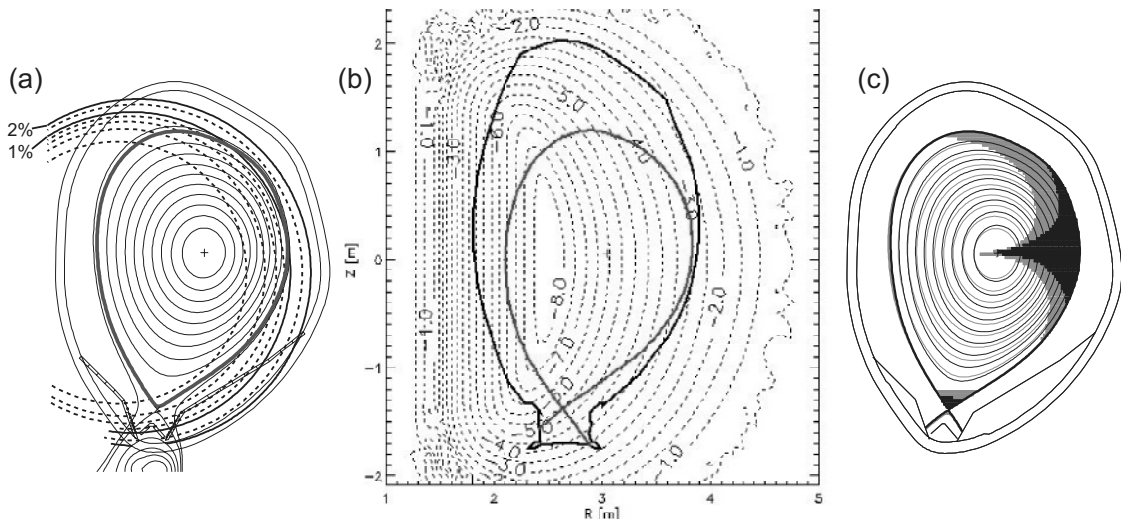


Fig. 1. (a) and (b) Plasma configuration for similarity experiments with ripple amplitude in JT-60U (a) and JET (b). Linear (log) scale is used for JT-60U (JET). (c) Comparison of "quasi" ripple well structure between JT-60U plasmas without (gray) and with (black) FSTs.

2. Experimental Result

2.1 Effect of toroidal field ripple using matched plasma configuration

The toroidal magnetic field of 3.1T in previous experiments was determined so as to match non-dimensional parameters between two devices at 1.08MA and 1.8MA. However, only small reduction of toroidal field ripple can be expected at 3.1T. Therefore, the toroidal

magnetic field of 2.2T at 1.08MA was selected from view points of the availability of edge diagnostics in JET and of the level of ripple reduction. Figure 1(c) shows the comparison of "quasi" ripple well structure [3] evaluated at a section where the maximum local ripple exists in the case with FSTs. The required injection power to achieve the given absorbed power of $\sim 8.5\text{MW}$ was reduced from 14.1MW without FSTs to 11.9MW with FSTs, which corresponds to the reduction of the loss power fraction ($P_{\text{loss}}/P_{\text{inj}}$) from 39% to 29%. Since the reduction of fast ion losses mitigated the formation of an inward electric field, which causes the toroidal rotation in the direction counter to the plasma current (ctr-rotation), plasmas with FSTs can rotate in the co-direction. In these operational conditions, NBI power scan and density scan were performed to investigate the effect of toroidal field ripple and toroidal rotation.

The value of electron density and temperature at the top of the pedestal are compared in Fig. 2. In this figure, only the data from type I ELMy H-mode plasmas are plotted. When we applied a constant gas puffing of $7\text{Pa}\cdot\text{m}^3/\text{s}$, a degradation of pedestal pressure was observed together with a change of ELM characteristic, where ELM type was changed to mixture of type I ELM and type III ELM. The variation of the data and achievable pressure were similar in both cases with and without FSTs. In the previous experiments, an improvement of pedestal performance was observed, when perpendicular NBIs were replaced with N-NBI, as shown by diamonds in Fig. 2. We had considered that a reduction of fast ion losses and consequent reduced ctr-rotation were possible candidates to explain the improved pedestal pressure at the time. After installation of FSTs, smaller ctr-rotation than previous experiments was obtained in some plasmas. However, no clear improvement was observed as shown in Fig. 2.

The achieved total pedestal pressure (p_{ped}) including ion pressure as a function of the toroidal rotation frequency (V_T) measured at the top of T_i pedestal is plotted in Fig. 3. The achievable p_{ped} of about 5kPa was similar between the plasma with and without FSTs except for the plasma with N-NBI, and no clear dependence on V_T was observed so far. The H-mode performance, H_H factor, was also similar in plasmas with and without FSTs. Therefore, a dependence of H_H factor on pedestal pressure was similar.

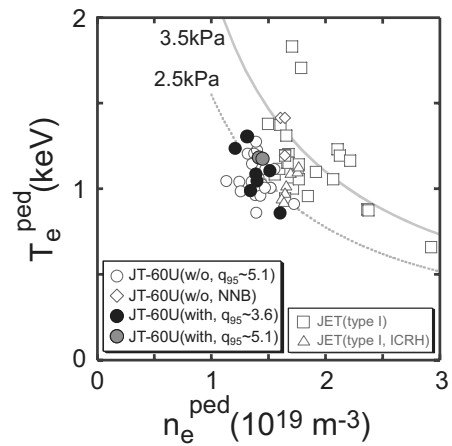


Fig. 2. Comparison of electron density and temperature at pedestal between plasmas with and without FSTs together with corresponding JET data.

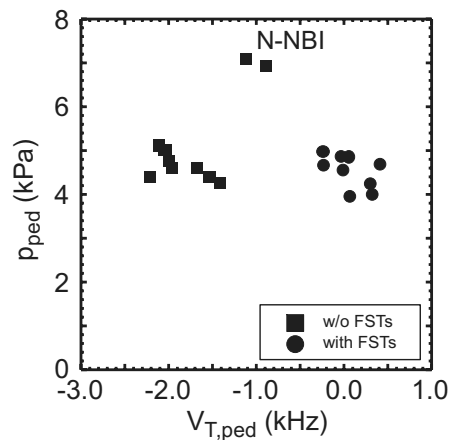


Fig. 3. Comparison of total pedestal pressure as a function of toroidal rotation frequency measured at T_i pedestal between plasmas with and without FSTs.

In contrast to pedestal and H-mode performance, remarkable changes in ELM characteristic were observed after the installation of FSTs. Although the pedestal stored energy was similar as shown in Fig. 3, the ELM energy loss (ΔW_{ELM}) became 1.5-2.5 times higher. On the other hand, the reduction of the ELM frequency (f_{ELM}) was smaller than the increase in the ΔW_{ELM} . Therefore, the ELM loss power ($P_{ELM}=f_{ELM}\times\Delta W_{ELM}$) became larger as shown in Fig. 4(a). As for the f_{ELM} , it is noted that ELM frequency dependence (f_{ELM}/P_{sep}) follows the other H-mode experiments [4, 5] as shown in Fig. 4(b). This result suggests that a change in ELM frequency dependence is related to the change in the edge toroidal rotation.

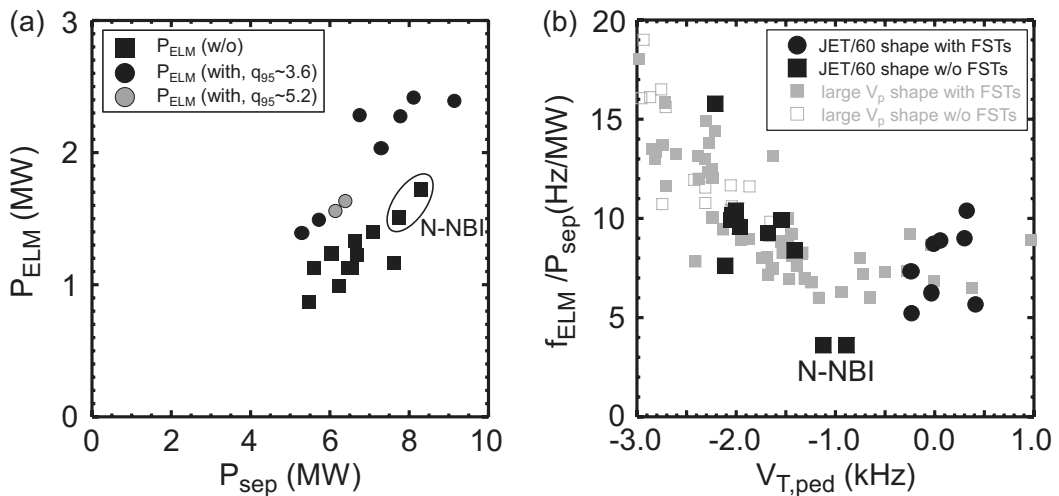


Fig. 4. (a) ELM loss power as a function of power through the separatrix. (b) Normalized ELM frequency as a function of toroidal rotation frequency at the top of pedestal.

2.2 Effect of local ripple well region near X_p

There is a local ripple well region near X_p even after the installation of FSTs as shown in Fig. 1(c), because FSTs were only installed from midplane to the top of the plasma. The effect of local ripple well region was also investigated, because the ASCOT simulation including an effect of ripple induced thermal ion losses indicates that a ripple near X_p has significant contribution to the thermal ion confinement [6]. In the experiment, pedestal performance between high and low X_p configurations was compared using the same plasma parameters in Sec. 2.1. A high X_p configuration was obtained by shifting plasma configuration up by 14cm as shown in Fig. 5.

Achieved plasma profiles are compared in Fig. 6. No considerable difference between two configurations was observed. Time evolution of W_{dia} during the power scan was also similar. The ELM frequency of ~ 80 Hz in the low X_p configuration was higher than that of ~ 60 Hz in the high X_p configuration. The main reason of different ELM frequency was considered due to higher recycling level in the low X_p

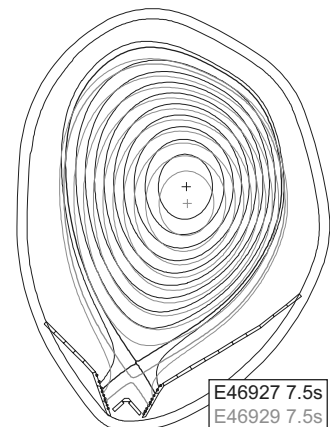


Fig. 5. plasma shape in high and low X_p configurations.

configuration, because the difference in toroidal rotation was not so large and edge profiles were similar. These experimental observations indicate that the effect of local ripple well near X_p on the pedestal performance is small. In addition to this, ELM frequency seems to be more sensitive to the recycling level than pedestal parameters.

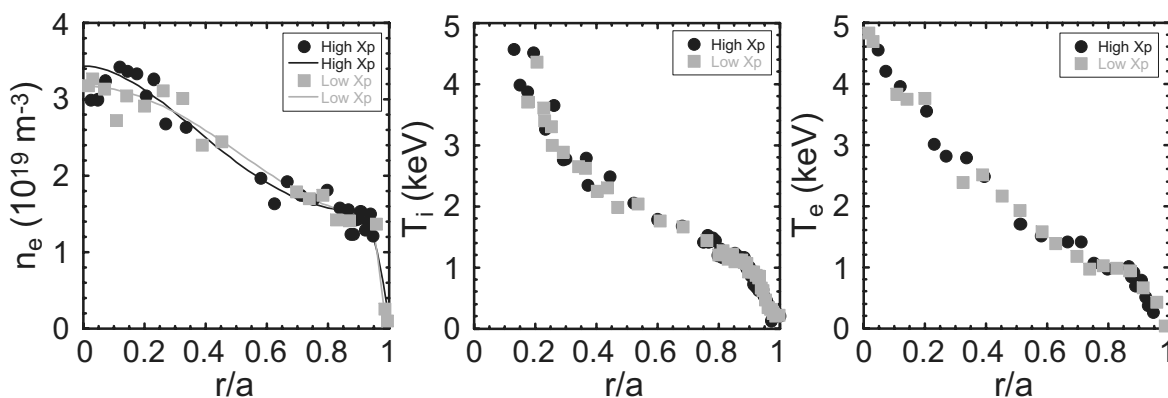


Fig. 6. Comparison of plasma profiles between high and low X_p plasma configuration.

3. Summary and Discussion

Effects of toroidal field ripple on pedestal performance and ELM characteristics were investigated by comparing plasmas with and without FSTs using JET/JT-60U similarity configuration. Although the reduction of fast ion losses and consequent reduced counter plasma rotation were achieved, no significant improvement of pedestal performance has been observed. On the other hand, a change in ELM size, which resulting in higher P_{ELM}/P_{sep} , was clearly observed. The ELM frequency dependence on the toroidal rotation was similar to that observed in the dedicated H-mode experiments with large plasma configuration. The effect of local ripple well region near X_p was also investigated using upper shifted plasma configuration. The comparison of plasma profiles between high and low X_p configuration revealed that the effect of the local ripple well near X_p on the pedestal performance was small (at least in case without gas puffing). In order to understand effects of toroidal field ripple and/or toroidal rotation, more experiments and analysis will be needed to connect other experimental results, because the improvement of pedestal pressure was observed when the ctr-rotation became small in other H-mode experiments [4]. In addition to this, the reason of the improvement of the pedestal performance and ELM characteristics using N-NBI should also be understood in future experiments.

References

- [1] Saibene, G., *et al.*, Nucl. Fusion **47**, 969 (2007).
- [2] Lonroth, J., *et al.*, Plasma Phys. Control. Fusion **49**, 273 (2007).
- [3] Shinohara, K., *et al.*, Plasma and Fusion Research **1**, 007 (2006).
- [4] Urano, H., *et al.*, Nucl. Fusion **47**, 706 (2007).
- [5] Kamiya K., *et al.*, Plasma and Fusion Research **2**, 005 (2007).
- [6] V. Parail *et al.*, 32nd EPS Conference on Plasma Phys. Tarragona, 27 June - 1 July 2005 ECA Vol.29C, O-2.008 (2005).

5.4 ELM Frequency Dependence on Toroidal Rotation in the Grassy ELM Regime [1]

N. Oyama, Y. Kamada, A. Isayama, H. Urano, Y. Koide,
Y. Sakamoto, M. Takechi, N. Asakura and the JT-60 Team

The grassy ELM regime found in JT-60U is one of small ELM regimes in a low-collisionality region. The grassy ELMs are characterized by a high frequency and localized periodic collapse at the edge. So far, the safety factor (q_{95}), triangularity (δ), poloidal beta (β_p) and edge toroidal rotation have been found to be important plasma parameters in determining access to the grassy ELM regime. Although the grassy ELM regime seems to be a common small ELM regime in tokamaks, further investigation is needed in order to understand the effect of toroidal rotation on the access to the grassy ELM regime, so that the applicability to ITER can be discussed, because the ASTRA code predicts a small toroidal rotation frequency of 0.26 kHz for ITER in the fusion gain of 10 standard scenario.

In an attempt to investigate the effect of the toroidal rotation on ELM characteristics in JT-60U, systematic scans in the level of toroidal rotation and β_p were performed in high q_{95} (>6) and high δ (>0.53) plasmas by varying the combination of tangential and perpendicular NBIs. As ctr-rotation increased, the ELM frequency clearly increased up to ~ 1400 Hz independently of β_p in the range $0.84 < \beta_p < 1.88$ at $\delta > 0.53$. Even in plasmas with zero rotation and balanced NBIs, a higher ELM frequency of ~ 400 Hz compared with that in typical type I ELMs has been observed without large ELM energy loss (ΔW_{ELM}). When the plasma rotation frequency becomes higher than ~ 1 kHz in co-direction, on the other hand, type I ELMs with frequency of ~ 20 Hz have been observed. In a series of toroidal rotation scans, no degradation in the pedestal pressure was observed. In the grassy ELM regime, ΔW_{ELM} was estimated to be several kJ based on the fast drop in the edge temperature, and its ratio to the pedestal stored energy to be less than 1%. The small ΔW_{ELM} in the grassy ELM regime was characterized by the narrow radial extent of the collapse of the temperature pedestal. Likewise, the ELM-affected area seemed to be constant within the spatial resolution of the diagnostics in the grassy ELM regime for a range of ELM frequencies from ~ 200 Hz to ~ 1400 Hz.

Comparing the response to a change in the toroidal rotation frequency between the high δ plasmas ($\delta > 0.53$) and configurations with slightly lower δ ($\delta \sim 0.43$) shows that higher δ seems to increase the threshold of toroidal rotation frequency where there is a transition from the grassy ELM regime to the type I ELM regime. The requirement of toroidal rotation frequency for access to the grassy ELM regime may be less stringent in highly shaped plasmas. In other words, high δ plasmas may have a wider operation window in the toroidal rotation.

Reference

[1] Oyama, N., *et al.*, Plasma Phys. Control. Fusion **49** (2007) 249.

6. MHD Instability and High-Energy Ions

6.1 Control of Growth of Neoclassical Tearing Mode by Central Co-ECCD [1, 2]

A. Isayama, N. Oyama, H. Urano, T. Suzuki, M. Takechi, S. Ide, Y. Kamada, T. Ozeki, K. Nagasaki¹⁾, and the JT-60 team

1) Institute of Advanced Energy, Kyoto University, Uji, Kyoto 611-0011, Japan

In a fusion reactor such as ITER, plasma operation with a high fraction of bootstrap current is expected to reduce the need for externally driven current. In such plasmas, however, neoclassical tearing modes (NTMs) would be excited. Since NTMs degrade plasma performance and sometimes cause a disruption, it is critically important to establish a scenario to control the NTMs. In JT-60U, stabilization of an $m/n=3/2$ NTM was previously demonstrated by identifying the mode location and optimizing the injection angle of electron cyclotron (EC) wave. Here, m and n are the poloidal and toroidal mode numbers, respectively. In this operational scenario, the EC wave was deposited at the center of the island.

As another scenario, we investigated the possibility of the control of a $3/2$ NTM by electron cyclotron current drive (ECCD) in the same direction as the existing plasma current (co-ECCD). Since co-ECCD decreases the safety factor in the central regime, the scale length of current profile will decrease at the mode rational surface, which will act to stabilize the NTM according to the modified Rutherford equation. In addition, since co-ECCD will enhance sawtooth oscillations as previously demonstrated in JT-60U [2], some stabilizing or destabilizing effects on an NTM are expected.

In experiments, behaviors of a $3/2$ NTM for no ECCD, 2-unit ECCD, and 4-unit ECCD were compared. Plasma parameters were as follows: plasma current $I_p=1.5$ MA, toroidal field $B_t=3.7$ T, safety factor at 95% of flux surface $q_{95}=3.9$. Without ECCD, a $3/2$ NTM appeared with ~ 20 MW neutral beam injection at $\beta_N \sim 1.6$ ($\beta_p=1.2$), and no sawteeth was observed throughout the discharge. For 2-unit ECCD (EC-driven current $I_{EC} \sim 70$ kA), sawteeth appeared soon after ECCD, and a $3/2$ NTM appeared at similar time as no ECCD case. While the growth rate of the $3/2$ NTM for the 2-unit ECCD was twice as large as that for no-ECCD, the mode amplitude saturated at similar level. For 4-unit ECCD ($I_{EC} \sim 130$ kA), the growth of a $3/2$ NTM was suppressed and the mode amplitude was kept $\sim 1/5$ of the other cases. The mode amplitude was kept low even after the EC wave was turned off, and sustained for more than 10 times energy confinement time. In both 2-unit ECCD and 4-unit ECCD cases, the $3/2$ NTM was not triggered by a sawtooth crash. Frequency spectrum of magnetic perturbations for the 4-unit ECCD showed that the mode frequency of the $3/2$ NTM was modulated by a sawtooth crash while such a modulation was not observed for the 2-unit ECCD case. This suggests that a sawtooth crash could affect the $3/2$ NTM. The value of β_N for the 4-unit was 6% higher than that for the 2-unit ECCD case, showing that it can be another candidate for NTM control.

References

- [1] Isayama, A., et al., Plasma Fusion Res. **1**, 030 (2006).
- [2] Isayama, A., et al., Proc. 21st IAEA Fusion Energy Conference, EX/4-1Ra (2006); submitted to Nuclear Fusion.
- [3] Isayama, A., et al., Plasma Fusion Res. SERIES **5**, 324 (2002).

6.2 Stabilization of an $m/n=2/1$ Neoclassical Tearing Mode by Electron Cyclotron Current Drive [1]

A. Isayama, N. Oyama, H. Urano, T. Suzuki, M. Takechi, N. Hayashi, K. Nagasaki¹⁾,
Y. Kamada, S. Ide, T. Ozeki and the JT-60 team

1) Institute of Advanced Energy, Kyoto University, Uji, Kyoto 611-0011, Japan

Suppression of NTMs is important to obtain and sustain a high-beta plasma. In previous JT-60U experiments, an $m/n=3/2$ NTM was completely stabilized by using a real-time NTM stabilization system, where the detection of the mode location and the optimization of the injection angle of EC wave were performed in real time. Also, preemptive NTM stabilization, where EC wave was injected to the anticipated mode location before the mode onset, was shown effective. In addition, a high-beta plasma with the normalized $\beta_N \sim 3$ was sustained for 5 times longer than the energy confinement time by suppressing NTMs.

Stabilization of an $m/n=2/1$ NTM by ECCD at the mode rational surface was performed. In particular, effect of ECCD location on stabilization was investigated in detail. Complete stabilization was achieved when the misalignment of ECCD location was less than about half of the full island width (~ 5 cm). Also the mode amplitude was found to increase when the misalignment was comparable to the island width. After the finer tuning of the ECCD location, a $2/1$ NTM has been completely stabilized only with one gyrotron (~ 0.6 MW). The ratio of the EC-driven current density to the bootstrap current density at the mode rational surface, j_{EC}/j_{BS} , which is a measure of the efficiency of NTM stabilization, was as low as ~ 0.5 .

Simulation of the stabilization of an $m/n=2/1$ NTM was performed using the TOPICS code combined with the modified Rutherford equation. The coefficients in the modified Rutherford equation were determined by comparing with experimental results. The TOPICS simulations were found to well reproduce the stabilization and destabilization of a $2/1$ NTM observed in JT-60U experiments with the same set of coefficients in the modified Rutherford equation. The TOPICS simulations also predicts that ECCD width has a strong effect on NTM stabilization.

Reference

[1] Isayama, A., et al., Proc. 21st IAEA Fusion Energy Conference, EX/4-1Ra (2006);
submitted to Nuclear Fusion.

6.3 Effect of Plasma-Wall Separation on the Stability of Resistive Wall Modes [1]

G. Matsunaga, M. Takechi, G. Kurita, T. Ozeki, Y. Kamada and JT-60 Team

For fusion reactor with an economically attractiveness, a resistive wall mode (RWM) that could limit β -value must be stabilized. The RWM is an instability of which growth time is slower to the order of the wall skin time due to the finite resistivity of the wall. It is predicted that the RWM stability, in particular the growth rate, strongly depends on the plasma-wall separation. Therefore, to clarify the effect of the plasma-wall separation on the RWM stability, we have performed current-driven RWM experiments in the JT-60U ohmic plasmas. In ohmic discharges, since a MHD stability is determined by only q -profile, the behavior of the MHD instability can be purely interpreted. In the experiment, the plasma was placed near the outer wall, and the plasma current was ramped up so as to destabilize the current-driven RWM. When the edge safety factor q_{eff} , which is q -value at about 97% of minor radius, was just below 3, a thermal collapse occurred due to an instability with a clear $m/n = 3/1$ mode structure. The growth time of this instability is about 10 ms which is the order of the skin time of the JT-60U wall $\tau_w = 10$ ms. Therefore, the instability has been identified as a current-driven RWM.

To investigate the effects of the plasma-wall separation on the RWM, the plasma-wall separation was changed from shot to shot, and the clearance feedback control was utilized to keep the plasma-wall separation constant in a shot. In consequence, it is found that the growth rates has the strong dependence on the wall position. Thus, the growth rate became smaller with decreasing the plasma-wall separation. Additionally, the observed growth rates have been compared with the AEOLUS-FT code, which is based on the resistive MHD equations with a resistive wall, and the model of the RWM dispersion relation. According to the AEOLUS-FT calculations, an $m/n = 3/1$ kink mode and an $m/n = 2/1$ tearing mode are unstable together under these experimental conditions. The dependence of the observed growth rate on the wall position is in qualitative agreement with an $m/n = 3/1$ kink branch, in contrast, it is quite different from an $m/n = 2/1$ tearing branch. However, in this comparison, the absolute value of the observed growth rates is about a factor 10 smaller than the dispersion relation with $\tau_w = 10$ ms. Taking into account the time scale of the equilibrium evolution, the observed growth rate could be smaller than a liner growth rate [2]. Actually, the reevaluated growth rates are consistent with the RWM dispersion relation with $\tau_w = 10$ ms. This point is required to investigate in future work.

References

- [1] G. Matsunaga et al., Plasma Phys. Control. Fusion **49**, 95 (2007)
- [2] J. D. Callen et al., Phys. Plasmas **6**, 2963(1999)

6.4 Identification of a Low Plasma-Rotation Threshold for Stabilization of the Resistive-Wall Mode [1]

M. Takechi, G. Matsunaga, N. Aiba, T. Fujita, T. Ozeki, Y. Koide,
Y. Sakamoto, G. Kurita, A. Isayama, Y. Kamada, and the JT-60 team

To realize an economical fusion reactor, stabilization of the low- n kink-ballooning mode is necessary. The growth rate of the external kink-ballooning mode can be reduced with a close-fitting conducting wall, and the resulting mode, the so-called resistive-wall mode (RWM), has a growth time corresponding to the time constant of the relaxation of the wall current. There are two different procedures for stabilizing RWM. The first is the feedback control stabilization using externally applied non-axisymmetric magnetic fields with coils in order to compensate for the diffusion of flux. The second is stabilization of RWM by toroidal plasma rotation. Both theories and experiments imply that the critical rotation velocity is around 1%–2% of the Alfvén velocity. The most significant problem in the previous experiment is that investigation of the critical rotation is performed with magnetic braking by adding an asymmetric magnetic field, the so-called error field. It has been pointed out that the error field plays a very important role in the destabilization of RWM and should be substantially reduced near the limit for the ideal mode without a wall, the so-called “no-wall limit”. Since RWM stability itself is affected by the error field, which is the origin of magnetic braking, we should not use magnetic braking in the investigation of critical rotation.

For investigating the critical rotation, we employ a weak reversed magnetic shear plasma with $I_p = 0.9$ MA and $B_t = 1.58$ T. Internal inductance of this plasma is decreased to $l_i = 0.8$ to decrease the no-wall limit. The clearance between the plasma surface and the first wall on the outer midplane is $\delta_0 = 20$ cm, which is equivalent to a ratio of the radius of the first wall to the plasma minor radius of $d/a = 1.2$. A very low rotation threshold was obtained in the JT-60U in an investigation of the critical rotation for stabilizing RWM by controlling the toroidal plasma rotation with changing the combination of tangential neutral beams (NBs) without magnetic braking. The observed critical rotation is $V_t \sim 20$ km/s and corresponds to 0.3% of the Alfvén velocity at the $q=2$ surface, much smaller than the previous prediction with magnetic braking. This low critical rotation does not increase as beta increases toward the ideal wall limit. Also an ITER relevant low rotation ($\sim 0.4\%$ of the Alfvén velocity) stabilization of RWM is demonstrated for 50 times the skin time of the first wall. These results indicate that for large plasmas such as in future fusion reactors with low rotation, the requirement of the additional feedback control system for stabilizing RWM is much reduced.

Reference

[1] Takechi, M., *et al.*, Phys. Rev. Lett. **98** (2007) 055002.

6.5 Confinement Degradation and Transport of Energetic Ions due to RSAEs and TAEs in Weak Shear Plasmas [1]

M. Ishikawa, M. Takechi, K. Shinohara, G. Matsunaga, Y. Kusama, A. Fukuyama¹⁾, V. A. Krasilnikov²⁾, Yu. Kashuck²⁾, T. Nishitani, A. Morioka, M. Isobe³⁾, M. Sasao⁴⁾ and JT-60 team

1) Kyoto University, 2) TRINITI (Russia), 3) NIFS, 4) Tohoku Univ.

Alpha particles play an important role in the plasma heating in burning plasmas. However, a high alpha particle pressure gradient can induce Magnetohydrodynamics (MHD) instabilities such as Alfvén Eigenmodes (AEs) (toroidicity-induced AEs (TAEs)) or Energetic particle modes (EPMs). These MHD instabilities can cause enhanced transport of alpha particles from the core region of the plasma, which could degrade the performance of burning plasmas. Moreover, lost alpha particles could also damage the first walls. Thus, the understanding of alpha particle transport due to these instabilities is the important research issue for ITER. Then, several kinds of AEs and EPMs have been predicted theoretically and observed experimentally and their effects on energetic ions have been studied in several Tokamak, ST and Helical devices. Recently, another type of AEs, whose frequency largely sweep with the time scale of a few hundreds millisecond and then saturate as the minimum value of the safety factor (q_{\min}) decreases, have been extensively studied. These frequency behavior can be explained by reversed-shear induced AEs (RSAEs) [2] and its transition to TAEs. In the previous studies in JT-60U, confinement degradation of energetic ions due to these AEs has been confirmed from the measurements of the total neutron rate. However, since the measured total neutron rate is a volume-integrated value, it has not been known how energetic ions are transported in the plasma and/or lost.

In the present work, in order to investigate radial transport of energetic ions due to these modes, line-integrated neutron emission profile are measured using a large neutron collimator array [3] and compared with the calculated value by a classical theory using a transport code TOPICS. As a result, it is found that energetic ions are transported from core region of the plasma due to these AEs for the first time. Further, changes in energy distribution and flux of the charge exchange (CX) neutral particle are measured [4] in order to investigate energetic ion transport in the velocity space. The changes in energy distribution of CX neutral fluxes suggest the radial transport is due to the resonance interaction between energetic ions and AEs. Thus, the results of the measurements of neutron emission profile and CX neutral particle flux indicate that radial transport of energetic ions is induced by the resonance interaction between energetic ions and AEs.

References

- [1] Ishikawa, M., et al., in Fusion Energy 2006 (Proc. 21st Int. conf. Chengdu, 2006) IAEA-CN-149/EX/5-2; submitted to Nuclear Fusion.
- [2] TAKECHI, M. et al., Physics of Plasmas **12**, 082509 (2005)
- [3] Ishikawa, M., et al., Rev. Sci. Instrum. **73**, 4237 (2002).
- [4] Ishikawa, M., et al., Rev. Sci. Instrum. **75**, 3963 (2004).

6.6 Orbit Following Calculation of Energetic Ions in the Design of Ferritic Insertion [1]

K. Shinohara, Y. Suzuki, S. Sakurai, K. Masaki, T. Fujita, and Y. Miura

The toroidal field (TF) ripple induces loss of energetic ions due to local mirror trapping (ripple trapped loss) and/or due to lack of symmetry of banana orbit (banana diffusion). Such enhanced transport of the energetic ions reduces the efficiency of the heating and current drive. To avoid such enhanced transport due to the ripple induced loss, installation of ferritic steel was proposed. The first experiment was carried out on JFT-2M to investigate the reduction of energetic ion loss by using ferritic steel. And the reduction of NB ion loss and the compatibility of ferritic steel with high performance plasmas were demonstrated [2, 3].

Through the valuable experience and results on ferritic insert experiments on JFT-2M, ferritic insertion on JT-60U was decided. The TF ripple reduction by the ferritic insertion is expected to contribute to the steady-state high-beta plasmas research, because the reduction of energetic ion loss brings: 1) enhancement of the heating and current drive “effective” efficiency, 2) extended pulse length of RF injection due to the reduced heat flux on antennas and improved coupling between antennas and a plasma with a smaller gap, 3) availability of wall stabilization without losing heating power, and 4) possibility of enhanced availability of the rotation control to improve the MHD stability and transport.

The design work was carried out aiming at effective, machine-safe, and short-term installation. In the design work, the enhanced confinement of energetic ions and absence of the large heat flux on the first wall has been assessed for the NB ions (two co-tangential, two counter-tangential, seven perpendicular positive ion-based neutral beams and one co-tangential negative ion-based neutral beam) by using the Fully three Dimensional magnetic field Orbit-Following Monte-Carlo code, which was developed under the ferritic insert program in JFT-2M. We investigated several configurations of ferritic insertion. In the final design, the loss power ratio to the injected NB power is reduced by larger than 10 % in a large volume plasma.

References

- [1] K. Shinohara, et. al., Plasma Fusion Res. **1**, 007 (2006)
- [2] K. Shinohara, et.al. , Nucl. Fusion **43**, 586 (2003)
- [3] K. Tsuzuki, et.al., Nucl. Fusion **43**, 1288 (2003)

6.7 Observation of Spontaneously Excited Waves in the Ion Cyclotron Frequency Range [1]

M. Ichimura¹⁾, H. Higaki²⁾, S. Kakimoto¹⁾, Y. Yamaguchi¹⁾, K. Nemoto¹⁾, M. Katano¹⁾,
M. Ishikawa, S. Moriyama, T. Suzuki

1) University of Tsukuba, 2) Hiroshima University

In magnetically confined plasmas, fluctuations in the ion cyclotron range of frequency (ICRF) may be driven by the presence of non-thermal ion distribution. In burning plasma experiments on JET and TFTR, ion cyclotron emissions (ICEs) have been observed in the ion cyclotron frequency and its higher harmonic regions [2,3]. Two types of magnetic fluctuations are detected on JT-60U: one is due to high energy D ions from neutral beam (NB) injections and the other is due to fusion products (FPs) of ³He and T ions. FP-ICEs will become a significant diagnostic tool for fusion reactions. The precise study of the excitation mechanism is important for future burning plasma experiments.

On JT-60U, deuterium NBs (positive ion based P-NBs and negative ion based N-NB) are used to realize the high performance operation. ICRF antennas are used as pick up loops for detecting the electrostatic and/or electromagnetic fluctuations. Two sets of ICRF antennas, which are installed with the distance of 1.67 m, are used in this experiment. Sharp frequency peaks that correspond to the fundamental and 2nd harmonic cyclotron frequencies of ³He ion near the outer midplane edge of the plasma appear when the tangential P-NBs (80keV, 4MW) are injected. After perpendicular P-NBs (80keV, 8MW) are injected, relatively broad peaks due to D ions are detected. A peak with the lowest frequency appears after tangential N-NB (450keV, 3MW) is injected, which is considered to be due to T ions. The amplitude of peaks due to ³He ions becomes small when the density increases, even if the emission of neutrons becomes large. On the other hand, the amplitude of the peak due to T ions appears when the emission of fusion neutrons becomes large enough. The wave excitation mechanism will be related not only to the fusion reaction but also to the plasma parameters. By using two antenna straps arrayed in the toroidal direction, the toroidal mode structure can be determined. Fluctuations due to D ions have almost no phase difference between two straps, that is, small k_{\parallel} and will behave as electrostatic waves. On the other hand, peaks due to FP-ions have finite phase differences and different wave numbers in the toroidal direction. The wave number of the modes due to ³He and T ions is estimated to be around 3 and 10 m^{-1} , respectively, which is determined from the measurement of phase differences among three different straps. It is observed that peaks due to FP-ions are sometimes split into doublet shape as observed in JET burning experiments. The phase differences of both peaks are measured and indicate that the two waves are traveling in both toroidal directions.

The first measurement of the toroidal wave numbers of ICEs has been done. Experimental results support the excitation of the magnetoacoustic cyclotron instability is the possible origin of FP-ICEs.

References

- [1] M.Ichimura, et al., Submitted to Nuclear Fusion.
- [2] G.A.Cottrell et al., Nuclear Fusion, **33** (1993) 1365.
- [3] R.O.Dendy, et al., Phys. Plasmas **1** (1994) 1918.

7. Plasma Control and Operational Limit

7.1 Plasma Shape Calculation in a Magnetic Environment with Ferritic Steel Tiles [1, 2]

K. Shinohara, S. Sakurai, K. Tsuzuki¹⁾, Y. Suzuki, O. Naito, K. Kurihara, T. Suzuki, Y. Koide

1) The Institute of Applied Energy

A precise plasma control on a large tokamak is one of the most important issues to avoid a crucial damage caused by large plasma current and TF strength. In particular, a plasma shape has a strong connection to energy confinement performance, and stability as well as safe operation. Since the reconstruction of a plasma shape and equilibrium is based on magnetic measurements, its accuracy depends on how the magnetic field only from a plasma can be detected by excluding the other components of magnetic fields.

For the 2005-2006 experimental campaign, we have installed the ferritic steel tiles (FSTs) with high magnetism in order to improve the confinement of energetic beam ions [3]. Under such an environment with the FSTs, the sensors additionally pick up the total magnetic field including the field produced by the FSTs. The magnetic field by the FSTs is a consequence of the non-linear interactions between the FSTs and the plasma, and between the FSTs and the poloidal field coils. The real-time control could be difficult if the non-linearity were strong. The strength of the non-linearity had been marginal on the preliminary rough estimation.

In the JT-60U, the code for the real-time plasma position and shape control is based on the Cauchy Condition Surface (CCS) method. Considerations on the available computational resources in real-time control suggested that we should revise the code using the following simple model. The FST influence on the sensors is evaluated in the model expressed by the functions as shown in Eq. 1, which were newly formulated through the numerical simulation and the fitting of the numerical results.

$$\psi_{fe}^j(t) \approx \sum f_i^j \left\{ \bar{B}_{ext}(\bar{X}_i, t - \Delta t) \right\}, \quad \bar{B}_{fe}^j(t) \approx \sum g_i^j \left\{ \bar{B}_{ext}(\bar{X}_i, t - \Delta t) \right\} \quad (1),$$

where ψ_{fe}^j is a magnetic flux by the FSTs, B_{fe}^j is a magnetic field by the FSTs, i is the group number (The FSTs are divided into four groups in the poloidal direction, considering computing resources). j is the index of a mesh point at the plasma region and each magnetic sensor, Δt is a calculation interval of the CCS control system, \bar{X}_i shows the representative position of the group i and \bar{B}_{ext} is the external magnetic field at each group due to plasma current and poloidal field coils, which is derived from CCS calculation results on one time slice, Δt , before the present time.

Using the modified CCS code, we evaluated the effect of the FSTs on the JT-60U. It came to be understood that the FST effect of the magnetic field is very small less than 0.5 % of the field without the FSTs, on a plasma region. This implies that the non-linearity is so small in average that the iterative time to converge the FST magnetism effect is acceptable for a real-time control. The effect, however, on some specific magnetic sensors is still large, approximately 10 %, and should be taken into account in the calculation for the precise position control, because the distance between the FSTs and magnetic sensor is rather close.

The real-time plasma shape control has been successfully carried out by employing this new version of CCS code under the environment with the FSTs on the actual plasma operation.

References

- [1] K. Shinohara *et al.*, Nucl. Fusion **47** (2007) 997.
- [2] K. Shinohara *et al.*, Fusion Energy 2006 (Proc. 21st Int. Conf. Chengdu, 2006), IAEA-CN-149/FT/P5-32 and http://www.naweb.iaea.org/nanc/physics/fec/fec2006/baners/ft_p5-32.pdf.

7.2 Real-time Control of Current Profile in High-beta Plasmas [1]

T. Suzuki, S. Ide, T. Oikawa, T. Fujita, M. Seki, G. Matsunaga, M. Takechi,
O. Naito, K. Hamamatsu, M. Sueoka

In 2004, real-time control of the safety factor profile $q(r)$ was demonstrated in a low β -plasma by controlling current drive (CD) location through control of parallel refractive-index (N_{\parallel}) of lower-hybrid (LH) waves [2]. The control system was modified for application to high- β plasmas, aiming at development of weak magnetic-shear operation, such as the ITER hybrid-scenario. Thus, the modified system controls the minimum of the safety factor (q_{\min}) that characterizes current profile in the weak-shear plasma. Here, the N_{\parallel} is properly selected to drive as much current at appropriate location under limited LH power, since the current drive efficiency is a function of the N_{\parallel} . It must be noted that driven current becomes small in a high- β plasma, since electron density becomes large due to good confinement. Instead of controlling N_{\parallel} , the LH power P_{LH} is controlled to control q_{\min} . Increase in the off-axis LHCD current with P_{LH} reduces central Ohmic current, since total plasma current I_p is fixed. Then the central current density decreases and q_{\min} increases with P_{LH} . The real-time control follows the equation $dp_{\text{LH}}/dt = -\alpha(q_{\min} - q_{\min,\text{ref}})$, where $q_{\min,\text{ref}}$ is a given reference.

The control was applied to high- β_p mode plasma ($I_p=0.8$ MA, $B_t=2.5$ T, $q_{95}=5.9$) having initial q_{\min} of about 1.2. The normalized beta β_N was about 1.3-1.6 produced by 11 MW of NB heating. After the application of the q_{\min} control, the reference $q_{\min,\text{ref}}$ was increased from 1.3 to 1.7 taking 3 s, then the q_{\min} followed the reference and reached 1.7. When the q_{\min} was controlled fixed at 1.7, central electron temperature ($r/a<0.3$), line averaged electron density and stored energy started increasing, which shows formation of an internal transport barrier (ITB). The q profile measured by the MSE diagnostic has a reversed shear structure and the position of q_{\min} was close to the foot of the ITB. The application of the real-time q_{\min} control changed the q profile and lead to the change in confinement. Due to the resulting increase in electron temperature and pressure, central Ohmic current and bootstrap current increased, leading to decrease in q_{\min} . However, the decrease in q_{\min} was recovered by the increase in P_{LH} by the control. The real-time q_{\min} control was demonstrated in such self-regulated plasma, where the pressure and current profiles are linked through the bootstrap current. In this plasma, the bootstrap current fraction and the non-inductive current fraction were 46 % and 87 %, respectively.

Applying the control to another high- β discharge ($I_p=0.8$ MA, $B_t=2.4$ T, $q_{95}=5.4$, $\beta_N=1.7$) with $m/n=2/1$ neo-classical tearing mode (NTM), q_{\min} was raised above 2 (due to overshoot of the control, actually) and the NTM was suppressed, because the resonant rational surface ($q=2$) was eliminated. The stored energy increased by 16 % with the NTM suppressed. This elimination of the resonant q surface using the real-time current profile control could be a new route to achieve high- β avoiding NTM.

References

- [1] T. Suzuki *et al.*, Nucl. Fusion **48** (2008) 045002.
- [2] T. Suzuki *et al.*, in Fusion Energy 2004 (Proc. 20th Int. conf. Villamoura, 2004) IAEA-CN-116/EX/1-3 and http://www-naweb.iaea.org/naweb/physics/fec/fec2004/papers/ex_1-3.pdf.

7.3 Off-axis NBCD Profile Measurement [1]

T. Suzuki, S. Ide, T. Oikawa, T. Fujita, M. Ishikawa, O. Naito, K. Hamamatsu

In the development of the advanced tokamak (AT) operation scenario, more emphasis has been placed on the optimization and control of current profile using external current drivers [1]. Although the on-axis current drive schemes such as on-axis NBCD and ECCD have been investigated well, study on the off-axis current drivers is still under way despite of their important role in producing weak or reversed magnetic shear for better stability and confinement. The most important off-axis current driver will be the off-axis NBCD, since it is planned to be used in ITER and JT-60SA in developing the AT operation scenario. Although the off-axis NBCD had been successfully used in optimizing the current profile and driving current in many high-performance discharges demonstrated in JT-60U, the off-axis driven current “profile” has not yet been identified, since the driven current was too small and difficult to measure. Here, we investigate the off-axis NBCD, exploiting a newly developed analysis technique [2] to evaluate small change in current profile and a newly equipped multi-chordal neutron emission profile diagnostic [3], as well as improvement in MSE diagnostic itself.

The off-axis NBCD (about 2MW) was applied in an ELMy H-mode plasma having steady current profile at $I_p=1.2\text{MA}$, $B_t=3.8\text{T}$, and high $q_{95}=5.4$ to avoid sawtooth instability. No MHD activity except ELMs was observed. Change in the pressure and the resulting bootstrap current was minimized by replacing one perpendicular heating NB with the off-axis co-tangential NB for NBCD. Thus, change in the total current profile is attributed to the change in the NB driven current. Using the new analysis technique that evaluates temporal change in current profile with respect to a reference current profile [2], we found that the change in the total current profile by the off-axis NBCD was spatially localized at about $r/a=0.65-0.8$. The loop-voltage-profile analysis confirms that the NBCD current is spatially localized at the same location. Moreover, change in the neutron emission profile (by 17%) confirms spatially localized increase in the number of the beam ions at about the same location. The change in the emitted neutrons is attributed to the beam ions by the off-axis NBCD, since estimated thermal ion contribution (th-th) to neutron yield is about 10%. Thus, both the current profile and neutron profile measurements confirm the spatially localized NBCD current at the same location. The measured NBCD profile was compared with the calculation by the ACCOME code. Although the integrated NBCD currents by the measurement (106 ± 41 kA) and the calculation (90 kA) agreed with each other, the peak of the measured profile is slightly outward shifted than the calculation by about 20% of the minor radius. The reason is not understood yet. The same discrepancy between the measurement and calculation was observed in another plasma having different plasma current ($I_p=0.8$ MA). The reason of discrepancy in the CD locations in the measurement and the calculation will be studied further.

References

- [1] T. Suzuki *et al.*, Nucl. Fusion **48** (2008) 045002.
- [2] T. Suzuki *et al.*, J. Plasma Fusion Res. **80** (2004) 362.
- [3] M. Ishikawa *et al.*, Rev. Sci. Instrum. **73** (2002) 4237.

7.4 Real-time Measurement and Feedback Control of Ion Temperature using Filter CXRS and RTP Systems [1]

M. Yoshida, S. Kobayashi¹⁾, H. Takenaga, S. Sakata, Y. Kamada and the JT-60 Team

1) Institute of Advanced Energy, Kyoto University

A real-time feedback control of the pressure profile is essentially important in sustaining high performance plasmas. In previous studies on JT-60U, concerning the real-time feedback control of plasma parameters, an electron density control has been demonstrated by a interferometer with gas-puffing, and an electron temperature control has also been carried out by a fast electron cyclotron emission radiometer with neutral beams (NBs). On the other hand, a real-time feedback control system for ion temperature (T_i) has not been established due to lacks of a high time-resolution diagnostic and a rapid analytical scheme.

In this study, a three-filters charge exchange recombination spectroscopy (CXRS) system with minimum time resolution of 0.16 ms (maximum: 12 channels) [2] has been developed for the real-time measurement and feedback control of T_i profiles. The T_i and plasma rotation velocity (V_r) are determined by the ratios of the intensity at the central wavelength channel to that of the shorter wavelength channel and to that of the longer wavelength channel. We also developed this analytical scheme for rapidly calculating T_i and V_r . In order to improve the dynamic range, the passband of each filter used for the fast CXRS diagnostic is optimized for the target value of $T_i \sim 0.1 - 20$ keV and $V_r \sim -400$ km/s - +400 km/s. In order to demonstrate the local T_i control, the local transport time scale has been estimated by a beam perturbation experiment [3]. The time scale of real-time T_i profile control should be about 10 ms, and the time resolution of T_i measurement should be about a few ms. Real-time processor system has also been improved by utilizing advantage of the filter CXRS method. The system accumulates raw data from filter CXRS for 4 ms, and processes them to T_i , where the processing time is only 2 ms owing to filter CXRS. Utilizing this filter CXRS system, real-time control of the central T_i has been demonstrated in ELMy H-mode plasmas ($I_p=1.2$ MA, $B_T=2.67$ T). The number of NB units (U) is determined as, $U=U^{base}+G_P\Delta T(t)+G_D(\Delta T(t)-\Delta T(t-\Delta t))/\Delta t$, where U^{base} , G_P , G_D and ΔT in keV represent the number of base NB units, proportional gain, differential gain and the difference between the reference value of T_i (T_i^{ref}) and the observed value (T_i^{obs}), respectively. The G_P value is calculated by the relation between U and the central T_i ($r/a \sim 0.3$). For the control of central T_i , we adopted $U^{base}=2$, $G_P=8$, and $G_D=0.4$. Using these gains, the central T_i agrees with T_i^{ref} within $\Delta T \sim 0.5$ keV (<10% of T_i^{ref}), where injected units of NB heating were successfully controlled in real time.

References

- [1] M. Yoshida *et al.*, Trans. Fusion Sci. Technol. **51** (2007) 301.
- [2] S. Kobayashi *et al.*, J. Plasma Fusion Res. **79** (2003) 1043.
- [3] M. Yoshida *et al.*, Plasma Phys. Control. Fusion **48** (2006) 1673.

7.5 Real-time Control of Ion Temperature Gradient [1]

S. Kobayashi¹⁾, M. Yoshida, H. Takenaga, S. Sakata, Y. Kamada and the JT-60 Team

1) Institute of Advanced Energy, Kyoto University

In fusion plasmas, the real-time feedback control of the pressure gradient is subject not only for sustaining the high performance plasma with internal transport barrier (ITB) but also for avoiding the disruptive MHD instabilities due to the steep pressure gradient. The real-time control of the ion temperature profile is key issue for the control of the pressure gradient in the high performance plasmas, since the steep ion temperature gradient has been observed in the ITB plasmas. Recently, we developed the high time-resolved measurement system of the ion temperature profile and its rapid analytical scheme using the filter charge exchange recombination spectroscopy [2]. Utilizing the filter CXRS system to the real-time monitor of the ion temperature profile, we carried out the demonstration of the feedback control of the ion temperature gradient (grad-T_i) in JT-60U [1]. In order to control grad-T_i , two categories of the neutral beam (NB) heating, core and edge heating, were used whose deposition profiles have each peak at the core and peripheral regions, respectively. The number of NB units U_{NB}^k was determined by the following formula using the difference between the measured ion temperature gradient and the reference one ΔT , $U_{\text{NB}}^k = G_p^k \Delta T(t) + G_d^k (\Delta T(t) - \Delta T(t-\Delta t))/\Delta t$, where G_p^k and G_d^k are the proportional and differential gains. The superscript of “k” denotes the species of the core and edge NB heating units.

The feedback control experiment of grad-T_i was demonstrated in the ELMy H-mode plasmas with ITB ($I_p/B_t = 1.0\text{MA}/2.27\text{T}$). The reference value of the temperature gradient $\Delta T_{\text{REF}}/\Delta R$ was pre-programmed to be in the range from -6.9 to -2.8 keV/m at the measurement positions between $\rho = 0.26$ to 0.65. The maximum NB units for the base, core and edge heating was 3 (= 6 MW) each other. We adopted the same proportional gain by 1.2 for core and edge heating, that is, the minimum value of the controllable grad-T_i was equivalent to $\pm 0.8\text{keV/m}$ and the total NB unit for core and edge heating was kept constant. The core and edge NB heating was controlled in real time according to the difference in grad-T_i . In the earlier phase of the discharge, measured gradient $\Delta T_{\text{CXR}}/\Delta R$ reached to the reference value, and $\Delta T_{\text{CXR}}/\Delta R$ was almost controlled to the reference in the ramp down phase. In the re-ramp up phase, however, $\Delta T_{\text{CXR}}/\Delta R$ did not recover up to the reference due to the occurrence of the MHD instabilities. The hysteresis-like characteristics of grad-T_i obtained from the transient response analysis shows the increase in the central T_i using the additional core heating is required to recover the grad-T_i in the case where ITB was degraded.

References

- [1] S. Kobayashi *et al.*, Plasma Fusion Res. **2** (2007) S1049.
- [2] M. Yoshida *et al.*, Trans. Fusion Sci. Technol. **51** (2007) 301.

7.6 Burn Control Simulation Experiments [1, 2]

K. Shimomura¹⁾, H. Takenaga, H. Tsutsui¹⁾, H. Mimata¹⁾, S. Tsuji-Iio¹⁾, Y. Miura, K. Tani, H. Kubo, Y. Sakamoto, H. Hiratsuka, H. Ichige, I. Yonekawa, M. Sueoka, Y. Kawamata, R. Sakamoto²⁾, S. Kobayashi³⁾, R. Shimada¹⁾

1) Tokyo Institute of Technology 2) National Institute for Fusion Science,
3) Institute of Advanced Energy, Kyoto University

Burning plasma is in a self-organized state, where plasma pressure and heating power are strongly coupled through α -particle heating and this coupling could easily cause a thermal excursion without burn control. In order to study burn controllability in the self-organized state, burn control simulation experiments were conducted in non-burning DD plasmas by using a burning plasma simulation scheme. Two neutral beam (NB) groups were used, where one simulates α -particle heating and the other simulates external heating. The 11 positive-ion based NB units were divided into the two groups. The injected NB power was about 2.2 MW/unit. The number of injected NB units for α -particle heating simulation group was controlled proportionally to the measured DD neutron yield rate (S_n) using a real-time control system. On the other hand, the number of injected NB units for external heating simulation group was determined with a feedback control system against the stored energy (W). The control interval for the NB system is 0.01 s.

The experiments were conducted in ELMy H-mode plasmas at $I_p = 1.0$ MA, $B_T = 2.1$ T and $q_{95} = 4.1$ and reversed shear (RS) plasmas with an internal transport barrier at $I_p = 1.0$ MA, $B_T = 3.7$ T and $q_{95} = 6.8$. The values of W and S_n were controlled at nearly constant values in both ELMy H-mode and RS plasmas. However, variation of the NB power for the external heating simulation was larger in the RS plasmas than that in the ELMy H-mode plasma, indicating that larger control margin is necessary for the RS plasmas. In order to understand the physical mechanism for the difference between ELMy H-mode and RS plasmas, we conducted numerical analysis using the 1.5-dimensional transport code TOPICS. The burning plasma simulation scheme was incorporated into the code. The calculation results indicated that the larger variation experimentally observed in the RS plasma couldn't be explained by the difference of the thermal diffusivity profiles or their temperature dependence. The linkage between the thermal diffusivity and the heating power could trigger the larger variation of the NB power for the external heating simulation in the RS plasma.

References

- [1] K. Shimomura *et al.*, Fusion Eng. Des. **82** (2007) 953.
- [2] H. Takenaga *et al.*, Fusion Sci. Technol. **50** (2006) 76.

7.7 Response of Fusion Gain to Density in Burning Plasma Simulation [1]

H. Takenaga, H. Kubo, M. Sueoka, Y. Kawamata, M. Yoshida, S. Kobayashi¹⁾,
Y. Sakamoto, S. Tsuji-Iio²⁾, K. Shimomura²⁾, H. Ichige, H. Hiratsuka, R. Sakamoto³⁾,
and Y. Miura

1) Institute of Advanced Energy, Kyoto University 2) Tokyo Institute of Technology,
3) National Institute for Fusion Science

A burning plasma simulation scheme has been developed, in order to experimentally introduce the linkage between pressure and heating profiles, similar to the alpha particle heating, in the DD non-burning plasmas. In the previous scheme [2, 3], the NB heating power proportional to the DD neutron yield rate was injected for the simulation of alpha particle heating. In this scheme, dominant fusion reaction process and temperature dependence of the neutron yield rate are different from a real DT burning plasma. These differences make response of the fusion gain different from response in the real DT burning plasma. For the improvement of the burning plasma simulation scheme, the heating power for the simulation of alpha particle heating was calculated in real-time as $P^\alpha \sim \bar{n}_e^2 f(T_i)$ using real-time measurements of line averaged electron density (\bar{n}_e) and ion temperature (T_i) at $r/a \sim 0.3$. Here, $f(T_i)$ is a function for consideration of the ion temperature dependence of the DT fusion reaction rate.

Response of a simulated fusion gain to the density was investigated in the new scheme with constant heating power for the simulation of external heating (P^{ex}), in order to understand burn controllability by the fuel density in a fusion reactor. Here, the simulated fusion gain was defined as $5P^\alpha/P^{\text{ex}}$. When temperature dependence of the fusion reaction rate was assumed to be proportional to square of ion temperature as in the range of $T_i = 10\text{-}20$ keV, density dependence of the simulated fusion gain stronger than square of density was observed. Transport analysis using the 1.5 dimension transport code TOPICS indicated that the strong density dependence is induced due to both change in a confinement improvement factor and change in a pressure profile. In the scheme used here, density and ion temperature profiles were not considered due to the limitation of real-time measurements. However, the density and the ion temperature measured with higher weight on its central value were used. Therefore, the effects of change in the pressure profile can be considered in the scheme. On the other hand, the simulated fusion gain increased proportionally to \bar{n}_e^2 even with decrease in confinement improvement factor after gas-puffing, when the fusion reaction rate was assumed not to depend on the ion temperature as in the range of $T_i = 40\text{-}100$ keV.

References

- [1] H. Takenaga *et al.*, Nucl. Fusion **48** (2008) 035011.
- [2] H. Takenaga *et al.*, Fusion Sci. Technol. **50** (2006) 76.
- [3] K. Shimomura *et al.*, Fusion Eng. Des. **82** (2007) 953.

7.8 Magnetic Flux Constant Control

H. Takenaga, S. Ide, M. Sueoka, Y. Kawamata, K. Kurihara

1. Introduction

JT-60U has demonstrated the discharges with full non-inductive current drive [1] and even with bootstrap current over drive [2]. In these discharges, a constant current was sometimes applied in the center solenoid coil (F-coil), in order to prevent inductive magnetic flux input. The inductive magnetic flux can be also injected by the vertical coils, i.e. VR- and VT-coils whose currents were changed for horizontal position control and triangularity control, respectively. When plasma beta increases, the VR-coil current should be increased to keep the horizontal position constant. This change in the VR-coil current induces the inductive magnetic flux. In order to demonstrate the discharges with full non-inductive current drive and bootstrap current over drive clearly by preventing the inductive magnetic flux input even when plasma beta changes, magnetic flux constant control was introduced. In this control, the inductive magnetic flux induced by the vertical coils is cancelled using the F-coil.

2. Control Logic

Two kinds of the magnetic flux were prepared for the control. One is the magnetic flux measured with the magnetic probe located on the vacuum vessel near the inner midplane (flux loop #8). In this case, the magnetic flux at the plasma surface is not exactly constant. The other is the surface magnetic flux calculated in real time by Cauchy Condition Surface (CCS) method [3]. One of these can be selected for the control.

The F-coil voltage (V_F^{Com}) is controlled as follows,

$$V_F^{\text{Com}} = (I_F^{\text{Observed}}(t) + I_F^{\text{Cancel}}(t)) \times R_F + I_F^{\text{Cancel}}(t) \times G_F^{\text{DDC}} [V],$$

where I_F^{Observed} is the observed F-coil current in unit of A, I_F^{cancel} is the F-coil current necessary for keeping the flux constant in unit of A, R_F is the F-coil resistivity in unit of Ω and G_F^{DDC} is the gain. The value of I_F^{Cancel} is calculated as follows,

$$I_F^{\text{Cancel}}(t) = -(\phi_{\text{in or surface}}^{\text{Observed}}(t) - \phi_{\text{in or surface}}^{\text{Observed}}(t_0)) / \phi_{\text{in or surface}}^{\text{F-coil}} [A],$$

where $\phi_{\text{in or surface}}^{\text{Observed}}$ is the magnetic flux at the inner position (in) measured with the magnetic probe or the surface magnetic flux (surface) calculated by CCS and $\phi_{\text{in or surface}}^{\text{F-coil}}$ is the magnetic flux produced by the F-coil current of 1 A at the inner position (in) or at the inner plasma surface on midplane (surface). t_0 denotes the start time of the magnetic flux constant control.

3. Experimental Results

The magnetic flux constant control was developed in OH discharges. Figure 1 shows waveforms of the discharge with the inner magnetic flux constant control. The magnetic flux constant control was applied from $t=10$ s, resulting the decrease in the plasma current. The inner magnetic flux was well controlled at constant value as shown in Fig. 1 (b), although the outer magnetic flux measured with the magnetic probe (flux loop #2) was slightly varied. The VR- and VT-coil currents decreased due to decrease in the plasma current. The F-coil current was recharged. The horizontal position moved inward for less than 2 cm. The control coefficient for the VR-coil current is not zero in the term related to the difference between measurement and reference of the plasma current. However, during the magnetic flux constant control, this coefficient set to be zero, because the plasma current was not controlled to the reference and consequently there is a large difference. Therefore, the horizontal position controllability might become worse.

The surface magnetic flux constant control was also applied as shown in Fig. 2. The magnetic flux constant control was applied from $t=12$ s. The plasma current jump was observed just after the control started, and then, the plasma current decreased. The surface magnetic flux calculated by CCS in real time was well controlled at constant value as shown

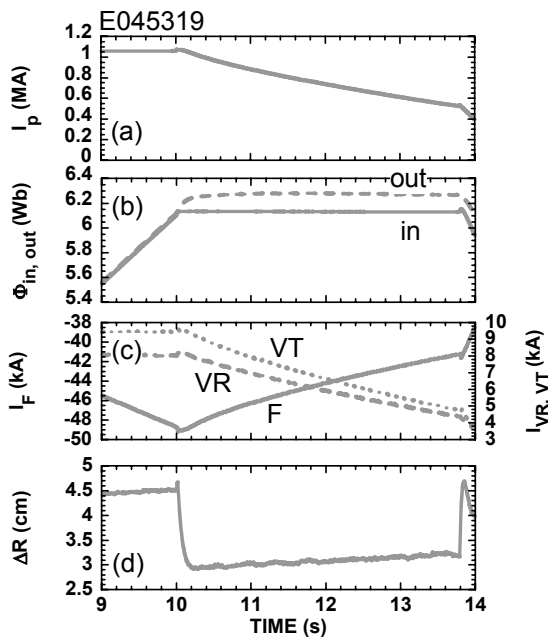


Fig. 1 Waveforms of (a) plasma current, (b) inner magnetic flux (flux loop #8) (solid line) and outer magnetic flux (flux loop #2) (dashed line), (c) F-coil current (solid line), VR-coil current (dashed line) and VT-coil current (dotted line) and (d) horizontal position with the inner magnetic flux constant control. Magnetic flux constant control was started from $t = 10$ s.

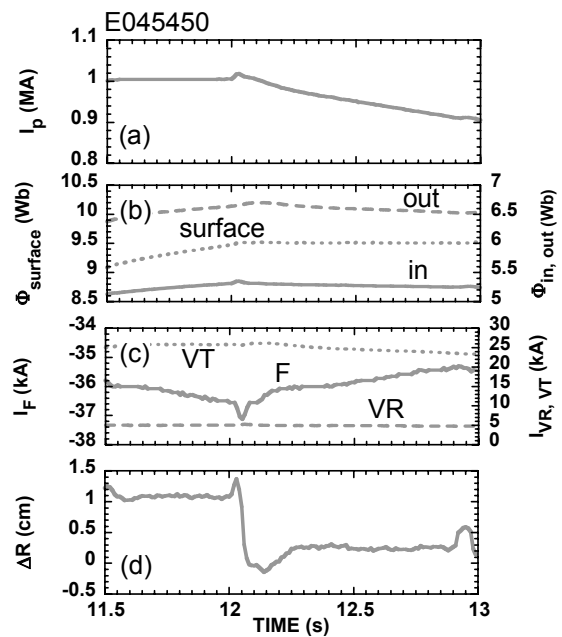


Fig. 2 Waveforms of (a) plasma current, (b) surface magnetic flux (dotted line), inner magnetic flux (flux loop #8) (solid line) and outer magnetic flux (flux loop #2) (dashed line), (c) F-coil current (solid line), VR-coil current (dashed line) and VT-coil current (dotted line) and (d) horizontal position with the surface magnetic flux constant control. Magnetic flux constant control was started from $t = 12$ s.

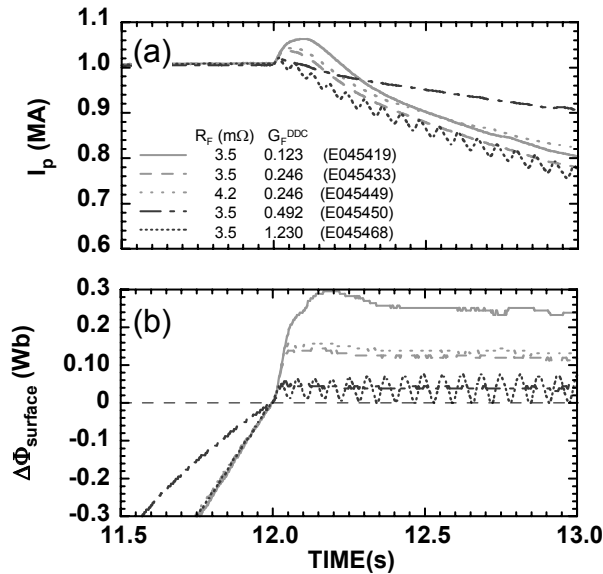


Fig. 3 (a) Plasma current and (b) difference of surface magnetic flux from the value at start of the control ($t = 12$ s).

value). Also, these values decreased with increasing G_F^{DDC} . At $G_F^{DDC} = 0.492$, the plasma current jump and the difference of the surface magnetic flux became smallest. In the case of $G_F^{DDC} = 1.23$, the plasma current was oscillated due to too much higher gain, although the plasma current jump and the difference were almost the same as those in the case of $G_F^{DDC} = 0.492$. The values of $R_F = 3.5$ m Ω and $G_F^{DDC} = 0.492$ could be optimum values.

4. Summary

The magnetic flux constant control was introduced, in order to demonstrate clearly the discharges with full non-inductive current drive and bootstrap current over drive. In this control, the inductive magnetic flux input by the vertical coils was cancelled using the F-coil. The control was demonstrated by using the inner magnetic flux measured by the magnetic probe (flux loop #8) or the surface magnetic flux calculated by CCS in real time. The control was optimized by changing the coil resistivity and the control gain. The optimization was achieved at the coil resistivity of 3.5 m Ω and the gain of 0.492.

References

- [1] A. Isayama *et al.*, Nucl. Fusion **43** (2003) 1272.
- [2] Y. Takase *et al.*, Fusion Energy 2006 (Proc. 21st Int. Conf. Chengdu, 2006), IAEA-CN-149/EX/1-4 and http://www-naweb.iaea.org/naweb/physics/fec/fec2006/papers/ex_1-4.pdf.
- [3] K. Kurihara, Fusion Eng. Des. **51-52** (2000) 1049.

7.9 Plasma Current Start-up Experiment by ECH

T. Maekawa¹⁾, H. Tanaka¹⁾, M. Uchida¹⁾, T. Yoshinaga¹⁾, Y. Takase²⁾, S. Ide

1) Graduate School of Energy Science, Kyoto University

2) Graduate School of Frontier Sciences, The University of Tokyo

1. Introduction

Removal of the central solenoid from a tokamak reactor is an attractive option to simplify the central structure of reactors. However, on the other hand, we need alternative methods to initiate the discharge and start-up and ramp-up the plasma current. ECH and ECCD are potentially attractive candidates for this purpose since plasma initiation and current start-up and ramp-up could be realized simultaneously. The requirement is only an injection of microwave power from a small launcher remote from the plasma without additional structures in the vicinity of the plasma. While a number of experiments in small devices have been done and successful [1-3], it is highly required to demonstrate its feasibility for reactors in large devices such as JT-60U.

In this campaign, we have attempted ECH start-up experiment on JT-60U and obtained 17 kA of plasma current by microwave pulses from four 110 GHz gyrotrons (0.3-0.8 MW for each tube and 2-4 seconds duration). This level of current deformed significantly poloidal field from the external field, but the field itself was still of open field structure. The microwave beams were directed toward the point on the inboard wall crossed with the mid-plane as shown in Fig. 1, with an oblique angle (~ 20 degrees from perpendicular direction to the toroidal field at the injection points to the drift direction of the expected current carrying electrons) and with the O-mode polarization. With this angle, $\sim 80\%$ of the O wave power that remains after passing through the ECR layer is mode converted into X wave power upon mirror reflection on the inboard wall. Previous experiments in small devices and also theoretical considerations predict that initial plasma current can be generated without external induction field if a weak external vertical field is applied [1]. We used VT and VR coils for vertical fields and examined various combinations of currents of these coils.

2. Results and Discussions

The decay index of vertical field, $n = -(\text{dBv}/\text{dr})(r/\text{Bv})$, should be in the range $0 < n < 1.5$ for the plasma loop to be stable for both the positional displacements in vertical and radial directions. While, unfortunately any combination of VT and VR currents can not produce appropriate vertical fields that fulfill this criterion all the way in the vacuum vessel, we done first attempt with the decay index profile (a) in Fig. 2. The three cases of ECR layers at

R=2.55m, 2.60m and 2.8m were investigated. The microwave power from three gyrotrons was injected with the maximum pulse width of 3 seconds. A current generation was observed only when the ECR layer was set to be at R=2.55 m. In this shot the Bv field was initially set to be Bv=65 Gauss and then ramped down to 39 Gauss during 1.5 seconds after ECH turned on. Amount of pre-filling deuterium before ECH pulse was 0.15 Pa m³ and no gas was injected after ECH turned on. A small current seemed to be generated at the onset of ECH. The current increased during Bv decreased from 42 Gauss to 39 Gauss. The current looked constant during the final 1.5 seconds of ECH pulse, where Bv was kept constant at Bv=39 Gauss. The generated current and its profile were analyzed by using the flux signals from the flux loops 1 to 15 attached the vacuum vessel and displayed in Fig. 1. The obtained current was ~7 kA. The current location is significantly shifted from the ECR layer to the lower field side (Fig.1(a)). Furthermore it is strongly shifted vertically upward. It is noted that the current loop has no positional stability for vertical movement in this location since the Bv decay index in this location is negative. Finally, current generation was obtained only when ECR layer was set at most inboard side. Although in this case the region of positive Bv decay index is most broad around the ECR layer, the observed current location is unstable to the vertical displacement.

The result suggested that we need vertical fields that have positive decay indices all the way in the vessel. In JT-60U, such a field can be obtained with the outboard VT coils (no inboard VT coil) as shown in the case (b) in Fig.2. Therefore, next experiment was done by using the Bv fields from the outboard VT coils only (no use of inboard VT coil and VR coil). The fields have positive decay index all the way in the vessel. In this case, a current of 18 kA was obtained. Its distribution is shown in Fig. 1(b). Although the maximum plasma current is increased by 2.5 times compared with the first attempt, the current channel is quite near the outboard wall. This bad location suggests lack of the positional stability for the radial displacement. This may be due to inappropriate decay index profile of the present Bv fields from the VT-out coil currents alone. The decay index quickly increases over 1.5 at R > 3.3.

We searched for some appropriate Bv profiles which meet the positional stabilities for both the vertical and horizontal displacements simultaneously. An addition of VR coil fields with a very small current was found to improve the decay index as shown in the case (c) in Fig.2. The third attempt was done by using this field and the results are shown in Fig.1(c) and Fig.3. Almost the same current of ~17kA was obtained. Although there is no clear closed flux surface, the current position is significantly apart from the outboard wall. Plasma images shown in Fig.3 suggest strong plasma wall interaction at the wall near the ECR layer. The images also suggest that while the discharge takes place at the ECR layer, the plasma expands quickly toward the lower field side and at the same time an initial current appears.

The current locations above three cases are always far from the ECR layer. There is a

possibility that the wave power is absorbed near the upper hybrid resonance (UHR) layer via mode conversion to the electron Bernstein waves from the X-waves reflected from the inboard wall and the current is also generated near the UHR layer. However the UHR layer seems to be near the ECR layer since the electron density estimated from the tangential interferometer chord shown in Fig.3 is quite low. Thus there is no reasonable explanation for the location of the current position and the absorption mechanism at the moment.

References

- [1] T. Yoshinaga *et al.*, Phys. Rev. Lett. **96** (2006) 125005.
- [2] H. Tanaka *et al.*, Fusion Energy 2006 (Proc. 21st Int. Conf. Chengdu, 2006), IAEA-CN-149/EX/P6-6 and http://www-naweb.iaea.org/naweb/physics/fec/fec2006/papers/ex_1-4.pdf.
- [3] A. Ejili, Nucl. Fusion **46** (2006) 709.

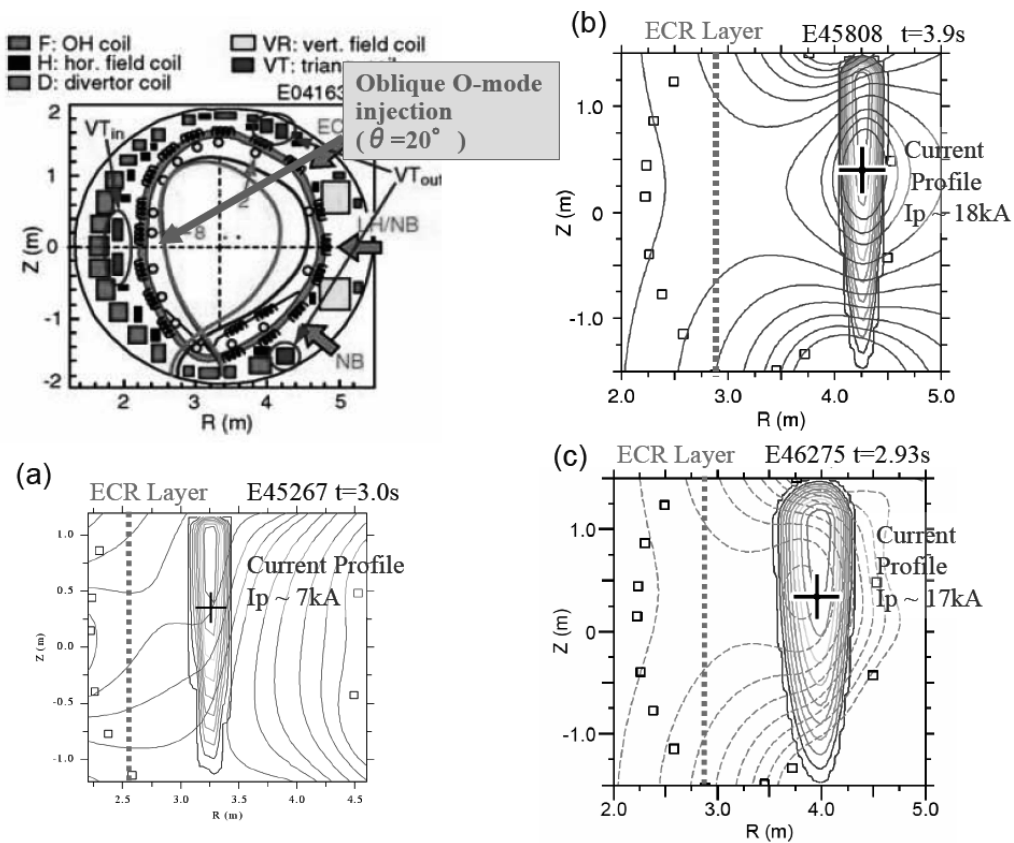


Fig.1 Cross section of JT-60U vacuum vessel and poloidal coils, and plasma current profiles obtained for the Bv decay indices in figure 2 ((a),(b) and (c) in this figure corresponds to (a), (b) and (c) in figure 2, respectively.

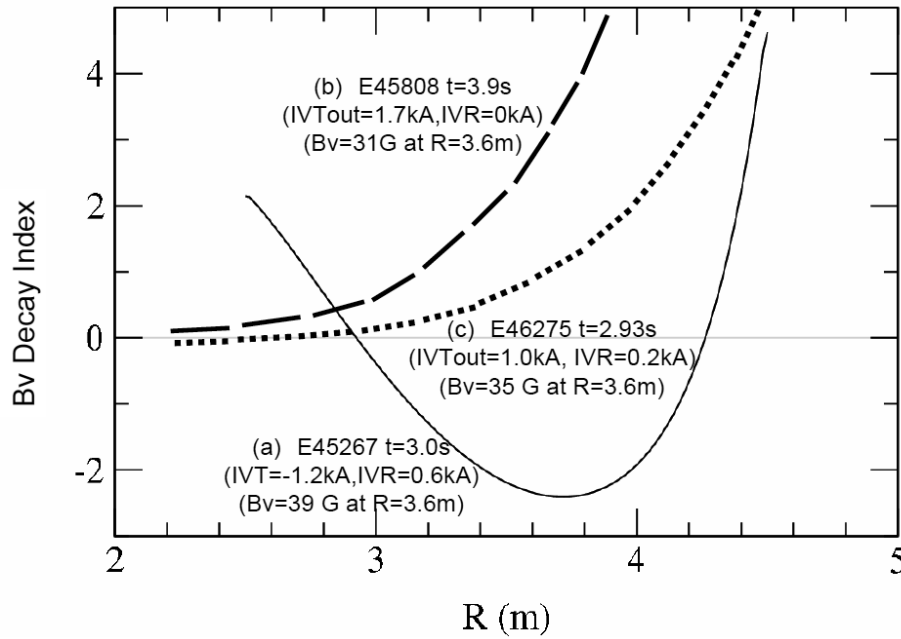


Fig.2 Radial profiles of decay index of vertical field for shots (a)E45267 (solid line), (b)E45808 (dashed line) and (c)E46275 (dotted line).

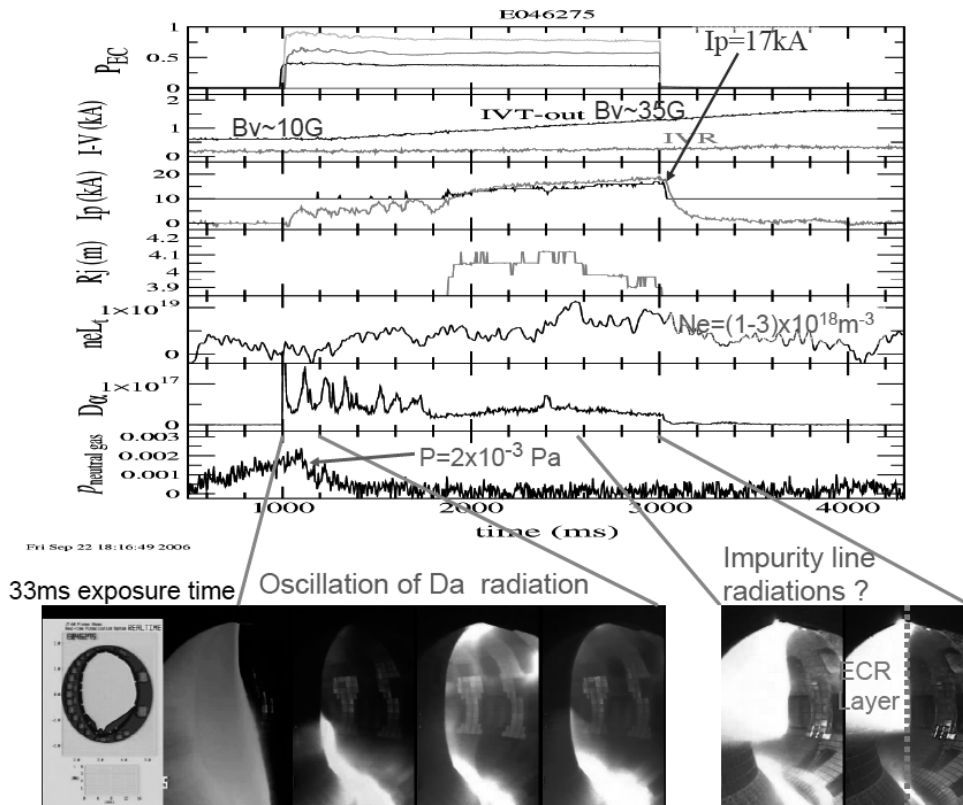


Fig.3 Wave forms of E46275 and plasma images from tangential camera.

7.10 Interlock of Neutral Beam Injection for Small Dome-separatrix Gap

H. Takenaga, M. Sueoka, Y. Kawamata, K. Kurihara

1. Introduction

Extension of neutral beam (NB) heating duration to 30 s performed in 2003 leads large energy input [1]. In 2005-2006 experimental campaign, the long pulse operation was performed with a small distance between the pumping duct and strike point to maximize the divertor pumping. In order to avoid large heat load to the dome for safety, a new interlock has been introduced. In the new interlock, the NB injection is stopped when the gap between the dome and the separatrix is smaller than a critical value.

2. Control Logic

The gap between the dome and the separatrix is calculated in real time by Cauchy Condition Surface (CCS) method [2]. Three gaps are introduced in this interlock. These are the outer gap (Gap_{out}) between the outer dome wing and the outer divertor leg, the inner gap (Gap_{in}) between the inner dome wing and the inner divertor leg and the top gap (Gap_{top}) between the dome top and the X-point. The definitions are illustrated in Fig. 1. The inner and outer gaps are taken as a minimum value among the gaps calculated at the positions on the dome wing with 1 cm interval from the dome top. The gaps are compared with critical values every 10 ms. Number of timing, at which the gap becomes smaller than the critical value, is counted separately for three gaps. When one of the counted number reaches a certain value (typically 10 counts), the NB injection is stopped. Once the NB injection is stopped, the NB is not injected for 0.1 s. Then, the NB is injected when all three gaps become larger than the critical values. When the number of the NB injection stop reaches 10, the NB is never injected through the discharge.

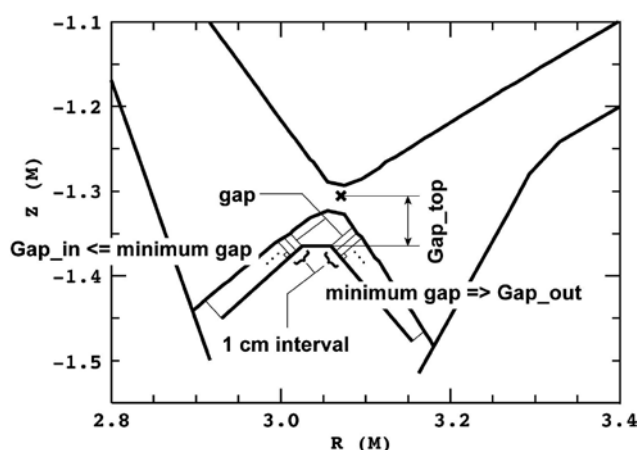


Fig. 1 Definitions of Gap_{out}, Gap_{in} and Gap_{top}.

3. Application to Experiments

The interlock was demonstrated with the critical value of 2.5 cm for Gap_{out}, 0.5 cm for Gap_{in} and 2.5 cm for Gap_{top}. Figure 2 (a) shows calculated Gap_{out}. The closed

symbols show the timing at which Gap_out is smaller than the critical value of 2.5 cm. When the counted number reached 10 at $t = 12.75$ s (see Fig. 2 (b)), the NB injection was stopped at least for 100 ms as shown in Fig. 2 (b). Then, NB was re-injected at $t = 13.15$ s, when Gap_out became larger than the critical value (see Fig. 2 (c)). At the same time, the counted numbers became zero. In this discharge, Gap_in and Gap_top were larger than the critical value through the discharge. Although waveform of the injected NB power was delayed from waveform of the NB injection command, the interlock correctly worked.

In the case with Gap_out close to the critical value, the oscillation was sometimes observed in Gap_out and the NB injection power as shown in Fig. 3. The value of Gap_out decreased with increasing the plasma beta during the NB injection and Gap_out increased with decreasing the plasma beta during OH phase. Consequently, the NB power was modulated as shown in Fig. 3. In this case, the number of the NB injection stop was limited to 10. After the NB was stopped 10 times, the NB injection was not restarted.

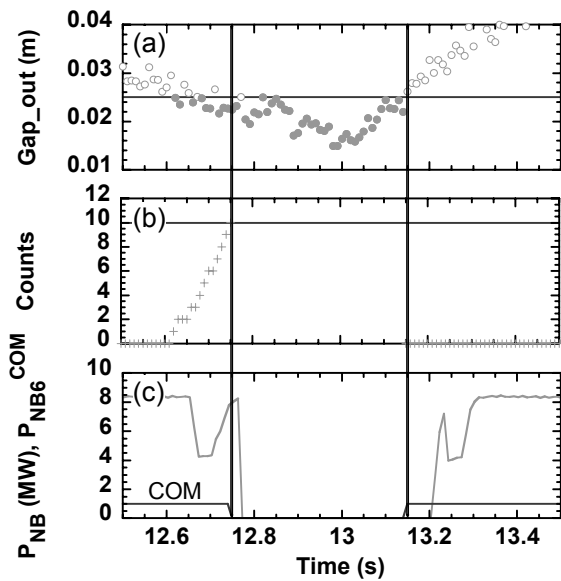


Fig. 2 Waveforms of (a) Gap_out, (b) count of timing at which Gap_out is smaller than the critical value (0.025 m) and (c) NB injection power and command of NB injection. Closed and open circles in (a) show the timing at which Gap_out is smaller and larger than the critical value, respectively. Horizontal lines show the critical values. Vertical lines show the timing of NB off and on.

4. Summary

In order to avoid large heat load to the dome, a new interlock has been introduced. In the new interlock, the NB injection is stopped when the gap between the dome and the separatrix is smaller than the critical value. It is confirmed that the new interlock works correctly.

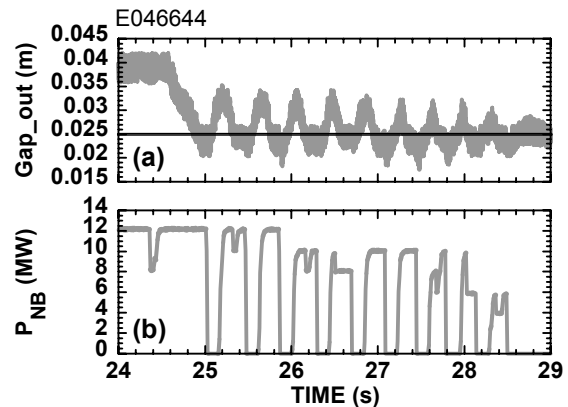


Fig. 3 Waveforms of (a) Gap_out and (b) NB injection power. Horizontal line in (a) indicates the critical value.

References

- [1] S. Ide and the JT-60 Team, Nucl. Fusion **45** (2005) S48.
- [2] K. Kurihara, Fusion Eng. Des. **51-52** (2000) 1049.

7.11 Gas Fuelling from High-field-side in ELMy H-mode Plasmas

H. Takenaga, Y. Miyo, T. Nishiyama, A. Kaminaga, T. Sasajima, K. Masaki,
J. Bucalossi¹⁾, E. Tsitrone¹⁾, J. Gunn¹⁾, C. Grisolia¹⁾

1) Association Euratom-CEA, CEA Cadarache, CEA-DSM-DRFC,

1. Introduction

In a fusion reactor, high density operation close to the Greenwald density with high confinement is essential to achieve a high fusion gain, where efficient and reliable fuelling system compatible with the high confinement operation is required. Gas-puffing is widely used due to its high reliability, but huge gas-puffing rate owing to its low efficiency is concern for confinement degradation and massive tritium retention. For improving the low efficiency, pellet injection and supersonic molecular beam injection (SMBI) have been developed. A high-field-side (HFS) injection has exhibited an advantage compared with a low-field-side (LFS) injection for both pellet injection and SMBI. The HFS pellet injection shows deeper deposition than the LFS pellet injection and compatibility with the high confinement at high density [1]. For the SMBI in Tore Supra, the tolerable number of particles is higher in the HFS injection than in the LFS injection [2]. For the LFS injection, harmful MHD activity is triggered (locked modes) above a certain amount of injected particles. In addition, the HFS gas-puffing provides the most reliable H-mode access in spherical torus such as MAST [3] and NSTX [4]. On the other hand, the effect of the HFS gas-puffing is not investigated much in conventional tokamaks.

In JT-60U, the SMBI system has been installed both on HFS and LFS in collaboration with CEA Cadarache [1]. The injector head installed inside the JT-60U vacuum vessel is the same as that installed in Tore Supra [2]. However, the vacuum seal material used inside the injector head damaged owing to the long baking (~month) at high temperature of 300°C. Therefore, the SMBI operation was not available due to the leak of working gas. Gas fuelling was only available by opening the valve located outside the vacuum vessel in a short period. In order to investigate the effect of the HFS gas fuelling on the confinement degradation, the HFS gas fuelling was carried out using the SMBI system.

2. High-Field-Side Gas Fuelling System

Figure 1 shows schematic drawing of the SMBI system, which is designed for the operation with a frequency of 8-10 Hz and 2 ms duration per pulse. The original SMBI operation is as follows. The compressor works for each pulse. A pressure wave produced by the compressor travels inside the tube towards the injection head where it accelerates an

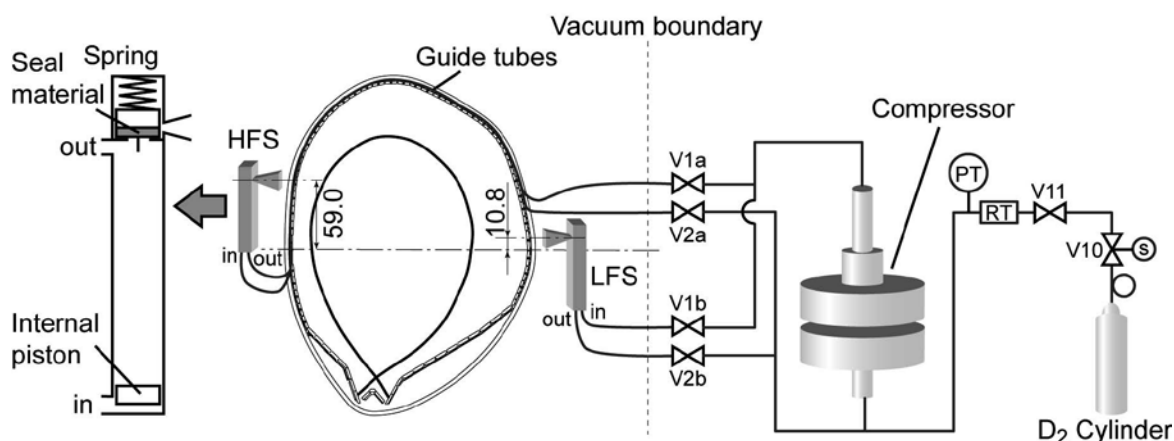


Fig.1 Schematic drawing of the supersonic molecular beam injection system

internal piston inside the injector head that strikes the valve. The valve is closed by a strong spring and the impact of the accelerated internal piston shortly open the valve (1-2 ms). Then, some fraction of the gas is lost throughout the nozzle due to the valve aperture. The injector heads were installed both on HFS at $Z = 59.0$ cm and LFS at $Z = 10.8$ cm. The inner diameter of the guide tubes is 6 mm and the length of the guide tube is about 10 m for the HFS and 5 m for the LFS, respectively.

After several tests, the problem of the vacuum seal appeared in the injector heads. The seal material (Parofluor : V8545-75) was damaged due to the long baking at high temperature of 300°C . As a result, the leak was found in both injector heads. Therefore, the operation of SMBI was not available. Gas fuelling was only possible by opening the valve mounted outside the vacuum vessel (V2a). First, working gas (D_2) was filled behind the V2a valve. The V11 valve was closed before the discharge to avoid huge gas injection. The valves of V1a, V1b, V2a and V2b are closed for the interlock when the vacuum pressure in the JT-60U vacuum vessel reaches 0.04 Pa. The number of fuelled particles was estimated from the reduction of the pressure in the reservoir tank (RT). The pressure in the RT was measured with the pressure transmitter (PT).

The linkage between the SMBI system and the JT-60U control system (ZENKEI) has

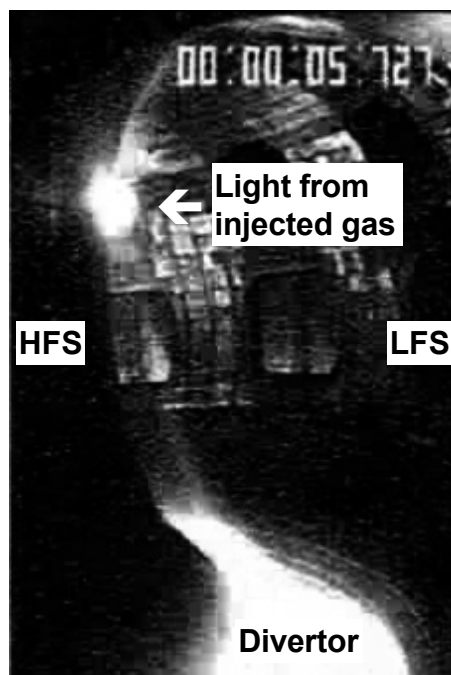


Fig. 2 Picture of TV camera viewing inside the vacuum vessel during gas fuelling from the HFS.

not been completed. Therefore, the switch for opening the V2a valve was on by hand and the open duration was controlled by Personal Computer.

3. Experimental Results

Figure 2 shows a picture of the TV camera viewing inside of the JT-60U vacuum vessel tangentially. Emission from the gas fuelled from the HFS was observed about 1 s after the opening of the V2a valve and it can be seen for several seconds. The gas was fuelled slowly due to the long guide tube. The emission seems to be localized outside the separatrix, indicating that a large fraction of the fuelled gas was ionized outside the separatrix.

Figure 3 shows waveforms of the discharge with the HFS gas fuelling at the plasma current of 1.0 MA and the toroidal magnetic field of 2.1 T. The HFS gas fuelling started around $t \sim 6$ s. The background pressure was set to be 0.18 MPa and the V2a valve opened for 200 ms. The total particle fuelling rate was estimated to be 48 Pam^3 in this discharge. The density started to increase from $t \sim 6.7$ s. The line averaged electron density normalized by the Greenwald density (\bar{n}_e/n_{GW}) increased from 0.5 at $t \sim 6.5$ s to 0.58 at $t \sim 8.0$ s. The stored energy decreased with the constant neutral beam (NB) heating power of ~ 11.5 MW similar to the LFS particle fuelling case using the gas-puffing system. The base of the $D\alpha$ emission intensity also increased from $t \sim 6.7$ s due to the HFS gas fuelling. The ELM frequency increased from ~ 100

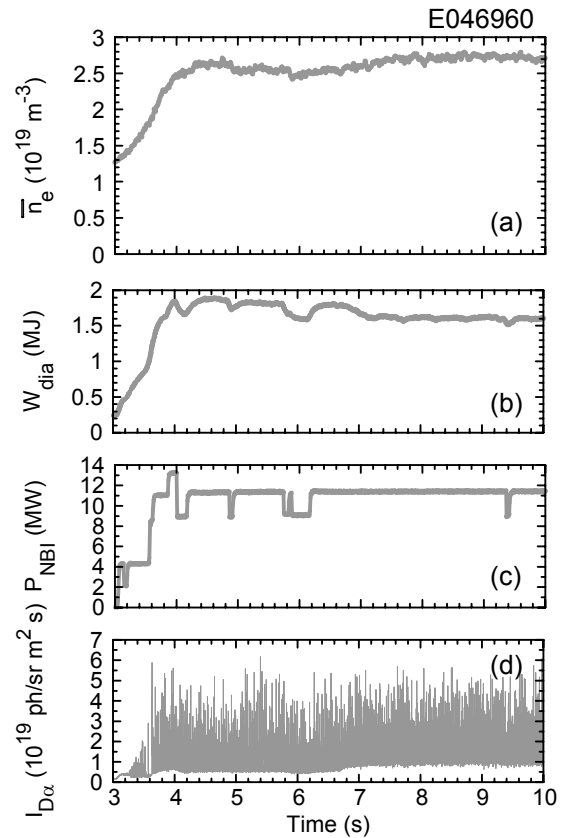


Fig. 3 Waveforms of (a) line averaged electron density, (b) stored energy, (c) NB heating power and (d) $D\alpha$ emission intensity from the outer divertor in the discharge with the HFS gas fuelling.

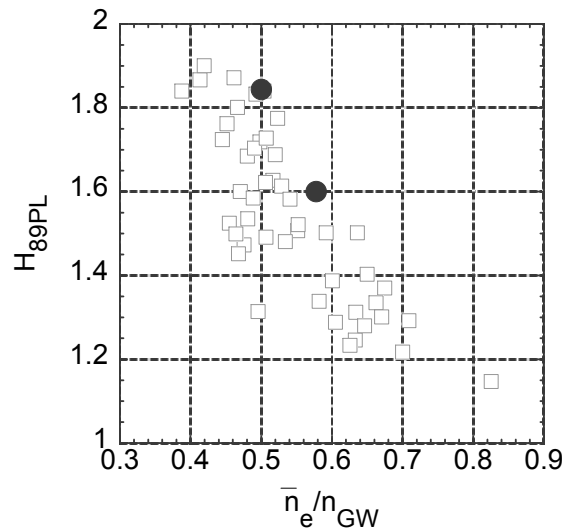


Fig. 4 H_{89PL} as a function of the line averaged electron density normalized by the Greenwald density. Closed circles and open squares show the data with the HFS gas fuelling and the normal LFS gas-puffing, respectively.

Hz at $t \sim 6.5$ s to ~ 160 Hz at $t \sim 8.0$ s.

The confinement improvement factor (H_{89PL}) over the ITER89 L-mode power law decreased from 1.84 at $\bar{n}_e/n_{GW} = 0.5$ ($t \sim 6.5$ s) to 1.6 at $\bar{n}_e/n_{GW} = 0.58$ ($t \sim 8.0$ s) with the HFS gas fuelling. The confinement degradation is similar to that with the normal LFS gas fuelling using the gas-puffing system as shown in Fig. 4. The advantage of the HFS gas fueling was not observed on the confinement degradation at high density.

4. Summary

The HFS gas fuelling was performed using the SMBI system. The confinement degradation was observed as well as the LFS gas-puffing. Since the SMBI operation provides deeper fuelling, effect of the fuelling profile should be investigated after the seal material will be improved for the long baking at high temperature.

Acknowledgement

This work was partly supported by JSPS, Grant-in-Aid for Scientific Research (B) No. 17360447.

References

- [1] H. Takenaga *et al.*, Proc. 33rd EPS Conference on Plasma Physics **30I** P-4.112 (2006).
- [2] J. Bucalossi *et al.*, Fusion Energy 2003 (Proc. 19th Int. Conf. Lyon, 2002) IAEA-CN-94/EX/P4-04 and http://www-pub.iaea.org/MTCD/publications/PDF/csp_019c/pdf/exp4_04.pdf.
- [3] R. Maingi *et al.*, Nucl. Fusion **43** (2003) 969.
- [4] A.R. Field *et al.*, Plasma Phys. Control. Fusion **44** (2002) A113.

7.12 Density Limit in Discharges with High Internal Inductance [1]

H. Yamada^{1,2)}, H. Takenaga, T. Suzuki, T. Fujita, T. Takizuka, Y. Kamada,
N. Asakura, T. Tuda, M. Takechi, G. Matsunaga, Y. Miura

1) National Institute for Fusion Science

2) The Graduate University for Advanced Studies, SOKENDAI

High densities exceeding the Greenwald limit by a factor of 1.7 have been obtained in discharges with high internal inductances of ℓ_i as high as 2.8. The internal inductance is controlled by ramping down the plasma current. In addition to the extension of the operational regime limited by disruptions, confinement performance remains as good as an H_{89PL} factor of 1.5 even above the Greenwald limit. It should be noted that the plasmas studied here is L-mode. If the improvement of confinement or stability leading to the higher temperature is realized, the density limit in tokamak may be improved as well, in particular, in L-mode where the MHD stability limit is less deterministic role to characterize the edge plasma parameter than in H-mode. While the earlier work of a high ℓ_i study [2] has indicated that core confinement improvement due to enhancement of the poloidal field, the additional improvement of the tolerance against the high density is turned out to be correlated with high edge temperature in this study. The normalized density when the detachment characterized by the decrease in a $D\alpha$ signal at the divertor occurs is even higher in the case with higher ℓ_i . These comparisons have indicated that the improvement in thermal and particle transport does exist in the periphery and the edge in the high ℓ_i plasmas, and mitigation of the density limit is observed coincidentally. Major parametric studies on the effect of heating power on the density limit suggest that the density limit does not depend on or is not sensitive to the heating power. Nonetheless, the present study suggests the improvement of the edge electron temperature in high ℓ_i discharges and motivates the effect of heating power on the edge temperature in these discharges. Two discharges with the same enhanced ℓ_i and different heating power (4 and 10 MW) have been compared. In the case with higher heating power, the edge temperature can be kept higher for the given density and consequently the discharge survives in the higher density regime. This comparison supports the hypothesis that large magnetic shear due to high ℓ_i provides confinement improvement and consequent high edge temperature mitigates the density limit. Although the high ℓ_i discharge studied here lies outside of the usual parameter space for a steady-state operation of tokamak, demonstration of a stable discharge with good confinement beyond the Greenwald limit suggest that the magnetic shear at the edge is one key parameter to uncover physical element of the operational density limit.

References

- [1] H. Yamada *et al.*, Nucl. Fusion **47** (2007) 1418.
[2] Y. Kamada *et al.*, Nucl. Fusion **33** (1993) 225.

8. Divertor and SOL plasmas

8.1 Particle Control in Long-pulse High-density H-mode Plasmas [1, 2]

T. Nakano, H. Kubo, N. Asakura, H. Takenaga, K. Shimizu and H. Kawashima

In order to investigate potential deuterium retention mechanisms, the wall-pumping rate, evaluated by the particle balance analysis, was investigated for a systematic set of data. During a 30s-H-mode discharge, the wall-pumping rate decreased with a decay constant of several seconds (transient phase), and then became constant (steady-state phase) .

The transient wall-pumping was ascribed to the recovery of the vessel deuterium inventory between discharges: the amount of the inventory decreased by releasing deuterium and the capacity to retain deuterium recovered due to a decrease of the tile temperature. The strong correlation between the temperature of the tiles around the entrance of the divertor and the number of deuterium atoms released between discharges suggests that the transient wall-pumping is due predominantly to these tiles.

During the steady-state phase, in discharges at a density lower than 80 % of the Greenwald density n_e^{GW} , the wall-pumping rate was negative, i.e., outgassing. Even with the outgassing, the constant-density plasmas with the energy confinement and the ELM activity were maintained. It was found that the outgassing rate correlated with the increase in the tile temperature around the outer strike point. This is because the decrease rate of the saturation amount in the carbon material against the material temperature has an approximately constant gradient [3, 4].

In discharges at a density of 80 % of n_e^{GW} , which were performed later in order, the wall-pumping rate was positive. To evaluate the co-deposition rate, the hydrocarbon flux was measured spectroscopically. On the assumption that the ratio of deuterium to carbon in the deposition layer is 0.05 [5], the net deposition rate of the hydrocarbon of > 60% is necessary to explain the positive wall-pumping rate. However, this net deposition rate is higher than the rate calculated by the local carbon transport simulation code [6]. Hence it is concluded that the co-deposition of deuterium with carbon does not account for the positive wall-pumping rate. The net deposition rate should be investigated further experimentally, for example, by a QMB technique.

Further, the phenomena which suggest the dynamic equilibrium between particle flux to the wall and particle retention flux were found; under a constant electron density, controlled by the feed-back control system of the gas-puffing rate, if the divertor-pumping speed increased, the outgassing-rate increased. For another example, if the gas-puffing was reduced to reduce the electron density, the outgassing-rate increased. In both the cases, the particle flux to the wall is considered to decrease, leading to the increase of the outgassing-rate. In other words, the wall-pumping rate seems to depend on the particle flux to the wall. This equilibrium have an important influence on a design of

divertor-pumping systems to control the density. Hence further investigation is needed in particular by simulation studies which consider this equilibrium.

References

- [1] Nakano, T. *et al.*, *J. Nucl. Mater.* **363-365** (2007) 1315.
- [2] Nakano, T. *et al.*, “Particle control in long-pulse H-mode discharges of JT-60U” *Nucl. Fusion*, accepted for publication (2008).
- [3] Moller, W. *J. Nucl. Mater.* **162 -164** (1989) 138.
- [4] Matsuhiro, K. *et al.*, in Fusion Energy 2000 (Proc. 18th Int. Conf. Sorrento, 2000) (Vienna: IAEA) CD-ROM file FTP1/22.
- [5] Tanabe, T. *Fusion Eng. Des.* **81** (2006) 139.
- [6] Ohya, K. *et al.*, *J. Nucl. Mater.* **363-365** (2007) 78.

8.2 Ar Injection under Wall Saturated Condition

N. Asakura, T. Nakano, H. Kubo

1. Introduction

Reduction of heat loading appropriate for the plasma facing component (PFC) such as the divertor is crucial for a fusion reactor. Impurity gas seeding is one of techniques to decrease the peak heat flux both in steady-state and transient phases. Power handling by large radiation power loss has been studied in the ELMy H-mode plasmas with argon (Ar) gas seeding [1, 2] since good confinement ($HH \geq 0.85$) was obtained up to high density ($\bar{n}_e/n^{GW} \sim 0.8-0.9$, n^{GW} is the Greenwald density) and large radiation fraction ($P_{rad}/P_{abs} \sim 0.7-0.8$). On the other hand, control of the large radiation in the good energy confinement plasma was not established under the wall saturating condition in the long discharges.

Experiment to change the Ar puffing rate was performed, just after a series of the long pulse ELMy H-mode discharges for the particle balance study under the wall saturating condition [3]. However, experiment proposals for sustainment of the high radiation plasma in the long pulse discharge were cancelled.

2. Ar seeding experiment

Response of the radiation power against the Ar gas seeding was investigated in the Type-I ELMy H-mode plasma, as shown in Fig.1, where the plasma parameters and equilibrium configuration were similar to those for the long pulse experiments: $I_p = 1.2$ MA, $B_t = 2.3$ T, $P_{NB} = 12$ MW, target $\bar{n}_e = 1.9 \times 10^{19} \text{ m}^{-3}$, $R_p = 3.40$ m, $a_{mid} = 0.90$ m and the plasma triangularity of $\delta = 0.25$. The divertor plasma configuration is efficient for divertor pumping as shown in Fig. 2. Density feedback is used to increase just before Ar injection as shown in Fig.1 (b), and during the Ar injection it is sustained to Greenwald fraction ($f^{GW} = \bar{n}_e/n^{GW}$) of 0.65.

Ar gas is injected with a large rate of $1.8 \text{ Pam}^3/\text{s}$ during $t = 6.0 - 6.5$ s to produce the

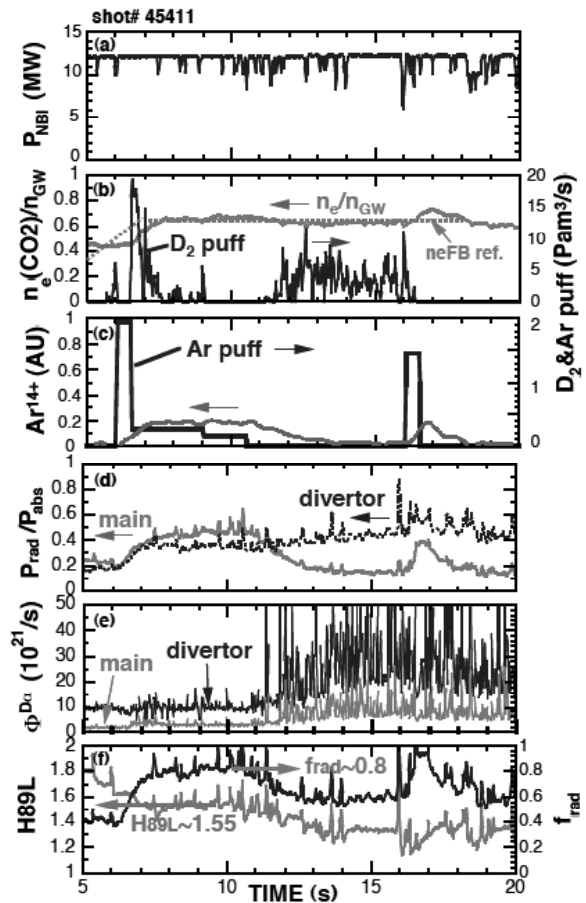


Fig.1 Time evolutions of (a) NBI power, (b) Greenwald fraction of electron density and D_2 gas puff rate, (c) Ar gas puff rate and Ar^{+14} intensity, (d) radiation power at main plasma and divertor, (e) recycling fluxes in main plasma and divertor, (f) H-factor and total radiation fraction.

radiating edge, as shown in Fig.1 (c). Then, it is reduced to a small rate of $0.18 \text{ Pam}^3/\text{s}$ (i.e. $\sim 1.0 \times 10^{19} \text{ Ar/s}$) during $t = 6.5 - 9.0 \text{ s}$, and $0.1 \text{ Pam}^3/\text{s}$ during $t = 9.0 - 10.5 \text{ s}$. Just after reducing the Ar puff rate ($t = 7 \text{ s}$), Ar^{+14} in the core region is saturated. \bar{n}_e is also increased from 2.0×10^{19} to $3.2 \times 10^{19} \text{ m}^{-3}$, where the density normalized Greenwald density, $f^{\text{GW}} = \bar{n}_e/n^{\text{GW}}$, corresponds to $0.42 - 0.68$, respectively. At the same time, enhancement of the radiation power both at the main plasma edge, $P_{\text{rad}}^{\text{main}}$, and at the divertor, $P_{\text{rad}}^{\text{div}}$, is largely increased, to 4.8 and 4.4 MW , respectively, and total radiation fraction of $P_{\text{r}}^{\text{tot}}/P_{\text{NB}}$ is increased from 0.4 to 0.8 . The large radiation plasma is sustained during 4 s ($t = 7 - 11 \text{ s}$) until stopping the constant Ar puffing ($t = 10.5 \text{ s}$). Tile temperature at the outer strike point measure by a thermocouple, T_{wall} , increases from 350 to 620°C at the end of the discharge ($t = 25\text{s}$), which is reduced by $\Delta T_{\text{wall}} \sim 40^\circ\text{C}$ due to the large radiation loss.

During the short sustaining period of the large radiation fraction, relatively high energy confinement of $H_{89\text{L}} = 1.50$ ($\text{HH} \sim 0.85$) is maintained, compared to the ELMy H plasma with deuterium puffing during $t = 12 - 16 \text{ s}$ ($H_{89\text{L}} \sim 1.35$ and $P_{\text{rad}}/P_{\text{abs}} \sim 0.55$ at $\bar{n}_e/n_{\text{GW}} \sim 0.65$). At the same time, during the Ar injection, ELM characteristics changes from Type-I to Type-III, and both steady-state and ELM heat fluxes are decreased. ELM frequency (f_{ELM}) is increased to $300\text{-}500 \text{ Hz}$, and ELM energy loss fraction ($W_{\text{ELM}}/W^{\text{ped}}$) is reduced from 0.06 to 0.02 .

After stopping the Ar puff, Ar^{+14} in the plasma core and $P_{\text{rad}}^{\text{main}}$ are decreased in 1.5 s , while large $P_{\text{rad}}^{\text{div}}$ is maintained using feedback control of D_2 gas puff to sustain $f^{\text{GW}} = 0.65$. Type-I ELM activity appears again since power to the SOL, i.e. $P_{\text{SOL}} (= P_{\text{abs}} - P_{\text{rad}}^{\text{main}})$, is increased from 6.0 to 8.4 MW , while the energy confinement is degraded and the pedestal $T_e^{\text{ped}} (= 0.8 \text{ eV})$ and $T_i^{\text{ped}} (= 1.1 \text{ keV})$ were not improved. Mechanism to change between the Type-1 and Type-III ELMs will be investigated.

3. Summary

Power handling by large radiation power loss and its sustainment were studied in the ELMy H-mode plasmas on JT-60U with argon (Ar) gas seeding. The large radiation fraction ($f_{\text{rad}} \sim 0.8$) was maintained during the Ar seeding ($\sim 4\text{s}$) in relatively good confinement ($\text{HH} \geq 0.85$) and high density ($\bar{n}_e/n^{\text{GW}} \sim 0.7$). At the same time, transient heat loading due to Type-1 ELMs was mitigated. Study of sustaining the radiation loss in the good confinement plasma using the radiation feedback is postponed as a future work.

References

- [1] Hill K., et al., FEC 2002, Lyon, IAEA-CN-94-EX-P2-03.
- [2] Kubo H., et al., Phys. Plasmas **9** (2002) 2127.
- [3] Nakano T., et al., J. Nucl. Matters. **363-365** (2007) 1315.

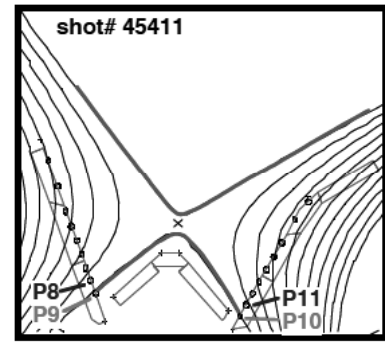


Fig.2 Divertor plasma configuration effective for the divertor pumping.

8.3 Metal Impurity from the Ferritic Steel Tiles

T. Nakano, H. Kubo, N. Asakura, K. Shinohara, Y. Koide,
G. Matsunaga and M. Takechi

1 Introduction

Compared to JET, the toroidal ripple is larger in JT-60U because the number of the toroidal field coils is smaller in JT-60U (18 coils) than in JET (32 coils) and the toroidal field coils are located closer to the vacuum vessel in JT-60U than in JET. The toroidal field ripple induces ion loss, in particular fast ions. It has been reported that the ripple-induced ion loss is presumably one of the reasons for lower pedestal pressure in JT-60U than in JET [1]. In order to reduce the toroidal ripple, in 2005, ferritic steel tiles, which contains 8% of Cr and 2% of W, were installed [2]. However, in discharges aiming to achieve high β_N over the no wall limit, the plasma configuration is set close to the first wall to utilize wall stabilization effects. The particle flux to the first wall and the ferritic steel tiles becomes high, leading to high impurity generation flux. In the case that metal such as ferritic steel is used for the first wall component, significant radiation loss from the metallic ions in the core plasma is one of the concerns. This report describes impurity contamination with the ferritic steel tiles and comparison of the plasma effective charge before and after the ferritic steel installation.

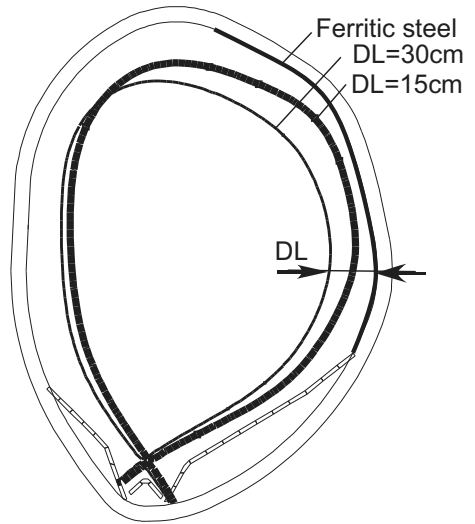


Fig. 1: Location of ferritic steel (thick curve on the surface of the vacuum vessel) and plasma separatrix of high β_N discharges with a distance between the separatrix and the surface of the vacuum vessel at the mid-plane of (DL) 15 cm (thick curve) and 30 cm (thin curve).

2 Results: Metal impurity contamination in high β_N plasmas

Two discharges with identical auxiliary controllable parameters (a plasma current: 0.9 MA, a toroidal magnetic field: 1.7 T, a neutral beam heating power: 18 MW, a plasma triangularity: 3.0, a safety factor at the 95% of flux surface: XX) except the plasma separatrix configuration are compared: in one discharge, the distance between the plasma separatrix and the first wall at the mid-plane (DL) is 15 cm, and in the other one, 30 cm, as shown in Fig. 1.

Figure 2 shows the spectra observed from these two discharges. As shown in the figure, the intensity of O VI at 15 nm is close in these discharges. However, the intensities of the metal lines, for example, W XLV at 6.09 nm, Cr XIX at 11.4 nm, Ni XXVI at 16.5 nm and Fe XXIV at 19.2 nm, are significantly higher in the discharge with

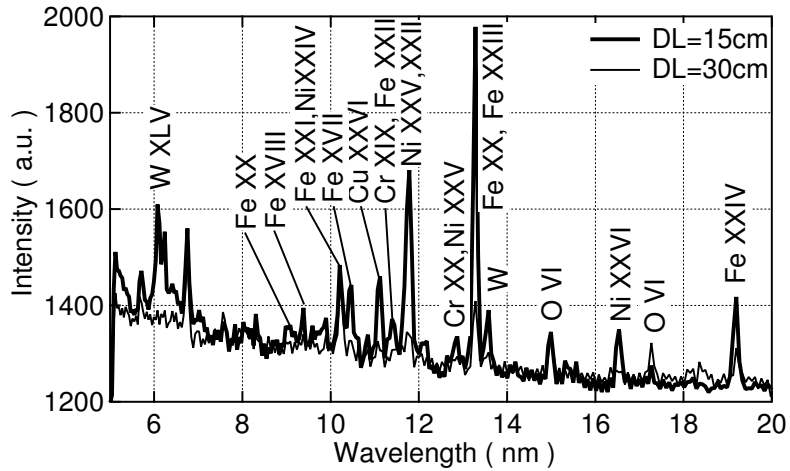


Fig. 2: (a) Spectra from the high β_N discharge with a distance between the plasma separatrix and the surface (DL) of 15 cm (thick curve) and 30 cm (thin curve).

DL=15cm than those in the other discharge with DL=30 cm. In a similar discharge with DL = 20 cm, the intensities of these metal lines are lower by $\sim 10 - 20\%$ than those with DL=15cm. From these results, the distance between the plasma separatrix and the first wall should be longer than 20 cm in order to suppress the metal impurity generation in the conditions for the high β_N discharges.

3 Results: Plasma effective charge in standard discharges

In order to estimate the metal impurity content, a plasma effective charge (Z_{eff}) before and after the ferritic steel installation is compared. Before the ferritic steel installation, the database of the plasma effective charge had been developed for OH, L-mode and H-mode plasmas with the standard plasma shape [3]. A discharge with identical auxiliary controllable parameters to the above standard plasma was performed after the ferritic steel installa-

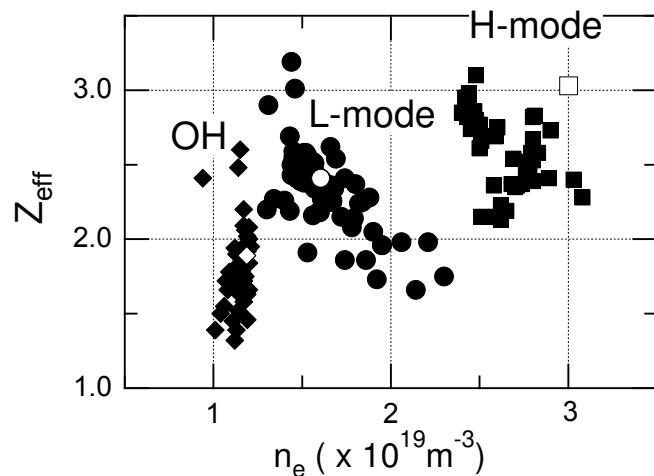


Fig. 3: Plasma effective charge of OH, L- and H-mode plasmas taken from the standard configuration discharges [3] before and after the ferritic steel installation (solid and open symbols, respectively)

tion. As shown in Fig. 3, Z_{eff} of the OH and the L-mode plasmas are in the range of the database. However, Z_{eff} of the H-mode plasma is beyond the database range. The metal impurity accumulation is often observed in particular in the case the neutral beam against the plasma current direction is injected. The mechanism of the high Z impurity accumulation has not been fully understood. This is also one of the issues for future fusion devices with metal plasma facing materials such as tungsten.

References

- [1] Saibene, G. *et al.*, *Nucl. Fusion* **47** (2007) 969.
- [2] Shinohara, K. *et al.*, *Nucl. Fusion* **47** (2007) 997.
- [3] Nakano, T. *et al.*, *J. Nucl. Mater.* **313-316** (2003) 149.

8.4 Understanding the SOL Flow in L-mode Plasma on Divertor Tokamaks, and Its Influence on the Plasma Transport [1]

N. Asakura, and ITPA SOL and divertor topical group

Recent progress in the SOL plasma flow research was reviewed in 17th PSI conference in Hefei, China. Understanding of parallel plasma flow in the scrape-off layers (SOL flow) has recently progressed with development of diagnostics such as Mach probes and impurity plume to measure the SOL flow pattern over several poloidal locations. From experiment results mainly from L-mode plasmas in many divertor tokamaks such as JT-60U, Alcator C-Mode, JET, ASDEX-Upgrade, TCV and ToreSupra, all Mach probe measurements showed common SOL flow pattern: subsonic plasma flow with parallel Mach number ($M_{//}$) of 0.2-0.4 is generated from the Low-Field-Side (LFS) SOL for the ion ∇B drift towards the divertor, and $M_{//}$ is increased to 0.5-1 at the High-Field-Side (HFS) SOL and divertor. At the same time, radial profile of the SOL flow changes with poloidal location in the SOL. TV camera measurement of impurity brightness image, i.e. “plume”, using local impurity gas puff such as CH₄, N₂, He has been developed in C-MOD and DIII-D, and confirmed subsonic plasma flow at HFS, LFS and plasma top SOLs, basically similar to the Mach probe results.

The SOL flow pattern can be explained mainly by a combination of two driving mechanisms, i.e. (1) classical drifts in the flux surfaces (B_t -dependent component) and (2) in-out asymmetry in radial diffusion/transport (basically B_t -independent component). In addition to (2), effects of (3) HFS divertor detachment and (4) intense gas puffing and divertor pumping, were found in recent experiments in JT-60U, thus the fast SOL flow is increased to the sonic level at the HFS (in JT-60U and C-MOD). The former mechanism enhances the fast SOL flow towards the HFS divertor at the plasma top (in JET and ToreSupra) and LFS SOL for the ion $\mathbf{B} \times \nabla B$ drift towards the divertor and low density case. Quantitative determinations of drifts in the SOL and influence of cross-field diffusion on parallel transport are crucial for determination of the multi-dimensional pattern of the fast SOL flow. Implication of these models has been recently progressed in plasma fluid simulations such as SOLPS-5, UEDGE, EDGE2D: most codes have incorporated drift effects, and asymmetric diffusion was modeled, which so far qualitatively explained experimental results.

The fast SOL flow plays an essential role in impurity shielding from the main plasma (Puff & pump in DIII-D and JT-60U) and carbon deposition profile on the HFS divertor tiles (for most carbon wall tokamaks). At the same time, it will influence the performance on core plasma such as edge rotation and L-H transition (in C-MOD). All processes (1)-(4) will exist in reactor, and quantitative determination of their effects under various plasma conditions such as ELMy H-mode and detached divertor are crucial for diveror design and operation.

Reference

[1] Asakura, N. and ITPA SOL and divertor topical group, J. Nucl. Mater. **363-365** (2007) 41.

8.5 ELM Propagation Characteristics in Scrape-Off Layer [1]

N. Asakura, N. Ohno ¹⁾, H. Kawashima, G. Matsunaga, N. Oyama,

T. Nakano, H. Miyoshi ¹⁾, S. Takamura ¹⁾, Y. Uesugi ²⁾

1) Nagoya Univ., 2) Kanazawa Univ

Radial transport of the ELM plasma in the scrape-off layer (SOL) has been recently studied in order to understand heat and particle loading to the first wall as well as the divertor. In ELMy H-mode discharges ($I_p = 1\text{MA}$, $B_t = 1.8\text{T}$, $P_{NB} = 4.5\text{-}5\text{ MW}$), time scale and radial distribution of the ELM plasma propagation were determined both at high-field-side (HFS) and low-field-side (LFS) SOL using three reciprocating Mach probes with 500 kHz sampling.

After start of large MHD turbulence due to ELM, large and short multi-peaks were found in time evolution of plasma flux (j_s) mostly at LFS midplane, which was enhanced by the factor of 10-50 with relatively large floating potential (up to $\pm 400\text{ V}$). Time lag from start of magnetic turbulence was increased with the radial distance from the separatrix, and the result can be interpreted as radial propagation of the large j_s peak towards the first wall: the velocity was increased from 0.4-1.5 km/s near separatrix to 1.5-3 km/s at the far SOL. ELM propagation to plasma facing components ($\tau_{\perp}^{mid}(peak) = 40\text{-}80\ \mu\text{s}$) was faster than the parallel convection time to the divertor ($\tau_{\parallel}^{SOL-LFS} \sim 100\ \mu\text{s}$) and the measured time lags ($\tau_{\parallel}^{div}(start) \sim 100\ \mu\text{s}$ and $\tau_{\parallel}^{div}(peak) \sim 150\ \mu\text{s}$). Radial distribution was characterized by a wide e-folding length of 7.5 cm. These large peak fluxes, accompanied by high temperature plasma of a few 100 eV, will cause local heat and particle loadings to the PFCs.

Radial scale of the ELM plasma (filaments) was investigated from duration of the large j_s^{mid} signals (δt_{pk}^{mid}), and most δt_{pk}^{mid} was short (4-10 μs) over the LFS midplane. Corresponding radial scale was 0.3-1.8 cm near separatrix ($\Delta r^{mid} < 5\text{ cm}$) and it was increased to be 1 - 4 cm at the far SOL. Local deposition image of particle flux to LFS baffle as well as dynamics of the filament-like structure were measured with the fast TV camera viewing LFS divertor with 3-6kHz sampling, and the radial scale of 3-5 cm was comparable with the filament scale evaluated from the probe measurement.

ELM plasma transport was determined at the HFS SOL and divertor. Large plasma flux was measured with short delay of $\leq 20\ \mu\text{s}$ only near separatrix ($\Delta r^{mid} < 0.4\text{cm}$) maybe due to conduction and fast electrons. Such fast heat loading to the HFS divertor generated large neutral desorption and increased the plasma pressure, then producing the flow reversal over a wide SOL region. At the same time, large and short convective plasma from the LFS SOL was transported to the HFS divertor. Such transient convective fluxes affect particle transport at the HFS divertor, and it may play an important role in deposition profiles of impurity.

Reference

[1] Asakura, N., et. al., submitted to Nuclear Fusion 2007.

8.6 ELM Propagation at High-Field-Side SOL and Divertor

N. Asakura, H. Kawashima, G. Matsunaga, N. Oyama, T. Nakano, N. Ohno ¹⁾
 1) Nagoya Univ.

1. Introduction

Experimental data on edge and SOL plasma dynamics during ELMs has recently progressed by use of time-resolving diagnostics. Evolution of ELM filaments is of great interest understanding heat and particle transport from the plasma edge to Plasma Facing Components (PFC) such as the divertor and the first wall. Time evolution of the ELM plasma has been measured with reciprocating Mach probes at different poloidal locations (i.e., outer midplane, divertor null-point, and above the inner baffle) [1, 2], and the sampling system was recently improved in order to measure the fast response of the plasma (500 kHz) and those were synchronized with the principal fast diagnostics such as D_α emission and magnetic coils. Especially noteworthy are measurements of filament structures and their transport at the inner (high magnetic-field-side, HFS) SOL.

2. Plasma flow profile in SOL

Figure 1 shows radial profiles of ion and electron temperatures, electron density and toroidal rotation velocity at the plasma edge, which are measured between ELMs. The electron temperature, density and toroidal component of the parallel plasma flow in the SOL are measured by the Mach probes. Here, data during transient period (~ 5 ms) in each ELM are excluded, and the radial coordinate is mapping to the LFS midplane. Electron and ion temperatures, electron density and toroidal rotation velocity at the pedestal top (T_e^{ped} , T_i^{ped} , n_e^{ped} and v_t^{ped}) are 0.8 - 0.9 keV, 1.0 - 1.2 keV, $1.4 - 1.6 \times 10^{19} \text{ m}^{-3}$ and $\sim 28 \text{ km/s}$, respectively. The loss fraction of the pedestal stored energy, $(\Delta W_{ELM}/W^{ped})$, due to Type-I ELMs is evaluated to be 0.09 - 0.12, where $W^{ped} \equiv 3/2 n_e^{ped} (T_e^{ped} + T_i^{ped}) / V_p^{ped}$, and the plasma volume inside the pedestal (V_p^{ped}) is 70 m^3 .

In the SOL, an in-out asymmetry of T_e is observed, while HFS and LFS n_e are comparable. These result in a lower plasma pressure at the HFS SOL than that at the LFS SOL. During the steady-state period, the plasma flow in the SOL is generally observed from the LFS SOL to

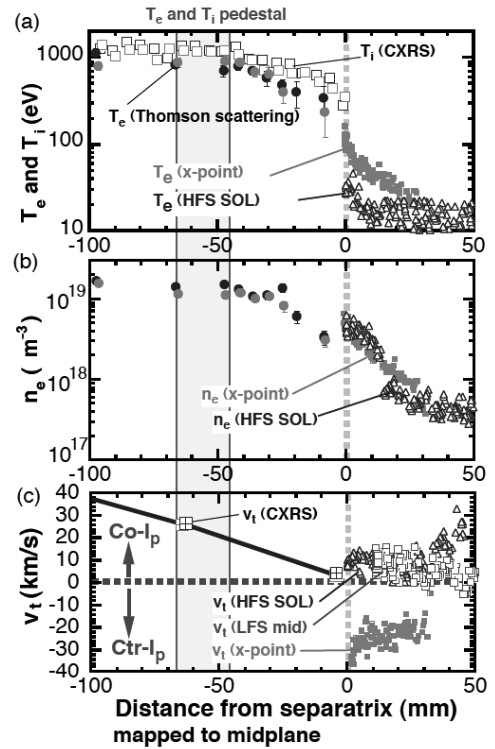


Fig.1 Radial profiles: (a) ion and electron temperatures, (b) electron density, (c) toroidal rotation velocity at the plasma edge. Radial location is mapping to the LFS midplane radius. Vertical band show edge pedestal of the ion and electron temperature profiles.

the HFS divertor through the SOL opposite the X-point region [3]. The toroidal component of the SOL flow is evaluated as $v_t^{SOL} = M_{//} C_s^{SOL} (B_t/B_{//})$, where the Mach number ($M_{//}$) is calculated from the ratio of ion saturation currents at the ion- and electron-sides of the Mach probe [4]: $M_{//} = 0.4 \ln[j_s^i/j_s^e]$, and C_s^{SOL} is the plasma sound velocity. Here, $M_{//}$ near the separatrix is relatively low (0.2 - 0.3) in the LFS midplane and above the HFS baffle, and $v_t^{SOL} \sim 10$ km/s is larger than that measured just inside the separatrix ($v_t^{edge} \sim 3$ km/s), but lower than v_t^{ped} . A subsonic level of $M_{//} \sim 0.45$ near the divertor X-point is observed, which corresponds to $v_t^{SOL} = -20$ to -30 km/s.

3. ELM filament propagation at HFS SOL

Plasma transport in the HFS SOL plays an important role on particle control and impurity transport. In particular, the transient plasma transport produced by the ELM, i.e. filament structure and the dynamics in the HFS SOL, is presented.

Figure 2 shows the time evolution of D_α brightness at the HFS and LFS divertors, \tilde{B}_p, j_s at the upstream and downstream sides of the HFS Mach probe (j_s^{HFS-up} and $j_s^{HFS-down}$) and j_s at the HFS strike point ($j_s^{div-HFS}$) during an ELM event. The local distance from the separatrix to the Mach probe is 1.1 cm, which corresponds to just outside of the separatrix mapping to the LFS midplane ($\Delta r^{mid} = 0.3$ cm). Multi-peaks appear only in j_s^{HFS-up} with the delay of $53 \mu\text{s}$ after t_0^{MHD} . The large peak observed on the LFS is not seen in $j_s^{HFS-down}$, although $j_s^{HFS-down}$ does increase after $\Delta t = 53 \mu\text{s}$. During the j_s^{HFS} increase, j_s at the HFS strike-point ($j_s^{div-HFS}$) also increases but again a large peak is not observed.

Figure 3 shows an expanded time evolution of the D_α brightness at the main plasma and the HFS divertor, j_s^{HFS-up} and $j_s^{HFS-down}$. During the early period of the j_s^{HFS} increase ($\Delta t = 50 - 250 \mu\text{s}$), seven large peaks appear in j_s^{HFS-up} at $\Delta t = 66, 110, 130, 148, 180, 202$ and $242 \mu\text{s}$. The peak duration (δt_{pk}^{mid}) is between 10 and 22 μs , which is comparable to those measured at the LFS midplane. The separation of the maxima (τ_{p-p}^{mid}) is between 25 and 55 μs , which is larger than that at the LFS midplane. The peak values of j_s^{HFS-up} ($j_s^{HFS-up}(peak)$) are between 5.6×10^5 and $9.8 \times 10^5 \text{ Am}^{-2}$, and they are significantly larger than $j_s^{HFS-down}$ ($\sim 1.2 \times 10^5 \text{ Am}^{-2}$). Large enhancement in j_s^{HFS-up} shows that the fast parallel flow towards the HFS divertor is associated with the filaments, and the corresponding $M_{//}^{HFS}$ reaches close to the sonic level

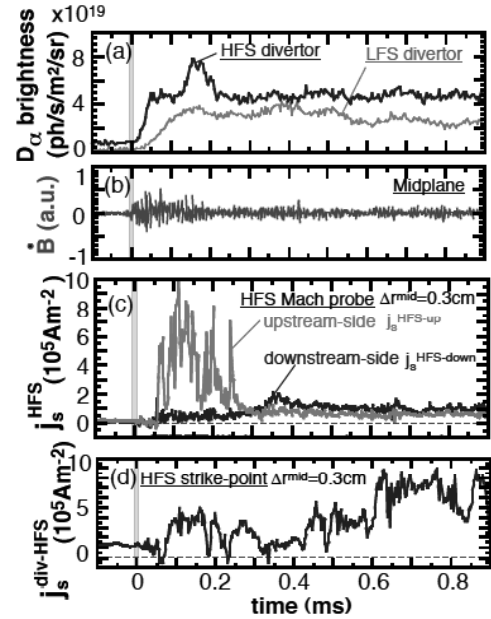


Fig.2 Time evolutions: (a) D_α brightness in LFS/HFS divertors, (b) magnetic fluctuations, (c) ion saturation currents at the up-stream and down-stream sides of the HFS Mach probe ($\Delta r^{mid} = 0.3$ cm) as a function of delay from a large B_p turbulence start.

(0.7 to 1). Delays of the first to fourth j_s^{HFS-up} peaks ($\Delta t = 68 - 145 \mu s$) measured are smaller than the characteristic time of the convective transport from the LFS midplane to the HFS Mach probe, i.e., $\tau_{//}^{LFS-HFS} = L_s^{LFS-HFS}/C_s^{ped} = 186 \mu s$ ($L_s^{LFS-HFS} = 55$ m). On the other hand, delay of the first peak is slightly larger than the convection time from the HFS midplane to the HFS Mach probe: $\tau_{//}^{HFS-HFS} = L_s^{HFS-HFS}/C_s^{ped} = 46 \mu s$ ($L_s^{HFS-HFS} = 12$ m). Thus, provided that ELM filaments extend to the HFS edge and they are ejected into SOL, those delays can be explained as convection from the HFS midplane to the probe.

Figure 4 (a) shows the radial distributions of the large j_s^{HFS-up} peaks ($j_s^{HFS}(peak)$), the maximum base-level after appearance of the large peaks ($j_s^{HFS}(base)$) and j_s^{HFS-up} between ELMs ($j_s^{HFS}(ss)$). Enhancement factors of $j_s^{HFS}(peak)$ are 20 - 50, which are comparable to those at the LFS midplane (10-50). Large enhancement (30-50) of $j_s^{HFS}(peak)$ is often observed near the separatrix ($\Delta r^{mid} < 0.6$ cm). On the other hand, in the outer flux surfaces, large $j_s^{HFS}(peak)$ values are not observed and e-folding length of $j_s^{HFS}(peak)$ mapping to the LFS midplane is $\lambda_{peak}^{HFS} = 3.2$ cm, which is about a half that at the LFS midplane ($\lambda_{peak}^{mid} = 7.5$ cm).

The Mach numbers for $j_s^{HFS}(peak)$, $j_s^{HFS}(base)$ and $j_s^{HFS}(ss)$ are shown in figure 4 (b): $M_{//}^{HFS}(peak)$, $M_{//}^{HFS}(base)$ and $M_{//}^{HFS}(ss)$. $M_{//}^{HFS}(peak)$ increases from 0.2 - 0.3 away from the separatrix to near unity as close to the separatrix: a sonic level of the fast SOL flow is observed near the separatrix ($\Delta r^{mid} < 0.8$ cm). The delay of $j_s^{HFS}(peak)$, $\tau^{HFS}(peak)$, is plotted in figure 4 (c). Characteristic times of the convective transport from the LFS midplane, $\tau_{//}^{conv}(probe-LFS)$, and from the HFS midplane, $\tau_{//}^{conv}(probe-HFS)$, are also shown, assuming a

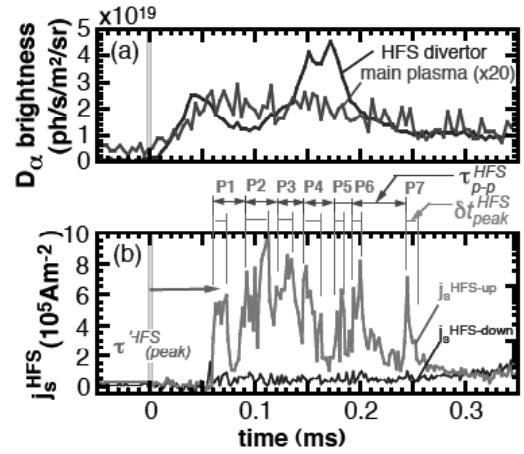


Fig.3 Enlarged time evolutions: (a) D_α brightness in the main plasma and the HFS divertor, (b) j_s^{HFS} at upstream and downstream sides of the HFS Mach probe. Delay of the first j_s^{HFS} peak, separation and duration of these peaks are shown by $\tau^{HFS}(peak)$, τ_{p-p}^{HFS} and δt_{pk}^{HFS} .

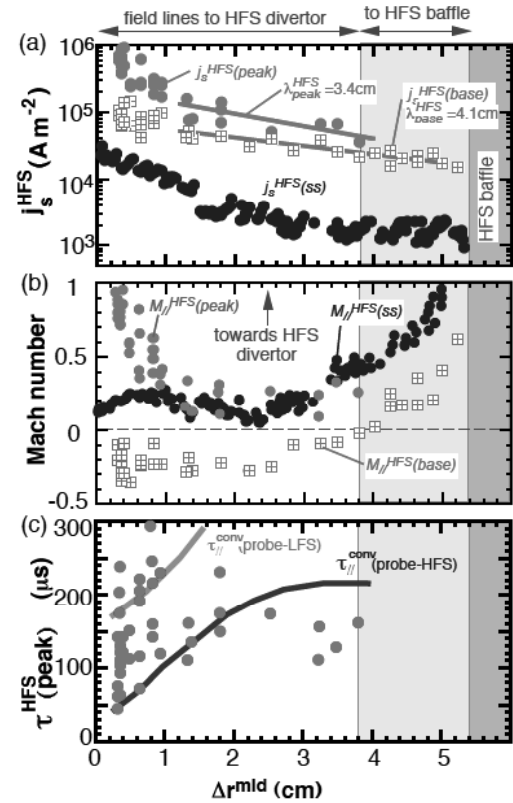


Fig.4 Radial distributions: (a) j_s^{HFS} peaks (thick circles), maximum base-level (squares) during ELMs, and j_s^{HFS} between ELMs (thin circles) measured at upstream-side of HFS Mach probe, (b) Mach numbers for $j_s^{HFS}(peak)$, $j_s^{HFS}(base)$, $j_s^{HFS}(ss)$, (c) delay of j_s^{HFS} peaks.

constant C_s^{ped} of 2.9×10^5 m/s along the field lines length varying with the radial position of the HFS probe. $\tau^{HFS}(peak)$ is comparable or larger than $\tau_{//}^{conv}(probe-HFS)$, except in the far SOL ($\Delta r^{mid} > 2$ cm). The ELM filaments are ejected into the HFS SOL, but the radial extent of the filament is mostly limited to flux surfaces in the narrow region ($\Delta r^{mid} < 1$ cm.)

After the appearance of the multi-peaks, the flow reversal of the SOL plasma occurs over a wide SOL region ($\Delta r^{mid} < 4$ cm). As a result, the plasma and impurity transport at the HFS SOL and divertor is influenced by two transient convective fluxes during the ELM event: one is the large, short convective flow caused by the filaments, and another is the flow reversal over a wide SOL region, both of which will play an important role in impurity transport.

4. Discussion and Summary

Filament size and mode number are investigated from the database of the j_s^{HFS-up} peak duration (δt_{pk}^{HFS}) and separation of the multi-peaks (τ_{p-p}^{HFS}). τ_{p-p}^{HFS} can be determined near the separatrix and scattered between 18 and 64 μ s. Average values are $\delta t_{pk}^{HFS} = 24$ μ s and $\tau_{p-p}^{HFS} = 38$ μ s. The poloidal scale of the plasma filament at the HFS SOL is evaluated from δt_{pk}^{HFS} by $\delta z_{pk}^{HFS} = \delta t_p^{HFS} \cdot v_i^{ped} \cdot \tan(\beta)$, provided that the plasma filament is formed along the local field line pitch angle of $\beta = 6^\circ$ at the Mach probe, and that the toroidal rotation at the HFS SOL corresponds to $v_i^{ped}(HFS) = v_i^{ped}(R^{HFS}/R^{LFS})$, where $v_i^{ped} \sim 28$ km/s, the major radii at the HFS and LFS Mach probes are $R^{HFS} = 2.7$ m and $R^{LFS} = 4.3$ m. Then, δz_{pk}^{HFS} is 2 – 6 cm for $\delta t_{pk}^{HFS} = 10 - 30$ μ s. The toroidal mode number is estimated to be $n = 18 - 44$ from separation time of $\tau_{p-p}^{HFS} = 20 - 50$ μ s. Averaged filament size and mode numbers are comparable to those at the LFS SOL, suggesting the filament extends to the HFS SOL at least when it is ejected into the SOL. However, $n > 20$ is too high to understand by conventional MHD (peeling-ballooning) model, and thus further study is necessary.

In summary, large multi-peaks of the ion saturation current appear during the early period of the ELM events (< 100 μ s after start of the large magnetic activity) at both the HFS SOL and the LFS midplane, which shows that plasma filaments propagate to the first wall and the divertor plates. Several filaments appear near separatrix ($\Delta r^{mid} < 0.4$ cm) of the HFS SOL. At the same time, convective transport with $M_{//} = 0.5-1$ was observed with short propagation time to the HFS Mach probe above the baffle ($\tau^{HFS} = 53$ μ s), which is faster than parallel convection transport time from the LFS midplane (~ 186 μ s). Filaments thus may extend to the HFS plasma edge and they are ejected into the HFS SOL, producing fast propagation of the filaments to the HFS SOL and divertor. This convection flux causes large neutral desorption at the HFS divertor and "flow reversal" over a wide radial range of the HFS SOL.

References

- [1] Asakura N., et al., *Plasma Phys. Control. Fusion* **44** A313 (2002).
- [2] Asakura N., et al. *J. Nucl. Matter.* **337-339** 712 (2005).
- [3] Asakura N. and ITPA SOL and divertor Topical Group *J. Nucl. Matter.* **363-365** 41 (2007).
- [4] Hutchinson I.H., *Phys. Rev. A* **37** 4358 (1988).

8.7 Transient Response of Divertor Plasma during Transition to ELM Free H-Mode Phase [1]

H. Takenaga, N. Oyama, N. Asakura

LH transition has been associated with a sharp drop of $H\alpha$ or $D\alpha$ emission intensity together with increases in edge density and temperature. The $H\alpha/D\alpha$ emission intensity is considered in relation to the particle transport at the main plasma edge. However, $H\alpha/D\alpha$ emission intensity expresses the particle flux to the divertor plates rather than the particle flux from the main plasma. The particle flux from the main plasma is much smaller than that to the divertor plates in large tokamak devices such as JT-60U, because a large fraction of the recycled neutral particles ionizes in the divertor region. Therefore, it is necessary to investigate the response of the divertor plasma against the change of the particle and heat fluxes from the main plasma in order to understand the key mechanisms determining the behavior of the $H\alpha/D\alpha$ emission intensity observed in various conditions of the H-mode phase. The mm-wave interferometer has been developed for measuring the line-integrated electron density at the upper stream of the divertor plasma. The mm-wave interferometer can measure the fast response of divertor plasma density, although this device has difficulty in covering the entire divertor region. For interpreting the measured results as physical mechanisms governing the phenomena in the wide divertor region, comparison with numerical simulation results is effective. The 2-D fluid divertor code UEDGE has been developed for understanding the heat and particle transport characteristics of the divertor and SOL plasmas.

A drop in divertor plasma density was observed during the transition to the ELM free H-mode phase as well as the drop in $D\alpha$ emission intensity. The time scale for the drop in divertor plasma density ranged from a few ms to several tens of ms. 2-D fluid divertor code simulations using the UEDGE code indicated that the time scale for the divertor plasma density drop was ranged from several tens of ms to a hundred ms, when thermal and particle diffusivities were instantly reduced in the main plasma edge with a constant recycling coefficient. When it was assumed that the recycling coefficient decreased with a decrease in heat flux and increased with a decrease in particle flux, the time scale was reduced to a few ms in the simulations accompanied by a reduction of edge thermal diffusivity. These results indicate that the sharp drop of the divertor plasma density concomitant with the sharp drop of the $D\alpha$ emission intensity on a time scale of a few ms can be ascribed to the change of plasma-wall interaction depending on the heat flux to the divertor plates.

Reference

[1] Takenaga, H. *et al.*, Plasma and Fusion Research, **1** (2006) 046.

8.8 Fluctuation Characteristics of the L-mode SOL Plasmas

N. Ohno¹⁾, H. Tanaka¹⁾, N. Asakura, S. Takamura²⁾ and Y. Uesugi³⁾

1) Nagoya University, 2) Aichi Institute of Technology, 3) Kanazawa University

1. Introduction

Intermittent convective plasma transport, so-called “plasma blobs” has been observed in low-field-side (LFS) scrape off layers (SOLs) of several tokamak devices, which is thought to play a key role for cross-field transport. It has strong influence on recycling processes and impurity generation from a first wall. Theory predicts that plasma blobs move toward first wall at LFS due to $E \times B$ drift, where the charge separation in a plasma blob is driven by gradient and curvature of magnetic field. Then, it is expected that the property of blobby plasma transport is quite different in high-field-side (HFS) SOLs in comparison with that in LFS SOL. However, there has been little observation on electrostatic fluctuation in HFS SOL so far. It becomes one of the most important issues to reveal an influence of plasma blobs on cross-field transport in the HFS SOL. Furthermore, the analysis of the fluctuation property is required to understand the generation mechanism of plasma blobs and to predict the cross-field transport, including non-locality of transport in the edge plasma turbulence.

In this section, detailed comparison between fluctuation characteristics at HFS and LFS SOLs will be made in the L mode plasma using reciprocating Langmuir probes[1]. Statistical analysis based on probability distribution function (PDF) is employed to describe intermittent (non-diffusion) transport in SOL plasma fluctuations[2].

2. Statistical analysis based on probability distribution function (PDF)

In the JT-60U, three reciprocating Mach probes are installed at LFS mid-plane, HFS and just below the X-point as shown in Fig. 1. The fluctuation property was investigated from fast sampling (500kHz) signals of the ion saturation current (j_s) measured at HFS and LFS SOLs. Figure 2 shows radial profiles $\langle j_s \rangle$ and fluctuation level $(\delta j_s / \langle j_s \rangle)$. $\delta j_s / \langle j_s \rangle$ is gradually increased at LFS SOL, while at HFS SOL, $\delta j_s / \langle j_s \rangle$ is small (<10%) and decreased with Δr .

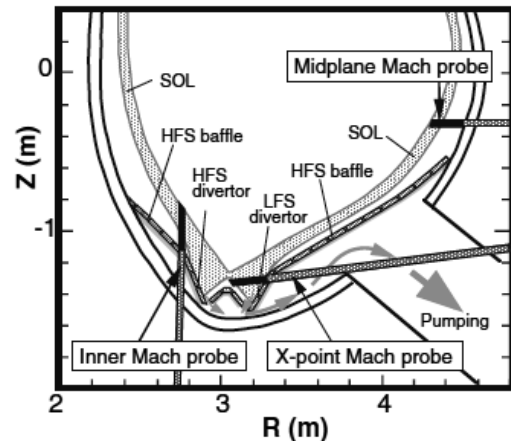


Fig. 1 Plasma cross-section and location of reciprocating probes in the JT-60U.

The detailed feature of the fluctuation can be investigated by a probabilistic analysis. We have analyzed fluctuation property of j_s based on probability distribution function (PDF). The PDF is an important statistical quantity for turbulence research. In order to obtain PDF, we construct a histogram of the time evolution of j_s . Figure 3 shows the PDFs of j_s in same radii ($3\text{cm} < \Delta r < 6\text{cm}$) at HFS and LFS SOLs. For fully random signal, a PDF has a Gaussian profile shown by dashed lines in Fig. 3. The PDF at LFS SOL is non-Gaussian profile and skewed positively, suggesting non-diffusive plasma transport (blobby transport) frequently occurs at LFS midplane. On the other hand, the PDF at HFS SOL is close to Gaussian distribution with less coherent events. Deviation of PDF from a Gaussian profile can be quantitatively characterized by skewness $S = \langle x^3 \rangle / \langle x^2 \rangle^{3/2}$. Fig. 2(c) shows skewness of the PDF at LFS SOL becomes maximum around $\Delta r = 5\text{ cm}$ and is positive value in wide radii ($\Delta r < 10\text{ cm}$). On the other hand, the skewness at HFS SOL is smaller than that at LFS SOL.

In order to reveal the typical burst's profile at LFS SOL, conditional averaging method was employed. Fig. 4(a) shows the typical time evolution of j_s at LFS SOL. In this method, large bursts of j_s with a peak above three times as large as the standard deviation of the original signal (dashed line in (a)) are selected and averaged in the same time domain. The result indicates that the positive spikes have the common property of

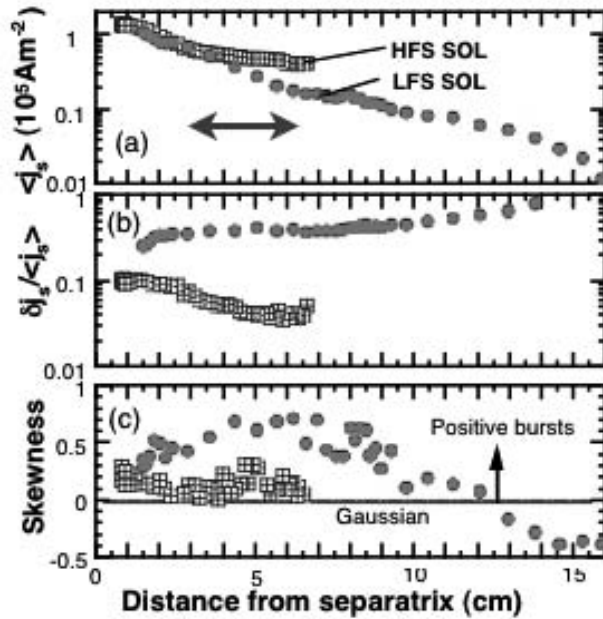


Fig.2 (a) j_s profiles measured with LFS midplane (circles) and HFS (squares) Mach probes in L-mode. (b) fluctuation level of j_s , (c) skewness.

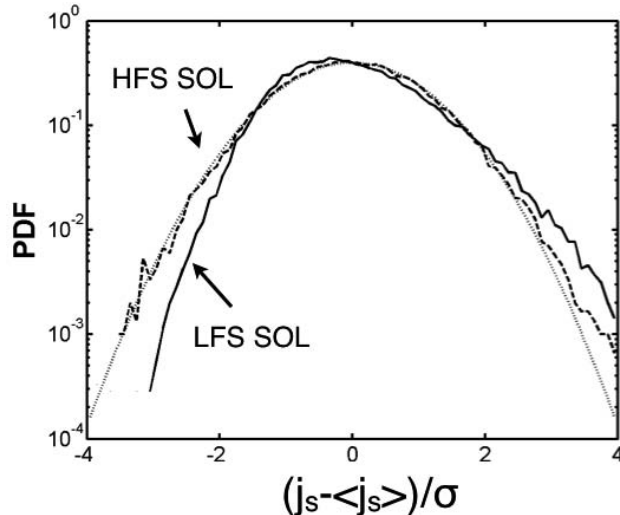


Fig.3 Log-linear plots of probability distribution function (PDF) of j_s measured at LFS and HFS SOLs.

a rapid increase and slow decay shown in Fig. 4(b). This feature is similar to that of theoretical prediction for plasma blobs. The conditional average of V_f measured simultaneously using a probe tip 5 mm inside of the probe tip for j_s shows that V_f changes from positive to negative with respect to $\langle V_f \rangle$ as a large burst of j_s passes by. This result gives the internal potential structure of plasma blobs. The plasma blob velocity also can be estimated by using delayed time between the peaks of j_s and V_f to be about 425 m/s.

3. Scaling Feature of Fluctuation

The scaling features of the fluctuation can be studied by mean of Fourier analysis. Figure 5 shows spectral density $S(f)$ of j_s at HFS and LFS SOLs. There are no peaks in $S(f)$. The shapes of the spectral density allow one to conclude whether the scaling behavior of a time series can be described by power-law dependences of the type $S(f) = f^{-\alpha}$. The power spectrum of the turbulent fluctuations quantifies the properties of the process. A self-organized criticality (SOC) model was proposed to analyze non-local plasma transport in tokamaks[1], which predicts a power law dependence, $S(f) = f^{-1}$. In LFS SOL, scaling sub-range with respect to the frequency is clearly observed in Fig. 5. Typical value of the scaling exponent α of the power spectra in the scaling sub-range is 1.3, which is different from the SOC prediction.

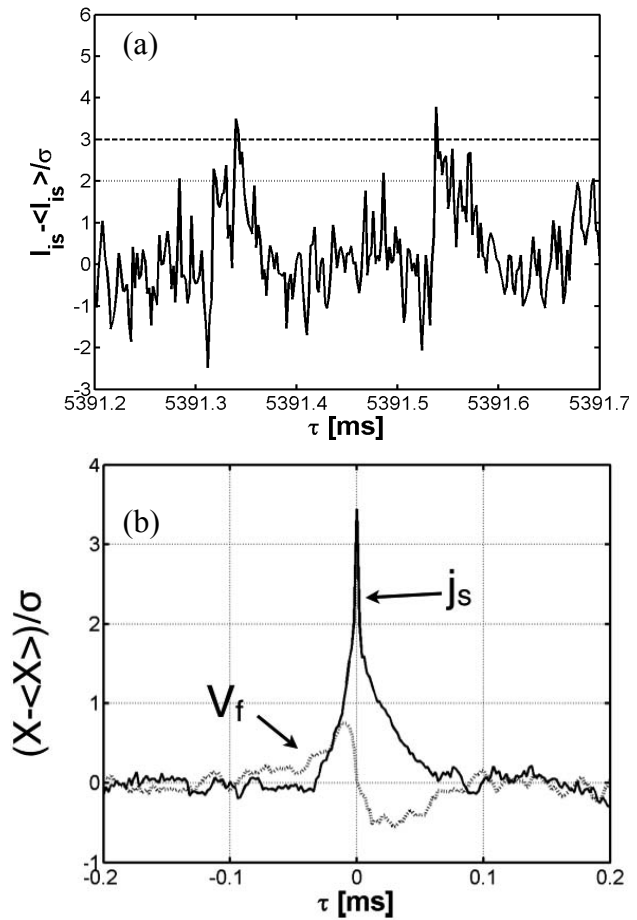


Fig.4 (a) Time evolution of j_s , (b) conditional averaging results of j_s and floating potential V_f at LFS SOL.

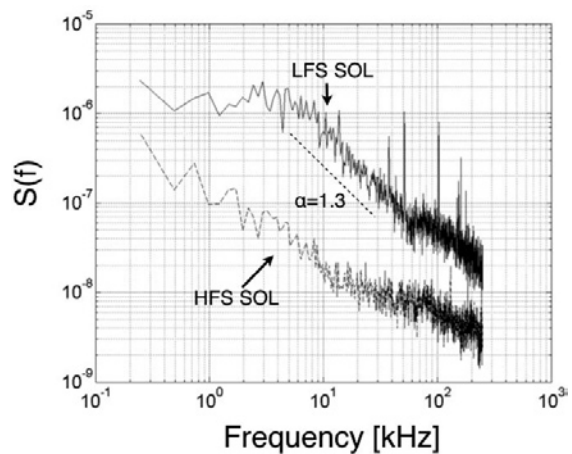


Fig.5 Power spectra of j_s at LFS and HFS SOLs.

We have also analyzed statistics of duration-time of j_s with positive burst events, where a positive burst is defined by a positive spike with an amplitude above twice of the standard deviation of the original signal (dotted line in Fig.4(a)). It is found, for the first time, that the PDF for the duration time τ shows a statistical self-similarity fluctuation property both at LFS and HFS SOLs as shown in Fig. 6, because the logarithmic plot of the PDF gives the power factor scaling $P(\tau) = \tau^{-\beta}$. β corresponds to a capacity fractal dimension. Larger β indicates that the plasma turbulence is developed to have finer vortex structure at HFS SOL. On the other hand, coherent structure associated with plasma blobs in plasma turbulence could reduce the β in LFS SOL.

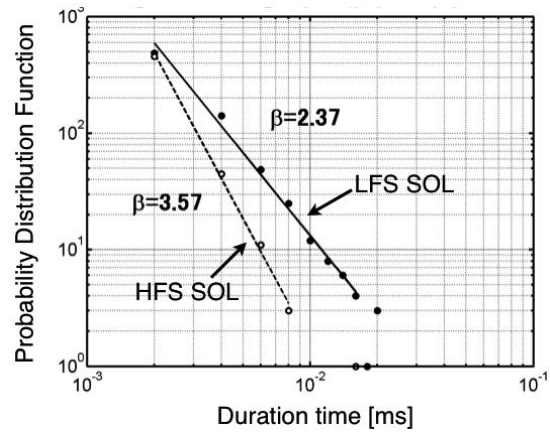


Fig.6 Probability distribution function of the duration time of bursts. Power law fits are shown by solid and dashed lines.

References

[1] Asakura, N., et al., J. Nucl. Mater. **337-339** (2005) 712-716.
 [2] Miyoshi, H., et. al. 32nd EPS Plasma Physics Conference, Tarragona (2005) P1.045.

8.9 Temporal Evolutions of Electron Temperature and Density with ELM in the Divertor Plasma

T. Nakano, N. Asakura, S. Kajita, H. Kawashima, H. Kubo, K. Fujimoto, N. Ohno and K. Shimizu

1 Introduction

ELM (Edge Localized Mode) is an intermittent heat- and particle-exhausting activity occurring at the edge of the main plasma in H-mode discharges. According to the multi-machine database [1], one type-I ELM pulse expels 20 % of the plasma stored energy in the pedestal region, 65 % of the expelled energy is transported to the divertor, and the divertor plates are exposed for 100 – 1000 μ s. From this database, it is predicted in ITER that the heat load around the strike point is higher than 5 GWm^{-2} on the assumption that the plasma stored energy in the pedestal region is 100 MJ, the exposure duration 500 μ s and the exposed divertor area 5 m^2 . This heat flux is higher than that measured in JT-60U by one order [2], and is high enough for carbon materials used around the strike points to sublime. Given that the ELM exposure duration is 100 – 1000 μ s in JT-60U [3], the plasma parameters measured at the frequency of 10 kHz are required to discuss the temporal evolution of the divertor plasma quantitatively. In the present work, with a newly-employed measurement technique, simultaneous measurement of the three He I lines at a high frequency of 20 kHz, temporal evolutions of the electron temperature and density are determined.

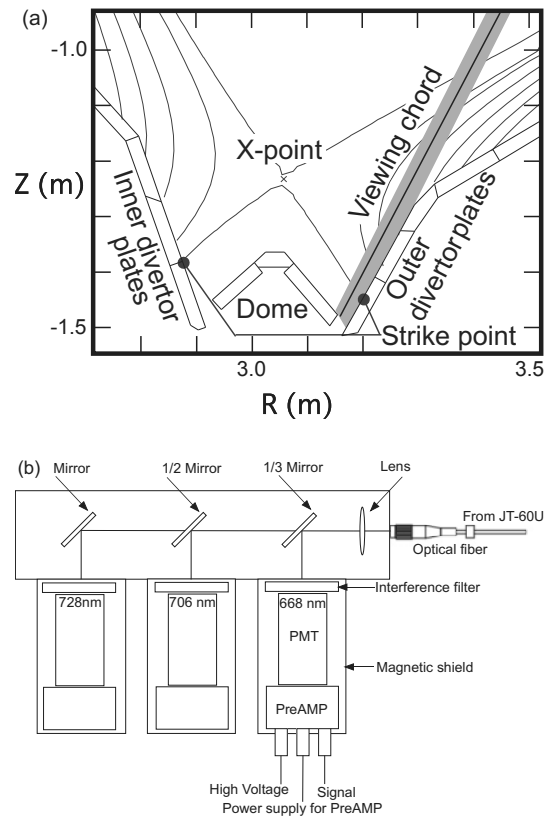


Fig. 1: (a) a schematic view of the divertor structure, the magnetic configuration, the viewing chords for He I lines (thin line) and D_α line (shade) measurement, and (b) the spectrometer for the He I lines.

2 Experimental

Figure 1 (a) shows the viewing chord for the spectroscopic measurement for the He I lines, which is parallel to the outer divertor plates and passes near the outer strike point. The emission from the divertor plasma, most of which comes from around the strike

point is transmitted through an optical fiber to a spectrometer shown in Fig. 1 (b). In the spectrometer, 1/3 of the incident light is reflected at the 1/3 mirror, transmits through the interference filter, and is detected by the absolutely calibrated photo-multiplier. The central transmission wavelength of the interference filter is 668.0 nm, the transmission band width 4.6 nm, and the peak transmittance 75 % for He I ($2p\ ^1P - 3d\ ^1D$: $\lambda = 667.8$ nm) line. Similarly, the absolute intensities of He I ($2p\ ^3P - 3s\ ^3S$: $\lambda = 706.5$ nm) and He I ($2p\ ^1P - 3s\ ^1S$: $\lambda = 728.1$ nm) line are measured. In addition, the intensity of D_α line is simultaneously measured along a similar viewing chord shown in Fig. 1 (a), which is on a poloidal cross section 60 degree apart in the toroidally opposite direction to the plasma current. The intensities of the three He I lines and D_α line are sampled, respectively, at 20 kHz and 250 kHz with a synchronized clock.

The present measurement was performed with an ELMy H-mode deuterium plasma with the plasma current of 1.0 MA, the toroidal magnetic field of 1.9 T and the neutral beam heating power of 20 MW. The electron temperature, the ion temperature and the electron density at the top of the pedestal were, respectively, 1.0 keV, 1.3 keV and $1.6 \times 10^{19} \text{ m}^{-3}$, the ELM frequency ~ 120 Hz (Type-I ELM), the expelled plasma stored energy ~ 20 kJ and the plasma stored energy at the pedestal region ~ 470 kJ. The waveforms of the D_α and the He I lines shown in, respectively, Fig. 2 (a) and (b) were obtained by averaging 134 ELMs during a steady-state ELMing phase to reduce statistical errors. In the averaging operation, the time of $t=0$ for each ELM was set at the peak of the D_α line intensity with an intensity of $4.5 - 5.5 \times 10^{19} \text{ ph sr}^{-1} \text{ m}^{-2} \text{ s}^{-1}$. It is noted that the origin of helium is a working gas for discharge cleaning.

3 Results and discussion

The intensity ratio, He I (728.1 nm) / He I (706.5 nm) is sensitive to electron temperature, and is not very sensitive to electron density, indicating a good measure of electron temperature [4]. This sensitivity is due to different electron-impact-energy dependence of the excitation cross sections to $3s\ ^1S$ and to $3s\ ^3S$ from the ground state of helium. Hence, qualitative change of the electron temperature is valid, even in the case that the excitation cross sections are averaged with a non-Maxwellian electron velocity distribution, although absolute temperature may not be correct. In contrast, the intensity ratio, He I (667.8 nm) / He I (728.1 nm), is sensitive to electron density, and is not very sensitive to electron temperature, indicating a good measure of electron density [4]. This is due to l -changing processes (excitation and de-excitation by electron impact) between $3s\ ^1S$ and $3d\ ^1D$ (l : an azimuthal quantum number) : at low density, the ratio of the population density of $3s\ ^1S$ to that of $3d\ ^1D$ is close to the ratio of the excitation rates to the respective levels from the ground state, and with increasing electron density, the ratio becomes close to the ratio of statistical weight of these levels.

These two intensity ratios were calculated with a collisional-radiative model for a

neutral helium [5]. From comparison of the calculated and the measured intensity ratio, the electron temperature and density were determined. As shown in Fig. 2 (c), the electron temperature starts increasing at $t = -450 \mu\text{s}$ from 70 eV, reaches 80 eV, stays for $150 \mu\text{s}$, and then, drops rapidly to 60 eV before it gradually recovers in about $3000 \mu\text{s}$. The electron density also starts increasing at $t = -450 \mu\text{s}$, continues to increase until $t = -100 \mu\text{s}$, and then the constant density phase lasts for $300 \mu\text{s}$ before it decreases rapidly, and then, gradually.

The temporal evolutions of the electron temperature and density are interpreted as follows:

I. $t = -450 \mu\text{s}$: the conductive power flow and probably also the convective particle flow from the main plasma caused by the ELM start reaching the divertor plasma. It is difficult to determine whether the increase of the electron temperature is ascribed to the conductive power flow or the convective particle flow because the time resolution of the present measurement ($50 \mu\text{s}$) is much lower than and comparable to, respectively, the conductive (*several μs*) and the convective transport time ($120 \mu\text{s}$) along the field line from the mid-plane to the outer strike point. In the case the increase of the electron temperature is dominated by the conductive power, the electron temperature may not be correct due to a possibility of a non-Maxwellian electron velocity distribution. In the case the increase of the electron temperature is dominated by the convective particles, the electron temperature is valid because of shorter electron temperature relaxation time of the divertor plasma and the plasma transported with the ELM ($\sim 10 \mu\text{s}$) compared to the transport time from the X-point to the outer strike point ($\sim 20 \mu\text{s}$). In any case, the qualitative change is valid as already described.

At the same time, the neutral particles released from the divertor plates start increasing due to an increase of the divertor plate temperature and also due probably to the start of the recycling of the incident ions to the divertor plates originating from the ELMs. Ionization of the released neutrals starts and produces plasma, resulting in an increase of electron density.

II. $t = -400 \sim 0 \mu\text{s}$: the conductive power flow and the convective particle flow

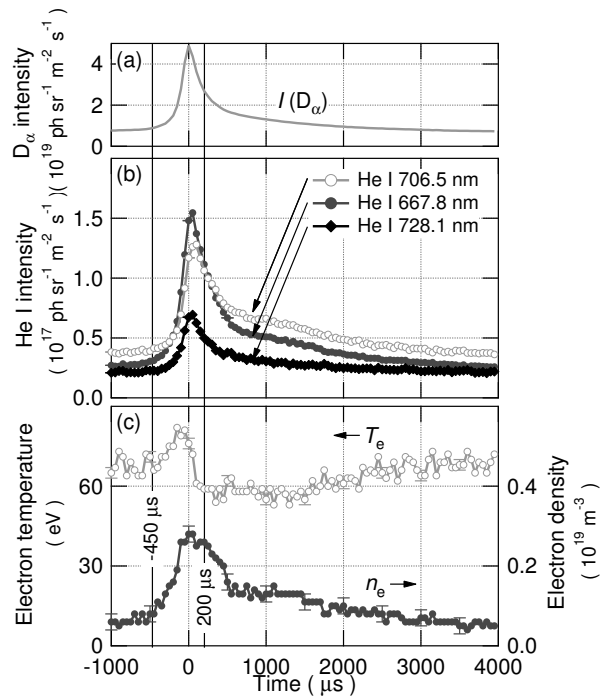


Fig. 2: Waveforms of (a) the intensity of D_α line, (b) the intensities of He I lines, and (c) the determined electron temperature and density. Error bars are shown every 10 data.

continue reaching the divertor, indicated by continuously increasing electron temperature and density.

III. $t = 0 \sim 200 \mu\text{s}$: at $t = 100 \mu\text{s}$, the conductive power flow and the convective particle flow into the divertor decrease rapidly while the electron energy is being consumed through the ionization of the neutrals. Thus, the electron temperature drops. Ionization of neutrals is still occurring and producing electrons. Thus, the electron density is kept.

IV. $t = 200 \sim 500 \mu\text{s}$: with decreasing incident ion flux, the recycling flux decreases, and then, the ionization flux decreases. Hence the electron production rate decreases, resulting in a decrease of the electron density.

V. $t > 500 \mu\text{s}$: with further decreasing incident ion flux, the electron density decreases, and then becomes constant in $3000 \mu\text{s}$. Similarly, the electron temperature recovers in $3000 \mu\text{s}$, resulting from the decrease of electron energy consumption and probably also from the recovery of the temperature around the pedestal.

4 Summary

The temporal evolutions of the electron temperature and density in the divertor plasma with ELM were investigated with simultaneous measurement of the three He I lines with sufficiently high time resolution to discuss the dynamics of the divertor plasma: the electron temperature starts increasing with increasing D_α intensity from 70 eV, reaches 80 eV, stays for $150 \mu\text{s}$, and then, drops rapidly to 60 eV at the peak of the D_α intensity, before it gradually recovers in about $3000 \mu\text{s}$. The increase of the electron temperature is ascribed to the conductive power and the convective particle flow into the divertor. Next, the electron temperature decreases due to the consumption of the electron energy through the ionization of neutrals with decreasing power and particle flow. Then, the electron temperature gradually increases with decreasing ionization flux.

The electron density also starts increasing with increasing D_α intensity, continues to increase, and then, becomes constant around the peak of the D_α intensity for $300 \mu\text{s}$, before it decreases rapidly, and then, gradually. The increase of the electron density is ascribed to an increase of the electron production rate through the ionization of recycled neutrals, which originates from the particles expelled from the pedestal by the collapse. The convective particle flow into the divertor decreases, resulting in a decrease of the recycling flux, a decrease of the ionization flux, and then, a decrease of the plasma production rate in the divertor. Consequently, the electron density in the divertor decreases. Further, the electron density gradually decreases.

References

- [1] Loarte, A. *et al.*, *Plasma Phys. Control. Fusion* **45** (2003) 1549.

- [2] Higashijima, S. *et al.*, *J. Nucl. Mater.* **363-365** (2003) 1123.
- [3] N. Asakura, N, Ohno *et al.*, “ELM Propagation Characteristics in JT-60U SOL”
Nucl. Fusion , submitted.
- [4] Kubo, H. *et al.*, *J. Plasma and Fusion Res.* **75** (1999) 945.
- [5] Goto, M. *J. Quant. Spectrosc. Radiat. Transf.* **76** (2003) 331.

8.10 Revisited : Measurement of Chemical Sputtering Yields

T. Nakano, K. Tsuzuki, S. Higashijima, H. Kubo and N. Asakura

1 Introduction

Carbon materials, in particular, carbon fiber composite materials are widely used for plasma-facing components such as a divertor plate because of the high thermal shock resistance, the high thermal conductivity, the high melting point and the low atomic number. But one of the negative properties of carbon materials is a chemical reaction with hydrogen, resulting in release of hydrocarbons. This erosion is one of the key factors to determine the lifetime of the carbon divertor plates in ITER. Hence the chemical sputtering yield has been measured in almost all fusion experimental devices with carbon divertor plates. However, the sputtering yields determined by a spectroscopic measurement technique are substantially different from one another. This discrepancy arises from variety of the emission rates of the CH spectral bands. To reduce this variety, the emission rates should be measured at the same device as the sputtering yield is measured because the emission rates depend on the transport of the radicals of the sputtered hydrocarbons, which is significantly affected by the divertor geometry. In the present report, the emission rates of CH, CD and C₂, originating from CH₄, CD₄, C₂H₄ and C₂H₆ were measured. With the measured emission rates, the chemical sputtering yields of CH₄, CD₄, C₂H_y and C₂D_y were determined.

2 Experimental

Figure 1 shows the present experimental set-up for the measurement of the emission rates. From the gas-puff nozzle at the outer divertor plate, one species of the following hydrocarbons, CH₄, CD₄, C₂H₄ and C₂H₆ every one pulse was injected into the outer divertor plasma. The flow rate of the hydrocarbons is determined from the decrease of the pressure at the chamber just upstream of the nozzle. Along the viewing chord on the same poloidal cross-section of the gas-puff nozzle (hereafter Vg), the intensities of the CH and the C₂ spectral bands, originating from the injected hydrocar-

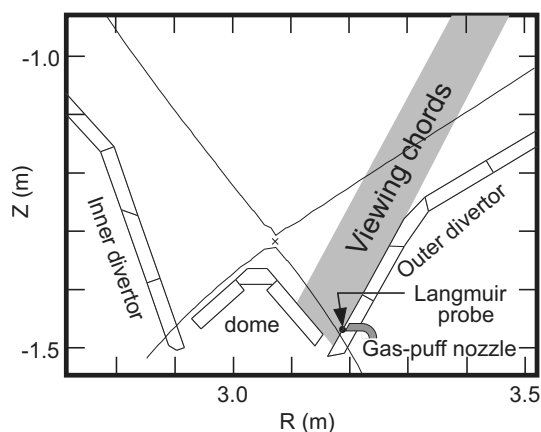


Fig. 1: *Cross-sectional view around the divertor. Viewing chord for the spectroscopic measurement, location of the gas-puff nozzle, and the magnetic configuration are shown. Another viewing chord and a Langmuir probe are positioned on different poloidal cross-sections.*

bons, were measured. Along another viewing chord on a different poloidal cross-section (hereafter Vb), toroidally apart by ~ 100 mm, the intensities of the CH and the C_2 spectral bands, originating from the intrinsic chemically-sputtered hydrocarbons were measured. The electron temperature and the ion flux were measured by a Langmuir probe, which is positioned on a different poloidal cross-section from the gas-puff nozzle.

The present measurement was performed in an L-mode discharge with the plasma current of 1.5 MA, the toroidal magnetic field of 3.6 T, the neutral beam heating power of 4.4 MW. With a gradual increase of the line-averaged electron density of the main plasma by the gas-puffing, the electron temperature at the outer strike point decreases down to 12 eV as shown in Fig. 2 (a). The C_2H_4 injection speed is almost constant as shown in Fig. 2 (b). Both the CH intensities measured along the Vg and the Vb chord increase while the difference of these two intensities are constant as shown in Fig. 2 (c). Because this difference is the net CH emission intensity originating from the injected C_2H_4 , the ratio of the injected C_2H_4 flux to the CH emission intensity originating from the injected C_2H_4 is evaluated on the assumption that the injected C_2H_4 is lost by dissociation, ionization and charge transfer processes in the observation volume. This ratio is referred as to $LEP_{C_2H_4}^{CH}$, which stands for C_2H_4 Loss – Events/CH Photon, Hereafter, the similar expressions for the other injected hydrocarbons are used.

Hereafter, the similar expressions for the other injected hydrocarbons are used.

3 Result of the measurement of the CH and the C_2 emission rates

From similar experiments, $LEP_{CH_4}^{CH}$, $LEP_{CD_4}^{CD}$, $LEP_{C_2H_4}^{CH}$, $LEP_{C_2H_4}^{C_2}$, $LEP_{C_2H_6}^{CH}$, and $LEP_{C_2H_6}^{C_2}$ were determined. In Fig. 3, these LEP values are shown as a function of the electron temperature at the outer strike point. As shown in Fig. 3 (a), both $LEP_{CH_4}^{CH}$ and $LEP_{CD_4}^{CD}$ decrease with decreasing electron temperature. But the dependence on the

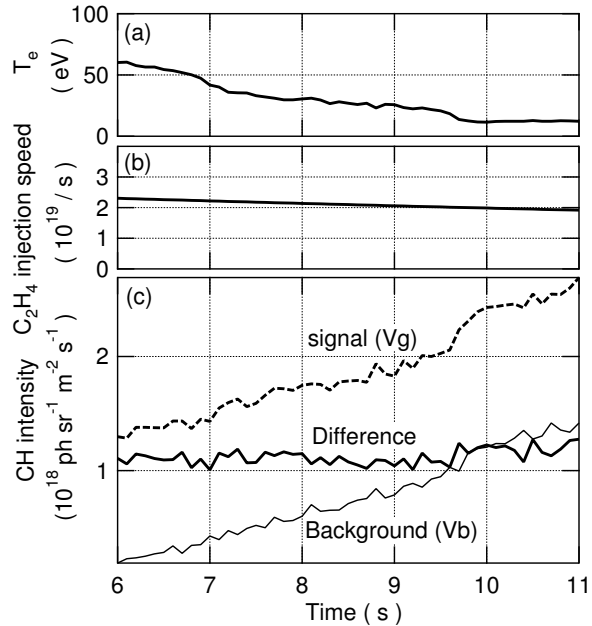


Fig. 2: Waveforms of (a) the electron temperature at the outer strike point, (b) C_2H_4 injection speed, (c) the CH intensity measured along the viewing chord on the same poloidal cross-section of the gas-puff nozzle (Vg), the CH intensity along the viewing chord on the different poloidal cross-section (Vb), and the difference of these two CH intensities.

electron temperature is weaker than $LEP_{CH_4}^{CH}$ measured in PISCES-A [1]. This is the case for $LEP_{C_2H_4}^{CH}$ and $LEP_{C_2H_4}^{C_2}$ as shown in Figs. 3 (b) and (c), respectively: the $LEP_{C_2H_4}^{CH}$ and $LEP_{C_2H_4}^{C_2}$ values determined in the present work indicate very weak dependence on the electron temperature while those measured in PISCES indicate much stronger dependence. The dependence of $LEP_{C_2H_6}^{CH}$ and $LEP_{C_2H_6}^{C_2}$ on the electron temperature is stronger compared with $LEP_{C_2H_4}^{CH}$ and $LEP_{C_2H_4}^{C_2}$.

It is interesting to compare $LEP_{C_2H_4}^{CH}$ and $LEP_{C_2H_6}^{CH}$. As shown in Fig. 3 (b), $LEP_{C_2H_4}^{CH}$ is larger than $LEP_{C_2H_6}^{CH}$, indicating that the CH emission originating from $LEP_{C_2H_6}^{CH}$ is stronger than that from $LEP_{C_2H_4}^{CH}$. This comparison qualitatively indicates that the probability of CH radial production in the break-up chain from C_2H_6 is larger than that from C_2H_4 . One of the reasons for this result is that the number of CH bonds in C_2H_6 is larger than that in C_2H_4 . This is the case for comparison of $LEP_{C_2H_4}^{C_2}$ and $LEP_{C_2H_6}^{C_2}$. The C_2 emission originating from C_2H_4 is stronger than that from C_2H_6 , showing the difference of relative ratio of the number C_2 bonds to C_2H_4 and to C_2H_6 .

4 Result of the chemical sputtering yield

With the measured LEP values, the chemical sputtering yields in Ref. [2], which were evaluated with the LEP values measured in PISCES-A [1], are revised. Because it is impossible to determine the ratio of C_2H_4 sputtering flux $\Gamma^{C_2H_4}$ to C_2H_6 sputtering flux $\Gamma^{C_2H_6}$ in the present work, this ratio is assumed to be $\alpha : (1 - \alpha)$, i.e., $\Gamma^{C_2H_4} = \alpha \cdot \Gamma^{C_2H_6}$, and $\Gamma^{C_2H_6} = (1 - \alpha) \cdot \Gamma^{C_2H_6}$. Then, the measured CH and C_2 intensity, respectively $I_{CH}^{measured}$ and $I_{C_2}^{measured}$, are expressed as

$$I_{CH}^{measured} = I_{CH}^{CH_4} + I_{CH}^{C_2H_4} + I_{CH}^{C_2H_6}$$

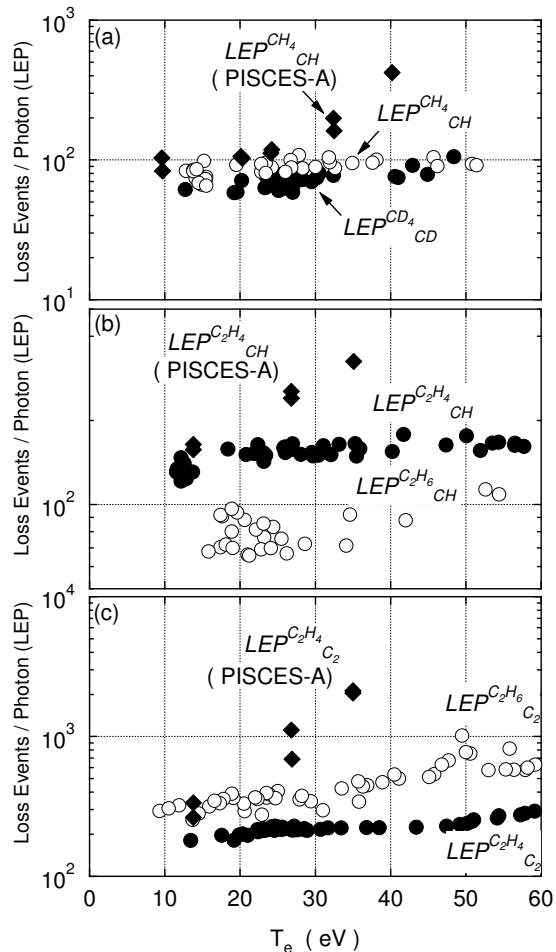


Fig. 3: (a) $LEP_{CH_4}^{CH}$, $LEP_{CD_4}^{CD}$, (b) $LEP_{C_2H_4}^{CH}$, $LEP_{C_2H_6}^{CH}$, (c) $LEP_{C_2H_4}^{C_2}$, and $LEP_{C_2H_6}^{C_2}$ as a function of the electron temperature. $LEP_{CH_4}^{CH}$, $LEP_{C_2H_4}^{CH}$, and $LEP_{C_2H_4}^{C_2}$ measured in PISCES-A [1] are also shown.

$$\begin{aligned}
 &= \Gamma^{\text{CH}_4} / LEP_{\text{CH}}^{\text{CH}_4} + \Gamma^{\text{C}_2\text{H}_4} / LEP_{\text{CH}}^{\text{C}_2\text{H}_4} + \Gamma^{\text{C}_2\text{H}_6} / LEP_{\text{CH}}^{\text{C}_2\text{H}_6} \\
 &= \Gamma^{\text{CH}_4} / LEP_{\text{CH}}^{\text{CH}_4} + \Gamma^{\text{C}_2\text{H}_y} \left(\alpha / LEP_{\text{CH}}^{\text{C}_2\text{H}_4} + (1 - \alpha) / LEP_{\text{CH}}^{\text{C}_2\text{H}_6} \right), \quad (1) \\
 I_{\text{C}_2}^{\text{measured}} &= I_{\text{C}_2}^{\text{C}_2\text{H}_4} + I_{\text{C}_2}^{\text{C}_2\text{H}_6} \\
 &= \Gamma^{\text{C}_2\text{H}_4} / LEP_{\text{C}_2}^{\text{C}_2\text{H}_4} + \Gamma^{\text{C}_2\text{H}_6} / LEP_{\text{C}_2}^{\text{C}_2\text{H}_6} \\
 &= \Gamma^{\text{C}_2\text{H}_y} \left(\alpha / LEP_{\text{C}_2}^{\text{C}_2\text{H}_4} + (1 - \alpha) / LEP_{\text{C}_2}^{\text{C}_2\text{H}_6} \right), \quad (2)
 \end{aligned}$$

where Γ^{CH_4} indicates CH_4 sputtering flux. From these equations, Γ^{CH_4} and $\Gamma^{\text{C}_2\text{H}_y}$ can be evaluated, and the sputtering yield of CH_4 and C_2H_y , respectively Y_{CH_4} and $Y_{\text{C}_2\text{H}_y}$, defined as the ratio of $\Gamma^{\text{CH}_4} / \Gamma_{\text{ion}}$ and $\Gamma^{\text{C}_2\text{H}_y} / \Gamma_{\text{ion}}$ and are determined, where the ion flux is denoted by Γ_{ion} .

Figure 4 (a) shows the CH_4 and the CD_4 sputtering yield at $\alpha = 0.5$, i.e., $\Gamma^{\text{C}_2\text{H}_4} = \Gamma^{\text{C}_2\text{H}_6}$. The bars for the CD_4 sputtering yield DO NOT indicate the statistical error but indicate the possible range of the CD_4 yield, determined by α : at $\alpha = 1$, the sum of the second and the third term of Eq. 1 becomes the smallest because $LEP_{\text{C}_2\text{H}_4}^{\text{CH}}$ is larger than $LEP_{\text{C}_2\text{H}_6}^{\text{CH}}$. Hence Γ^{CH_4} takes the largest value. On the contrary, at $\alpha = 0$, Γ^{CH_4} takes the smallest value. Similarly in Fig. 4 (b), the C_2H_y and the C_2D_y yields are shown. In Fig. 4 (c), the total sputtering yields, defined as $Y_{\text{CH}_4} + 2 \times Y_{\text{C}_2\text{H}_y}$ are shown. The possible range determined by α is smaller than the size of the symbols. Hence it is concluded that the ratio of $\Gamma^{\text{C}_2\text{H}_4}$ to $\Gamma^{\text{C}_2\text{H}_6}$ does not have serious influence on the total sputtering yield.

References

- [1] Pospieszczyk, A. *et al.*, UCLA-PPG-1251 (1989).
- [2] Nakano, T. *et al.*, Nucl. Fusion **42** (2002) 689.

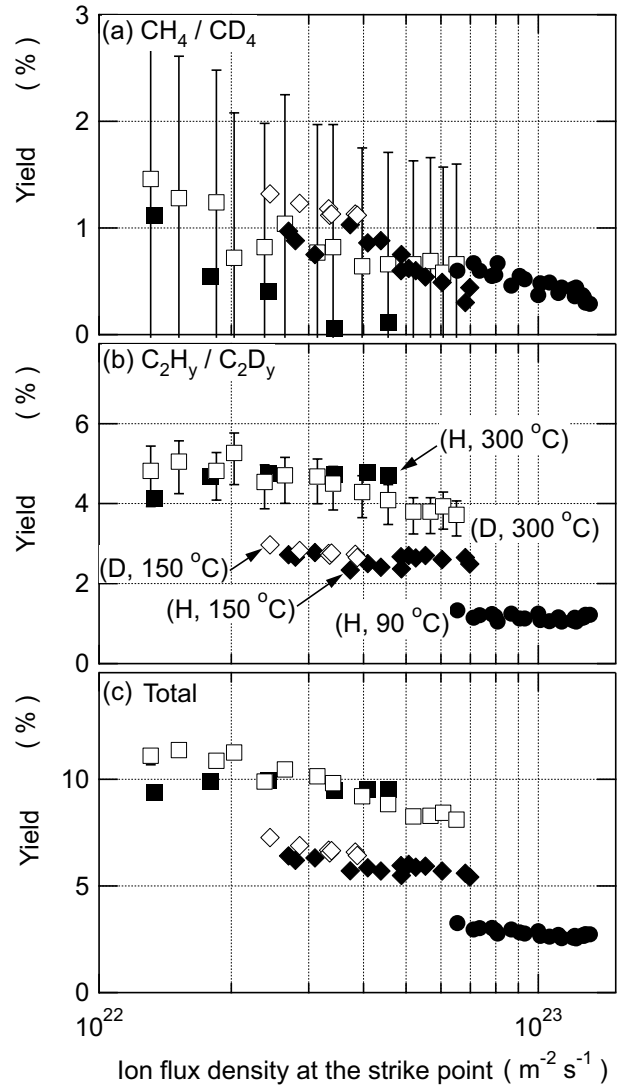


Fig. 4: (a) the CH_4 , the CD_4 , (b) the C_2H_y , the C_2D_y , and (c) the total sputtering yields as a function of ion flux density at the strike point.

8.11 Volume Recombination of C^{4+} in Detached Divertor Plasmas [1]

T. Nakano, H. Kubo, N. Asakura, K. Shimizu, S. Konoshima, K. Fujimoto,
H. Kawashima and S. Higashijima

In order to investigate the radiation power from C^{3+} in detached divertor plasmas with MARFE, C IV lines were measured by a VUV spectrometer and by a visible spectrometer simultaneously. When an X-point MARFE was formed, the C IV emissivity peaked around an X-point. From the absolute intensity of C IV lines emitted from the peak, the population density ratio of the C^{3+} excited levels was determined, and then analyzed with a collisional-radiative model. The result of the analysis indicated that the population density of the excited levels was composed of the ionizing and the recombining plasma component with an electron temperature of 6.3 eV and an electron density of $7.8 \times 10^{20} \text{ m}^{-3}$; the levels with $n \leq 4$ were dominated by the ionizing plasma component and the levels with $n \geq 5$ by the recombining plasma component.

By using the collisional-radiative model with these evaluated parameters and C IV brightness, the line-radiation power was evaluated: the line-radiation power from the ionizing plasma component of C^{3+} is 60 % of the total radiation power (1.4 MWm^{-2}) measured by a bolometer with a similar viewing chord. In contrast, the line-radiation power from the recombining plasma component is only 2 % of the total radiation power. However, the volume recombination flux of C^{4+} and e^- into C^{3+} is larger by two orders of magnitude than the ionization flux of C^{3+} . Hence the ionization state balance between C^{3+} and C^{4+} is dominated by the recombination from C^{4+} into C^{3+} rather than the ionization from C^{3+} into C^{4+} , which is the case for usual divertor plasma conditions such as attached plasmas. From this result, the recombination is presumably one of the sources of C^{3+} . This will be investigated by comparison of the ionization flux of C^{2+} and the recombination flux of C^{4+} into C^{3+} in near future.

Further, from the population density ratio of the $n = 9$ level to the $n = 7$ level, the distribution of the electron temperature was estimated: the electron temperature was ~ 10 eV at the edge of the MARFE region, and decreased toward the X-point down to 2 eV. From this spatial gradient of the electron temperature, complicated structures of the elementary process and the radiation power of C^{3+} in the MARFE region are suggested: at the very center of the MARFE region ($T_e \sim 2$ eV), the volume recombination is dominant and the radiation power is low. At the edge of the MARFE region, the excitation from the ground state of C^{3+} to low excited levels such as 3p is significant, resulting in significant line-radiation. As a result, the radiation power from C^{3+} has a hollow profile rather than a peaked profile.

In near future, the two-dimensional distribution of the electron temperature will be evaluated from the two-dimensional population ratio, for example, the $n = 9$ level to the $n = 7$ level. Then, the two-dimensional distributions of the radiation power and the ionization/recombination balance are investigated from two dimensional distribution

of C IV emissivities. For this purpose, improvement of the tomography reconstruction technique [2] is necessitated. This method will be applicable for carbon ions in other ionization states and deuterium to investigate the rest of the radiation power ($\sim 40\%$).

References

- [1] Nakano, T. *et al.*, *Nucl. Fusion* **47** (2007) 1458.
- [2] Fujimoto, K. *et al.*, *Plasma and Fusion Res.* **2** (2007) S1121.

8.12 Ionizing and Recombining Components of Deuterium Emission in Detached Divertor Plasmas

K. Fujimoto, T. Nakano, H. Kubo, K. Sawada¹⁾, H. Kawashima, K. Shimizu, and N. Asakura

1) Shinshu University

1. Introduction

In tokamak fusion reactor, heat and particle control is essential to prevent damage of the plasma facing component. The poloidal divertor is the most promising method for the heat and particle control. In detached divertor plasmas, the ionization and recombination occur contiguously [1, 2]. The D₂ molecules and D atoms released from divertor plates ionize at the higher temperature plasma (ionizing plasma, $T_e > 5$ eV). The D⁺ ions transported to the divertor region recombine at the lower temperature plasma (recombining plasma, $T_e < 1$ eV). Two-dimensional spectroscopic measurement of the deuterium emission is effective to determine the spatial distribution of the ionizing and recombining plasma in a detached divertor plasma.

To investigate the formation mechanism of a detached divertor plasma, the deuterium Balmer-series lines in a divertor plasma were measured two-dimensionally. Spatial distributions of the deuterium Balmer-series lines emission were reconstructed with tomography techniques [3]. The ionizing and recombining components of the deuterium Balmer-series lines emission were discussed with the collisional-radiative model.

2. Two-dimensional Distribution of the Deuterium Balmer-series Lines Emission

A wide-spectral-band spectrometer with a CCD detector was used to observe deuterium Balmer-series lines. As shown in Fig.1, the spectrometer has 92 view channels (vertically 60 channels, horizontally 32 channels) with a spatial resolution of ~ 1 cm. From 1 to 17 channels of the horizontal channels are interrupted by the divertor dome top. The spectrometer covers a spectral range of 350 - 800 nm. Since the deuterium Balmer-series lines distribute from 360 to 656 nm, they can be measured with the spectrometer simultaneously. An ND filter which reduces the D _{α} line emission by $\sim 1/10$ is installed in the spectrometer to obtain the dynamics range of 10^5 .

The deuterium Balmer-series lines were measured in an L-mode plasma. The plasma current, the toroidal field, and the NBI heating power were 0.9 MA, 1.2 T, and 3.5 MW, respectively. The electron density normalized by the Greenwald density limit was 43 % in the inner detached divertor plasma and 65% in the detached divertor plasma. The deuterium

Balmer-series lines from D_α line ($n=2-3$, where n is the principal number, 656.3 nm) to D_0 line ($n=2-10$, 379.8 nm) emission were observed simultaneously.

The maximum entropy method (MEM) was used as a tomography technique [4]. The MEM is suitable for reconstructions with a small number of projections and well used for the plasma analysis [5]. The two-dimensional distribution of the

D_α line emission in a discharge with the detached inner divertor plasma and the attached outer divertor plasma is shown in Fig.2 (a). In the inner divertor region, the D_α line emission is stronger above the inner strike point and extends upward along to the inner divertor plates. In the outer divertor region, the D_α line emission is stronger on the outer divertor plates. The horizontal strong emission from just under the X-point to the outer divertor plates is false distribution due to the reconstruction error. The peak intensity of the strongly emitted region is $\sim 2 \times 10^{21}$ ph/sr/m³/s in the inner divertor region and $\sim 3 \times 10^{20}$ ph/sr/m³/s in the outer divertor region. The two-dimensional distribution of the D_α line emission in a discharge with the detached inner and outer divertor plasmas is shown in Fig.2 (b). In the inner divertor region, the D_α line emission is stronger above the inner strike point and extends along to the inner divertor plates. In the outer divertor region, the D_α line emission is stronger around the outer divertor plates and the strong emission area spreads. The peak intensity of the strongly emitted region is $\sim 2 \times 10^{21}$ ph/sr/m³/s in the inner divertor region and $\sim 4 \times 10^{21}$ ph/sr/m³/s in

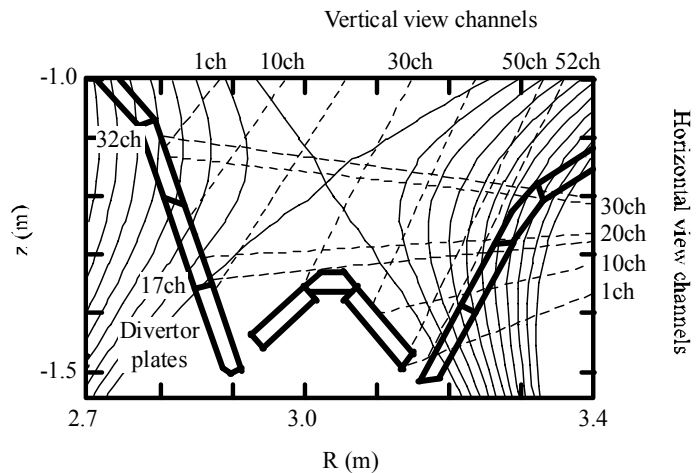


Fig.1. The view channels of the wide-spectral-band spectrometer.

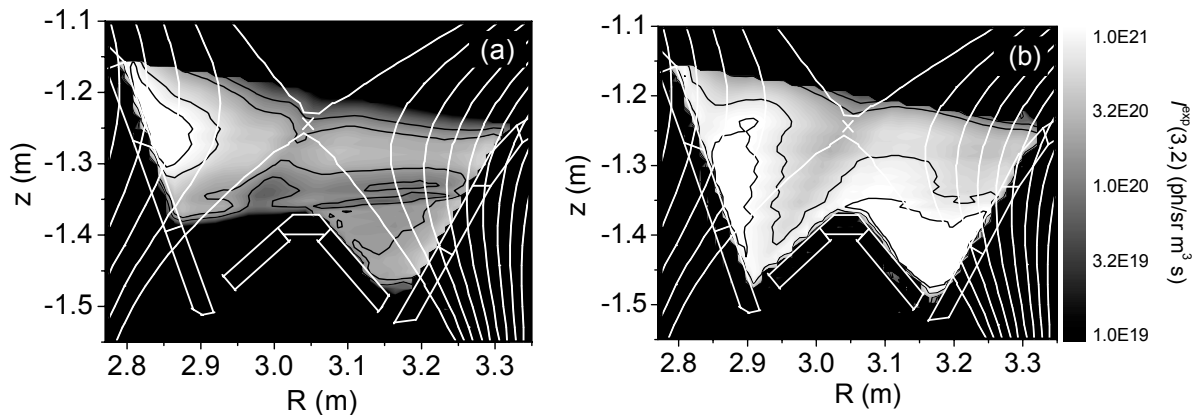


Fig.2. Two-dimensional distributions of the D_α line emission (a) in a discharge with the detached inner divertor plasma and the attached outer divertor plasma (b) in a discharge with the detached inner and outer divertor plasmas. The contour lines are 1×10^{19} , 5×10^{19} , 1×10^{20} , 5×10^{20} , and 1×10^{21} ph/sr m⁻³ s.

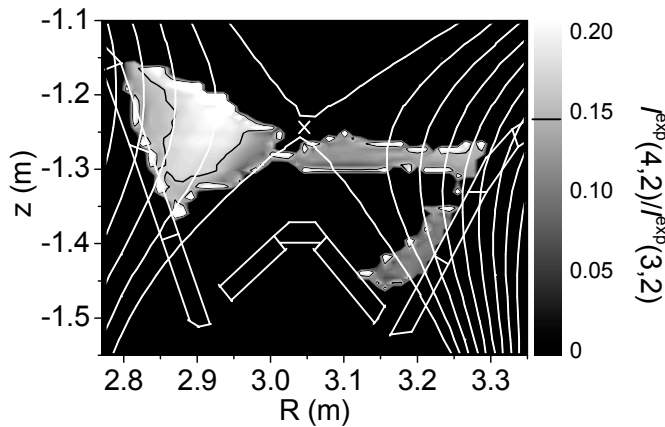


Fig.3. Two-dimensional intensity ratio of the D_β line to D_α line, $I^{\text{exp}}(4, 2)/I^{\text{exp}}(3, 2)$.

The population density can be expressed a sum of an ionizing and recombining components.

$$\begin{aligned} I(p, q) &= A(p, q)n(p) \\ &= A(p, q)\{R_1(p)n_e n(1) + R_0(p)n_e n_i\}, \end{aligned} \quad (1)$$

where $A(p, q)$ is the A-coefficient from p -level to q -level, $R_1(p)$ is the ionizing population coefficient at p -level, $R_0(p)$ is the recombining population coefficient at p -level, n_e is the electron density, n_i is the ion density, and $n(1)$ is the atom population density at the ground state [6]. The $R_1(p)$ and $R_0(p)$ are the function of the electron density and electron temperature. The first term of eq. (1) is the ionizing component and the second term is the recombining component. Figure 3 shows the experimental intensity ratio of the D_β ($n=2-4$, 486.1 nm) line to D_α line, $I^{\text{exp}}(4, 2)/I^{\text{exp}}(3, 2)$, in the inner detached plasma. The region with high $I^{\text{exp}}(4, 2)/I^{\text{exp}}(3, 2)$ ratio distributes in the inner divertor region along the magnetic field lines. As already mentioned in Fig.2 (a), since the deuterium emission under the X-point to the outer divertor plates is false, the distribution of the $I(4, 2)/I(3, 2)$ in that area is not correct. The theoretical intensity ratio with the collisional-radiative model, $I^{\text{th}}(4, 2)/I^{\text{th}}(3, 2)$, is shown in Fig.4. The intensity ratio becomes large, when the recombining component of the emissions is dominant. The boundary line between the pure ionizing and pure recombining is 0.14, which is expressed as

the outer divertor region. Though the D_α line emission above the inner strike point changes less, that around the outer strike point increases by more than ten times.

3. Ionizing and Recombining Component in the Inner Detached Divertor Plasma

An emission intensity from p -level to q -level, $I(p, q)$, is a function of the deuterium atom population density at p -level, $n(p)$.

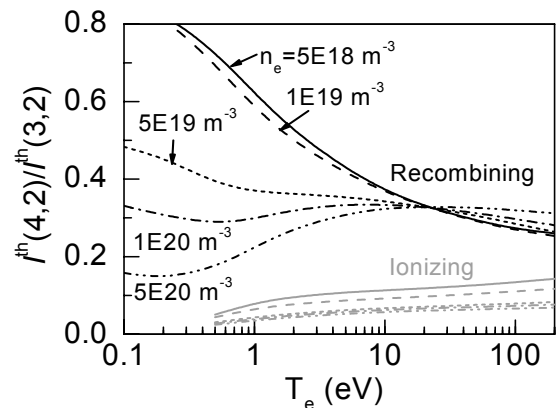


Fig.4. The intensity ratio of the D_β line to D_α line calculated with a collisional-radiative model. The gray lines correspond to pure ionizing and the black lines correspond to pure recombining.

contour lines in Fig.4.

In Fig.3, the recombining component is dominant above the inner strike point along to the separatrix. Though $I^{\text{exp}}(4, 2)/I^{\text{exp}}(3, 2)$ is ~ 0.1 on the separatrix field line in the inner divertor region, it can be explained to be the recombining component with $T_e < 0.5$ eV in Fig.4. The ionizing component is dominant on the upper divertor plates in the inner divertor region. Consequently, the two-dimensional structure of attached and detached region in the partially detached divertor plasma is obtained. On the outer divertor plate, the ionizing component is dominant on the D_α and D_β line emission. The plasma in the outer divertor region is attached.

We have a plan to determine the two-dimensional distribution of the electron temperature, the electron density, and the deuterium atom density. The spatial distribution of the ionizing and recombining plasma will be studied.

References

- [1] Lumma, D., et al, *Phys. Plasmas*, **4**, 2555-2565 (1997).
- [2] Kubo, H., et al, *J. Nucl. Mater.*, **337-339**, 161-165 (2005).
- [3] Fujimoto, K., et al, *Trans. Fusion Sci. Tec.*, **51**, 247 (2007) ..
- [4] Skilling, J., et al., *Mon. Not. Astr. Soc.*, **211**, 111-124 (1984).
- [5] Iwama, N., et al., *J. Plasma Fusion Res.*, **82**, 399-409 (2006).
- [6] Fujimoto, T., "Plasma spectroscopy", *International series of monographs on physics 123*, Oxford science publications.

8.13 Evaluation of the Electron Distribution Function for Detached Plasma

Y. Sadamoto¹⁾, K. Uehara, N. Asakura, H. Kawashima, H. Kubo,
T. Nakano, H. Takenaga, K. Fujimoto, H. Amemiya²⁾, Y. Saitou³⁾

1) Department of Physics, Joetsu University of Education, Joetsu, Niigata 943-8512, Japan

2) Graduate School of Science and Engineering, Chuo University, Bunkyo, Tokyo 112-8551, Japan

3) Department of Electrical and Electronic Engineering, Utsunomiya University, Utsunomiya, Tochigi 321-8505, Japan

1. Introduction

The evaluation of the electron temperature and energy in tokamak boundary plasmas is an important issue for estimation of energy flows and particle flows to divertor plates. The electron temperature obtained from a semi-logarithmic plot of electron current-voltage characteristics for a detached plasma in the JT-60U divertor region [1] is larger than that measured with the Thomson scattering method for a detached plasma in the DIII-D divertor region [2]. There are no evaluations of electron distribution functions in JT-60U. The purpose of this research is to evaluate the electron temperature and energy from electron velocity distribution functions of the divertor plasma in JT-60U.

2. Method of the electron velocity distribution function

The electron velocity distribution function f is obtained from the numerical first-derivative of the smoothed probe current I_p at the probe voltage V_p in the basis of the following equation [3]: $f(v_x) = [m/(ne^2S)] dI_p/dV_p$ with $v_x = [2e(V_s - V_p)/m]^{1/2}$, where v_x is the velocity perpendicular to the effective probe surface S , m is the electron mass, n is the density, e is the elementary charge, and V_s is the space potential. Figures 1 a) and b) show an example of probe current-voltage characteristics and its electron distribution function, where the horizontal axis energy E stands for $E = e(V_s - V_p)$. The electron temperature T_{ep} agrees with the value obtained from

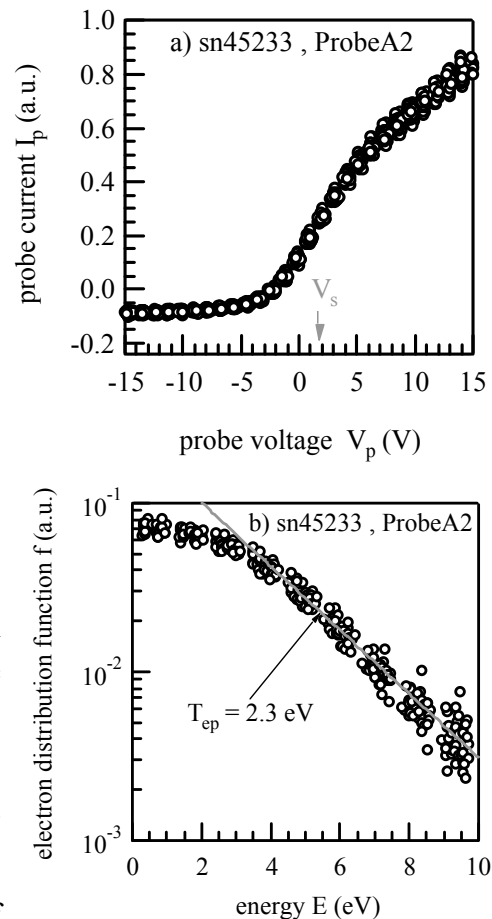


Fig. 1. a) an example of probe current-voltage characteristics and b) its electron velocity distribution function, where the horizontal axis stands for $E = e(V_s - V_p) = m v_x^2/2$.

a semi-logarithmic plot of electron current-voltage characteristics. It should be noted that the electron distribution function can be evaluated if the probe voltage of the single probe can be fully swept up to the space potential V_s .

3. Experimental results

3-1 Transition from an attached plasma to a detached plasma

A divertor plasma and positions of Langmuir probes are indicated in Fig. 2. Figure 3 shows time histories of the ion saturation current I_{is} and the electron temperature T_e evaluated from a semi-logarithmic plot of electron current-voltage characteristics at the probe A7. The ion saturation current and the electron temperature rapidly decrease at $t \sim 18$ s. At the outer strike point probe A7, the divertor plasma shifts from an attached plasma to a detached plasma at $t \sim 18$ s.

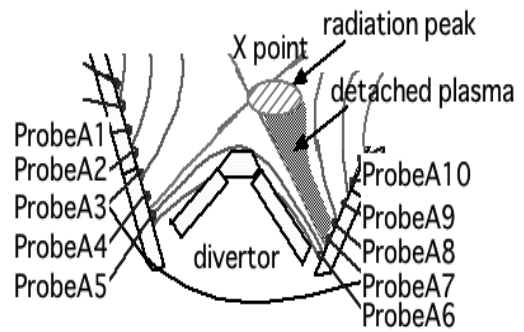


Fig. 2. Divertor plasma and Langmuir probes.

3-2 Electron velocity distribution function of the attached plasma

The electron distribution functions at the probe A7 are presented in Fig. 4 for the attached plasma of $t = 14 - 17.5$ s. The value of the distribution function at $E = 0$ is normalized to unity. The electron distribution function obtained experimentally fits the Maxwellian distribution function $f = \exp(-E/T_{ep})$ with $T_{ep} = 12$ eV.

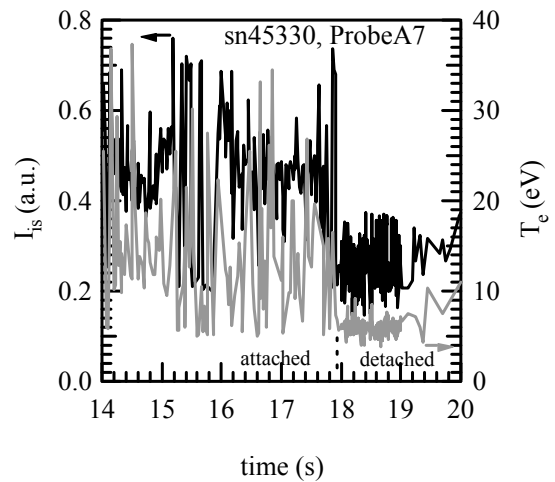


Fig. 3 Time histories of the ion saturation current I_{is} and the electron temperature T_{ep} measured with the probe A7.

3-3 Electron velocity distribution function of the detached plasma

When the X-point MARFE and the plasma detachment occur at $t > 18$ s as is shown in Figs. 2 and 3, the electron distribution functions at the outer strike point probe A7 are presented in Fig. 5. The electron distribution function obtained experimentally is

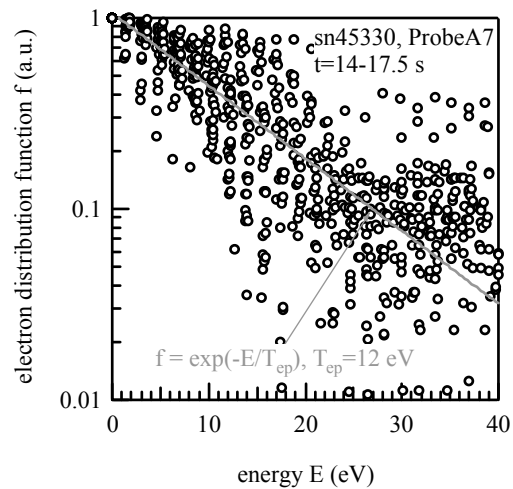


Fig. 4. Electron distribution function f vs energy E at the probe A7 for the attached plasma of $t = 14 - 17.5$ s.

reconstructed with a combination of the Maxwellian distribution function $f_1 = a_1 \exp(-E/T_{e1})$ and the drifted Maxwellian distribution function $f_2 = a_2 \exp[-(E^{1/2}-E_0^{1/2})^2/T_{e2}]$. Then, $a_1 = 0.94$, $T_{e1} = 3.6$ eV, $a_2 = 0.65$, $E_0 = 6.0$ eV, and $T_{e2} = 2.5$ eV. However, a combination of two Maxwellian distribution functions $g_1 = b_1 \exp(-E/T_{e1})$ and $g_2 = b_2 \exp(-E/T_{e2})$ does not give the experimental distribution function. Other distribution functions at probes A6 and A8-A10 are also formed by a combination of the Maxwellian distribution function and the drifted Maxwellian distribution function as are represented in Figs. 6-9. Figure 10 shows E_0 , T_{e1} , T_{e2} , and T_{ep} for various probe positions. The spatial profile of the electron temperature T_{ep} agrees with the conventional probe data for the detached and attached regions in the JT-60U divertor plasma [1]. The electron temperatures T_{e1} and T_{e2} are almost equal and change from 1 eV at the probe A6 to 5 eV at the probe A10. The values of T_{e1} and T_{e2} are about half of T_{ep} and are almost equivalent to the electron temperature measured with the Thomson scattering method in the DIII-D divertor region [2]. The drift energy E_0 increases from probe A6 to probe A8 and decreases from probe A8 to probe A10; the probe A8, where E_0 has the maximum value, is placed at the boundary of the detached region and the attached region. At this boundary, a plasma flow becomes the maximum [1].

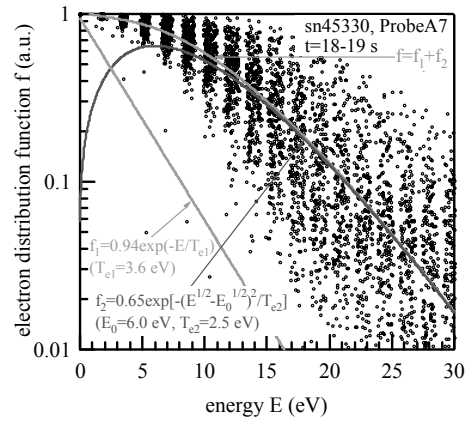


Fig. 5. Electron distribution function f vs energy E at the probe A7 for the detached plasma of $t = 18 - 19$ s.

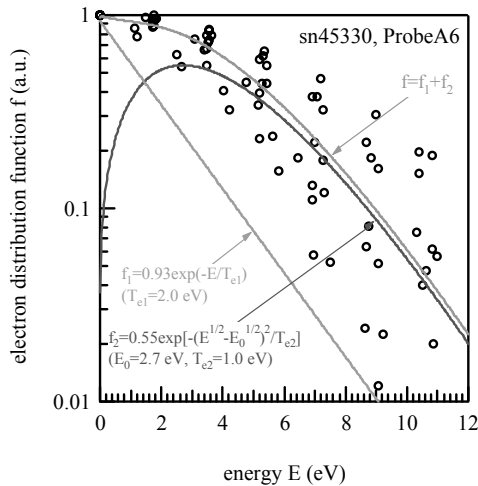


Fig. 6. Electron distribution function f vs energy E at the probe A6 for the detached plasma of $t = 18 - 19$ s. Fitting parameters are $a_1 = 0.93$, $T_{e1} = 2.0$ eV, $a_2 = 0.55$, $E_0 = 2.7$ eV, and $T_{e2} = 1.0$ eV.

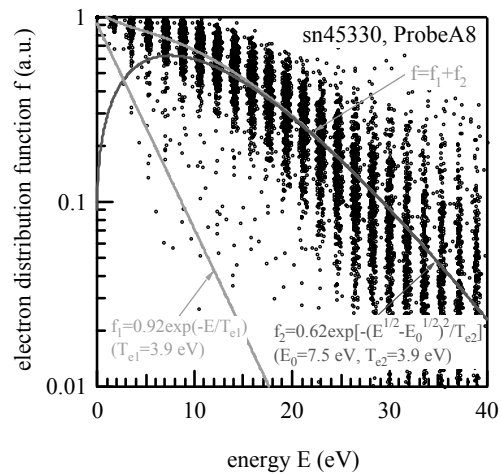


Fig. 7. Electron distribution function f vs energy E at the probe A8 for the detached plasma of $t = 18 - 19$ s. Fitting parameters are $a_1 = 0.92$, $T_{e1} = 3.9$ eV, $a_2 = 0.62$, $E_0 = 7.5$ eV, and $T_{e2} = 3.9$ eV.

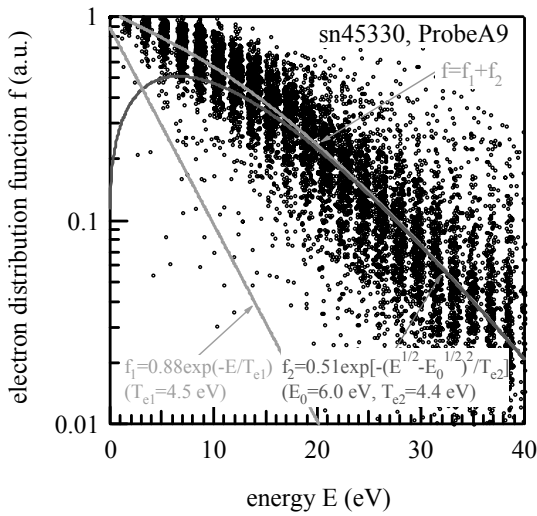


Fig. 8. Electron distribution function f vs energy E at the probe A9 for the detached plasma of $t = 18 - 19$ s. Fitting parameters are $a_1 = 0.88$, $T_{e1} = 4.5$ eV, $a_2 = 0.51$, $E_0 = 6.0$ eV, and $T_{e2} = 4.4$ eV.

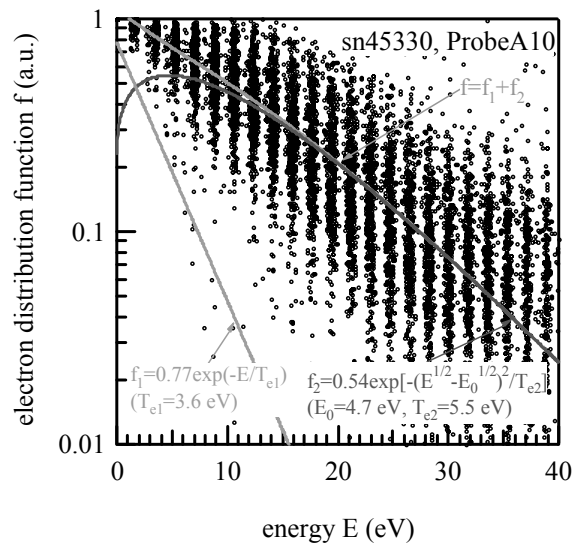


Fig. 9. Electron distribution function f vs energy E at the probe A10 for the detached plasma of $t = 18 - 19$ s. Fitting parameters are $a_1 = 0.77$, $T_{e1} = 3.6$ eV, $a_2 = 0.54$, $E_0 = 4.7$ eV, and $T_{e2} = 5.5$ eV.

4. Conclusions

The electron velocity distribution function can be evaluated from the numerical first-derivative of the probe current at the probe voltage. The electron distribution function is formed by a combination of the Maxwellian distribution function and the drifted Maxwellian distribution function for the detached plasma. The electron drift energy reaches its maximum value at the boundary of the attached and detached regions. However, the electron distribution function fits the Maxwellian distribution function for the attached plasma.

References

- [1] N. Asakura et al.: Nucl. Fusion 39(1999) 1983.
- [2] A. W. Leonard et al.: Phys. Rev. Lett. 78 (1997) 4769.
- [3] K. Uehara et al.: Jpn.J. Appl. Phys. 42 (2003) 657.

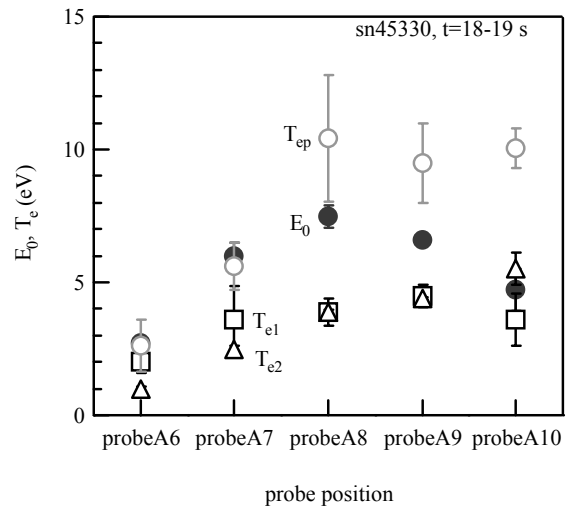


Fig. 10. Spatial profile of the electron temperatures T_{ep} , T_{e1} , T_{e2} , and the drift energy E_0 .

8.14 Modeling of Divertor Pumping Using SOLDOR/ NEUT2D Code

H. Kawashima, K. Shimizu, T. Takizuka, N Asakura, H. Takenaga, T. Nakano, S. Sakurai

To characterize the divertor pumping for particle and heat control in the SOL/divertor, simulations using the SOLDOR/ NEUT2D code developed originally [1] were performed to the JT-60U long pulse discharge [2]. The simulation reproduces the neutral pressure and pumping flux in the exhaust chamber at the experiment by treating the desorbed flux from the wall similar as the gas puff flux (Fig.1). Heat loads on the divertor targets satisfy the heat balance consistently.

Parametric survey shows the pumping efficiency (ratio of pumping flux to generated flux around the divertor targets) [3] increasing with the pumping speed. It is found that the pumping speed higher than the present capability ($26 \text{ m}^3/\text{s}$) is necessary for the active particle control under the wall saturation condition. On the other hand, shortening the strike-point distance (distance from extension point of the private dome wing on the divertor target to the strike point) from 10 cm to 2 cm, the pumping efficiency is enlarged by a factor of 1.5 with increase of the viewing angle from strike point to pumping slot and the incident flux into exhaust chamber. A virtual tilt of the divertor targets to 15° vertically enhances the pumping efficiency by a factor of 1.2 with a low target heat load.

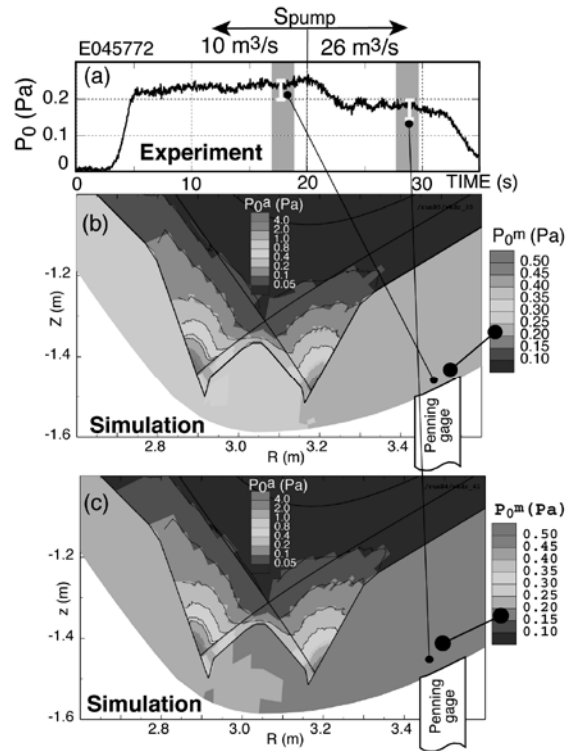


Fig.1 (a); Time evolutions of neutral pressure in front of penning gage, when the pumping speed S_{pump} is increased from $10 \text{ m}^3/\text{s}$ to $26 \text{ m}^3/\text{s}$ at $t = 20$ s in JT-60U long pulse discharge under the wall saturation condition. (b) and (c); Simulated contour plots of neutral pressure (molecular pressure in the exhaust chamber and atom pressure in the divertor region) for (b) $S_{\text{pump}}=10 \text{ m}^3/\text{s}$ and (c) $S_{\text{pump}}=26 \text{ m}^3/\text{s}$.

References

- [1] Kawashima, H., et al., Plasma and Fusion Research **1**, 031-1 (2006).
- [2] Kawashima, H., et al., J. Nucl. Matter. **363-365**, 786 (2007).
- [3] Kawashima, H., et al., Fusion Eng. Design, **81**, 1613(2006).

8.15 A New Fast Velocity-Diffusion Modelling for Impurity Transport in Integrated Edge Plasma Simulation [1]

K. Shimizu, T. Takizuka, H. Kawashima

For compatibility of high confinement core plasma with strong radiative divertor, it is necessary to establish the control method for impurity retention in the divertor region. A number of 2D multi-fluid divertor code have been developed for investigation of the impurity and plasma transport. The impurity transport is solved as one species of fluids in their codes. We have proceeded to another approach for impurity modelling [2]. Monte-Carlo (MC) approach is superior to the fluid model from the aspect of flexibility of modelling. Interactions between impurities and walls, and kinetic effects can be easily included into the modelling. With the use of the MC code, however, the impurity transport has been studied under fixed parameter of background plasma to date. For a consistent analysis, we are aiming at coupling of IMPMC code into a 2D divertor code (SOLDOR/NEUT2D) [3]. This task is very difficult due to a significant amount of computational time and noise in MC calculation.

When a conventional MC algorithm is employed for scattering process in velocity space, the impurity ions must be traced with a time step Δt much shorter than the slowing-down time τ_s . It follows that the MC code requires a huge amount of computational time, especially in case of detached plasma. We develop a new diffusion model using analytical solution of Langevin equations, which can significantly reduces the computational time. Its speed attains more than 100 times faster than the conventional MC method. The performance of IMPMC is further optimized on the massive parallel computer. Thereby the IMPMC is combined with a so-called divertor code, and a self-consistent modelling of divertor plasma and impurity transport is successfully achieved. The integrated code, SONIC (SOLDOR/NEUT2D/IMPMC) is characterized by treatment for kinetic effects and complicated dissociation process of methane. As initial simulations with SONIC, the dynamic evolution of X-point MARFE in JT-60U is investigated. Neutral carbons chemically sputtered from the dome in the private region can deeply penetrate into the main plasma and are subsequently ionized/recombined near the X-point. The resultant carbon ions cause large radiation during MARFE phase. The SONIC code, which contains impurity kinetic effects and consistent interactions with plasma and impurity, is expected to clarify the generation and transport of impurities, e.g. erosion and redeposition of carbon target plates.

References

- [1] Shimizu K., et al., J. Nucl. Mater. **363-365** (2007) 426.
- [2] Shimizu K., et al., J. Nucl. Mater. **220-222** (1995) 410.
- [3] Shimizu K., et al., J. Nucl. Mater. **313-316** (2003) 1277.

9. Plasma Facing Materials

9.1 Hydrogen Retention and Carbon Deposition in Plasma Facing Wall and Shadowed Area [1]

K. Masaki, T. Tanabe¹, Y. Hirohata², Y. Oya³, T. Shibahara⁴, T. Hayashi, K. Sugiyama¹,
T. Arai, K. Okuno³, N. Miya

1) Kyushu University, 2) Hokkaido University, 3) Shizuoka University, 4) Nagoya University

In order to evaluation of fuel inventory and understand its retention process, hydrogen isotope retention and carbon deposition for the plasma facing surfaces and plasma shadowed area of the JT-60U have been examined.

Poloidal profiles of erosion/deposition in the divertor region were quite non-uniform with heavy deposition in the inner divertor and the outer dome wing, while the outer divertor and the inner dome wing were erosion dominant regions. Hydrogen retention was well correlated to the carbon deposition. Under the operation with the vacuum vessel kept at 570 K, the highest hydrogen retention (H+D) of $\sim 16 \times 10^{22}$ atoms/m² was found at the redeposited layers on the outer dome wing also with the highest concentration of ~ 0.13 in (H+D)/C. For the erosion dominant region, hydrogen (H and D) was retained only in surface layers. Furthermore, D retained near surface layers was appreciably replaced by H during hydrogen operation subsequently made.

On the collector probes which were placed at the plasma-shadowed area underneath the dome with the vessel temperature of ~ 420 K, ~ 2 μ m-thick redeposited layers were found. The total amount of the redeposited carbon underneath the dome region was estimated to be ~ 0.013 kg and the deposition rate was estimated to be $\sim 8 \times 10^{19}$ C atoms/s. This redeposition rate is much smaller than that on the divertor tile surface, but a little larger than the calculated dust production rate. The hydrogen (H+D) retention in the layers was $\sim 1.4 \times 10^{23}$ atoms/m², and (H+D)/C was ~ 0.8 , which was the same level as that observed in JET. In addition, D/H in the layers (~ 3.6) was also very high compared with ~ 1 for the redeposited layers on the plasma facing wall tiles (the vessel temperature: 570 K). Those higher values of D/H and (H+D)/C in the layers on the collector probes are attributed to the lower vessel temperature.

The lower D/H in the layers on the plasma facing surface indicates that isotope exchange during tokamak discharge seems effective and DD operation after DT operation could remove significant amount of T retained in the plasma facing surface during the DT operation. However, the rather deep penetration of D observed in the depth profiles for the main chamber wall is difficult to remove. Thus hydrogen retention in the main chamber wall is very important because its surface area is huge, and more detailed examination is considered necessary to make realistic inventory evaluation.

Reference

[1] K. Masaki, et al., Nucl. Fusion **47**, 1577(2007).

9.2 Long-Term Erosion and Re-Deposition of Carbon in the Divertor Region [1]

Y. Gotoh¹, T. Tanabe², Y. Ishimoto, K. Masaki, T. Arai, H. Kubo, K. Tsuzuki, N. Miya

1) Nihon Advanced Technology, 2) Kyusyu University,

Studies on erosion/re-deposition at the plasma facing walls of fusion experimental devices are indispensable for elucidation and control of (1) impurity generation, transport and accumulation processes, (2) hydrogen isotope behaviors and long-term tritium inventories in a vacuum vessel and for (3) lifetime evaluation of divertor plates. The aim of the present study is to show poloidal profiles of erosion/redeposition in the W-shaped divertor of JT-60U, especially focusing to those on the dome area (private flux region) and the outer pumping slot.

In-out asymmetry in the erosion/redeposition was confirmed at the inner and the outer divertor tiles used in the W-shaped JT-60U during the experimental campaign from 1997 to 2002 ; erosion dominates the outer divertor tiles, whereas redeposition the inner divertor tiles with the maximum thickness of 230 μm . The poloidal distribution of the thickness of the redeposited layers on the inner divertor was very similar to that of the divertor-hit-points distribution, though the former slightly shifted to the inboard side. The erosion maximum on the outer divertor clearly shifted to the outboard side from the most frequent divertor-hit-points.

In the dome area, the opposite in-out asymmetry appeared. The inner dome was mostly eroded, while the outer dome wing tile was covered by the redeposited layers with their thickness increasing from the dome top to the bottom end of the maximum thickness of 120 μm . The redeposited layers show columnar structure. In the toroidal direction, the axes of the columns inclined towards the clock-wise direction of the torus, while poloidally towards the outer divertor side. Poloidal and toroidal distributions of the thicknesses and orientations of the columns indicate that the observed redeposition on the outer dome wing is caused by transport of carbon atoms eroded at the outer divertor tile. The inner dome wing was mostly eroded. All these observations indicate that local carbon transport toward the inboard side plays an important role on carbon redeposition processes.

Long-term net deposition of carbon in the divertor region is 0.55 kg. About 60 % of the net deposition originated from the erosion in the divertor area, while remaining 40% should be attributed to the erosion at the first wall (main chamber). Carbon redeposition rate was 9×10^{20} C/s for integrated NBI heating duration time during the experimental campaigns. The net deposition is much smaller than JET, probably owing to fine tile alignment, higher surface temperature, and divertor structure avoiding carbon transport to plasma shadowed area.

Reference

[1] Gotoh, et al., J. Nucl. Mater., **357**, 138 (2006)

9.3 Modeling of Asymmetric Redeposition Distribution between Inner and Outer Regions of W-Shaped Divertor [1]

K. Ohya¹⁾, K. Inai¹⁾, T. Tanabe²⁾, H. Takenaga

1) The University of Tokushima, 2) Kyushu University

Tritium retention is a critical problem for next-step fusion reactors with carbon plasma-facing components. In present large tokamaks, most of the hydrogen isotopes are retained in the carbon deposition layers on the components in the divertor. Recently, the deposition profile and hydrogen retention in large tokamaks were found to be dependent on the structure of the divertor, including the asymmetry between inner and outer regions. Erosion was dominant on the outer divertor plate, whereas deposition was dominant on the inner plate. Localized heavy deposition has also recently been observed in the private flux region of the W-shaped divertor in JT-60U [2,3], in which the outer dome wing plate was mostly covered by deposition. The heaviest deposition was observed on the underside of the wing that did not directly face the plasma.

We modeled true-size divertor plates and dome wings from the inner and outer regions of the W-shaped divertor in JT-60U. The erosion and redeposition patterns on the plates were calculated using EDDY [4], which treats transport of impurities released from the plates in the plasma. The code also simulates dynamic material mixing processes, which is a main difference from other impurity transport codes. Furthermore, energy-dependent reflection and dissociation of hydrocarbons on the surface was employed in addition to a well-used constant sticking coefficient of each hydrocarbon on the plate. The plasma density used for calculation was $\sim 10^{20} \text{ m}^{-3}$ above the divertor plate and the decrease along the plate was slower for the inner region than for the outer region. The ion and electron temperatures were lower for the detached inner region than for the attached outer region; at a major part of the inner plate, both temperatures were $\sim 1 \text{ eV}$, whereas for the outer plate the ion and electron temperatures were 5 eV and 10 eV , respectively, which increased with the distance toward the outer baffle.

Hydrocarbons released from the outer divertor plate are immediately ionized when entering the plasma and are redeposited near the release position. But they are subjected to re-erosion by the successive bombardment of plasma ions, resulting in small effective sticking. On the whole, most area of the outer divertor plate are eroded agreeing with observed distributions of erosion depth. In contrast, the inner divertor plate is dominated by deposition and the observed poloidal distribution of the thickness of the redeposited carbon layers agrees with incoming carbon flux from the plasma without re-erosion owing to lower temperature. Due to much lower-temperature ($\sim 1 \text{ eV}$) of the private plasma in the outer region, the neutral carbon/hydrocarbon species are locally redeposited at the bottom edge of the outer dome wing adjacent to the bottom of the outer divertor plate.

References

- [1] K. Ohya, et al., J. Nucl. Mater., **363-365**, 78(2007).
- [2] Y. Gotoh, et al., J. Nucl. Mater. **313-316**, 370(2003).
- [3] Y. Gotoh, et al., J. Nucl. Mater. **357**, 138(2006).
- [4] K. Ohya, Physica Scripta T124, 70(2006).

9.4 Transport of Carbon Impurity using $^{13}\text{CH}_4$ Gas Puffing

Y. Nobuta, K. Masaki, T. Arai, A. Sakasai, N. Miya, T. Tanabe¹

1) Kyusyu University, Interdisciplinary Graduate School of Engineering Science, Department of Advanced Energy Engineering Science, 6-10-1, Hakozaki, Higashi-ku, Fukuoka 812-8581

1. Introduction

Carbon material is a candidate for the divertor target plate of ITER because of its low atomic number and good thermal properties, while the main concern of carbon as a plasma facing material is to retain a large amount of hydrogen isotopes by co-deposition and high erosion rate by energetic hydrogen bombardment. The carbon deposition and the erosion would drastically increase tritium inventory in the vacuum vessel and decrease the lifetime of the divertor target plate on ITER, respectively. In many tokamaks, an appreciable asymmetry of deposition/erosion between inner and outer divertor has been observed; the inner divertor is deposition dominated and the outer divertor erosion dominated.

In JT-60U, to clarify carbon transport causing such in/out asymmetry in the divertor area, $^{13}\text{CH}_4$ gas puff experiments were carried out in Nov. 2004, in which $^{13}\text{CH}_4$ gas was puffed into outer divertor SOL plasmas and poloidal distributions of ^{13}C deposited on dome and divertor tiles at P-8 section were investigated previously [1]. Recently, the toroidal distribution of ^{13}C has been analyzed. Here, the carbon transport in divertor area is discussed based upon these results.

2. Experimental

The $^{13}\text{CH}_4$ gas puffing experiments were conducted at the last day of the 2004 experimental campaign to avoid the effects of following plasma discharges on the distribution of ^{13}C deposition. Figure 1 shows the toroidal position of the $^{13}\text{CH}_4$ gas puffing nozzle (Fig.1 (a)) and the poloidal position of the nozzle located at P-8 section (Fig.1 (b)). In order to introduce the $^{13}\text{CH}_4$ gas into the outer SOL plasmas, the outer separatrix position was positioned at poloidally a little inboard side from the nozzle position. L-mode plasmas were used for the experiment in order to avoid the deposition due to ELM. The total of $\sim 2 \times 10^{23}$ $^{13}\text{CH}_4$ molecules were puffed into the L-mode plasmas of $I_p = 1.0$ MA and $B_T = 2.5$ T. The duration of NBI heating in a discharge was about 30 seconds and 13 plasma discharges were repeated under the similar condition. After the $^{13}\text{CH}_4$ gas puffing experiment, a total of 30

tiles in P-8 and P-5 (toroidally 60° apart from P-8) sections were extracted. Depth profiles of ^{13}C deposited on the tiles were obtained by using Quadrupole SIMS (ADEPT-1010, Ulvac-Phi). The ^{13}C areal density was evaluated by integrating the intensity ratio ^{13}C and ^{12}C and assuming the bulk density of the deposition layers to be 0.91 g/cm^3 in the present work [2].

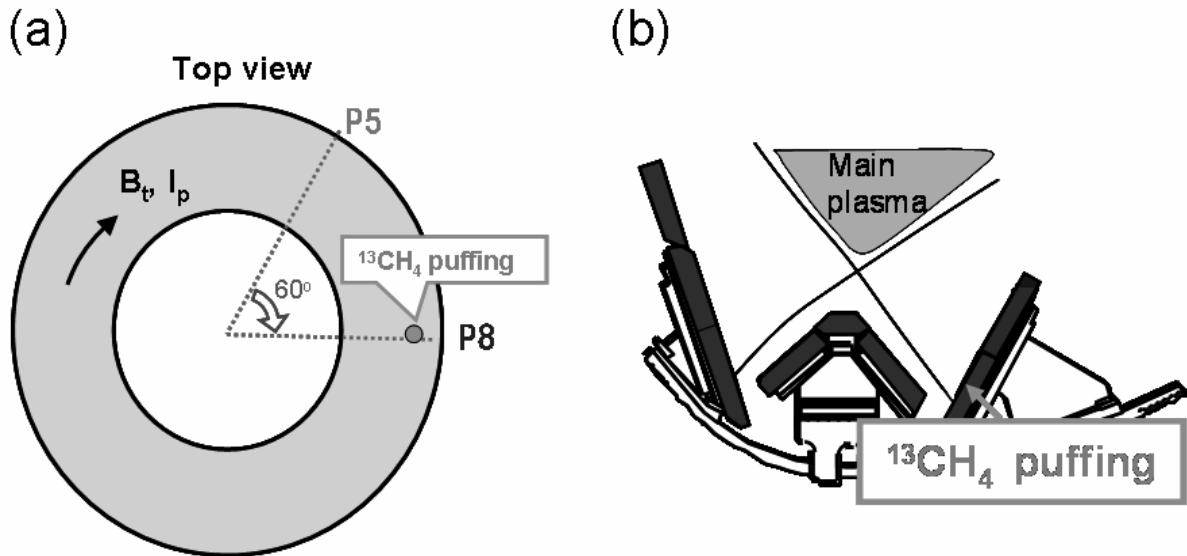


Fig.1 (a) Toroidal position of the $^{13}\text{CH}_4$ gas puffing nozzle in P-8 section and (b) poloidal position of the nozzle. The nozzle was positioned a little outboard side from the outer separatrix.

3. Results and discussion

Figure 2 shows the poloidal distribution of ^{13}C deposited on the tiles in P-8 section [1]. The peak position of the ^{13}C distribution on the outer divertor tile well corresponds to the peak frequency of the strike point. The ^{13}C deposition on the inner and outer dome-wing tiles had the deposition profile sharply decreasing to the dome top. This result indicates that the ^{13}C particle flux to the dome-wing tile surface decreases toward the dome top and/or the ^{13}C

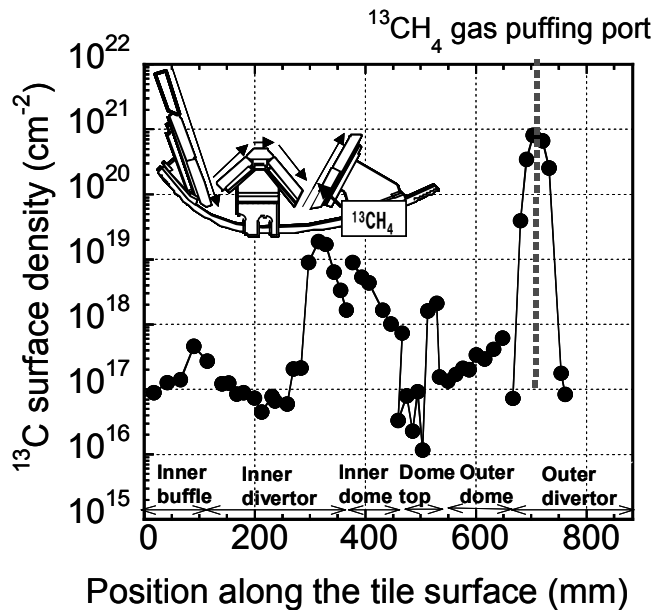


Fig.2 Poloidal distribution of ^{13}C deposited on the tiles in P-8 section [1].

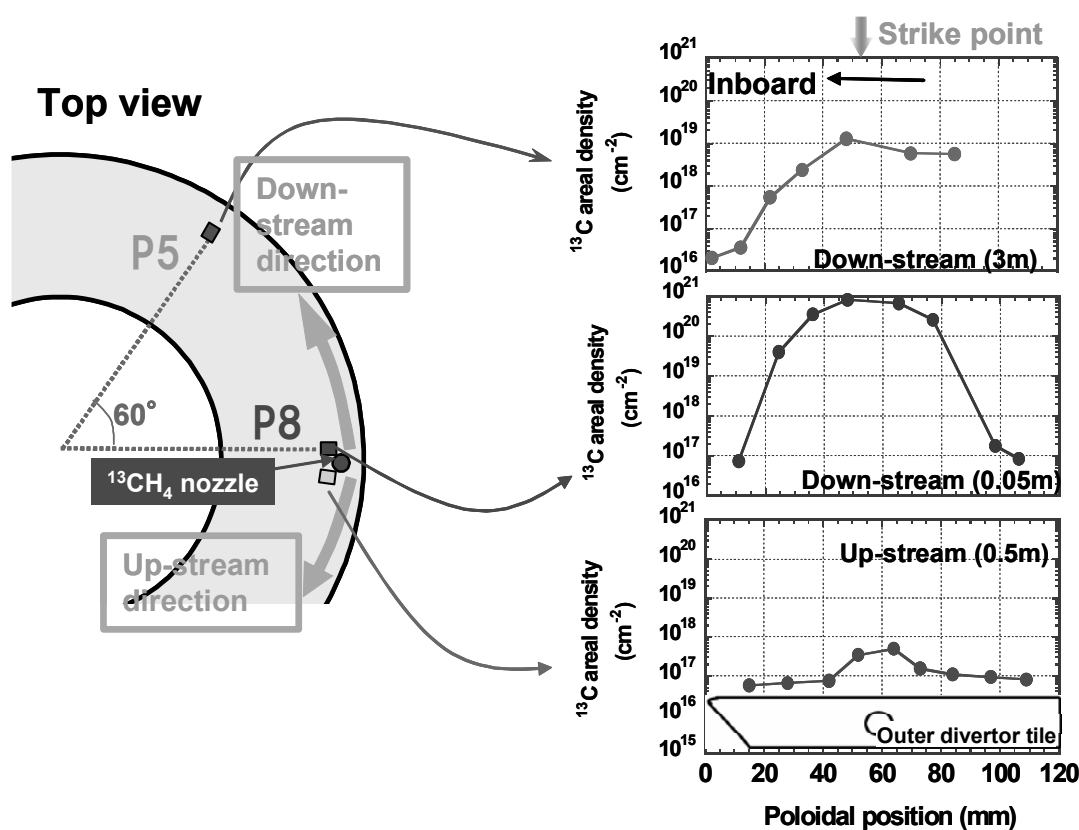


Figure 3 Toroidal positions of outer divertor tiles used for analysis and ^{13}C gas puffing nozzle (left), and poloidal distribution of ^{13}C deposited on the outer divertor tiles in P-8 and P-5 sections (right).

deposited near the dome top is re-eroded by energetic hydrogen bombardment. It is reported that the inner dome-wing tile is erosion-dominated area in the case of general discharge experiments [3]. However, the ^{13}C deposition on the inner dome-wing tile was clearly seen after the $^{13}\text{CH}_4$ gas puffing experiment. An average interval between the inner dome-wing tile and the outer separatrix during the $^{13}\text{CH}_4$ gas puffing experiment was larger than that of general discharge experiments. This might be one of the reasons that the ^{13}C deposition on the inner dome-wing tile occurred.

Figure 3 shows the poloidal distribution of ^{13}C deposited on the outer divertor tiles located at P-8 and P-5 sections. In the outer divertor region, a large amount of ^{13}C was deposited on the tiles located at down-stream from the $^{13}\text{CH}_4$ puffing nozzle, whereas little amount of ^{13}C on the tiles located at up-stream. The ^{13}C areal density at the strike point was $\sim 1 \times 10^{19} \text{ cm}^{-2}$ on the tile located 3 meters away from the nozzle in down-stream direction and $\sim 5 \times 10^{17} \text{ cm}^{-2}$ 0.4 meters away in up-stream direction. This result would be caused by ionization of $^{13}\text{CH}_4$ molecules and a SOL plasma flow in the outer divertor region.

Figure 4 shows the poloidal distribution of ^{13}C deposited on the inner divertor tiles in P-8 and P-5 sections and the frequency of strike point during $^{13}\text{CH}_4$ gas puffing. ^{13}C was also

transported to the inner divertor tiles suggesting long-range transport through SOL. However, the poloidal deposition profile peaked at a little outboard side from the most frequent strike points [1]. This suggests an alternative carbon transport path through the private flux region. There was a large difference in the amounts of ^{13}C deposition between the two inner divertor tiles which located three meters away each other. A location of the source of carbon impurities in the outer divertor region might have a relation with a location where the carbon is re-deposited in the inner divertor region.

4. Conclusion

The carbon transport generated on the outer divertor region has been investigated using the $^{13}\text{CH}_4$ gas puffing in JT-60. On the surface of the inner and outer dome tiles, the ^{13}C areal density rapidly decreased towards the dome-top. This result indicates the ^{13}C flux to the dome-wing tiles surface decreases toward the dome top and/or the ^{13}C deposited near the dome top is re-eroded. The poloidal distribution of the ^{13}C areal density on the inner divertor tiles had a peak at a little outboard side of the inner strike point. It might be caused by a transport through the private flux region. In the outer divertor region, ^{13}C was deposited only in the down-stream direction indicating ^{13}C ion particles are transported to down-stream by a plasma flow. To investigate the carbon transport more closely, ^{13}C deposition in the gap of the divertor and dome-wing tiles will be analyzed.

References

- [1] Y. Ishimoto et al., "Transport of carbon impurity using $^{13}\text{CH}_4$ gas puffing in Jt-60U", submitted in J. Nucl. Mater.
- [2] Y. Ishimoto, et al., J. Nucl. Mater., **350**, 301 (2006).
- [3] Y. Gotoh, et al., J. Nucl. Mater., **357**, 138 (2006).

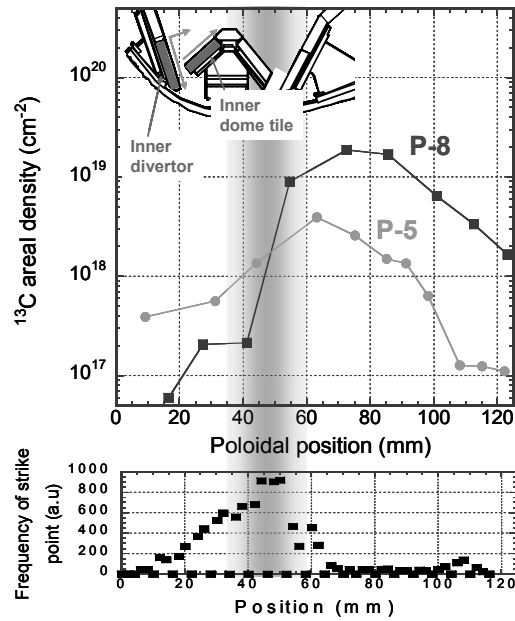


Fig.3 Poloidal distribution of ^{13}C deposited on the inner divertor tiles in P-8 and P-5 section (upper) and frequency of strike-point during $^{13}\text{CH}_4$ gas puffing (below).

9.5 Distribution of Hydrogen Isotopes Retained in the Divertor Tiles

Y. Hirohata¹⁾, T. Tanabe²⁾, Y. Oya³⁾, K. Shibahara⁴⁾, M. Oyaidzu³⁾, K. Sugiyama²⁾,
A. Yoshikawa³⁾, T. Arai⁵⁾, K. Masaki⁵⁾, Y. Gotoh⁵⁾, K. Okuno³⁾, N. Miya⁵⁾

1) Hokkaido University, 2) Kyushu University, 3) Shizuoka University, 4) Nagoya University,
5) JAEA

It is a very important issue to evaluate retention properties of tritium and deuterium in in-vessel components of current devices from a viewpoint of safety for the next fusion reactor. In this study, distribution of hydrogen and deuterium retained in plasma facing surface and plasma shadowed surfaces of the graphite tiles used in the divertor region of JT-60U with the dual side pumping system was investigated by thermal desorption spectroscopy (TDS) and secondary ion mass spectroscopy (SIMS). All tiles were exposed to 6700 deuterium and hydrogen discharges, except those of the outer wing and the top of the dome unit (2400 discharges), for June 1997-October 1999 experiment period. Erosion was dominant in the outer divertor region and the inner dome wing of the dome unit while redeposition in the inner divertor region and the outer dome wing.

We found that deuterium retained in the near surface of all tiles was replaced by hydrogen during HH discharges made for tritium removal after DD discharge campaign. The D/H ratios in the tile were different depending on the location, i.e., 0.4~0.3 for the inner divertor tile, ~1.0 for the outer dome wing tile and ~0.08 for the outer divertor and other dome unit tiles [1], and was much smaller compared to the ratio of shots numbers of DD and HH discharges (~5.6). Such small D/H ratio is attributed to lower surface tile temperatures during HH discharges than that during DD discharge. The amount of retained hydrogen isotopes (H,D) was nearly proportional to the thickness of the carbon redeposited layers. Assuming homogeneous hydrogen distribution in the redeposited layers and carbon density of 0.9 g/cm³, (H+D)/C in the redeposited layers was determined from the linear relationship. The least concentration of (H+D)/C (~0.02) was found in the redeposited layers on the inner divertor tile. This value agrees well with H/C of ~0.03 observed for the redeposited layers on the divertor tiles exposed to HH discharges in the JT-60 [2], and (H+D)/C of ~0.032 in the inner divertor tiles exposed to the DD discharges in the JT-60U with the inner side pumping system [3]. The highest concentration of ~0.13 in (H+D)/C was found in the redeposited layers on the outer dome wing tile shadowed from plasma and facing to the pumping slot. In JT-60U, however, the carbon deposition in the shadowed area is very small, resulting in a smaller total retention in the divertor area compared to other large tokamaks.

References

- [1] Hirohata Y., et al., J.Nucl.Mater., **367-370**, 1260 (2007).
- [2] Shibahara T., et al., Nucl. Fusion, **46**, 841 (2006).
- [3] Shibahara T., et al., J.Nucl.Mater., **357**, 115 (2006).

9.6 Hydrogen Isotope Behavior in the First Wall after DD Discharge [1]

Y. Oya¹⁾, Y. Hirohata²⁾, T. Nakahata¹⁾, T. Suda¹⁾, M. Yoshida³⁾, T. Arai⁴⁾, K. Masaki⁴⁾, K. Okuno¹⁾ and T. Tanabe³⁾

1) Shizuoka University, 2) Hokkaido University, 3) Kyushu University, 4) JAEA

Tritium retention in in-vessel components is one of critical safety issues for future fusion reactor. Recently, the evaluation of retention characteristics of hydrogen isotopes including tritium in the divertor area of JT-60U has been extensively performed. Owing to higher temperature operation of the vacuum vessel of JT-60U, the total hydrogen (H+D) retention in divertor region was smaller than those observed in other tokamak machines. It was found that hydrogen retention in each tile varied significantly depending on the tile location, and was clearly correlated to the thickness of the redeposition layers. Therefore in order to understand overall hydrogen isotope behavior in in-vessel components, hydrogen retention in the first wall should be examined. In this study, typical first wall tiles in JT-60U were picked up and surface morphology, erosion/deposition profiles and hydrogen isotope retentions were evaluated by scanning electron microscope (SEM), X-ray photoelectron spectroscopy (XPS), thermal desorption spectroscopy (TDS) and secondary ion mass spectrometer (SIMS).

It was found that the upper area of the first wall was covered by thick boron layers containing only 10% of carbon and D desorption from the layers started at lower temperatures than that from the redeposited carbon layers on the inner divertor. Hence most of D retained in the upper area were likely originated from boronization.

On the other hand, the lower part of the first wall was covered by thin mixed layers of carbon and boron. Accordingly, D desorption temperature was a little higher than that for the upper area but lower than hydrogen implanted in graphite. Hence it is difficult to decide whether boron in the layer is deposited or originated from boronization.

D/H ratio in the first wall was appreciably higher than that observed in the divertor tiles. The lower temperature of the first wall than that of the divertor tiles would prohibit desorption of D retained in the layers and/or replacement of D by H during HH discharges subsequently made after DD discharges. The injection of high energy deuteron originating from NBI into the first wall could have some contribution on the high D/H ratio.

Reference

[1] Oya, Y., et al., Fusion Science and Technol., **52**, 554(2007).

9.7 Deuterium Depth Profiling in JT-60U Tiles Using the $D(^3\text{He}, p)^4\text{He}$ Resonant Nuclear Reaction [1]

T. Hayashi, K. Sugiyama¹⁾, K. Krieger²⁾, M. Mayer²⁾, V. Kh. Alimov³⁾, T. Tanabe¹⁾, K. Masaki,
N. Miya

1) Kyushu University, 2) Max-Planck-Institut für Plasmaphysik, Germany

3) Institute of Physical Chemistry of the Russian Academy of Sciences, Russia

In a previous work, we have performed a quantitative NRA analysis of deuterium retained in the graphite tiles of JT-60U. The depth profile given by NRA using the 350keV deuterium beam was limited within 2 μm from the surface [2], which was not thick enough to discuss deuterium retention in detail. Therefore, the deuterium depth profile in deeper regions should be investigated in order to understand the plasma-wall interaction in more detail. In the present study, we have made a quantitative depth analysis of deuterium in plasma-facing graphite tiles by means of the $D(^3\text{He}, p)^4\text{He}$ resonant nuclear reaction. The maximum depth which can be analyzed is about 14×10^{23} carbon atoms/ m^2 corresponding to 16 μm for graphite of 1.7 g/cm^3 .

The deuterium retention in tiles covered with redeposited carbon layers was high. In the divertor region, the high D/C of 0.07 was found in the outer dome wing tiles, but their D/C decayed rapidly with the depth corresponding to the thickness of the redeposited layers. In the thick redeposited layers on the inner divertor (ID) target tile, the depth profile shows a broad peak of D/C~0.03 and shows nearly constant concentration well beyond the present analyzing depth. This indicates that the trapped D in the shallow region was removed by H discharges due to isotope exchange.

In the case of the outer divertor target (OD) where redeposited layers were not observed, the D/C ratio was very low (<0.003) even near the surface. This can be attributed to the highest temperature of OD, ~1400 K, compared to that of ID (~1000 K). It is also notable that deuterium penetrates quite deep, though the concentration was quite low, suggesting molecular deuterium uptake in deeper region owing to high temperature.

Depth profiles of the first wall tiles, where some carbon particles were accumulated along with deuterium, show D was trapped in the near surface region with high concentration but decayed rapidly with the depth. In JT-60U, NBI heating was conducted during plasma discharges. The energetic deuterons injected by NBI escaped from plasma and impinged into the first wall region. It is most likely that D was accumulated due to both co deposition with carbon and the implantation of energetic deuterons caused by deuterium NBI in the first wall region. The highest D/C ratio of JT-60U was found to be 0.09 in the first wall region, which is higher than that of the divertor region due to the lower temperature.

References

- [1] T. Hayashi, et al., J. Nucl. Mater., **363-365**, 904 (2007).
[2] T. Hayashi, et al., J. Nucl. Mater., **349**,6(2006).

9.8 Ion Beam Analysis of H and D Retention in the Near Surface Layers of Plasma Facing Wall Tiles

K.Sugiyama¹⁾, T. Hayashi, K. Krieger²⁾, M. Mayer²⁾, K. Masaki, N. Miya and T.Tanabe¹⁾

1) Kyushu University, 2) Max-Planck-Institut für Plasmaphysik

Hydrogen retention characteristic in plasma facing material is a critical issue for the accumulation and removal of in-vessel tritium in next step reactors. JT-60U employs regularly deuterium discharges (DD discharges), and occasionally hydrogen discharges (HH discharges) before the vacuum vessel open to remove tritium generated by D-D discharges and retained in the plasma facing surface. Thus, study of both hydrogen (H) and deuterium (D) retention properties gives important information to understand the fuel retention mechanism. In this study, absolute amounts of H and D and their depth profiles in the near surface layers of the plasma facing carbon tiles were measured by means of Elastic Recoil Detection (ERD) analysis.

The samples were selected from the W-shaped divertor tiles (Carbon Fibre Composite) used from Jun. 1997 to Oct. 1998 (~ 3600 DD discharges), and the first wall tiles (graphite) used during Jun. 1991 to Oct. 1999 (more than 15000 DD discharges). In both cases, HH discharge operation was done before the tile removal: about 300 discharges in Oct. 1998 and about 350 discharges in Oct. 1999. The ERD analysis was conducted at Max-Planck-Institut für Plasmaphysik (IPP) with using 3.0 MeV $^4\text{He}^+$ beam obtained from a 3 MV tandem accelerator. The depth profiles of H and D were determined from the ERD spectra by using the SIMNRA program [1].

It was shown that H was dominantly retained within 1 μm depth. However, the depth profiles of H and D varied depending on the location of the tiles reflecting the incident energy of H and D and history of plasma exposures. The H profile of the erosion-dominant sample was peaked at the top surface and decreased with depth, while D was depleted at the top surface and increased with depth to attain a nearly constant concentration. Significant depletion of D at the top surface was attributed to the replacement by H during HH discharges. This indicates that tokamak discharge itself is effective for removal of the tritium retained in the erosion-dominant surface. The deposition-dominant sample kept constant H content into deep in the layer, indicating the HH discharges added deposited layer containing H on the deposited layer produced during the DD discharges.

(H+D)/C ratios were not very much high: it was ~ 0.07 at a maximum in the divertor samples except for the deposition on the dome outer wing tile, which was ~ 0.13. And it was ~ 0.15 at a maximum in the first wall samples. These values are smaller in comparison to D/C ratios reported in other tokamaks (up to 1.0). Previous laboratory experiments show that H/C ratio decreases with temperature increasing. For example, H/C in hydrogen saturated carbon layers at 600 and 700K are around 0.2 and 0.1, respectively. JT-60U was operated with 570 K base baking temperature and the temperature during a discharge could be higher (up to ~1100 K on the divertor tiles). Such high wall temperature contributes to reduce (H+D)/C in JT-60U compared to other tokamaks.

This work was carried out under the framework of JAEA - IPP collaboration.

Reference

[1] M. Mayer, SIMNRA User's Guide, Tech. Report IPP 9/113, Max-Planck-Institut für Plasmaphysik

9.9 Surface Studies of Tungsten Erosion and Deposition [1]

Y. Ueda¹⁾, M. Fukumoto¹⁾, M. Nishikawa¹⁾, T. Tanabe²⁾, N. Miya, T. Arai, K. Masaki,
Y. Ishimoto, K. Tsuzuki, N. Asakura

1) Osaka University, 2) Kyushu University

Tungsten is a leading candidate for plasma facing materials, i.e. divertors and armor materials of blanket first walls, due to a low physical sputtering yield, a high melting temperature, and a high thermal conductivity. On the other hand, accumulation of tungsten ions in core plasmas is a major concern. Therefore, reduction of tungsten erosion and accumulation is one of the important issues to prove compatibility of tungsten walls with high performance plasma operation. In terms of high Z wall experiments, ASDEX-U and Alcator-C Mod have provided important results. Plasma temperature and confinement of these devices, however, are quite different from those of ITER. Therefore, it is not sufficient to use their experimental results for the evaluation of tungsten divertor performance in ITER and DEMO.

For this purpose, tungsten erosion, migration and deposition have been studied in JT-60U. Thirteen W tiles have been installed in the outer divertor region and tungsten deposition on graphite tiles were measured by EDX (Energy Dispersive X-ray spectroscopy) and XPS (X-ray Photoelectron Spectroscopy). On the inner divertor tile, tungsten was mainly deposited around the inner strike position ($\sim 10^{18}$ atoms/cm²), similar to the ASDEX-U[2]. This suggests that tungsten transport from the outer divertor to inner divertor (especially around the strike position) is common phenomenon for divertor tokamaks. In addition, similar amount of tungsten deposited on the outer wing tiles of the dome and the tungsten deposition increased toward the lower end of the tile. This tungsten transport could be attributed to inward drift of tungsten ions in a private region or direct deposition of eroded tungsten atoms from the tungsten tiles during disruption or some other abnormal events.

By comparing deposition profiles of tungsten with ¹³C, puffed as ¹³CH₄ from the outer divertor position, deposition profiles showed similar tendency such that ¹³C and tungsten depositions had a peak around inner strike position and their surface densities on the outer wing increased toward the lower end of tiles (there is an evacuation slot). The ratio of tungsten deposition to ¹³C deposition, however, is higher on the outer wing tile than the inner divertor tile by about an order of magnitude at the same toroidal section as tungsten tiles were installed. The possible reasons are lower resputtering of deposited tungsten than deposited carbon on the outer wing tile or higher tungsten deposition rate on the outer wing tile. This is very important finding to understand migration mechanism of impurities generated at the outer divertor.

References

- [1] Y. Ueda, et al., *J. Nucl. Mater.*, **363-365**, 66(2007).
[2] K. Krieger et al., *J. Nucl. Mater.*, **241-243**, 734(1997).

9.10 Light Elements Behavior in Fusion Devices Studies with JT-60 and Oxygen Discharge

S. Konishi¹, H. Nakamura, K. Isobe, Y. Yamamoto¹, A. Kaminaga

1) Kyoto University

Control of tritium inventory in Tokamak vacuum vessel is one of the most important safety issues in ITER. Following the analysis of exhaust of discharge cleanings, we concluded the mechanism of co-deposit formation, that is suspected to be mainly controlled by carbon behavior during tokamak discharge. Also for the processing of co-deposit, introduction of oxygen into the vacuum vessel that has never been attempted in operating large tokamaks is expected to be effective. Moreover in general, the transport of the light elements and techniques to control material transport in terms of fusion reactor operation is important.

Fig.9.1 is the comparison of hydrocarbon species exhausted from the wall at 150 and 250°C. The clear increase of carbon removal at higher wall temperature 250°C is understandable from reported enhanced sputtering yield at higher temperature, 110°C : 170°C : 290°C = ~0.3 : 0.5~0.6 : 1 by Nakano et al. [1], but enhancement is far larger than it. One of the possible explanation is the reduction of redeposition of hydrocarbon caused by the difference of the surface temperature, that could also be suspected as the cause of difference of co-deposit in JT-60 and JET.

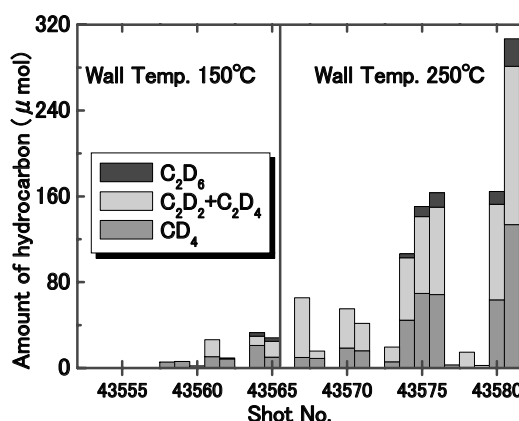


Fig.9.1 Exhaust of JT-60 tokamak discharge.

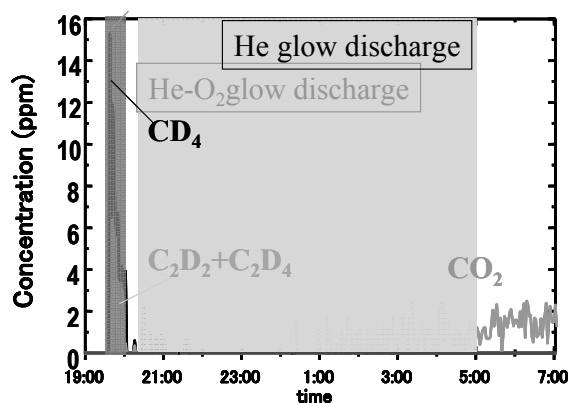


Fig.9.2 Oxygen glow discharge in JT-60.

Fig.9.2 shows the exhaust gas from the He-O₂ GDC 20 min., and following one night He GDC. As seen in the figure, hydrocarbons are detected in the first 20 min. discharge for both cases. The removal rate in He-O₂ GDC was approximately twice as much as that in the He GDC. In the following He-GDC, and continuous CO₂ emission is observed for the case after the He-O₂ GDC. Although only one preliminary result is available, He-O₂ GDC enhances carbon removal as the form of CH₄, by oxygen used as catalyst.

Reference

[1] T.Nakano et al , Nucl Fusion, **42**, 689(2002) .

10. Diagnostics

10.1 Modulation CXRS

K.Ida¹⁾, Y.Sakamoto, M.Yoshinuma¹⁾, S.Inagaki¹⁾, T.Kobuchi²⁾, G.Matsunaga, and JT-60 team
National Institute for Fusion Science, 2) Chubu University

The new technique to measure the first and second derivative of ion temperature profile has been developed using the charge exchange spectroscopy system with space modulation optics. The space observed is scanned up to 6cm (full width) with sine wave of modulation frequency up to 30Hz by shifting the object lens in front of the optical fiber bundle by 0.5mm using Piezo nano-translation stage. By scanning the observation point with this modulation optics, the radial points of the measurement can be multiplied by $M [= f_{\text{ccd}}/(2f_m)]$ if the plasma is in steady state, where f_{ccd} is frame rate of CCD detector of the spectrometer and f_m is a modulation frequency of Piezo stage. By choosing $f_{\text{ccd}} = 200\text{Hz}$ and $f_m = 10\text{Hz}$, the radial profile of ion temperature with 310 points are obtained every 50ms. In order to derive the first and second derivative of ion temperature from the modulation component of the time evolution of the ion temperature, Fourier analysis technique has been developed[1].

This technique gives a direct measurement of first and second derivative of ion temperature which does not require any assumption of fitting function, which causes significant ambiguity of the estimates of first and second derivative. For example the modified hyperbolic tangent often used to represent radial profile of ion temperature at the transport barrier can not represent asymmetric profile of first and second derivative. This technique will provide significant impact in the transport analysis, because temperature gradient and its error bar are directly derived. Moreover the radial profiles of second derivative (curvature) in the region of internal transport barrier (ITB) are measured with modulation charge exchange spectroscopy. In order to characterize the shape of ITB, the curvature asymmetric factor of $\zeta_p [= \langle dT_i^2/dr^2 \rangle / \langle |dT_i^2/dr^2| \rangle]$, where $\langle \rangle$ is the average in the region of ITB is introduced. This parameter indicates whether the ion temperature profile has positive or negative or zero curvature averaged in the ITB region. The ITB with zero averaged curvature is called symmetric curvature ITB, while the ITB with significant positive or negative averaged curvature is called asymmetric curvature ITB. In JT-60U, when the ITB region is wide and the temperature gradient is moderate, the ITB has symmetric curvature. However, the strong ITB with large temperature gradient in narrow region shows the asymmetry of curvature. (The change in curvature has been recognized as clear foot ITB and unclear foot ITB.) The spontaneous transition between the two ITB states with symmetric ($\zeta_p \sim 0$) and asymmetric ($\zeta_p = -0.4$) curvature of ion temperature is observed during the steady state phase in q profile in JT-60U[2].

References

- [1] Ida, K., submitted to Rev. Sci. Instrum.
[2] Ida, K., submitted to Phys. Rev. Lett.

10.2 Application of Phase Conjugate Mirror to Thomson Scattering Diagnostics [1]

T. Hatae, M. Nakatsuka¹⁾, H. Yoshida¹⁾, O. Naito

1) Osaka University

A high-performance phase conjugate mirror based on stimulated Brillouin scattering (SBS-PCM) has been applied to the Thomson scattering system in the JT-60U tokamak for the first time in order to improve the measurement performance (i.e. S/N ratio, temporal resolution). An SBS-PCM realized a high reflectivity of 95 % at a high input power of 145 W (2.9J, 50Hz). Using the SBS-PCM, two methods have been developed to increase the intensity of scattered light. For the first method, we have developed a new optical design to provide a double-pass scattering method with the SBS-PCM. In this optical design, a laser beam passing through the plasma is reflected by the SBS-PCM. The reflected beam passes the plasma again along the same path by means of the phase conjugation of the optically nonlinear stimulated Brillouin scattering process. Therefore, scattering events of 2 times occur, and it is expected that intensity of Thomson scattered light doubles. A double-pass Thomson scattering method using the SBS-PCM was demonstrated in JT-60U ohmic plasmas, resulting in an increase of the scattered light by a factor of 1.6, and the reduction of relative error by 66% for electron temperature measurement in contrast to single-pass scattering. A multi-pass Thomson scattering method in which the laser beam can be confined between a couple of SBS-PCMs is also proposed. It is estimated that the multi-pass scattering method generates the scattered light more than several times as large as that of the single-pass scattering method. For the second method, a high average-power YAG laser system has been developed using the SBS-PCM. The SBS-PCM effectively compensated thermal degradation at two amplifier lines, and the average power was increased by a factor of > 8 from 45 W (1.5J, 30Hz) to 373 W (7.46J, 50Hz). Based on the JT-60U laser design, conceptual design of a laser system (5J, 100Hz) with dual amplifier lines has been carried out for ITER edge Thomson scattering system. The design of combination of two beams is changed from JT-60U laser design. A circular beam is converted to an elliptic beam by a pair of cylindrical lenses. A mask having two circular holes makes two circular beams from the elliptic beam. Each beam is double-pass amplified using the SBS-PCM, and then extracted by a polarizer. There is a geometrical similarity between two beams extracted with the polarizer and two beams made with the mask, and this similarity is automatically produced by the phase conjugate effect. Therefore, this design is possible to realize alignment free-operation for combination of two beams.

Reference

[1] Hatae, T., et al., Rev. Sci. Instrum. **77**, 10E508 (2006).

10.3 Development of Polarization Interferometer Based on Fourier Transform Spectroscopy for Thomson Scattering Diagnostics [1]

T. Hatae, J. Howard¹⁾, Y. Hirano²⁾, O. Naito, M. Nakatsuka³⁾ and H. Yoshida³⁾

1) Australian National University, 2) National Institute of Advanced Industrial Science and Technology, 3)Osaka University

Recently, the use of a polarization interferometer based on Fourier transform spectroscopy for Thomson scattering diagnostics has been proposed [2]. It is possible that this method alleviate some of the disadvantages of conventional grating spectrometers. Furthermore, this method delivers a simple and compact system. We are developing the polarization interferometer for Thomson scattering diagnostics with YAG laser to demonstrate the proof-of-principle. For thermal electrons, the optical contrast of the interferogram with the Thomson scattered light at an appropriately chosen optical path delay, is a unique function of T_e and n_e using the polarization interferometer. A schematic of the polarization interferometer for Thomson scattering diagnostics is shown in Fig. 1. Scattered light is collected and introduced to the polarization interferometer through a fiber-optic bundle. The polarization interferometer consists of an objective lens as the fiber coupling optics, a band pass filter, a polarizer, a birefringent plate which gives optical path delay, a Wollaston prism, an imaging optics to detector, and dual APD (silicon avalanche photodiode) detectors. Dual APD detectors simultaneously observe both in-phase and anti-phase interferogram. The normalized intensity of the optical contrast which is a difference between in-phase and anti-phase interferograms gives a direct measure of T_e . Since proof-of-principle tests will be carried out in TPE-RX using the existing YAG laser Thomson scattering system before experiments in JT-60U, parameters for design of a prototype polarization interferometer are fixed as follows: $T_e \leq 1$ keV, $n_e \geq 5 \times 10^{19} \text{m}^{-3}$, scattering angle 90° . In an initial test using a blackbody radiation source, the magnitude of the change in fringe visibility agrees with the numerical calculation. This result confirms that, following suitable calibration, we will be able to sense visibility changes due to changes in the electron temperature.

References

- [1] Hatae, T., et al., Plasma Fusion Res. **2**, S1026 (2007).
 [2]Howard, J., Plasma Phys. Control. Fusion **48**, 777 (2006).

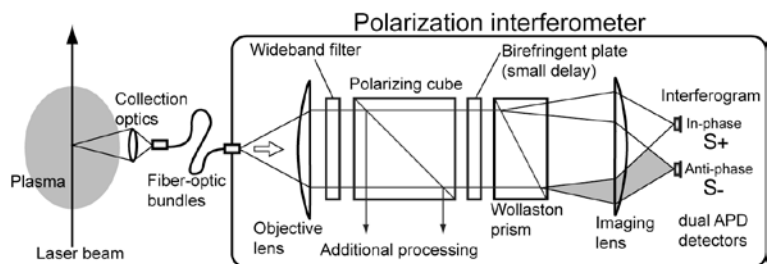


Fig. 1 Schematic of a polarization interferometer for Thomson scattering diagnostics.

10.4 Development of Fast Measurement System of Neutron Emission Profile Using a Digital Signal Processing Technique

M. Ishikawa, T. Itoga¹⁾, T. Okuji¹⁾, M. Nakhostin¹⁾, K. Shinohara, M. Baba¹⁾, T. Nishitani

1) Tohoku University

A measurement of neutron profile is of great importance for the knowledge of the profile of fusion power and the source of α -particles in burning plasmas and can also be used for plasma transport study in DD plasmas. Therefore, neutron emission profile measurement is one of the key diagnostics in ITER. In JT-60U Tokamak, neutron emission profile measurement has been performed using Stilbene neutron detectors (SNDs), which have been installed in the six channel neutron collimator system. The SND combines a Stilbene organic crystal scintillation detector (SD) with an analog n- γ pulse shape discrimination (PSD) circuit for elimination of γ -ray events. The SND has many advantages as a neutron detector, for example, excellent energy resolution and high gamma-ray suppression. So far, neutron emission profile measurement has played an important role in analysis of fast ion transport due to MHD instabilities such as Alfvén Eigenmode in JT-60U. However, the maximum count rate is limited to $\sim 1 \times 10^5$ cps due to the dead time in the n- γ DSP circuit. Such a maximum count rate is not enough in ITER experiments. Because the maximum count rate of neutron detectors of the neutron emission profile measurement in ITER is needed over 10^6 cps in order to meet the required 10 % accuracy. Therefore, upgrade of the maximum count rate of neutron detectors is one of important issues for ITER.

To overcome this issue, we have developed a digital signal processing (DSP) system for a SD, which will replace the analog PSD system. Our new DSP system is based on a Flash ADC (Acquis DC282, 8 G sampling/s). The data acquisition of this system is carried out as follow. Output signals from the photomultiplier anode of the SD are directly coupled to the Flash ADC and digitized continuously. After the acquisition is completed, the data are transferred to the PC via PCI Bus (133MB/s). In the PC, PSD between neutrons and gamma-rays is performed using an analyzing software. Then, one channel of the DSP system was installed in JT-60U and was applied for neutron measurement. It was found that the system could measure neutrons without saturation in count rate up to about 10^6 cps and also could measure changes in neutron energy spectrum due to changes in plasma condition. We are now developing the neutron profile measurement system combined with the DSP system and the conventional analog DSP system for more detailed analysis of fast ion transport.

This work is supported by Grant-in-Aid for Scientific Researches on Priority Areas from Ministry of Education, Culture, Sports, Science and Technology (No. 17044009)

Reference

[1] Ishikawa, M., et al., Rev. Sci. Instrum **77**, 10E706 (2006).

10.5 Density Fluctuation Measurement Using Motional Stark Effect Optics [1]

T. Suzuki, T. Fujita, N. Oyama, A. Isayama,
G. Matsunaga, T. Oikawa, N. Asakura, M. Takechi

MHD activities usually appear in high-pressure tokamak plasmas, and limit the performance of the plasmas. Detailed measurement of the spatial structure of the fluctuations induced by an MHD activity helps us to understand the nature and characteristics of the MHD activity. Thus, the motional Stark effect (MSE) diagnostic system has been modified to measure density fluctuation profile as a beam-emission spectroscopy (BES) diagnostic. By fast sampling (0.5-1 MHz) of the photo-multiplier signals, the system can simultaneously measure density fluctuation in addition to the pitch angle of the magnetic field. Advantage of the new MSE BES diagnostic is as follows. (1) Simultaneous measurement of the safety factor (q) and density fluctuation at the identical spatial points (30 channels) is possible. (2) MSE BES diagnostic is not strongly affected by the magnetic field strength, as the electron cyclotron emission (ECE) diagnostic is, so that fluctuation measurement in flexible plasma condition is possible. (3) Measurement of the density fluctuation even outside the plasma is possible as described below. Using the MSE BES diagnostic, the following two types of MHD activities have been identified and investigated.

In core plasma, density fluctuation induced by rotating tearing mode islands has been observed. An MHD fluctuation is observed from $t=7$ s at a frequency of ~ 2.2 kHz, using magnetic probes. The poloidal and toroidal mode numbers are 2 and 1, respectively. Several channels of the MSE BES diagnostic near $q=2$ surface detected the MHD fluctuation having the same temporal evolution of frequency. The phase of the fluctuations measured by the MSE BES diagnostic is inverted at the $q=2$ surface measured by the MSE diagnostic, where the phase of the electron temperature fluctuations measured by the ECE diagnostic is also inverted. The phase inversion of the density and temperature fluctuations indicates a rotating magnetic-island structure.

In the scrape-off layer (SOL) of ELMy H-mode plasmas, strong intermittent emission coinciding with ELM crashes has been observed, showing increase in the SOL density at the crashes. Correlation analysis showed that the increase in density propagates outward at 0.69-2.2 km/s along the MSE measurement points, since the time-lag of emission between adjacent channels (70 mm distance) is 67 ± 35 μ s. The propagation velocity is consistent with that obtained by Langmuir probe measurements [2].

This work was partially supported by Grand-in-Aid for Young Scientists B No. 18760650 and Grand-in-Aid for Scientific Research No. 16082209 from MEXT.

References

- [1] Suzuki, T., et al., *Rev. Sci. Instrum.* **77**, 10E914 (2006).
[2] Asakura, N., et al., *J. Nucl. Mater.* **337-339**, 712 (2005).

10.6 Improvement of Tomography Technique for Two-Dimensional Visible Spectroscopic System of Divertor Plasmas [1]

K. Fujimoto, T. Nakano, H. Kubo, K. Sawada¹⁾, T. Takizuka,
K. Shimizu, H. Kawashima, N. Asakura
1) Shinshu University

Detached divertor plasmas have attractive properties to reduce energy and particle flux onto the divertor tiles. In detached divertor plasmas, ionization of D_2 molecules and D atoms and recombination of D^+ ions occurs contiguously. To understand the ionization and recombination, deuterium Balmer-series line emissions from the divertor plasmas was observed with a wide-spectral-band spectrometer. The spectrometer has 92 view channels (vertically 60, horizontally 32 channels) with a spectral resolution of about 1 nm. The two-dimensional distribution of the deuterium Balmer-series line emissions has been reconstructed with an algebraic reconstruction technique. Then a geometric pattern appeared and the reconstructed distribution was not accurate. Three types of combination of the calculation grid and view lines have been examined for improvement of the tomography technique. The combinations, (a) the square grid and the parallel view lines (S-P combination), (b) the square grid and the experimental view lines (S-E combination), and (c) the parallel grid and the experimental view lines (P-E combination), are shown in Fig.1.

A model distribution assumed the deuterium Balmer-series lines emission of inner detached divertor plasmas is used for the reconstruction test. The two-dimensional distribution obtained in the S-P combination case spread in a crisscross. The peak value of the obtained distribution was 69% of the peak value of the model distribution, and the normalized square sum of errors, ΔE , is 0.28. Since the two-dimensional distribution obtained in the S-E combination case had a clear geometric pattern, this combination wasn't appropriate. The peak value was 44% and the ΔE was 0.71. In the two-dimensional distribution obtained in the P-E combination case, the geometric pattern disappeared. The peak value was 65% and ΔE was 0.50. The P-E combination was better compared to the distribution with the S-E combination.

The deuterium Balmer-series lines in a detached divertor plasma were measured in an L-mode discharge. The plasma current, the toroidal magnetic field, the NBI heating power, and the electron density normalized by the Greenwald density limit were 1.0 MA, 3.6 T, 4.4 MW, and 64%, respectively. Since the distribution of the D_β emission obtained using the S-E combination had a geometric pattern, this distribution wasn't accurate. The geometric pattern is disappeared using the P-E combination. Therefore, the reconstruction was improved using the P-E combination. The D_β emission was strong above the inner strike point and near the outer strike point. The emissive region in the inner divertor area spread along the magnetic field lines.

Reference

[1] Fujimoto, K., et al., Plasma and Fusion Research **2**, S2211 (2007)

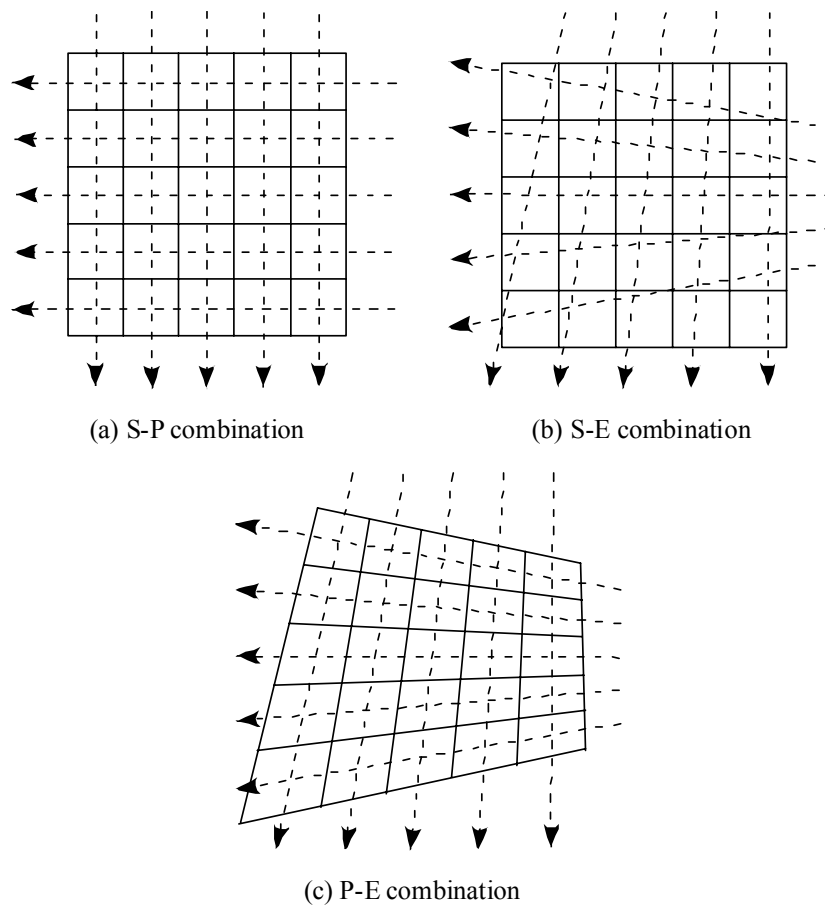


Fig.1 The combination of the calculation grid and the view lines,
(a) the square grid and view lines arranged parallel to the grid,
(b) the square grid and the experimental view lines,
(c) the grid arranged parallel to the view lines and the experimental view lines.

10.7 Measurements of Dust Movement in Main Chamber and Divertor

N. Asakura, H. Kawashima, N. Ohno¹⁾, T. Nakano, S. Takamura²⁾, Y. Uesugi³⁾

1)Nagoya Univ.2) Nagoya Univ, 3) Kanazawa Univ.

1. Introduction

Dusts in fusion devices will potentially cause damage to plasma facing components or viewing windows, and become impurity source, tritium reservoir in the shadowing area. Dust distribution in vacuum chamber has been investigated in tokamak and other magnetic fusion devices [1]. Trajectories of dust movement have been recently investigated in many fusion devices using visible and infrared TV cameras with fast frame rate of a few kHz. Study of dust transport from area where their source growing to final deposition area is necessary to understand influences on plasma performance and operation.

In the JT-60U tokamak, measurement of visible images emitted during their surface ablation started since 2006, using a fast TV camera located at tangential port. In this paper, measurements of dust movements in main chamber and divertor were presented. These results show velocity, direction and change of representative fast dust movements.

2. Fast TV camera measurement

Figure 1 shows the Fast TV camera system in JT-60U, and viewing scope is installed at a horizontal tangential port (P-17). Conventional plasma monitor camera is directory installed at the same port, and typical image of the plasma discharge and inside view of the vacuum vessel is shown in Fig. 2: dust image is observed as a bright line along the toroidal direction in one frame due to slow sampling rate of 30Hz. Optical image

is transferred to digital TV camera system (Photoron FastCAM II with full 6.5Gbyte memory) using 15m fiber-optics bundle consisting of 30000 quartz fine fibers. Images of the main and divertor plasmas can be measured by replacing two scopes for wide (35°) and narrow (9°) viewing angles, respectively, where spatial resolution corresponds to 1 and 0.3 cm

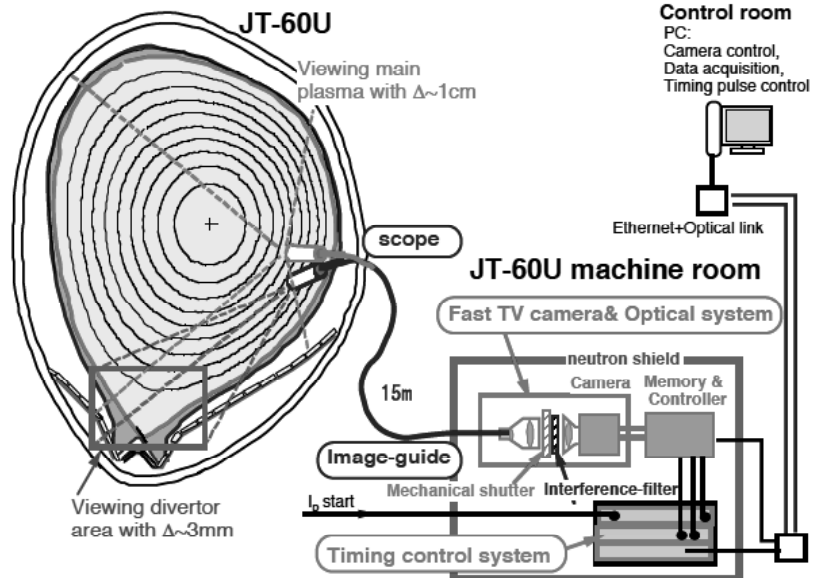


Fig. 1 Fast TV camera system in JT-60U. Wide and narrow viewing scopes are replaced for the main and divertor measurement, respectively. TV camera is incorporated in 10cm-thick polyethren neutral shield box at machine room, and controlled in control room.

at the focal distance (2.5-3 m). Typical frame rate and size of the fast TV camera were between 2 kHz for 1024x1024 pixels/frame and 8 kHz for 256x256 pixels/frame. Transmission of light guide is relatively low (~1/10) and its resolution of 30000 is smaller than resolution of camera pixels and the image intensifier. These determined the sampling rate and spatial resolution of the fast TV camera system.

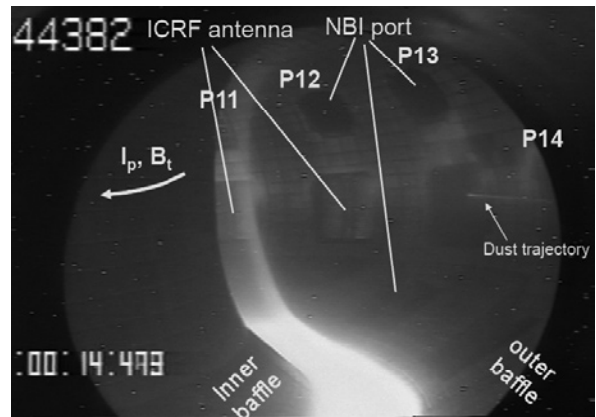


Fig. 2 Conventional CCD camera image of JT-60U L-mode hydrogen plasma, viewing from the same tangential port as fast TV camera. Dust trajectory is seen in the toroidal direction at right side.

3. Dust movement in main chamber

According to references 2 and 3, dust in fusion plasma is generally charged negatively ($Z \sim 10^3-10^4$), and the movement ($M_d dV_d/dt = F$) is determined by friction force by the SOL flow and diamagnetic and ExB drift flows (F_{fric}), Coulomb scattering (F_C), electro-static force by potential (F_E), gravitational force (F_g) and rocket force during ablation (F_{roc}). Line emission from the carbon and hydrogen ions is produced during dust ablation ($T_d > 2000-3000K$) in the SOL and edge plasmas, and life-time is determined by sputtering, RES, sublimation processes. Dust movement is also influenced

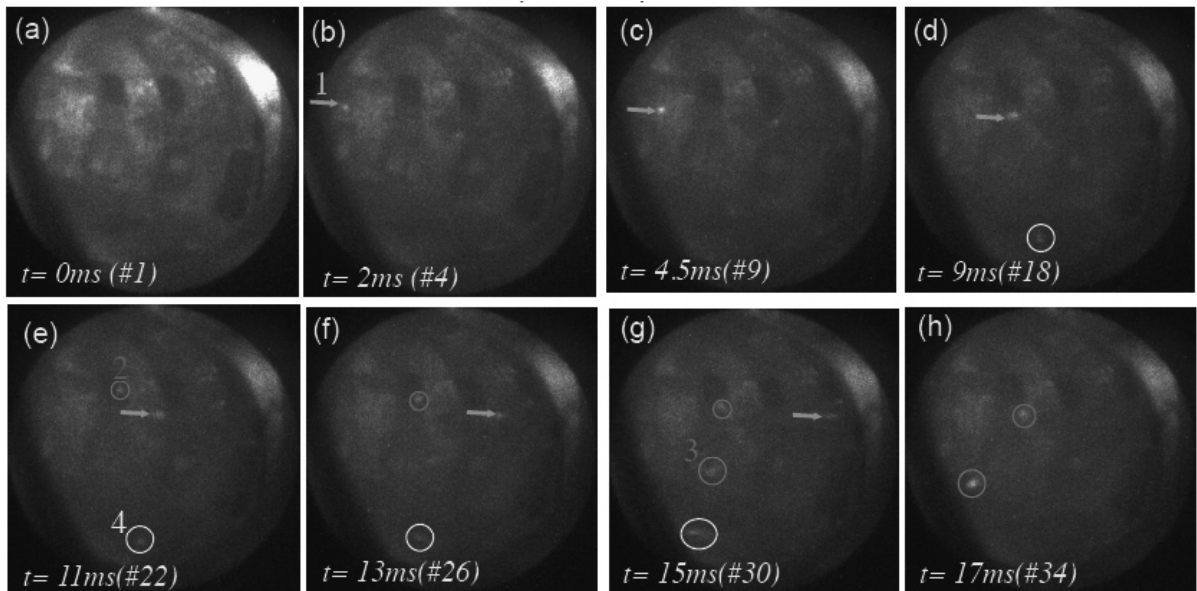


Fig. 3 Fast TV camera images and dust movement in ELMy H-mode plasma: E046034 (2kHz frame rate, full 1024x1024 image). ELM occurs at t=0ms (a). Dust (1) is moving from left (b) to right (g) direction. Dusts (2-4) appear and move to the different directions.

by specific geometry of Plasma Facing Component (PFC) such as the first wall and divertor as well as background plasma (core, SOL, sheath) and plasma turbulence (blob, ELM).

Trajectory and velocity of the relatively large emission image (a few mm) were measured in ELMy H-mode plasmas with relatively large injection power of 12-16MW as shown in Fig.3.

In main chamber, numbers of dust movements towards various directions, i.e. near-toroidally and/or near-poloidally, were observed, in particular, after large disruptions (power of a few MJ to the divertor and first wall) and long Glow-Discharge-Cleanin. For example, near-toroidal (ion drift/ co- I_p) movement of the emission (dust 1) was seen continuously in 28 frames. Trajectory of the ablating dust corresponded to 4.5m, thus the velocity is evaluated to be 0.32 km/s. Here, dust 2 moves slowly by 0.3-0.5 cm/12 frames in the poloidal and radial directions. It looks to move towards the main plasma after exhausted from NBI port with slow velocity of 0.05-0.1km/s. On the other hand, emissions from dust 3 and 4 are increased, thus they move towards the viewing port in the near toroidal (ion drift) direction.

In summary, many dusts move in the near-toroidal direction, and velocity is evaluated to be $V_{//}^d = 0.2-0.5$ km/s. The toroidal direction of the dust movement is consistent with that of the SOL flow, where $M_{//} \sim 0.3$ and $V_{//}^{SOL} = C_s M_{//} \sim 10$ km/s at the LFS midplane [4], but the $V_{//}^d$ is smaller than $V_{//}^{SOL}$, i.e. 2-5%.

4. Dust movement in divertor

Fast TV camera can measure the divertor area as shown in Fig. 4, with faster frame rate (6 kHz) and better special resolution (0.3cm). Many (small and large) dusts were observed in the high-field-side (inner) divertor just after ELM events, in particular, for the case that inner strike-point was located above that for the normal operations as shown in Fig. 4 (b). This is due to thermal stress on carbon deposition layers, which is caused by ELM heat and particle loadings to the fresh and thick carbon layers [1].

Movements of two dusts are shown in Fig. 4: dusts move in the toroidal and outboard directions after the ejection from the inner target. Toroidal velocities, $V_{//}$, are evaluated to be ~ 0.3 km/s ($=0.8$ m/2.7ms) and ~ 0.2 km/s ($=1$ m/5.5ms), which are similar to those at the main chamber. The direction (co- I_p direction) is consistent with measurement at the inner SOL [5]. On the other hand, specific movement of dusts was seen in low-field-side (outer) divertor: the dust moved towards separatrix (inboard) with the velocity of ~ 0.06 km/s and intensity of the emission was increasing. When ELM occurred, the direction of the movement changed away from separatrix (outboard).

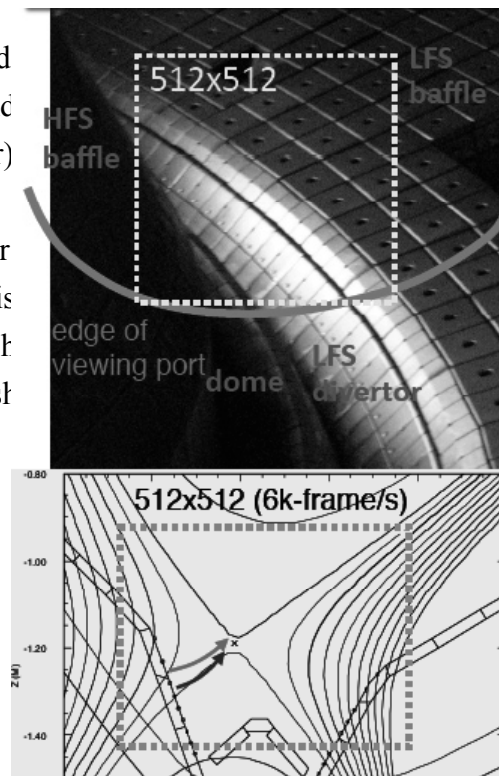


Fig. 4 (a) viewing area of the divertor scope with 6kHz sampling, 512x512 /frame. (b) plasma equilibrium in the divertor, and viewing area. Arrows show approximate trajectories of the dust movement from the inner target.

Change in background plasma parameter during the ELM event might influence on the dust movement.

As a result, ELM heat and particle loadings enhance dust ejection from the inner target, while plasma condition changes during the ELM to prevent the penetration of the dust into core plasma. Such dust dynamics is investigated in future.

5. Summary

Trajectory and velocity of emission image from dusts were measured with the fast visible TV camera from tangential port. In the main SOL, many dusts with various directions were observed, particularly, in the first shot after

hard disruptions (large ΔW_{dia}) and overnight (3-7 hours) He-GDC. Many dusts were ejected from the inner divertor, in particular, for the high strike-point case: large ELM heat and particle loading on thick deposition layers may enhance producing dusts due to large thermal stress. Velocity of toroidal movement (0.2-0.5km/s) was faster than that of poloidal/radial movement (0.05-0.1km/s). Toroidal movement was mostly towards the ion drift (I_p), which is consistent with the SOL flow measurement at HFS and LFS SOLs. Radial movement (at the LFS SOL) changed from inward to outward affected by change in the SOL plasma parameters at ELM. Systematic research will be planned from the start of 2007-8 experiments. At the same time, understanding of dust dynamics using the UEDGE/DUSTT simulation is initiated under collaboration with Kanazawa Univ.

Acknowledgments

This research was partly supported by the Grant-in-Aid for Scientific Research (B) 16360463 Japan Society for the Promotion Science.

References

- [1] Masaki, M., et al., J. Nucl. Mater. **337-339**, 553 (2005).
- [2] Krasheninnikov, S. I., et al., Phys. Plasmas **11**, 3141 (2004).
- [3] Krasheninnikov, S. I., et al., Plasma Phys. Control. Fusion **47**, A339 (2005).
- [4] Asakura, N., et al., Phys. Rev. Lett., **84**, 3093 (2000).
- [5] Asakura N., et al., Nucl. Fusion, **44** 503 (2004).

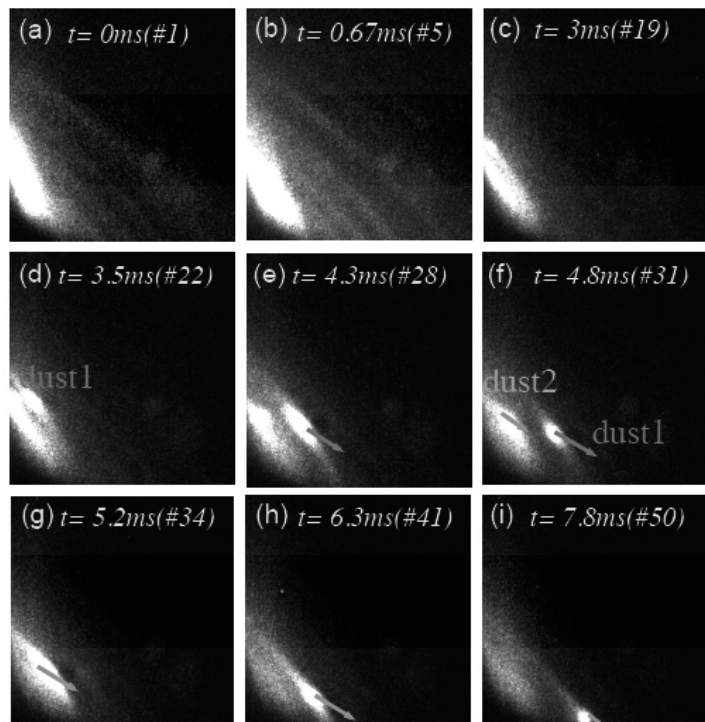


Fig. 5 Fast TV camera images and dust movement in ELMy H-mode plasma: E046950 (6kHz frame rate, 512x512 image). ELM occurs at $t=0\text{ms}$ (a). Dust (1) is moving from inner divertor target (d) to the outer and toroidal directions (f).

10.8 CO₂ Laser for Collective Thomson Scattering Diagnostic of α -particles in Burning Plasmas

T. Kondoh, T. Hayashi, Y. Kawano, Y. Kusama, T. Sugie, M. Hirata¹⁾, Y. Miura

1) Plasma Research Center, University of Tsukuba

A high-repetition and high-energy Transversely Excited Atmospheric (TEA) carbon dioxide (CO₂) laser for a collective Thomson scattering (CTS) diagnostic has been developed to establish a diagnostic method of confined α -particles in burning plasmas. To excite a single-transverse and single longitudinal mode, a continuous wave seed laser was injected to an unstable resonator with a cavity length of ~ 4.4 m as shown in Fig.1 and 2. Pulse energy of 18 J with a repetition rate of 10 Hz and 36 J with single shot operation has also been achieved in the multimode operation[1]. In order to obtain single-mode output, which is needed for CTS diagnostic, seed laser is injected into the cavity with unstable resonator. Pulse energy of 17 J with a repetition rate of 15 Hz has been achieved in a single-mode operation as shown in Fig. 3[2]. These results give a prospect for the CTS diagnostic on International Thermonuclear Experimental Reactor (ITER) which requires single-mode energy of 20 J with repetition rate of 40 Hz.

Preliminary design study of the CTS diagnostic in the tandem mirror GAMMA 10 shows that axial profiles of ion temperature will be obtained using a circumferential collection mirror of scattered power[2].

This work was supported by Grant-in-Aid for Scientific Research on Priority Areas "Advanced Diagnostics for Burning Plasmas" from the Ministry of Education, Culture, Sports, Science and Technology, No. 16082210.

References

- [1] Kondoh, T., et al., Rev. Sci. Instrum. **77**, 10E505 (2006).
[2] Kondoh, T., et al., Transactions of Fusion Science and Technology, **51**, 62 (2007).

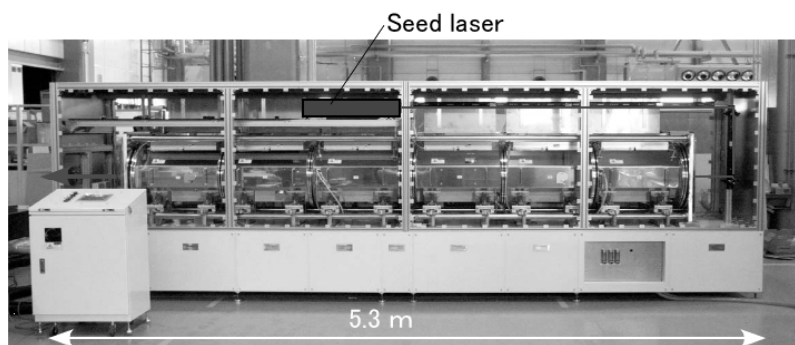


Fig. 1 Photograph of the high-repetition CO₂ laser developed for collective Thomson scattering diagnostic.

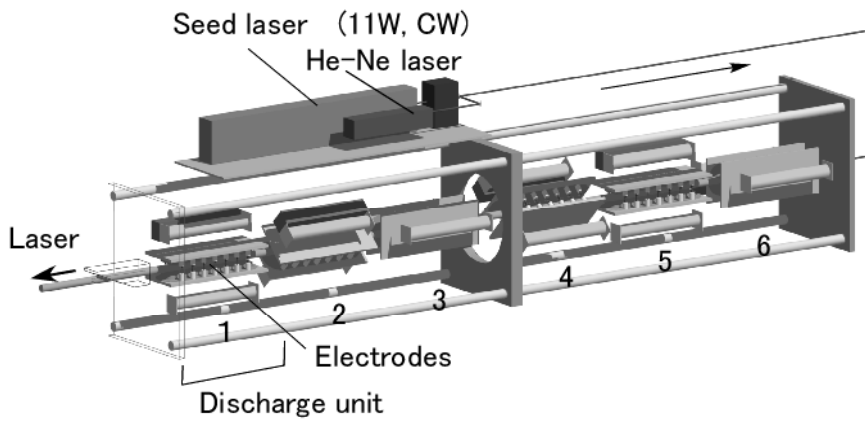


Fig. 2 Schematic view of the CO₂ laser. Six discharge units are combined in series to obtain high energy.

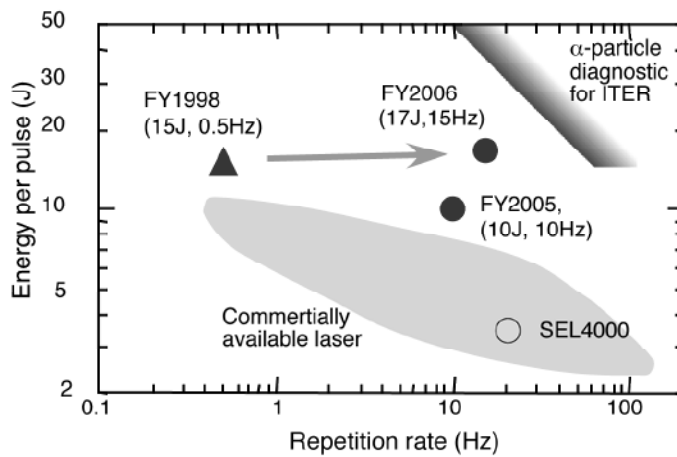


Fig. 3. Output energy of 17 J with a repetition rate of 15 Hz has been obtained. Target for ITER and commercially available lasers are also plotted.

10.9 High-Brightness and Low-Divergence Ion Gun for Lithium Beam Zeeman Polarimetry

A. Kojima, K. Kamiya, H. Iguchi¹⁾, T. Fujita, Y. Kamada

1) National Institute for Fusion Science

1. Introduction

Understanding of the structure formation of the edge pedestal region is one of the important issues for tokamaks. Particularly, the edge plasma current caused by the strong pressure gradient of H-mode plays an important role in the transport and MHD stability. Therefore, the measurement of the edge current profile at high time and spatial resolutions is expected in order to understand the behavior of the edge current and the impacts on the plasma performance.

The Zeeman polarimetry using a lithium beam probe (LiBP) has been developed on ASDEX, TEXT and DIII-D [1-3]. The pitch angle of the magnetic field line is measured from the polarization characteristics of the Zeeman component of the lithium $2^2S - 2^2P$ resonance line (670.8 nm). Because of the strong toroidal magnetic field (~ 4 T), clear Zeeman splitting (~ 0.08 nm) is expected in JT-60U. The LiBP has advantages in terms of the small beam radius and the large cross section for excitation. The lithium beam Zeeman polarimetry under constructing on JT-60U has a plan to realize the high time resolution by use of a high brightness lithium ion gun. Furthermore, the measurement at the high spatial measurement of the density and the edge fluctuation profiles are also planned.

2. Configuration of Lithium Beam Zeeman Polarimetry on JT-60U

The configuration of the Li beam Zeeman polarimetry on JT-60U is shown in Fig. 1. A thermionic ion source using β -eucryptite soaked to a porous tungsten disc and a neutralizer using the alkali metal vapor are utilized. The ion source with a diameter of 50 mm is a key point of the high-brightness ion gun. The acceleration electrodes give the beam extraction field of 500 kV/m. The divergence angle of the neutral beam depends on the focusing property of the beam optics and the location of the neutralizer. The well collimated beam is required for the diagnostic of the Zeeman polarimetry because the divergence of the beam causes the loss of the beam current at the observation area and the broadening of the Doppler shift of the emission line. As the distance from the neutralizer to the observation area is about 6.5 m in JT-60U case, the divergence angle within 0.13 degrees is required to attain the beam diameter of 30 mm which corresponds to the spot size in the observation area.

3. Numerical Simulation of Prototype Ion Gun [4]

A prototype ion gun has DIII-D type beam optics and ASDEX type neutralizer. The performance of the prototype ion gun is investigated by the numerical simulation taking into account the space charge effects. The TriComp beam simulation code (Field Precision LLC) is used for the simulation. Three different initial beam profiles at the ion source are assumed in the simulation, which are peaked, flat and hollow profiles. As a result of the simulation, the peaked profile has better focusing property than the hollow one. The divergence angle varies from -0.8 to 1.4 degrees in case of a beam energy of 30 keV, and the target value of 0.13 degrees is attained in only narrow range of radius as shown in Fig. 2(a). It shows that the total beam transport efficiency is low due to the large divergence angle. The peaked profile achieves the current of 0.9 mA at the observation area, while the current of 0.2 mA is obtained in the hollow case.

The obtained beam current linearly increases with the extracted current. However, it saturates and even reduces in larger current than 15 mA due to the increase of the beam divergence loss. The low efficiency of the prototype ion gun mainly arises from the divergence loss of the neutral beam. Therefore, the divergence angle is the most important parameter for the development of the ion gun on JT-60U because of the long transport of the neutral beam. The design study by use of the numerical simulation is necessary for the achievement of the low divergence ion gun.

4. Design Study of High-Brightness Low-Divergence Ion Gun

In order to improve the extracted current and the transport efficiency, the optimization of the beam optics is carried out by the numerical simulation. In the case of the prototype ion gun, the space charge limited current is 33 mA at beam energy of 30keV, however, the beam current is limited to 6.5 mA at beam energy of 10 keV. A low beam energy of 10 keV is required in JT-60U because a range of the pedestal electron density is $1\sim 3 \times 10^{19} \text{ m}^{-3}$. The reduction of the beam current at the low beam energy is a problem for the measurement at

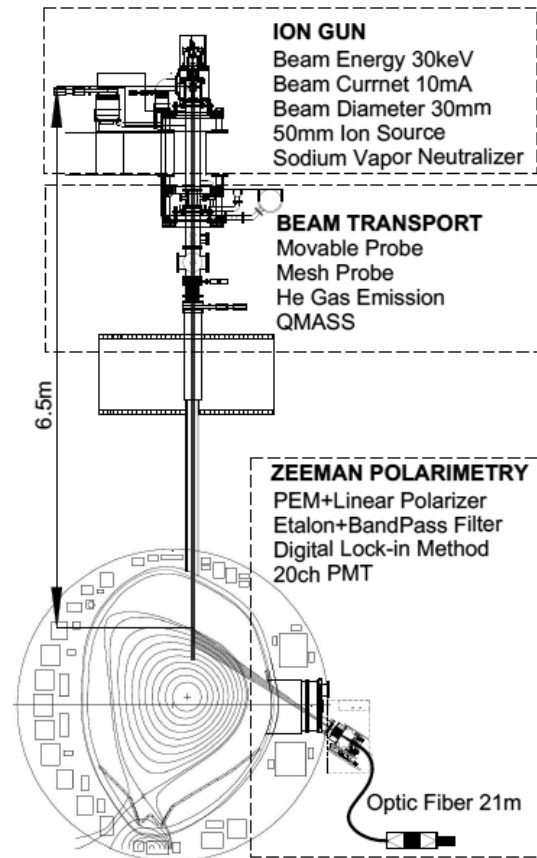


Fig.1. Schematic view of the configuration of Li beam Zeeman polarimetry on JT-60U.

low density plasma. Therefore, a new type of ion gun is designed as large beam current in a low beam energy. The new ion gun has an extraction electrode (extractor) to make the extraction electric field large even in a low beam energy as shown in Fig. 3. The ion beam is extracted by the extracted field of 600 kV/m independently of the beam energy, and decelerated to the target energy. Thus, the extracted current at the low beam energy is improved. Additionally, the large extraction field restrains the spreading of the low-energy and large-current beam.

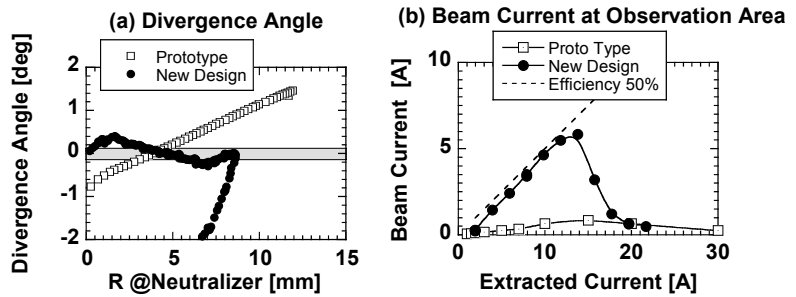


Fig.2. Results of the numerical simulation on the new type and the prototype ion guns. (a) Divergence angle at the neutralizer. (b) Obtained beam current at the observation area

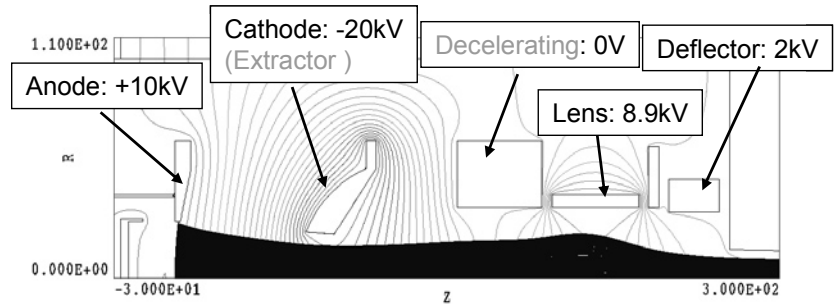


Fig.3. Configuration of the new type ion gun.

It is important for the optimization of the beam optics because the low-energy large-current beam is easy to spread due to the space charge effects. To improve the transport efficiency, the Einzel lens is optimized for the low energy beam dominated by the space charge. Since the focal point of the collimated beam is short in the case of large current beam, the distance from the Einzel lens and the neutralizer become short. The emission surface of the ion source is hollow type, which has the good convergence property. Then well collimated beam at a beam energy of 10 keV is achieved as shown in Fig. 2(a).

As a result, the transport efficiency is improved to 50% within the extracted current under 10 mA, and the beam current of 6 mA is obtained at the observation area as shown in Fig. 2(b). The increase of the beam energy gives better focusing property above the extracted current of 15 mA

5. Initial Results of Ion Beam Extraction by Prototype Ion Gun

The Li ion beam is extracted by the prototype ion gun in the mock-up test stand. The Li ions are produced by the contact ionization of the Li vapor to the porous tungsten disk. The tungsten disk is heated at the operation temperature of 1200°C by the mechanical heater with power of 1.5 kW. However, the mechanical heater has the temperature limit at 1200 °C, and then the sufficient temperature of the tungsten disk and large beam current have not been

obtained due to the radiation loss and the reduction of heat conduction. Therefore, the ion beam extraction has been tried by coating the molybdenum surface without the tungsten disk. The β -eucryptite of 1 g is coated on the molybdenum surface at a temperature of 1100 ° C. Figure 4 shows the experimental result of the voltage-current property of the power supply for the acceleration. The acceleration current of 11 mA is achieved for 150 second at the acceleration voltage of 30 kV. However, it is considered that the acceleration current does not exactly show the ion current because the acceleration current includes the extracted Li ion current and the back-flow of the secondary electron, For this reason, we use a multi-channel probe to measure the ion current at the position of the neutralizer. The probe measurements almost agree with the acceleration current as shown in Fig. 4. (a).

As a result, the large current extraction over 10 mA is demonstrated; however, the lifetime of the beam extracted from molybdenum surface is short which is about 3 Asec, and the operation is limited to one-time because of falling off of the coated β -eucryptite. Therefore, an ion source using the electron beam is under development to heat the porous tungsten disk to the sufficient temperature.

6. Summary

The Li ion gun is developed for the Zeeman polarimetry. The performance of the prototype ion gun is estimated by the numerical simulation. According to the simulation, the beam transport efficiency is low due to the broadening of the divergence angle. Therefore, the new ion gun is designed to improve the divergence angle and beaming extraction field.

The ion beam extraction of the prototype ion gun is carried out by the ion source coated with Mo. Then the large current extraction over 10 mA is demonstrated. For improvement of the life time of the ion source, the ion source using electron beam heating is under development.

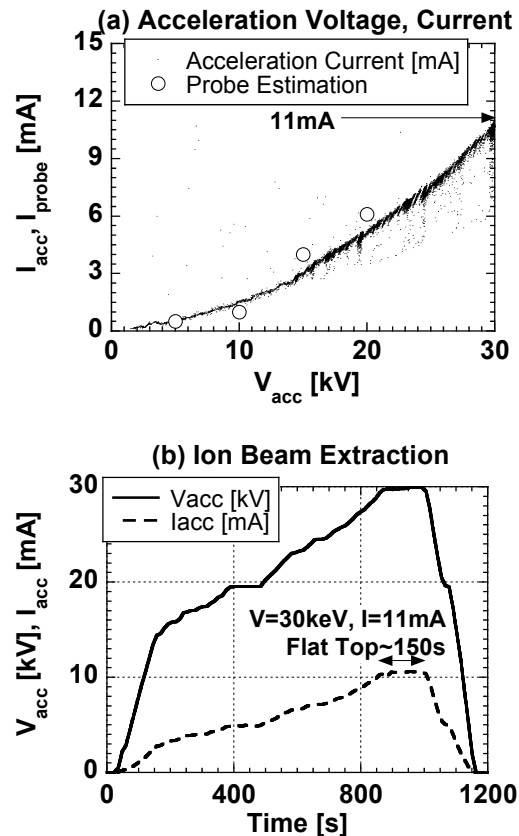


Fig.4. Results of the ion beam extraction. (a) Relation between the acceleration voltage and current. (b) Time evolution of the acceleration energy and current.

References

- [1] West, W. P., et al., Phys. Rev. Lett. **58**, 2758 (1987).
- [2] West, W. P., Rev. Sci. Instrum. **57**, 2006 (1986).
- [3] Thomas, D. M., et al., Rev. Sci. Instrum. **72**, 1023 (2001).
- [4] Kojima, A., et al., Plasma Fusion Res. **2**, S1104 (2007)

10.10 Fast Data Acquisition System Based on Digital Oscilloscopes for Fluctuation Measurements in a Long-Pulse Plasma [1]

G. Matsunaga, M. Takechi and K. Toi¹⁾

1) National Institute for Fusion Science

For fluctuation measurements in a long-pulse JT-60U tokamak plasma, we have developed a new data acquisition system with a fast sampling rate. This system is based on a powerful digital oscilloscope, which has very large acquisition memory up to 50 Mwords/ch, 1 MHz sample rate and 16-bit high resolution AD convertor. The system is composed of plural digital oscilloscopes and mass storages. On this system, most of data acquisition processes are executed at each digital oscilloscope. This feature of the system leads to an advantage that the processing loads are distributed among several digital oscilloscopes. Comparing with conventional data acquisition systems based on CAMAC modules, the system has several advantages as follows:

- Compatibility of fast sampling (≤ 1 MHz) with long duration (≤ 50 sec).
- Easiness of introduction (just connect, just acquire and monitor).
- Easiness of extension of the number of channels.
- Networking supported by the Ethernet technology.
- Reasonable cost.
- Distribution of processing load.
- Easy handling of massive data.

This system has been successfully employed for measurements of various fluctuations obtained through magnetic probes, beam emission spectroscopy and so on. These enable us to obtain high quality fluctuation data, for instance, fast frequency MHD events such as Alfvén eigenmodes (AE), neoclassical tearing modes (NTM), edge localized modes (ELM) and so on in a long pulse discharge. The size of the acquired data using this system has reached up to 10 GB/shot, so far. We plan to apply this system to other fluctuation measurements toward the next JT-60 experimental campaign.

Reference

- [1] G. Matsunaga et al., *Fusion Engineering and Design* **82**, 207 (2007)

11. Heating Systems

11.1 A 21 s, 3.2 MW D⁰ Beam Injection from Negative-Ion-Based NBI

M. Hanada, M. Kamada, L.R.Grisham, M. Kawai, Y. Ikeda and NBI heating Gr.

In JT-60U, it is intended to inject 10 MW D⁰ beams for 10 s using two large negative ion sources, each of which is designed to produce 22 A, 500 keV D⁻ ion beam. Recently, the beam pulse length is required to be extended up to 30 s in order to study quasi-steady state plasma in JT-60U. From the estimation of the power supply capacity, the injected beam power is limited to be < 4 MW for the injection time of 30 s. Under these conditions, a long pulse injection of the beams from the negative-ion-based NBI on JT-60 U was carried out by clarifying operational ranges for a stable voltage holding capability and an allowable grid power loading in the JT-60 negative ion source.

To choose the stable acceleration voltage, a correlation between the voltage holding capability and a light intensity of cathodeluminescence from the Fiber Reinforced Plastic insulator was carefully examined. As the result, the stable voltage holding capability without the beam acceleration was found to be < 420 kV where the light was sufficiently suppressed [1]. Since stable acceleration voltage with which is stable with beam acceleration was 70-80% of that without the beam acceleration, 320-340 kV was chosen as the beam acceleration voltage (V_{acc}).

In order to attain the beam pulse length of > 30 s, the grid power loading should be reduced to < 1 MW with which the surface temperature of the grid is calculated to be lower than the re-crystallization temperature (250 °C) of the grid material (oxygen-free cooper). The extraction voltage (V_{ext}) and the arc power (P_{arc}) were tuned to minimize the grid power loading while the injection power was maximized. At V_{acc}=340 kV, V_{ext}=5.5 kV and P_{arc}=180 kW, the maximum grid power loading was on the grounded grid, and was allowable level of 650 kW. The D⁻ ion beams of 30 A were produced with two ion sources and neutralized to 3.2 MW D⁰ beams by a gas neutralizer.

The pulse length of 3.2 MW D⁰ beam was extended step by step, and finally reached up to 21 s which was limited by the surface temperature interlock of the beam scraper without water cooling [2]. This is the first long pulse injection of > 20 s in a power range of > 3 MW in the world. No degradation of the negative ion production was observed due to the pulse extension. Moreover, the grid power loading was kept constant. The water temperature rise in the grids was saturated to be 40 °C at 18 s. This short saturation time suggests that the further extension of the beam pulse length can be achieved at this power level by the present grid cooling technology. By increasing the interlock level of the surface temperature on the beam scraper, the 30 s injection is to be carried out in the next campaign.

References

- [1] Hanada M., et al., IEEE Transactions on Dielectrics and Electrical Insulation, Vo. 14, No.3, p.572-576(2007).
- [2] Hanada M., et. al., Nuclear Fusion, Vol.47, No.9, p.1142-1146(2007).

11.2 Oscillation Control on the ECRF System and Performance of the LHRF Launcher

S. Moriyama, M. Seki, S. Ide, T. Fujii

1. Introduction

A high-power electron cyclotron range of frequency (ECRF) heating system was introduced into JT-60U to realize high performance plasmas by controlling profiles of electron temperature, plasma current and plasma pressure [1]. Its injection power was designed to be 3 MW for 5 s at 110 GHz with four 1 MW output gyrotrons. RF power of 3 MW for 2.8 s was injected into plasmas by 2002. Technologies, relevant to power increase, extension of the pulse duration, power modulation and so on, have been developing for various experiments. The technology on the extension of the pulse duration is most significant as the JT-60 discharge duration was increased from 15 s to 65 s in 2003. A tentative objective of the ECRF system is to inject 0.6 MW for 30 s in the limitation of the existing power. Then, a technique on the extension of pulse duration by anode voltage and heater current control has been developed. The anode voltage control can also be applied to the power modulation to study the electron heat transport [2].

On the other hand, main objective of the LHRF system in recent experiments is real time current profile control. Real time off-axis current profile control to maintain or to improve high performance in an advanced tokamak is the final goal. The safety factor (q) profile is reconstructed in real time by means of the multi point motional Stark effect (MSE) measurement, and to be feed back controlled to the reference q profile. Recent real time current profile control in recent high normalized beta (β_N) experiments succeeded to modify the q profile to suppress an MHD activity to raise β_N . For these purposes, extension of the LHRF pulse length aiming at 20 s has been tried.

2. Extension of ECRF Pulse Duration

The JT-60U gyrotron has a triode electron gun for flexible operation as shown in Fig. 1. On such a gyrotron, the gyrotron oscillation can be drastically controlled by small change of the anode voltage. Therefore, an anode voltage controller was developed, which was mainly composed of solid-state devices of 400 stages of Zener circuits as a variable resistance in Fig 1.

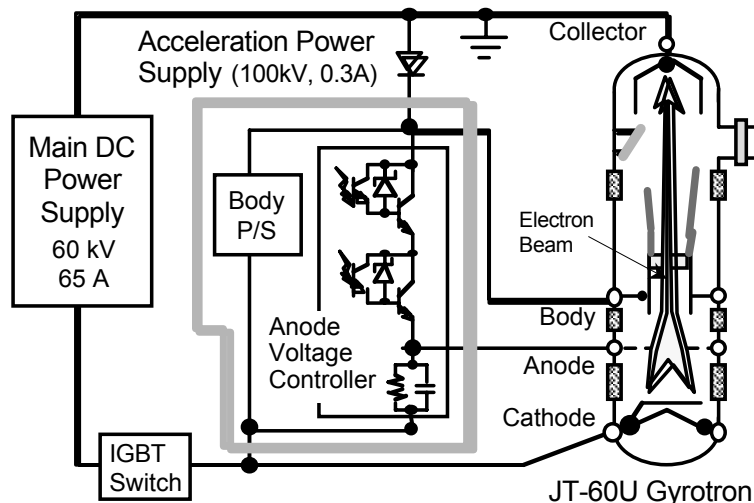


Figure 1. JT-60U gyrotron and its power supply system.

When the ECRF pulse duration would be extended to 30 s, the beam current decreased due to the cathode cooling and the gyrotron oscillation was terminated. After that, the beam current was turned off immediately to protect the gyrotron components from overheat. The anode voltage and heater current control solved this problem. As shown in Fig. 2, the gyrotron oscillation was recovered by adjusting the anode voltage within 80 ms, in which the turn-off of the beam current was delayed, when it was terminated. The pulse duration to the plasma was successfully extended up to 21 s so far in 2006 at gyrotron output power of 0.4 MW.

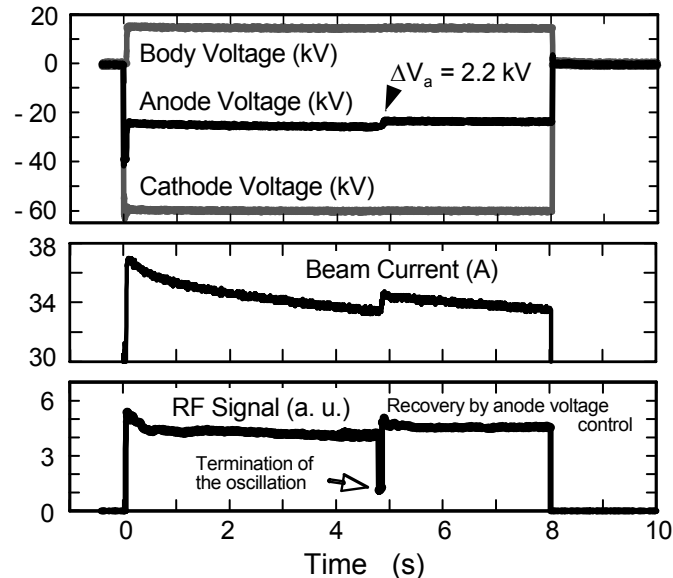


Figure 2. Recovery of the oscillation by anode voltage control.

3. ECRF Power Modulation

In order to study the electron heat transport in JT-60U, performances required for the ECRF power modulation were the modulation frequency range of 10 - 100 Hz and the modulated power of 1 MW. The anode voltage control was also applied to the power modulation, which was quite easier than the main DC voltage control since only several mA currents flowed on the anode line. Changing the anode voltage by only 3 - 4 kV, which was about 10 % of the anode voltage, could carry out the power modulation. So far, the achieved performances to the JT-60U plasmas are in the modulation frequency range of 10 - 500 Hz with modulation factor 80 % at the output power of 0.7 MW. At a test bench, trial to obtain higher modulation frequency required for experiments of neoclassical tearing mode (NTM) stabilization in near future have been performed. The modulation frequency up to 2.5 kHz was achieved so far with some improvements in the high voltage supplying circuit to the gyrotron and anode voltage controller.

4. Performance of the LHRF Launcher

LH experiments such as real time control of plasma current profile were performed using LH system, especially with 8-carbon grills around LHRF launcher mouth since August 2003. After one-year operation, no major damage was observed on the carbon grills itself, on the other hand some base plates as an attachment for the grill were melted. Main cause was

mis-working of the arc detector to protect LHRF antenna mouth at RF breakdowns. Therefore for suppression of damages around LH antenna mouth, checking lump of the arc detector is improved and detecting speed is increased. And a new protection device using ccd-camera is also introduced. The 6-modules without carbon grill are used for LH experiments, stable injections are obtained as 1.1 MW for 20 s (18.64 MJ) in 2006.

On the other hand, to improve insufficient electrical contact along the carbon grill, a new structural carbon grill is developed at a test bench by using "a diffusion bonding method". This new carbon grill is combined with a pedestal made of SUS. RF connection point exists between the pedestal and LH launcher mouth. In the RF connection point, a fine spring is inserted as a RF connector. The test module for the new carbon grill shows enough power capability of 0.5 MW - 10 sec at the test bench. This technology will be applicable to the LH launcher in JT-60U.

References

- [1] Y. Ikeda and A. Kasugai et al., Fusion Science Technology, vol. 42, pp. 435-451, 2002.
- [2] M. Cox and N. Deliyannis et al., Nuclear Fusion, vol. 33, pp. 1657-1676, 1993.

Acknowledgments

The authors wish to acknowledge dedicated efforts of the members of Japan Atomic Energy Agency in support of the JT-60 program. They also wish to express their gratitude for domestic and international collaborations for the JT-60 experiments.

国際単位系 (SI)

表1. SI 基本単位

基本量	SI 基本単位	
	名称	記号
長さ	メートル	m
質量	キログラム	kg
時間	秒	s
電流	アンペア	A
熱力学温度	ケルビン	K
物質質量	モル	mol
光度	カンデラ	cd

表2. 基本単位を用いて表されるSI組立単位の例

組立量	SI 基本単位	
	名称	記号
面積	平方メートル	m ²
体積	立方メートル	m ³
速度	メートル毎秒	m/s
加速度	メートル毎秒毎秒	m/s ²
波数	毎メートル	m ⁻¹
密度 (質量密度)	キログラム毎立方メートル	kg/m ³
質量体積 (比体積)	立法メートル毎キログラム	m ³ /kg
電流密度	アンペア毎平方メートル	A/m ²
磁界の強さ	アンペア毎メートル	A/m
(物質質量の)濃度	モル毎立方メートル	mol/m ³
輝度	カンデラ毎平方メートル	cd/m ²
屈折率	(数の) 1	1

表5. SI 接頭語

乗数	接頭語	記号	乗数	接頭語	記号
10 ²⁴	ヨタ	Y	10 ⁻¹	デシ	d
10 ²¹	ゼタ	Z	10 ⁻²	センチ	c
10 ¹⁸	エクサ	E	10 ⁻³	ミリ	m
10 ¹⁵	ペタ	P	10 ⁻⁶	マイクロ	μ
10 ¹²	テラ	T	10 ⁻⁹	ナノ	n
10 ⁹	ギガ	G	10 ⁻¹²	ピコ	p
10 ⁶	メガ	M	10 ⁻¹⁵	フェムト	f
10 ³	キロ	k	10 ⁻¹⁸	アト	a
10 ²	ヘクト	h	10 ⁻²¹	ゼプト	z
10 ¹	デカ	da	10 ⁻²⁴	ヨクト	y

表3. 固有の名称とその独自の記号で表されるSI組立単位

組立量	SI 組立単位			
	名称	記号	他のSI単位による表し方	SI基本単位による表し方
平面角	ラジアン ^(a)	rad		m ² ・m ⁻¹ =1 ^(b)
立体角	ステラジアン ^(a)	sr ^(c)		m ² ・m ⁻² =1 ^(b)
周波数	ヘルツ	Hz		s ⁻¹
力	ニュートン	N		m ² ・kg ² ・s ⁻²
圧力, 応力	パスカル	Pa	N/m ²	m ⁻¹ ・kg ² ・s ⁻²
エネルギー, 仕事, 熱量	ジュール	J	N・m	m ² ・kg ² ・s ⁻²
工率, 放射束	ワット	W	J/s	m ² ・kg ² ・s ⁻³
電荷, 電気量	クーロン	C		s ² ・A
電位差 (電圧), 起電力	ボルト	V	W/A	m ² ・kg ² ・s ⁻³ ・A ⁻¹
静電容量	ファラド	F	C/V	m ⁻² ・kg ⁻¹ ・s ⁴ ・A ²
電気抵抗	オーム	Ω	V/A	m ² ・kg ² ・s ⁻³ ・A ⁻²
コンダクタンス	ジーメン	S	A/V	m ⁻² ・kg ⁻¹ ・s ³ ・A ²
磁束	ウェーバ	Wb	V・s	m ² ・kg ² ・s ⁻² ・A ⁻¹
磁束密度	テスラ	T	Wb/m ²	kg ² ・s ⁻² ・A ⁻¹
インダクタンス	ヘンリー	H	Wb/A	m ² ・kg ² ・s ⁻² ・A ⁻²
セルシウス温度	セルシウス度 ^(d)	°C		K
光束	ルーメン	lm	cd・sr ^(c)	m ² ・m ⁻² ・cd=cd
照射 (放射能)	グレイ	Gy	J/kg	m ² ・m ⁻¹ ・cd=m ² ・cd
吸収線量, 質量エネルギー分与, カーマ線量当量, 周辺線量当量, 方向性線量当量, 個人線量当量, 組織線量当量	グレイ	Gy	J/kg	m ² ・s ⁻²
	シーベルト	Sv	J/kg	m ² ・s ⁻²

- (a) ラジアン及びステラジアンの使用は、同じ次元であっても異なった性質をもった量を区別するときの組立単位の表し方として利点がある。組立単位を形作る際のいくつかの用例は表4に示されている。
 (b) 実際には、使用する際には記号rad及びsrが用いられるが、習慣として組立単位としての記号“1”は明示されない。
 (c) 測光学では、ステラジアンの名称と記号srを単位の表し方の中にそのまま維持している。
 (d) この単位は、例としてミリセルシウス度m°CのようにSI接頭語を併せて用いても良い。

表4. 単位の中に固有の名称とその独自の記号を含むSI組立単位の例

組立量	SI 組立単位			
	名称	記号	SI 基本単位による表し方	
粘力のモーメント	ニュートンメートル	N・m	m ² ・kg ² ・s ⁻²	
表面張力	ニュートン毎メートル	N/m	kg ² ・s ⁻²	
角速度	ラジアン毎秒	rad/s	m ² ・m ⁻¹ ・s ⁻¹ =s ⁻¹	
角加速度	ラジアン毎平方秒	rad/s ²	m ² ・m ⁻¹ ・s ⁻² =s ⁻²	
熱流密度, 放射照度	ワット毎平方メートル	W/m ²	kg ² ・s ⁻³	
熱容量, エントロピー	ジュール毎ケルビン	J/K	m ² ・kg ² ・s ⁻² ・K ⁻¹	
質量熱容量 (比熱容量), 質量エントロピー	ジュール毎キログラム毎ケルビン	J/(kg・K)	m ² ・s ⁻² ・K ⁻¹	
質量エネルギー (比エネルギー)	ジュール毎キログラム	J/kg	m ² ・s ⁻² ・K ⁻¹	
熱伝導率	ワット毎メートル毎ケルビン	W/(m・K)	m ² ・kg ² ・s ⁻³ ・K ⁻¹	
体積エネルギー	ジュール毎立方メートル	J/m ³	m ⁻¹ ・kg ² ・s ⁻²	
電界の強さ	ボルト毎メートル	V/m	m ² ・kg ² ・s ⁻³ ・A ⁻¹	
体積電荷	クーロン毎立方メートル	C/m ³	m ⁻³ ・s ² ・A	
電気変位	クーロン毎平方メートル	C/m ²	m ⁻² ・s ² ・A	
誘電率	ファラド毎メートル	F/m	m ⁻³ ・kg ⁻¹ ・s ⁴ ・A ²	
透磁率	ヘンリー毎メートル	H/m	m ² ・kg ² ・s ⁻² ・A ⁻²	
モルエネルギー	ジュール毎モル	J/mol	m ² ・kg ² ・s ⁻² ・mol ⁻¹	
モルエントロピー, モル熱容量	ジュール毎モル毎ケルビン	J/(mol・K)	m ² ・kg ² ・s ⁻² ・K ⁻¹ ・mol ⁻¹	
照射線量 (X線及びγ線)	グレイ	Gy	J/kg	m ² ・s ⁻²
吸収線量	グレイ	Gy	J/kg	m ² ・s ⁻²
放射強度	ワット毎ステラジアン	W/sr	m ⁴ ・m ⁻² ・kg ² ・s ⁻³ =m ² ・kg ² ・s ⁻³	
放射輝度	ワット毎平方メートル毎ステラジアン	W/(m ² ・sr)	m ² ・m ⁻² ・kg ² ・s ⁻³ =kg ² ・s ⁻³	

表6. 国際単位系と併用されるが国際単位系に属さない単位

名称	記号	SI 単位による値
分	min	1 min=60s
時	h	1h=60 min=3600 s
日	d	1 d=24 h=86400 s
度	°	1°=(π/180) rad
分	'	1'=(1/60)°=(π/10800) rad
秒	"	1"=(1/60)'=(π/648000) rad
リットル	l, L	1l=1 dm ³ =10 ⁻³ m ³
トン	t	1t=10 ³ kg
ネーパ	Np	1Np=1
ベル	B	1B=(1/2) ln10(Np)

表7. 国際単位系と併用されこれに属さない単位でSI単位で表される数値が実験的に得られるもの

名称	記号	SI 単位であらわされる数値
電子ボルト	eV	1eV=1.60217733(49)×10 ⁻¹⁹ J
統一原子質量単位	u	1u=1.6605402(10)×10 ⁻²⁷ kg
天文単位	ua	1ua=1.49597870691(30)×10 ¹¹ m

表8. 国際単位系に属さないが国際単位系と併用されるその他の単位

名称	記号	SI 単位であらわされる数値
海里		1海里=1852m
ノット		1ノット=1海里毎時=(1852/3600)m/s
アール	a	1a=1 dam ² =10 ² m ²
ヘクタール	ha	1ha=1 hm ² =10 ⁴ m ²
バール	bar	1bar=0.1MPa=100kPa=1000hPa=10 ⁵ Pa
オングストローム	Å	1Å=0.1nm=10 ⁻¹⁰ m
バーン	b	1b=100fm ² =10 ⁻²⁸ m ²

表9. 固有の名称を含むCGS組立単位

名称	記号	SI 単位であらわされる数値
エルグ	erg	1 erg=10 ⁻⁷ J
ダイン	dyn	1 dyn=10 ⁻⁵ N
ポインズ	P	1 P=1 dyn・s/cm ² =0.1Pa・s
ストークス	St	1 St=1cm ² /s=10 ⁻⁴ m ² /s
ガウス	G	1 G ≐ 10 ⁻⁴ T
エルステッド	Oe	1 Oe ≐ (1000/4π) A/m
マクスウェル	Mx	1 Mx ≐ 10 ⁻⁸ Wb
スチルブ	sb	1 sb = 1cd/cm ² =10 ⁴ cd/m ²
ホト	ph	1 ph=10 ⁴ lx
ガリ	Gal	1 Gal = 1cm/s ² =10 ⁻² m/s ²

表10. 国際単位に属さないその他の単位の例

名称	記号	SI 単位であらわされる数値
キュリー	Ci	1 Ci=3.7×10 ¹⁰ Bq
レントゲン	R	1 R = 2.58×10 ⁻⁴ C/kg
ラド	rad	1 rad=1cGy=10 ⁻² Gy
レム	rem	1 rem=1 cSv=10 ⁻² Sv
X線単位	1X unit	1X unit=1.002×10 ⁻⁴ nm
ガンマ	γ	1γ=1 nT=10 ⁻⁹ T
ジャンスキー	Jy	1 Jy=10 ⁻²⁶ W・m ⁻² ・Hz ⁻¹
フェルミ	1 fermi	1 fermi=1 fm=10 ⁻¹⁵ m
メートル系カラット	metric carat	1 metric carat = 200 mg = 2×10 ⁻⁴ kg
トル	Torr	1 Torr = (101 325/760) Pa
標準気圧	atm	1 atm = 101 325 Pa
カロリ	cal	
マイクロン	μ	1 μ = 1μm=10 ⁻⁶ m

